

**AWARD NUMBER:**

W81XWH-18-1-0412

**TITLE:**

Characterization of Acute Exposure to Toxic Metals in Military Environments and Personnel

**PRINCIPAL INVESTIGATOR:**

Todd Giorgio, Ph.D.

**CONTRACTING ORGANIZATION:**

Vanderbilt University, Nashville, TN

**REPORT DATE:**

September 2021

**TYPE OF REPORT:**

Annual

PREPARED FOR: U.S. Army Medical Research and Development Command  
Fort Detrick, Maryland 21702-5012

DISTRIBUTION STATEMENT: Approved for Public Release;  
Distribution Unlimited

The views, opinions and/or findings contained in this report are those of the author(s) and should not be construed as an official Department of the Army position, policy or decision unless so designated by other documentation.

# REPORT DOCUMENTATION PAGE

Form Approved  
OMB No. 0704-0188

Public reporting burden for this collection of information is estimated to average 1 hour per response, including the time for reviewing instructions, searching existing data sources, gathering and maintaining the data needed, and completing and reviewing this collection of information. Send comments regarding this burden estimate or any other aspect of this collection of information, including suggestions for reducing this burden to Department of Defense, Washington Headquarters Services, Directorate for Information Operations and Reports (0704-0188), 1215 Jefferson Davis Highway, Suite 1204, Arlington, VA 22202-4302. Respondents should be aware that notwithstanding any other provision of law, no person shall be subject to any penalty for failing to comply with a collection of information if it does not display a currently valid OMB control number. **PLEASE DO NOT RETURN YOUR FORM TO THE ABOVE ADDRESS.**

<b>1. REPORT DATE</b> September 2021		<b>2. REPORT TYPE</b> Annual		<b>3. DATES COVERED</b> 01Sep2020-31Aug2021	
<b>4. TITLE AND SUBTITLE</b>  Characterization of Acute Exposure to Toxic Metals in Military Environments and Personnel				<b>5a. CONTRACT NUMBER</b>	
				<b>5b. GRANT NUMBER</b> W81XWH-18-1-0412	
				<b>5c. PROGRAM ELEMENT NUMBER</b>	
<b>6. AUTHOR(S)</b> Todd Giorgio, Ph.D.  E-Mail: todd.d.giorgio@vanderbilt.edu				<b>5d. PROJECT NUMBER</b>	
				<b>5e. TASK NUMBER</b>	
				<b>5f. WORK UNIT NUMBER</b>	
<b>7. PERFORMING ORGANIZATION NAME(S) AND ADDRESS(ES)</b>  Vanderbilt University 2201 West End Avenue Nashville, TN 37235				<b>8. PERFORMING ORGANIZATION REPORT NUMBER</b>	
<b>9. SPONSORING / MONITORING AGENCY NAME(S) AND ADDRESS(ES)</b>  U.S. Army Medical Research and Development Command Fort Detrick, Maryland 21702-5012				<b>10. SPONSOR/MONITOR'S ACRONYM(S)</b>	
				<b>11. SPONSOR/MONITOR'S REPORT NUMBER(S)</b>	
<b>12. DISTRIBUTION / AVAILABILITY STATEMENT</b>  Approved for Public Release; Distribution Unlimited					
<b>13. SUPPLEMENTARY NOTES</b>					
<b>14. ABSTRACT</b> Military personnel in modern conflicts are exposed to toxic metals from embedded fragments generated by explosive devices and inhaled near burn pits. Metal levels among veterans are centrally monitored, but to truly establish the impact of toxic metals on military personnel's health it is necessary to establish the peak exposure. No device exists to simultaneously detect and quantify multiple toxic metals in biological and environmental samples near the time of peak exposure. We hypothesize that a zinc oxide nanowire substrate decorated with gold nanoparticles and decorated with chelating ligands can sensitively detect toxic metals via surface-enhanced Raman spectroscopy (SERS). A patterned bed of ZnO nanowires will be grown and decorated with gold nanoparticles. Crown ethers identified based on selectivity for multiple toxic metals will functionalize the nanostructure. Sensitivity will be measured by parallel Raman studies of each selected ion coordinated with each crown ether, with and without plasmonic enhancement. Specificity will be assessed by SERS of each toxic metal in the presence of distractors. Selectivity of the crown ligands will be assessed by spectral analysis in the presence of distractors. Spectral analysis will also identify the optimal crown ethers for simultaneous, multiplexed sensing of the chosen toxic metals. Sensors in this optimized configuration will be fabricated and experimentally validated against predicted performance.					
<b>15. SUBJECT TERMS</b> None listed.					
<b>16. SECURITY CLASSIFICATION OF:</b>			<b>17. LIMITATION OF ABSTRACT</b>	<b>18. NUMBER OF PAGES</b>	<b>19a. NAME OF RESPONSIBLE PERSON</b>
<b>a. REPORT</b>	<b>b. ABSTRACT</b>	<b>c. THIS PAGE</b>			<b>19b. TELEPHONE NUMBER (include area code)</b>
Unclassified	Unclassified	Unclassified	Unclassified	192	USAMRDC

## TABLE OF CONTENTS

	<u>Page</u>
1. Introduction	3
2. Keywords	3
3. Accomplishments	3
4. Impact	15
5. Changes/Problems	15
6. Products	17
7. Participants & Other Collaborating Organizations	18
8. Special Reporting Requirements	20
9. Appendices	20

## **1. INTRODUCTION:**

Military personnel in modern conflicts are exposed to toxic metals from embedded fragments generated by explosive devices and inhaled near burn pits. To truly establish the impact of toxic metals on military personnel's health it is necessary to establish the peak exposure, often during deployment in areas of conflict, in order to establish future health risk as well as identify those most needing of early therapeutic monitoring or interventional strategies to mitigate potential health risk. Contemporary methods to assess biologic and environmental metals exposure are limited, being either unsuitable for field analysis or limited to single-analyte detection. No device exists to simultaneously detect and quantify multiple toxic metals in biological and environmental samples near the time of peak exposure in the field. The goal of this project is to design a portable sensor based on a zinc oxide (ZnO) nanowire substrate decorated with gold (Au) nanoparticles and decorated with chelating ligands can sensitively detect toxic metals via surface-enhanced Raman spectroscopy (SERS). The first part of this study is the fabrication and functionalization of the sensing substrate. A patterned bed of ZnO nanowires will be grown and decorated with gold nanoparticles. Crown ethers will be amended to present sulfhydryl group(s) to enable strong association with the gold nanoparticles. Crown ethers will be selected for, and experimentally confirmed to possess selectivity for uranyl, cadmium, aluminum, and lead. These toxic metals represent among the most important in health outcomes from embedded fragments and serve as the proof-of-principle for future expansion of this approach. At each step in the fabrication process, the substrate will be characterized by multiple optical and spectroscopic techniques. Detection sensitivity will be measured by parallel Raman studies of each selected ion coordinated with each crown ether, with and without plasmonic enhancement. Detection specificity will be assessed by SERS of each toxic metal in the presence of other ions and distractors. Selectivity of the crown ligands will be assessed by spectral analysis in the presence of other metal ions and distractors. Spectral analysis will also identify the optimal crown ethers for simultaneous, multiplexed sensing of the four initial toxic metals. Sensors in this optimized configuration will be fabricated and experimentally validated against predicted performance.

## **2. KEYWORDS:**

Crown Ethers; Zinc Oxide; Nanowires; Silver; Nanoparticles; Surface-Enhanced; Raman Spectroscopy; Microfluidics; Toxic Metals; Detection; Portable; Multiplexed; Trace; Polydimethylsiloxane; Chelation; Quantification

## **3. ACCOMPLISHMENTS:**

**What were the major goals of the project?**



- **Major Task 1: Design and fabricate an advanced sensor for toxic metals based on zinc oxide nanowires decorated with nanoscale gold and functionalized with metal capture chemistry.**
- Subtask 1: Prepare a mask using electron beam lithography to spatially localize deposition of the seed layer necessary to support the growth of zinc oxide nanowires.
- Subtask 2: Prepare zinc nanowire forests by hydrothermal growth from previously discussed seed layer.
- Subtask 3: Decorate zinc oxide nanowires with nanoscale gold by electron beam deposition.
- Subtask 4: Assess zinc oxide nanowires with and without gold decoration using scanning electron microscopy (including atomic compositional information by EDX), photoluminescence, and UV-Vis spectrophotometry.
- Subtask 5: Functionalize gold nanoparticles using cyclic polyethers (crown ethers) of various sizes and geometries. Initial crown ethers will be dibenzo functionalized, which are commercially available from 15-crown-5 (15 atoms in the crown, five of which are oxygen) through 30-crown-10. Cyclic polyethers will be amended to functionalize the cyclic polyether to the gold nanoparticles.
- Subtask 6: Assess cyclic polyether localization to the gold-decorated zinc oxide nanowires using scanning electron microscopy (including atomic compositional information by EDX) and infrared spectroscopy.
- **Major Task 2: Characterize sensor performance for the detection of toxic metals alone, in combination, and in the presence of known distractors present in biological and environmental samples.**
- Subtask 1: Measure the sensitivity of advanced sensors designed in Major Task 1 for detection of toxic metals with known military relevance. Selected toxic metal of interest will be measured over a range of relevant concentrations in the absence of other metals or potential sensing distractors in laboratory-scale Raman spectrometers, with appropriate parallel control studies.
- Subtask 2: Characterize the surface enhanced Raman signal amplification created by the interactions among cyclic polyether resonance and the gold nanoparticle surface, as enabled by careful quantitative calibrations and Raman spectroscopy measurements of cyclic polyethers and toxic metals in the absence of advanced sensors. Design a portable instrument based on solid state electronics for the multiplexed sensing of toxic metals at relevant concentrations.
- Subtask 3: Measure the specificity of advanced sensors for detection of toxic metals with known military relevance from explosive and burn pit exposures. Each toxic metal of interest will be measured over a range of relevant concentrations in the presence of other metals or distractors. These studies will be carried out in laboratory-scale Raman spectrometers with careful attention to quantitative characterization.
- Subtask 4: Computationally characterize the sensing of each toxic metal of interest in the presence and absence of other metals and sensing distractors. Select cyclic polyethers to provide optimal sensitivity and selectivity for each of the toxic metals of interest in a mixed sample over a relevant range of concentrations.
- Subtask 5: Prepare multiple advanced sensors on a single quartz substrate with each sensor functionalized with a different cyclic polyether as determined from Subtask 4.
- Subtask 6: Measure the specificity and selectivity of advanced sensors for detection of toxic metals with known military relevance from explosive and burn pit exposures. Each toxic metal of interest will be measured over a range of relevant concentrations in the presence of other metals or potential sensing distractors. These studies will be carried out in laboratory-scale Raman spectrometers with careful attention to quantitative characterization. Actual performance to be compared to performance predicted in Subtask 4.

**What was accomplished under these goals?**

**Summary of new results for the current year**

Most of the resources available to this project were expended prior to the current reporting year, which is the second year of no cost extension (NCE), primarily due to pandemic-associated delays. Targeted new studies from the originally proposed SOW were carried out during the 1<sup>st</sup> Q of 2021 to support (1) the preparation of a manuscript submitted for refereed publication and presentation at an international conference, (2) the preparation of the Ph.D. dissertation of the postdoctoral candidate principally working on this project and (3) the preparation of a manuscript submitted for publication in a peer-reviewed scientific journal.

### **Major Task 1, Subtask 1**

**Previously Reported:** We designed and 3D-printed two masks shown in Figure 1. The mask shown in (a) was designed to spatially localize ZnO seed layer deposition to two spots in the central portion of the proposed microchannel. The mask shown in (b) was designed to spatially localize metal nanoparticle deposition to one of these spots. This was done in order to compare SERS with non-SERS measurements. Figure 2 demonstrates through UV-Vis absorption spectra acquired of seeded and non-seeded substrates after hydrothermal nanowire growth indicates that patterning the ZnO seed layer is sufficient to pattern subsequent ZnO nanowire growth. The band-edge shoulder at sub-400 nm wavelengths present in the spectrum acquired of the seeded substrate indicates crystalline ZnO consistent with the presence of nanowires while the lack thereof in the spectrum acquired of the non-seeded substrate indicates a lack of nanowire growth through the absence of crystalline ZnO. Over the course of experimentation, it was deemed more advantageous to mask the channel with Kapton tape such that only the channel was exposed to deposition. This subtask is complete.

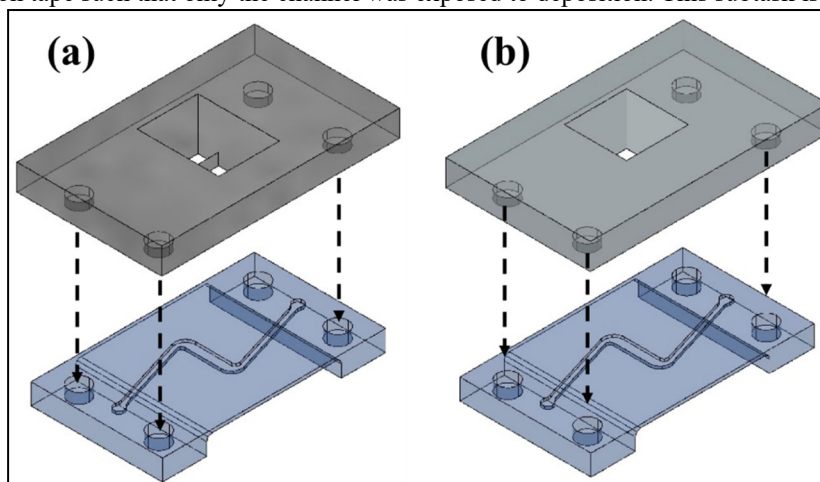


**Figure 1: AutoCAD designs for masks to pattern deposition of (a) ZnO seed and (b) metal nanoparticles**

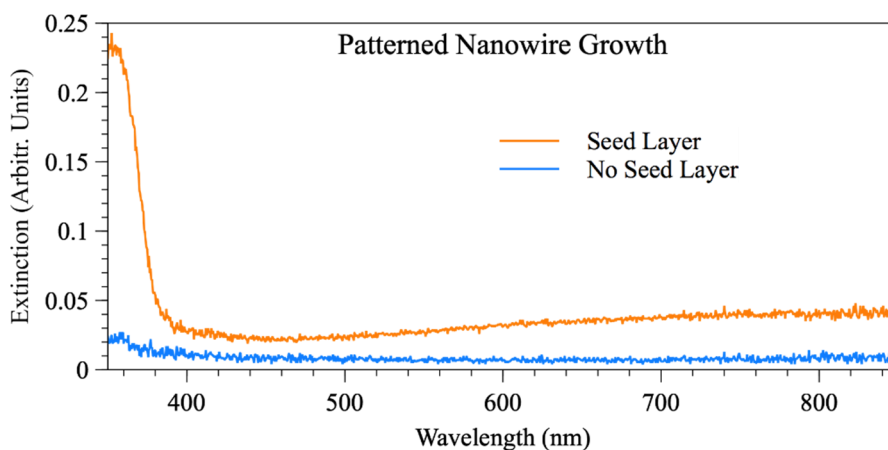


**Figure 2: UV-Vis absorption spectra of ZnO-seeded and unseeded substrates following ZnO nanowire growth**

### Major Task 1, Subtask 2

**Previously Reported:** Nanowire forests have been grown successfully on PDMS substrates. 100-nm ZnO seed layers were deposited on both thick (~1 mm) and thin (<0.2 mm) PDMS substrates, from which highly crystalline ZnO nanowires were grown successfully, as shown by SEM and photoluminescence (PL) under Subtask 4. This indicates that nanowire growth inside a microchannel is possible. Nanowires were successfully grown inside a PDMS channel, as shown by SEM and PL spectra under Subtask 4. A ZnO seed layer was deposited inside the channel via sputter deposition and annealed at 100 °C overnight. Nanowires were grown hydrothermally. This subtask is complete.

### Major Task 1, Subtask 3

**Previously Reported:** After ZnO nanowires were successfully grown on PDMS substrates, silver nanoparticles were deposited onto the sides of the nanowires via electron beam deposition. Silver was chosen to form nanoparticles rather than gold because silver nanoparticles have a plasmon resonance in a 400-600 nm range of wavelengths, while gold nanoparticles' plasmon resonance tends to sit in the range of 600-800 nm. The Raman systems available for this research are better-suited for use with green lasers rather than red or NIR lasers. Gold can later be substituted for silver, should it prove necessary. The presence of Ag nanoparticles was demonstrated by both SEM images pre- and post-deposition, as well as by the presence of plasmon-based light absorption demonstrated by UV-Vis spectra acquired pre- and post-deposition. SEM and UV-Vis are both presented in Subtask 4. A study was performed to optimize nanoparticle formation through deposition and anneal parameters to maximize surface enhancement within this paradigm. Through this study, it was determined that 7 nm of Ag deposited on ZnO at a rate of 0.1 Å/s and annealed at 50 °C for 2 hours resulted in the best surface enhancement, as demonstrated by Figure 3. Silver nanoparticles were successfully deposited on the sides of ZnO nanowires grown inside a PDMS microchannel. SEM and UV-Vis evidence of nanoparticle formation are presented in Subtask 4. This subtask is complete.

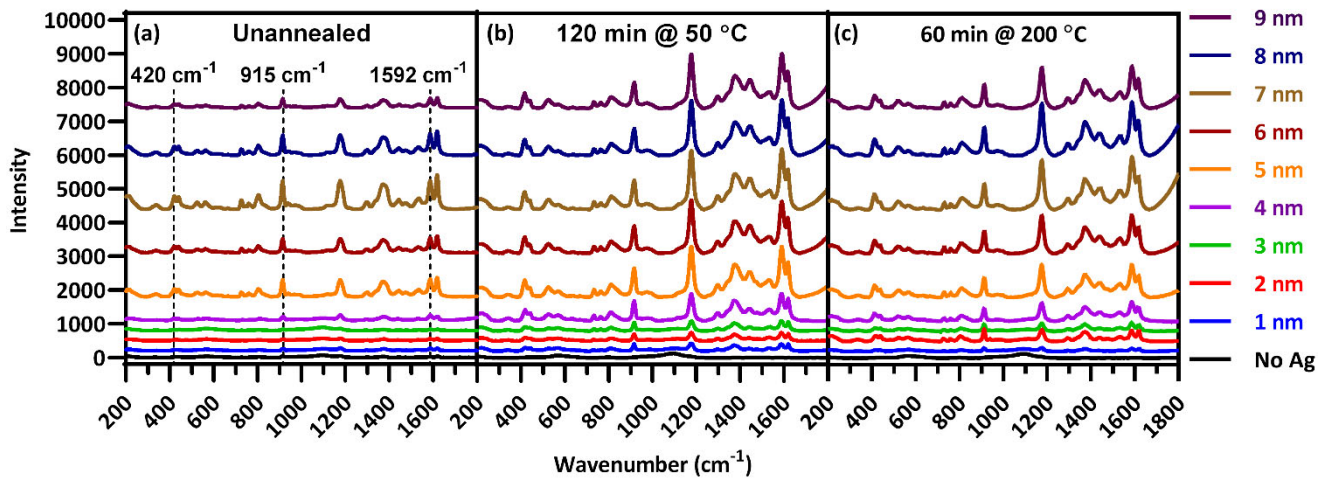


**Figure 3:** Raman spectra of crystal violet deposited on Ag-decorated ZnO substrates, of Ag thicknesses over a range of 1 – 9 nm and annealed at two different temperatures for two different times. (dotted lines represent

### Major Task 1, Subtask 4

**Previously Reported:** As stated in Subtask 2, ZnO nanowires on PDMS substrates were assessed using PL (Figure 4) and SEM (Figure 5). The PL peak at ~385 nm in Figure 4 results from the wide direct-bandgap nature of crystalline ZnO and indicates the presence of highly crystalline ZnO nanowires. Furthermore, a lack of photoluminescent emission in the visible region indicates a lack of defects in the ZnO crystal structure. The SEM images of Figure 5 indicate that this highly crystalline ZnO indeed takes the form of nanowires. They also confirm the single crystal nature of the nanowires since they have a hexagonal cross-section consistent with the wurtzite crystal structure of ZnO. As stated in Subtask 3, nanoparticle decoration on PDMS substrates was assessed using SEM imaging (Figure 6) and UV-Vis spectrophotometry (Figure 7). SEM images taken before and after nanoparticle deposition demonstrate the presence of nanoparticles on the sides of the nanowires. UV-Vis spectra acquired before and after nanoparticle deposition show the presence of a plasmon absorption peak centered at ~450 nm, consistent with Ag nanoparticle formation. Nanoparticle decoration in the PDMS channel was assessed using SEM imaging (Figure 8) before and after Ag deposition and PL spectroscopy (Figure 9) before deposition. SEM confirmed nanowire growth and PL confirmed nanowire crystallinity. UV-Vis spectra acquired after nanoparticle deposition and anneal (Figure 10) show the presence of a plasmon absorption peak centered at ~515 nm, consistent with Ag nanoparticle formation. UV-Vis spectra acquired before and after nanoparticle anneal demonstrate change to the plasmon peak spread and wavelength. It was decided that atomic compositional information was unnecessary for this work as the presence of Ag had been demonstrated for this fabrication process in a previous work[1]. This subtask is complete.

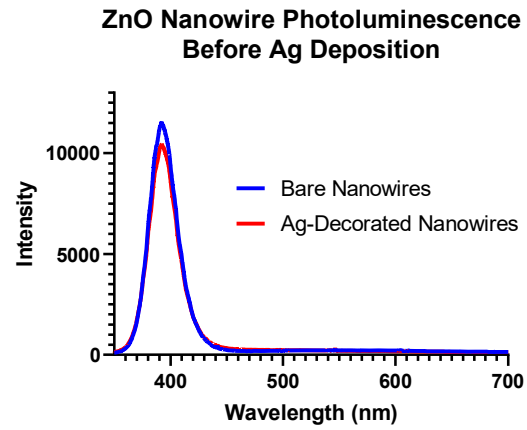


**Figure 4: Photoluminescent spectra of ZnO nanowires, demonstrating high crystallinity and few defects**

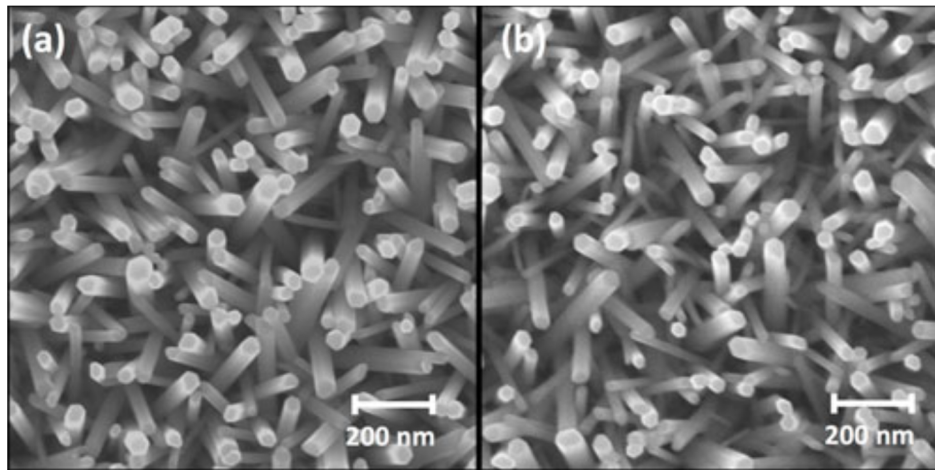


**Figure 5: SEM images of ZnO nanowires, confirming single crystal nanowire formation**

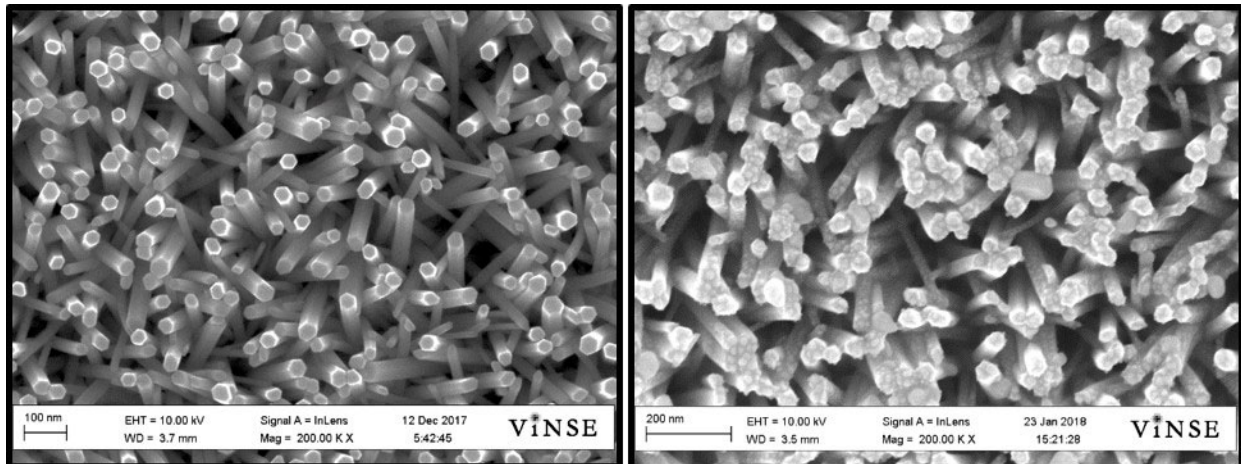


**Figure 6: SEM Images of ZnO nanowires before and after nanoparticle deposition, showing the presence of Ag nanoparticles on the sides of the nanowires.**

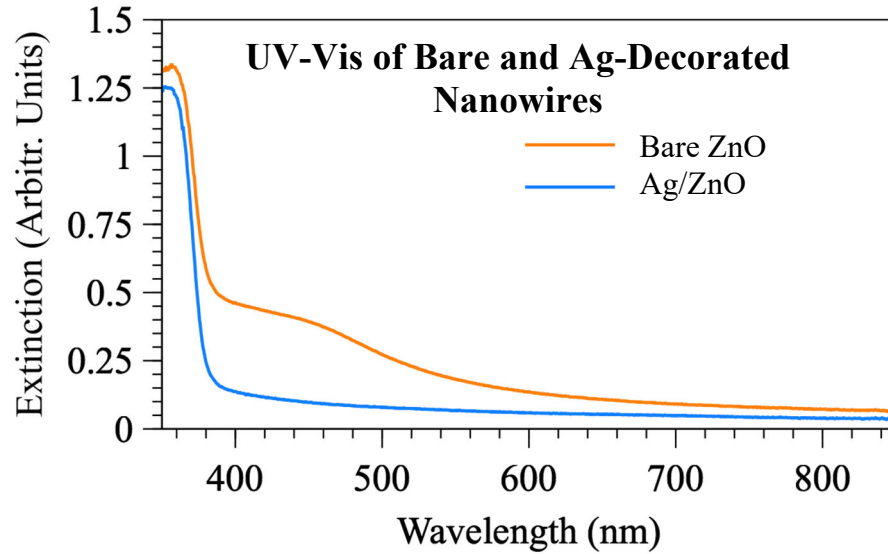


Figure 7: Extinction spectra of ZnO nanowires before and after Ag nanoparticle deposition

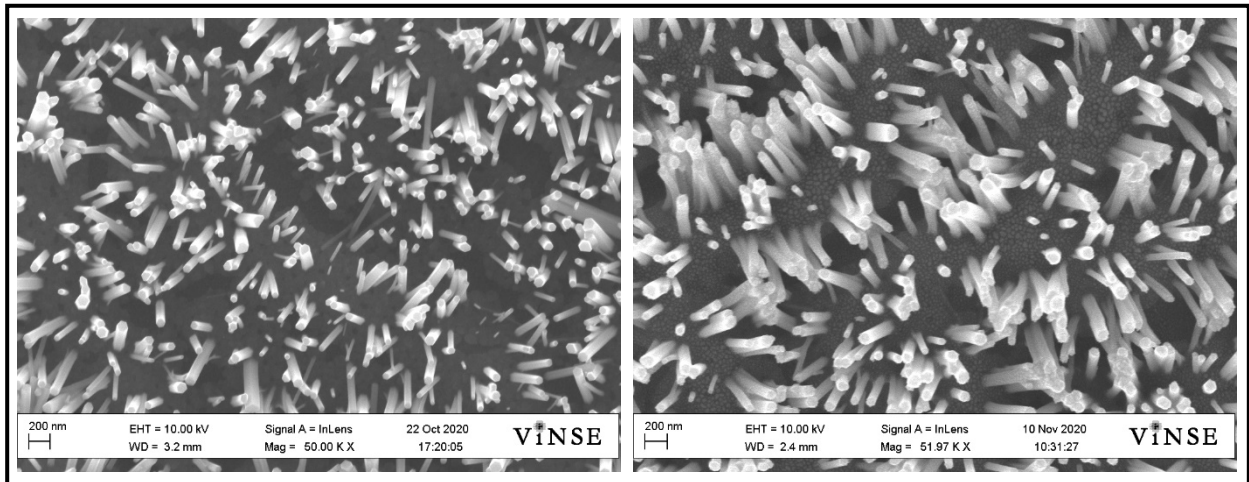


Figure 8: SEM images of ZnO nanowires inside PDMS microchannel before and after Ag nanoparticle deposition.

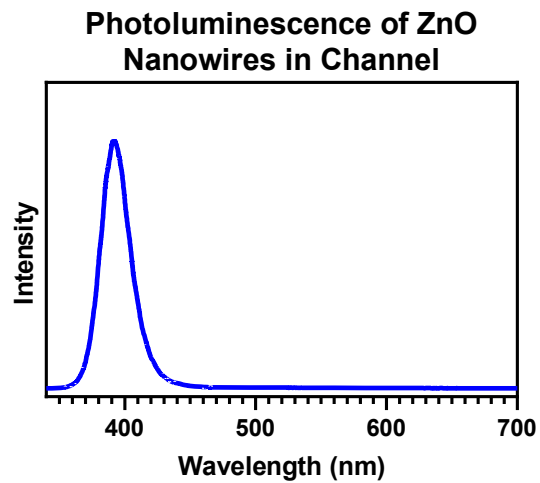


Figure 9: Photoluminescence spectrum of ZnO nanowires inside PDMS channel, demonstrating high crystallinity.



### UV-Vis: Ag/ZnO Nanowires in Channel

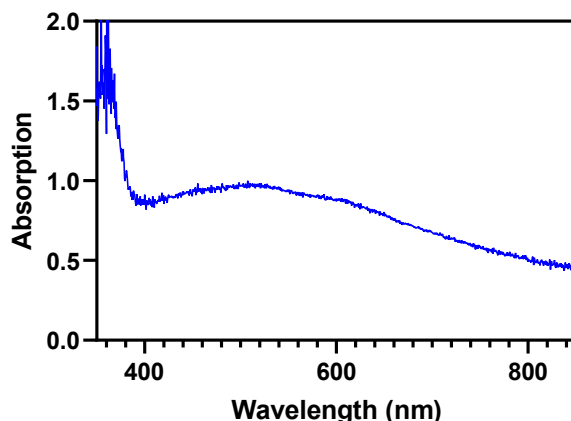


Figure 10: UV-Vis spectrum of Ag-decorated ZnO nanowires inside PDMS channel demonstrating plasmonic resonance.

#### Major Task 1, Subtask 5

**Previously Reported:** Ag-decorated ZnO nanowires on a fused silica substrate were successfully functionalized with 4'-aminobenzo-18-crown-6 (AB18C6). The substrate was placed in a 104  $\mu\text{M}$  solution of AB18C6 in 1:3 dimethyl sulfoxide (DMSO):DI Water. The solution was stirred for an hour, then left to incubate overnight. Samples of the solution before and after incubation with the substrate were acquired. Fluorescence and UV-Vis spectra were acquired of these samples and presented in Major Task 1, Subtask 6.

#### Major Task 1, Subtask 6

**Previously Reported:** This subtask is dependent on success in Subtask 5. While SERS of crown ethers inside a PDMS channel has not been successfully demonstrated, SERS has successfully detected down 1  $\mu\text{M}$  crystal violet in a PDMS channel (Figure 11). Functionalization of Ag/ZnO nanowires with AB18C6 was demonstrated by UV-Vis and fluorescence spectra in Figures 12 and 13 respectively as described in Major Task 1, Subtask 5. Both the absorption peak and fluorescence peak of AB18C6 in solution was reduced after incubation, indicating reduced concentration of AB18C6 in solution, demonstrating that AB18C6 decorated the Ag/ZnO substrate. Raman Spectra of Ag/ZnO substrates with and without AB18C6 were acquired in Figure 14, which demonstrated the presence of crown ether peaks.

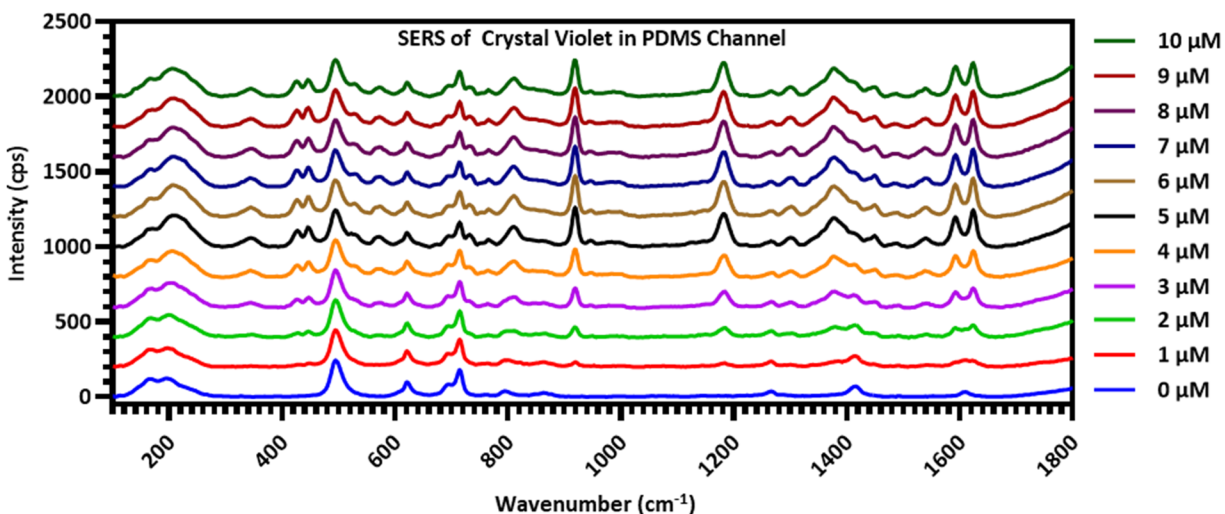


Figure 11: SERS of Crystal Violet over a concentration range of 1 – 10  $\mu\text{M}$ , demonstrating the ability to do SERS through the PDMS wall of a channel.

### UV-Vis: 10- $\mu$ M AB18C6

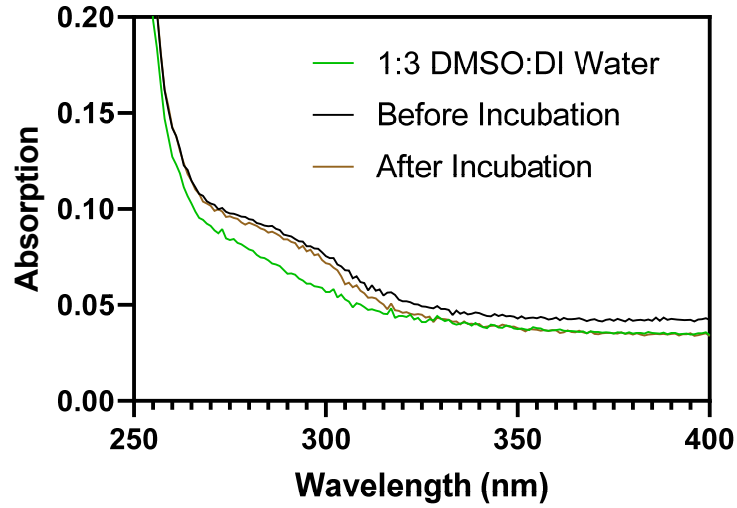


Figure 12: UV-Vis spectra taken of AB18C6 solution before and after incubation with an Ag/ZnO substrate, demonstrating decoration of the substrate with AB18C6 by reduced crown ether concentration in solution.

### Fluorescence: 10- $\mu$ M AB18C6

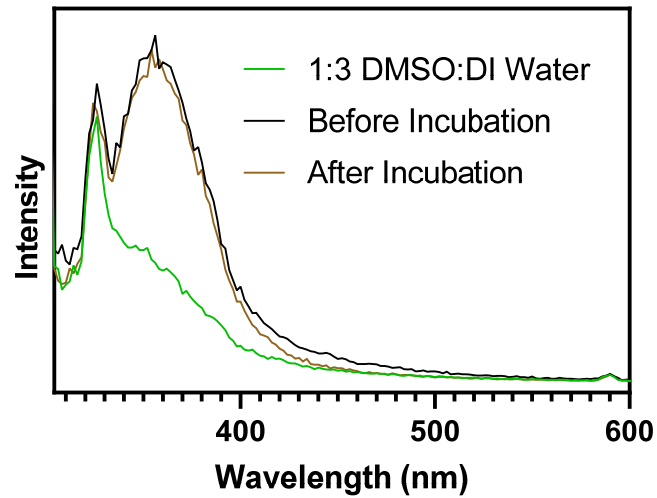


Figure 13: Fluorescence spectra taken of the AB18C6 solution before and after incubation with an Ag/ZnO substrate, demonstrating decoration of the substrate with AB18C6 by reduced crown ether concentration in solution.

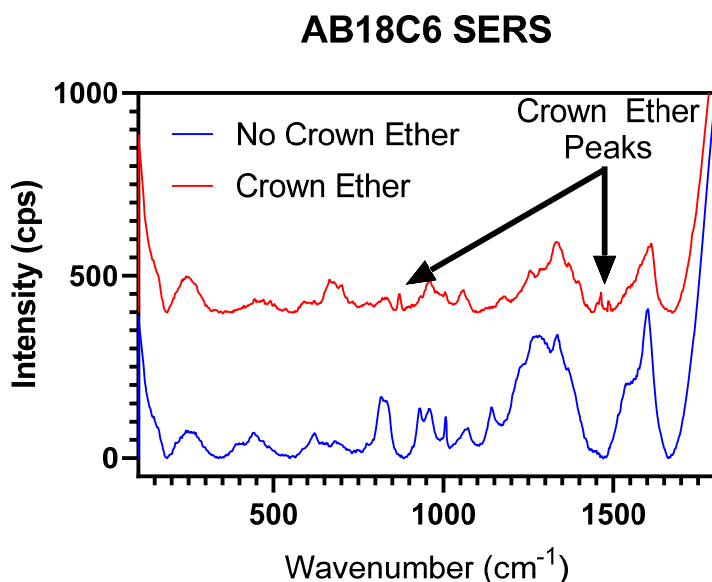


Figure 14: SERS spectra acquired of Ag/ZnO substrates with and without crown ether decoration, demonstrating clear presence of AB18C6 peaks.

#### Major Task 2, Subtask 1

**Previously Reported:** This subtask is dependent upon completion of Major Task 1. The nanowire-based sensor must be completed before true sensitivity of the sensor can be determined. However, work has been done toward using fluorescence as an additional sensitivity measure separate from SERS. Sarfo et. al. showed that 4'-aminobenzo-18-crown-6 has a broad fluorescence peak in the range of 300-400 nm when excited at 295 nm. When chelating metal ions, this fluorescence is quenched. We have had some difficulty replicating their results, but preliminary evidence shown in Figure 15 demonstrates that while the fluorescent peak of the crown ether is quenched in the presence of concentrations of arsenic and molybdenum ions equimolar to the crown ether concentration, it is not completely quenched. This indicates that fluorescence can be used as a check upon measuring SERS sensitivity.

**New Results:** To test the sensitivity of SERS detection through PDMS using the Ag-decorated ZnO nanowires, two 100  $\mu\text{m}$ -thick PDMS substrates were fabricated via soft lithography, labeled "P1" and "P2" and the Ag-decorated ZnO nanowires were fabricated on top. These substrates were placed face-down in 1 – 12  $\mu\text{M}$  solutions of melamine and SERS spectra were acquired, as shown in Figure 16. These results clearly demonstrate the sensor's ability to detect relevant concentrations of melamine free in solution, and indicate that the crown ether-metal ion capture scheme pursued in this research should yield detection of even more dilute analytes. In addition, We tested the ability of fluorescence and UV-Vis spectrophotometry to measure varying concentrations of metal ion capture by mixing solutions of 6.25 – 200  $\mu\text{M}$  molybdenum with 100- $\mu\text{M}$  solutions of AB18-C6 and acquiring fluorescence and UV-Vis spectra of each mixture, as shown in Figure 17. We detected clear step-wise changes in both fluorescence and UV-Vis spectra, indicating that both methods could be used to detect toxic metal chelation and validate SERS quantification.

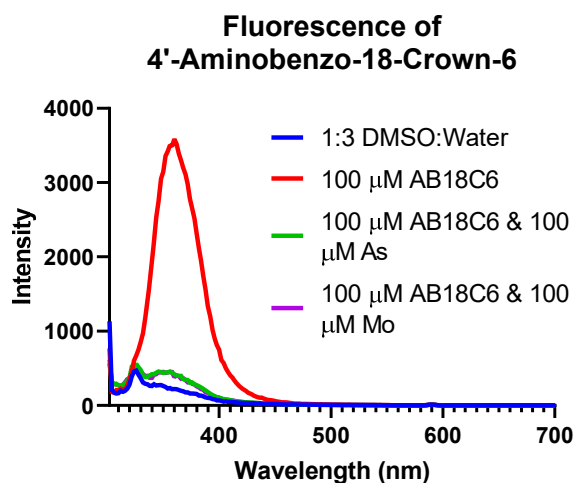


Figure 15: Fluorescence of 4'-aminobenzo-18-crown-6 with and without arsenic and molybdenum ions in a 1:3 DMSO:Water solution.



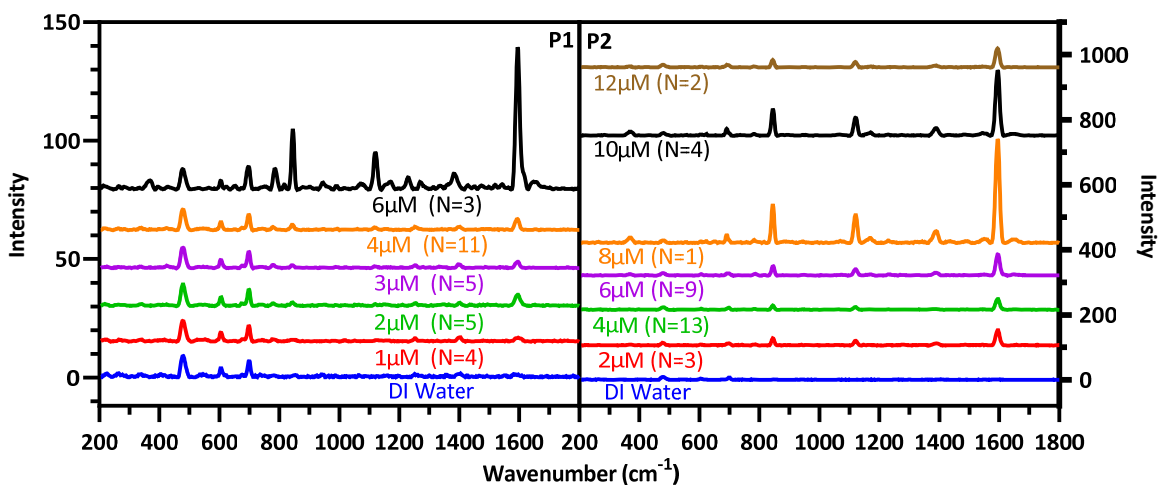


Figure 16: SERS spectra of melamine in DI Water, acquired through P1 on the left and P2 on the right. Number of spectra acquired for each concentration through each substrate in parentheses.

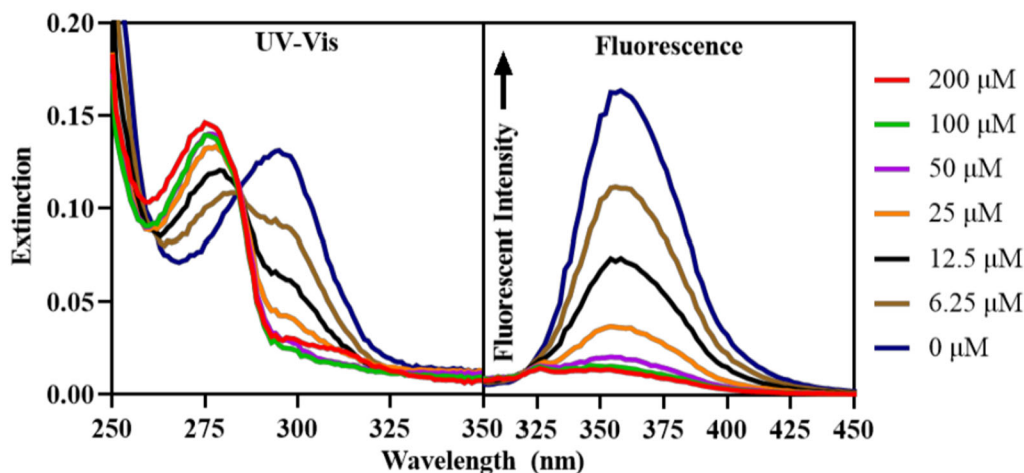


Figure 17: UV-Vis and fluorescence spectra of 100- $\mu\text{M}$  AB18C6 in 1:3 DMSO:Water mixed with varying concentrations of molybdenum, demonstrating a step-wise response to chelation based on the original concentration of molybdenum

### Major Task 2, Subtask 2

**Previously Reported:** This subtask is dependent upon completion of Major Task 1. However, it is important to determine whether acquiring Raman spectra through PDMS won't significantly interfere with the acquisition of crown ether spectra. To this end, Raman spectra were acquired of 25- $\mu\text{M}$  crystal violet through Ag-decorated ZnO nanowires on PDMS. Two different thicknesses of PDMS were used. The "thick" PDMS was about  $\sim 1.0$  mm while the "thin" PDMS was  $< 0.2$  mm. As shown in Figure 18, Raman spectra of crystal violet through the thick PDMS showed barely any enhancement, while spectra through the thin PDMS showed enhancement comparable to our previous work, which acquired SERS spectra of crystal violet through fused silica. This indicates that as long as the thickness of the microchannel wall through which spectra are acquired is controlled, enhanced Raman spectra can be acquired. This subtask is scheduled to be completed in Q1 of 2021.

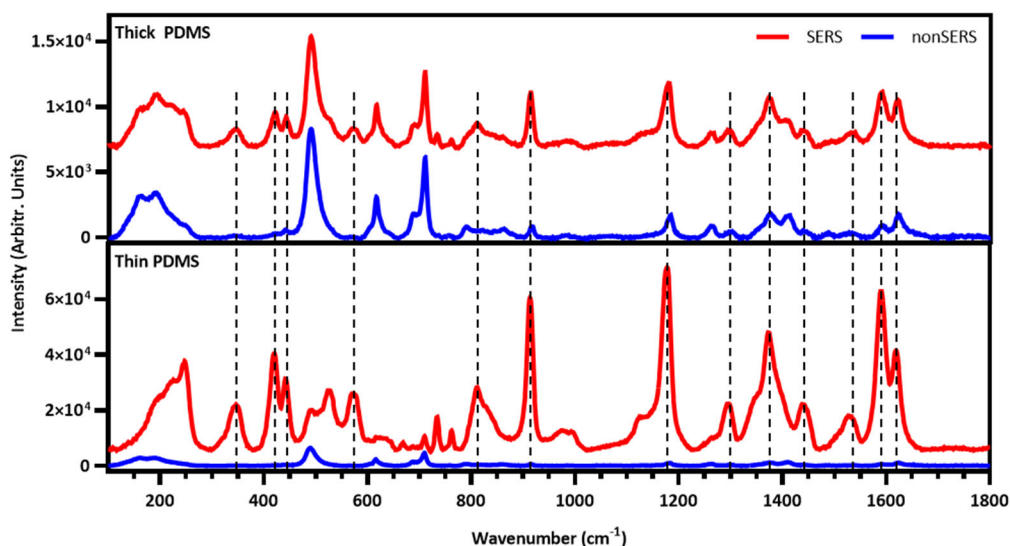


Figure 18: Raman spectra of 25  $\mu\text{M}$  crystal violet through (a) thick PDMS and (b) thin PDMS (dotted lines represent crystal violet-specific peaks)

### Major Task 2, Subtask 3

**Previously Reported:** This subtask is dependent upon completion of Major Task 1. However, the specificity of the crown ethers can be explored using UV-Vis spectrophotometry. Sarfo et. al. demonstrated that 4'-aminobenzo-18-crown-6 has an extinction peak around 300 nm. When the crown ether chelates a metal, this peak is reduced and a peak appears at about 280 nm. An optical extinction-based study was performed of the interactions between 4'-aminobenzo-18-crown-6 and a group of metal ions including metals on the Veteran's Association toxic metals biomonitoring panel, other toxic or potentially toxic metals, metals commonly found in the human body, and metals incorporated into the proposed biosensor. In total, this sweep included 22 metals and was performed in solutions of 1:1 DMSO:water and 1:3 DMSO:water (as performed by Sarfo et. al.). For the 1:1 DMSO:water solution (Figure 19), there was clear interactions between the crown ether and As, Hg, Al, Mo, Li, and W. For the 1:3 DMSO:water solution (Figure 20), Sarfo et. al. reported clear chelating of Pb, and none of Ba, Ca, Cd, Co, Cu, Hg, K, Li, Na, and Ni. However, we noted no discernable chelating of Pb. We did see chelating of several other metals including Mo, As, U, W, Cr, and Fe.

### Crown Ether/Metal Interactions in 1:1 DMSO/Water

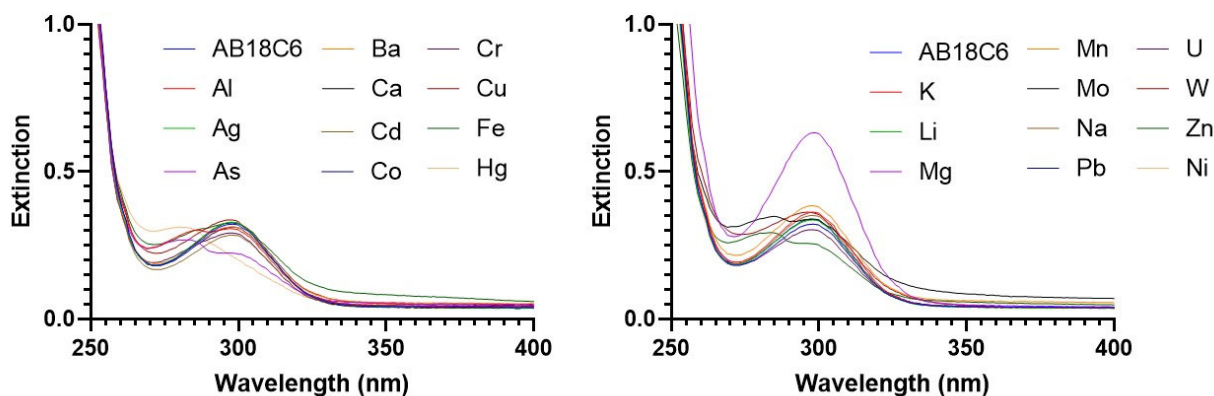


Figure 19: UV-Vis spectra of interactions between 4'-aminobenzo-18-crown-6 and 22 different metals in a 1:1 DMSO:water solution.

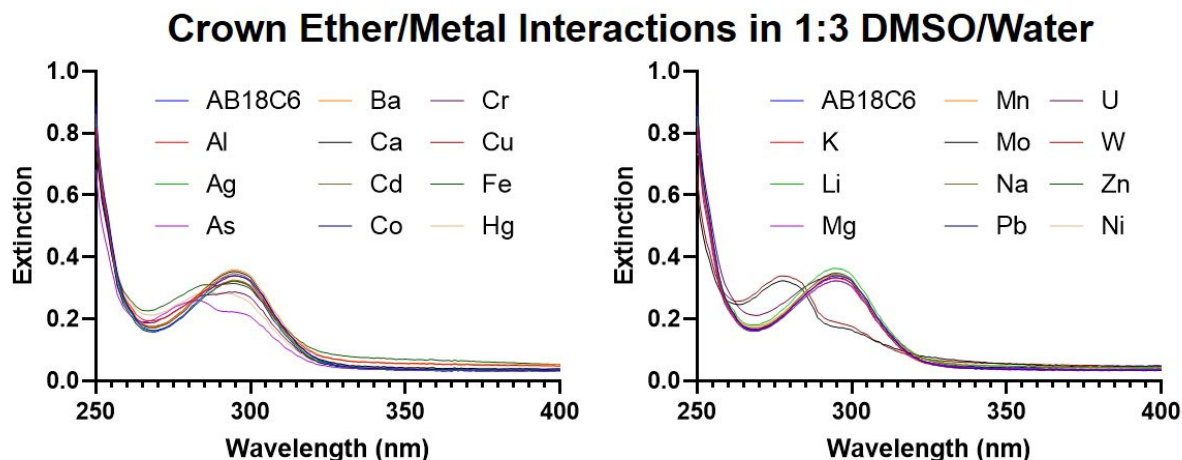


Figure 20: UV-Vis spectra of interactions between 4'-aminobenzo-18-crown-6 and 22 different metals in a 1:1 DMSO:water solution.

#### **Major Task 2, Subtask 4**

Completion of this subtask relies on the completion of Subtasks 2 and 3, to gather the information necessary for training an algorithm to identify chelated metals. Significant progress on this subtask is not anticipated.

#### **Major Task 2, Subtask 5**

Completion of this subtask requires completion of Subtasks 2 and 3. Significant progress on this subtask is not anticipated.

#### **Major Task 2, Subtask 6**

Completion of this subtask requires completion of Subtask 4. Significant progress on this subtask is not anticipated.

### **What opportunities for training and professional development has the project provided?**

We recruited a fourth-year undergraduate student double majoring in biomedical engineering and electrical engineering to participate on this project. She was trained in fluorescence spectroscopy and aspects of the chelation chemistry that is one foundation of this project. She carried out multiple studies, described in Major Task 2, Subtask 1. Some of these results were included in the manuscript that was accepted as a refereed conference paper (and presented from the podium). Ms. Xue was a co-author of that publication. The training and professional development she received in conducting the experiments, preparing the figures with statistical comparisons and writing some of the manuscript contributes to her applications for admission to graduate programs in engineering. Although it is too early, in general, to have outcomes of her application, I am pleased to report that Ms. Xue has received an offer of admission with full tuition/fees/stipend support from the Massachusetts Institute of Technology (MIT). Her admission to other highly competitive engineering programs is anticipated. Ms. Xue's involvement in this project was undoubtedly a positive factor in her graduate school admission.

### **How were the results disseminated to communities of interest?**

The crown ether chelation of metals and detection were published in a conference proceedings paper at the 6<sup>th</sup> World Congress of Recent Advances in Nanotechnology:

Cook AL, Xue F, Giorgio TD. Toxic Metals Chelation by 18-Crown-6 Ethers in Multiple Solutions and Quantification by Spectroscopic Techniques. *Proceedings of the 6<sup>th</sup> World Congress on Recent Advances in Nanotechnology*. 2021. DOI: 10.11159/nddte21.lx.202

This work was also presented from the podium at the 6<sup>th</sup> *World Congress on Recent Advances in Nanotechnology*; this was a virtual conference and presentations were recorded for asynchronous viewing.

**What do you plan to do during the next reporting period to accomplish the goals?**

A paper concerning the integration of the Ag-decorated ZnO nanowire substrate with microfluidic technology is scheduled to be re-submitted for Peer Review in Q1 of 2022.

**4. IMPACT:**

**What was the impact on the development of the principal discipline(s) of the project?**

The paper reporting the optimization of electron beam-deposited Ag nanoparticles on ZnO for maximizing SERS represents a systematic examination of the fabrication and anneal parameters of such nanoparticles and will inform future fabrication of such nanoparticles for similar sensing paradigms.

The conference proceedings paper reporting the chelation of metals with 4'-aminobenzo-18-crown-6 represents an examination of the chelation properties of said crown ether and will inform its future use in toxic metal ion detection.

**What was the impact on other disciplines?**

Nothing to Report.

**What was the impact on technology transfer?**

Nothing to Report.

**What was the impact on society beyond science and technology?**

Nothing to Report

**5. CHANGES/PROBLEMS:**

**Changes in approach and reasons for change**

**Previously Reported:** Silver nanoparticles were deposited on the ZnO nanowires rather than gold, because silver nanoparticles have plasmon resonances in the 400-600 nm wavelength range, while gold nanoparticles have plasmon resonances in the 600-800 nm range. Additionally, silver tends to better enhance Raman spectra than gold. The facilities available for this research are better suited for lasers in the former range rather than the latter. Kapton tape was used to mask the PDMS channel, rather than the previously described masks, as PDMS hydrophobicity unexpectedly hindered nanowire growth, requiring the entire channel to be coated in ZnO. For the same reason, ZnO seed was sputtered into the channel rather than deposited via e-beam. This was done in order to coat not only the bottom of the channel, but the walls in ZnO as well.

#### **Actual or anticipated problems or delays and actions or plans to resolve them**

*Describe problems or delays encountered during the reporting period and actions or plans to resolve them.*

**Previously Reported:** Difficulty has been encountered in replicating the results reported by Sarfo et. al. Specifically, while chelation of multiple metal ions (such as molybdenum and arsenic) by 4'-aminobenzo-18-crown-6 has been observed, this crown ether has failed to chelate lead ions, even under the same conditions reported by Sarfo et. al. Additionally, Sarfo reported in quantification of lead concentration via fluorescence[2]. Specifically, they reported a fluorescence peak at ~590 nm when excited at 295 nm that increased with increasing lead concentration. While the fluorescence of 4'-aminobenzo-18-crown-6 in Figure 7 exhibits a broad fluorescence peak between 300 and 400 nm that gets quenched when chelating molybdenum and arsenic, a sharp peak at 590 nm has not been observed. Based on the quenching in Figure 7, however, it is expected that this broad fluorescence peak can be used to quantify chelation via peak fluorescence quenching.

**Previously Reported:** In addition to our difficulties in replicating the results of Sarfo et. al., difficulty was encountered in ZnO nanowire growth. There came a point where nanowires stopped growing correctly. Instead of dense forests of nanowires as shown in Figures 4 & 5, nanowire growth was very sparse, as shown in Figure 11. After several weeks of troubleshooting, it was discovered that due to an aging quartz crystal microbalance in the electron beam deposition system being used, much less ZnO seed was being deposited than assumed. This resulted in replacement of the microbalance and nanowire growths performed since have reverted to a useful morphology.

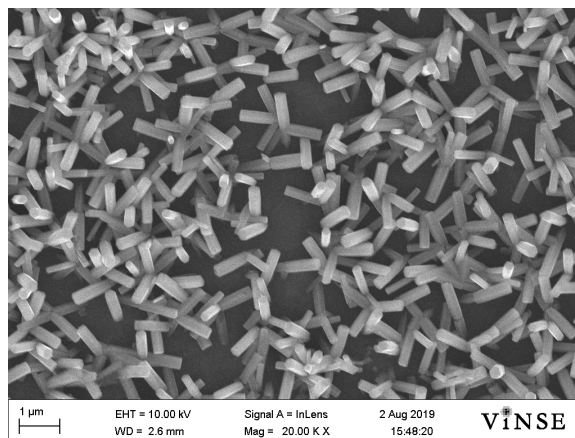


**Figure 19: SEM image of sparse nanowire growth**

#### **Changes that had a significant impact on expenditures**

Restrictions associated with the pandemic limited our access to laboratory facilities for about nine months during 2020-2021. We still operate under some capacity restrictions in labs/offices, requiring much of the non-experimental work to be carried out away from campus/at home. This slows the process of interpreting data, refining hypotheses and developing amended strategies.

We also suffered an awkwardly time loss of all local tools suitable for the appropriate deposition of ZnO on the PDMS substrates. We typically use the high vacuum deposition system at Fisk University (where Dr. Cook, the former predoctoral student, received his M.S. in physics and) where the PI (Dr. Giorgio) has collaborations and privileges. This instrument suffered a power supply failure that required repair at the manufacturer. The overall time from failure to restoration of service was more than three months. We attempted to use a similar instrument at Vanderbilt, but this tool was also unavailable due to routine maintenance at the same time as the Fisk instrument failure. In addition, the Vanderbilt instrument lacks the ability to rotate the target at a glancing angle during deposition (that is possible and utilized for this project on the Fisk instrument). We attempted to replicate the morphology of the ZnO deposition using a 'hack' of the Vanderbilt instrument, but this was unsuccessful. We then pivoted to a different ZnO deposition/growth approach, but this was far slower and significantly suppressed throughput for experimental work. By the time the Fisk instrument was repaired and revalidated, Dr. Cook was close to finishing his Ph.D. work.

**Significant changes in use or care of human subjects, vertebrate animals, biohazards, and/or select agents****Significant changes in use or care of human subjects**

Nothing to report.

**Significant changes in use or care of vertebrate animals**

Nothing to report.

**Significant changes in use of biohazards and/or select agents**

Nothing to report.

**6. PRODUCTS:**

- **Publications, conference papers, and presentations**

**Journal publications.**

This publication was disclosed in the last report, but had not appeared in print at that time. The complete citation follows:

*Cook AL, Haycock CP, Mu R and Giorgio TD: Optimization of Electron Beam-Deposited Silver Nanoparticles on Zinc Oxide for Maximally Surface Enhanced Raman Spectroscopy. Nanoscale Advances 2021, 3, 407-417. doi: 10.1039/d0na00563k*  
 PMID: none

The final manuscript from this project and Dr. Cook's Ph.D. studies has been prepared and submitted. We are presently addressing reviewer comments and anticipate resubmission of the amended manuscript during the 1<sup>st</sup> half of 2022.

*Cook AL and Giorgio TD: Fabrication of Silver-Decorated Zinc Oxide Nanowire Sensor in Microchannels for Surface-Enhanced Raman Spectroscopy. Lab on a Chip 2021, in review.*

**Books or other non-periodical, one-time publications.**

Dr. Andrew Cook was the principal predoctoral student conducting the studies for this project. He successfully defended his Ph.D. in April 2021 and submitted all of the requirements for his dissertation and Ph.D. later in 2021.

Dr. Andrew Cook; Ph.D. in BME; August 2021

'Surface Enhanced Raman Spectroscopy-Based Sensor for Portable, Multiplexed Detection of Toxic Metals in Urine' **Other publications, conference papers and presentations.**

This is a conference presentation that was conducted remotely due to pandemic restrictions:

*Cook AL, Xue F* and **Giorgio TD**: Toxic Metals Chelation by 18-Crown-6 Ethers in Multiple Solutions and Quantification by Spectroscopic Techniques. 6<sup>th</sup> World Congress on Recent Advances in Nanotechnology (RAN'21), Lisbon, Portugal, June 2021. Presentation, remote presentation due to SARS-CoV-2.

This is the associated refereed conference paper:

*Cook AL, Xue F* and **Giorgio TD**: Toxic Metals Chelation by 18-Crown-6 Ethers in Multiple Solutions and Quantification by Spectroscopic Techniques. 6<sup>th</sup> World Congress on Recent Advances in Nanotechnology (RAN'21), Lisbon, Portugal (but conducted virtually due to SARS-CoV-2 pandemic restrictions), June 2021. doi: 10.11159/nddte21.lx.202

- **Website(s) or other Internet site(s)**

Nothing to report.

- **Technologies or techniques**

Nothing to report.

- **Inventions, patent applications, and/or licenses**

Nothing to report.

- **Other Products**

Nothing to report.

## 7. PARTICIPANTS & OTHER COLLABORATING ORGANIZATIONS

**What individuals have worked on the project?**

Name: Andrew Cook  
 Project Role: Graduate Student  
 Researcher Identifier (e.g. ORCID ID): ORCID ID: 0000-0002-2859-8804  
 Nearest person month worked: 12

Contribution to Project: Mr. Cook has performed all of the research reported here.  
 Funding Support: The National Science Foundation and this award.

Name: Fan Xue  
 Project Role: Undergraduate student  
 Researcher Identifier: none  
 Nearest Person Month Worked: 1  
 Contribution to Project: Ms. Xue has performed experiments on the spectroscopy of crown ethers and toxic metal ions that appeared in the RAN'21 presentation and publication.  
 Funding Support: Ms. Xue conducted research for course credit.

**Has there been a change in the active other support of the PD/PI(s) or senior/key personnel since the last reporting period?**

Nothing to report.

**What other organizations were involved as partners?**

Fisk University provided facilities for this project, specifically use of an instrument that allows ZnO deposition while changing the angle of the substrate relative to the ion beam. This allows for more uniform deposition of the ZnO over the substrate surface; this approach is not available at Vanderbilt University.



## 8. SPECIAL REPORTING REQUIREMENTS

### COLLABORATIVE AWARDS:

### QUAD CHARTS:

## 9. APPENDICES:

Appendix A follows and contains:

- the final version of the Nanoscale Advances manuscript, as published,
- the final version of the RAN'21 refereed conference paper, as published,
- the manuscript submitted to Lab on a Chip and presently under amendment for expected submission during the 1<sup>st</sup> half of 2022
- the Ph.D. dissertation of Dr. Andrew Cook, accepted in 2021

### References

- [1] A. L. Cook, C. S. Carson, C. E. Marvinney, T. D. Giorgio, and R. R. Mu, "Sensing trace levels of molecular species in solution via zinc oxide nanoprobe Raman spectroscopy: Zinc oxide nanoprobe Raman," *J. Raman Spectrosc.*, vol. 48, no. 8, pp. 1116–1121, Aug. 2017, doi: 10.1002/jrs.5180.
- [2] D. K. Sarfo, E. L. Izake, A. P. O'Mullane, and G. A. Ayoko, "Molecular recognition and detection of Pb(II) ions in water by aminobenzo-18-crown-6 immobilised onto a nanostructured SERS substrate," *Sens. Actuators B Chem.*, vol. 255, pp. 1945–1952, Feb. 2018, doi: 10.1016/j.snb.2017.08.223.

## Appendix A

### Manuscripts, Publications and Dissertations

The manuscript identified below was submitted to *Lab on a Chip* in August 2021 and received reviewer comments in October 2021. We are currently carrying out amendments to this manuscript to address reviewer criticisms. We anticipate that a revised manuscript will be ready for submission during the first six months of 2022. A copy of the manuscript appears in this Appendix. Although the Appendix is not independently page numbered, the relative location of each product is indicated in the accompanying description, below. The *Lab on a Chip* manuscript begins on the next page (page 1 of the Appendix, page 1A) and ends on page 23A,

*Cook AL* and **Giorgio TD**: Fabrication of Silver-Decorated Zinc Oxide Nanowire Sensor in Microchannels for Surface-Enhanced Raman Spectroscopy. *Lab on a Chip* 2021, in review.

The conference paper below was submitted and accepted for presentation at the 2021 Recent Advances in Nanotechnology conference. The conference, originally scheduled for Lisbon, Portugal was transitioned into a virtual event. The manuscript was peer-reviewed and accepted for publication. A copy of the publication appears in this Appendix. The conference paper begins on page 24A and ends on page 30A,

*Cook AL, Xue F* and **Giorgio TD**: Toxic Metals Chelation by 18-Crown-6 Ethers in Multiple Solutions and Quantification by Spectroscopic Techniques. 6<sup>th</sup> World Congress on Recent Advances in Nanotechnology (RAN'21), Lisbon, Portugal (but conducted virtually due to SARS-CoV-2 pandemic restrictions), June 2021, peer-reviewed. doi: 10.11159/nddte21.lx.202

The publication below was reported in the previous annual report as 'accepted' and awaiting final publication including correction of typesetting errors and other non-scientific amendments. The final citation is below and a copy of this work as-published appears in this Appendix. The *Nanoscale Advances* publication begins on page 31A and ends on page 46A.

*Cook AL, Haycock CP, Mu R* and **Giorgio TD**: Optimization of Electron Beam-Deposited Silver Nanoparticles on Zinc Oxide for Maximally Surface Enhanced Raman Spectroscopy. *Nanoscale Advances* 2021, 3, 407-417. doi: 10.1039/d0na00563k PMID: none

The primary predoctoral student working on this project completed his Ph.D. degree requirements, successfully defended his dissertation and received his degree in 2021. A copy of his Ph.D. dissertation, as cited below, appears in this Appendix. The Ph.D. dissertation begins on page 47A and ends on page 170A,

*Cook AL*: 'Surface Enhanced Raman Spectroscopy-Based Sensor for Portable, Multiplexed Detection of Toxic Metals in Urine'. Ph.D. dissertation (Vanderbilt University) 2021.

See next page.



# Lab on a Chip

## **Fabrication of Silver-Decorated Zinc Oxide Nanowire Sensor in Microchannels for Surface-Enhanced Raman Spectroscopy**

Journal:	<i>Lab on a Chip</i>
Manuscript ID	LC-ART-08-2021-000756
Article Type:	Paper
Date Submitted by the Author:	24-Aug-2021
Complete List of Authors:	Cook, Andrew; Vanderbilt University, Biomedical Engineering Giorgio, Todd; Vanderbilt University, Biomedical Engineering

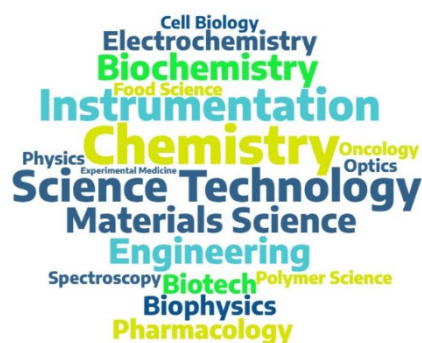
SCHOLARONE™  
Manuscripts

# Lab on a Chip

Devices and applications at the micro- and nanoscale

## Guidelines for Referees

Thank you very much for agreeing to review this manuscript for [Lab on a Chip](#).



The most important factor used to assess manuscripts that are submitted to *Lab on a Chip* is novelty. Papers should demonstrate novelty in both: (i) the device physics, engineering, and materials; and (ii) applications in biology, chemistry, medicine. Submissions that describe novelty in both device *and* application are most likely to be published. Outstanding papers featuring novelty in either the device or the application may also be published.

The work we publish is highly multi-disciplinary and should appeal to a wide variety of researchers including, but not limited to, those working in physics, medicine, engineering and biology. The scope of the journal is very broad, by design and as highlighted in our recent [Editorial](#) includes innovations in microfluidics, sensors, optics, electronics, imaging, materials, mechanical

components and more. \*Image created using citation data generated from Web of Science (Clarivate Analytics, 2021).

*Lab on a Chip's* Impact Factor is **6.799** (2020 Journal Citation Reports®)

*The following manuscript has been submitted for consideration as a*

## **FULL PAPER**

Original scientific work that has not been published previously. Full papers must represent a significant development in the particular field, and are judged according to originality, quality of scientific content and contribution to existing knowledge. Full papers do not have a page limit and should be appropriate in length for scientific content. Further information on article types can be found on our website.

Please consider these standards when making your recommendation for publication in *Lab on a Chip*:

- Use the journal scope and expectations to assess the manuscript's suitability for publication in *Lab on a Chip*.
- Comment on the originality, importance, impact and reliability of the science. English language and grammatical errors do not need to be discussed in detail, except where it impedes scientific understanding.
- State clearly whether you think the paper should be accepted or rejected, giving detailed comments that will both help the Editor to make a decision on the paper and the authors to improve it.

### **Professor Aaron Wheeler**

Editor-in-Chief

University of Toronto, Canada

### **Philippa Ross**

Executive Editor

Royal Society of Chemistry

Contact us

Please visit our [reviewer hub](#) for further details of our processes, policies and reviewer responsibilities as well as guidance on how to review, or click the links below.



What to do  
when you  
review



Reviewer  
responsibilities



Process &  
policies



Department of Biomedical Engineering

August 24<sup>th</sup>, 2021

Dear Dr. Manabu Tokeshi,

Please find enclosed our manuscript "Fabrication of Silver-Decorated Zinc Oxide Nanowire Sensor in Microchannels for Surface-Enhanced Raman Spectroscopy" submitted for publication in *Lab on a Chip*. This manuscript highlights the fabrication of a physically-deposited 3D surface-enhanced Raman scattering (SERS) substrate directly into PDMS microfluidic channel to simplify SERS-integrated channel fabrication. **This work is the first to report minimization of poly(dimethylsiloxane) (PDMS) interference through channel design and sensitive detection of free analytes in solution through the PDMS cap.**

The enclosed manuscript reports the effect of light scattering through PDMS on surface enhancement and design of a PDMS channel to minimize this scattering. This manuscript demonstrates effective SERS detection of multiple dilute analytes through thin PDMS substrates. Furthermore, this manuscript reports the fabrication of high quality ZnO nanowires decorated with physically-deposited silver (Ag) nanoparticles inside a PDMS microchannel.

The results reported in this manuscript demonstrate that dilute analytes can be detected via SERS through a PDMS microchannel, and that high-quality Ag-decorated ZnO nanowires can be fabricated directly into the microchannel, eliminating the need for alignment of a PDMS cap with a SERS-active substrate. Doing so simplifies the fabrication of SERS-active microfluidic channels while incorporating the inherent advantages of physically-deposited Ag nanoparticles. The focus on the development of a SERS-integrated microfluidic device for sensing dilute analytes makes this work appropriate for the *Lab on a Chip* journal.

This manuscript is composed of original research, has not been previously published, and is not in consideration for publication elsewhere. All authors have read and approved all versions of the manuscript, its content, and its submission to *Lab on a Chip*.

We look forward to receiving the reviewers' constructive critique of our work.

Sincerely,

A handwritten signature in blue ink, appearing to read "Todd D. Giorgio".

Todd D. Giorgio, Ph.D.  
Professor of Biomedical Engineering  
Professor of Chemical and Biomolecular Engineering  
[todd.d.giorgio@vanderbilt.edu](mailto:todd.d.giorgio@vanderbilt.edu)

## ARTICLE

## Fabrication of Silver-Decorated Zinc Oxide Nanowire Sensor in Microchannels for Surface-Enhanced Raman Spectroscopy

Andrew L. Cook,<sup>a</sup> and Todd D. Giorgio<sup>\*a</sup>

Received 00th January 20xx,  
Accepted 00th January 20xx

DOI: 10.1039/x0xx00000x

Surface-enhanced Raman spectroscopy (SERS) performed in microfluidic channels offers multiple benefits to sensitive and reliable detection of dilute analytes while utilizing the advantages of microfluidics, including small samples, high throughput, and portability. Physical deposition of metallic nanoparticles by techniques such as electron beam deposition results in dense populations of nanoparticles and hotspots between nanoparticles for sensitive detection. However, not only do physically deposited SERS-active surfaces necessitate additional steps during device fabrication, but surface fabrication is itself complicated by the constraints imposed by the microfluidic channel. This work demonstrated a robust approach to physical fabrication of a SERS-active substrates inside a poly(dimethylsiloxane) (PDMS) microfluidic channel. Direct growth of zinc oxide nanowires inside the PDMS channel and e-beam deposition of silver to coat the nanowires was performed before bonding PDMS to glass. This process enabled label-free SERS sensing of micromolar crystal violet and melamine with minimal spectral interference from the PDMS-based channel.

### Introduction

Surface-enhanced Raman spectroscopy (SERS) that is integrated with microfluidic technology offers the advantages of reduced sample consumption and reaction time, high detection efficiency, and portability as compared to state-of-the-art detection paradigms.<sup>1</sup> This integration is primarily pursued through either colloidal solutions<sup>2,3</sup> or stationary substrates.<sup>4–6</sup> Co-injection of SERS-active colloids with samples into microfluidic channels can provide efficient sensing and heat-dissipation, although this technique often suffers from aggregation, resulting in reduced reproducibility and poor mixing due to predominantly laminar flow in microfluidic channels.<sup>7</sup> Stationary substrates offer greater stability and reproducibility, although they are often less efficient than colloidal strategies because stationary substrates cannot be dispersed within sample fluids.<sup>8,9</sup>

SERS-active substrates based on nanowires decorated with metal nanoparticles such as silver (Ag) or gold (Au), can minimize the drawbacks associated with colloidal or stationary substrate sensing when fabricated within a microfluidic channel. This design offers the stability and reproducibility similar to stationary substrates, but can also provide the sensing efficiency of colloidal strategies due to their inherent 3-dimensional architecture.<sup>10,11</sup> Metal-decorated zinc oxide (ZnO) nanowires are an attractive platform for SERS sensing. ZnO is a biocompatible<sup>12</sup> wide direct-bandgap semiconductor with a band-edge emission of  $\sim 3.4$  eV<sup>13</sup> and a high exciton binding energy of 60 meV.<sup>14,15</sup> These properties make ZnO nanowires

electronically stable at room temperature<sup>14</sup> and transparent to visible and near-infrared (NIR) light,<sup>16</sup> reducing absorption of Raman scattered photons. Optical transparency is ideal for Raman spectra acquired through the substrate as is necessitated by the sensor and detector geometry we anticipate in microfluidic technology. In addition, ZnO has been demonstrated to increase surface enhancement due to charge transfer between ZnO and both Ag<sup>17</sup> and analytes directly adsorbed to the nanowires.<sup>18</sup> Additionally, ZnO possesses high electron mobility<sup>19</sup> and a large refractive index of approximately 2.0 in the visible region.<sup>20,21</sup> Combining these characteristics with the atomically smooth and highly faceted hexagonal single-crystal structure of ZnO nanowires can induce Mie scattering resonances. Mie scattering can reduce signal loss to scattering through waveguiding light.<sup>22</sup> and synergize with charge transfer to enhance Raman scattering up to  $10^5$ , in addition to the electromagnetic mechanism of SERS.<sup>23</sup>

During the fabrication of SERS-active microchannels, stationary substrates such as the Ag-decorated ZnO nanowires are usually fabricated on the glass wall of the channel. This is done to avoid spectroscopic interference by polymers commonly used to fabricate microfluidic channels such as poly(dimethylsiloxane) (PDMS) that has its own strong Raman spectrum. ZnO nanowire fabrication on glass lends itself to *in situ* fabrication techniques like hydrothermal growth and electroplating after microchannel fabrication. In particular, metal-decorated ZnO nanowires can be easily fabricated *in situ* hydrothermally,<sup>10,24,25</sup> however hydrothermal fabrication typically results in sparse metal nanoparticle formation.<sup>10</sup> In contrast, electron beam (e-beam) deposition as a physical technique forms denser nanoparticle distributions,<sup>11,22</sup> resulting in higher surface enhancement due to proximity-induced hotspots between nanoparticles.<sup>26</sup> However, one major drawback is that physical deposition of

<sup>a</sup> Department of Biomedical Engineering, Vanderbilt University, Nashville TN 37235, USA. E-mail: todd.d.giorgio@vanderbilt.edu

nanoparticles necessitates *ex-situ* SERS substrate fabrication on glass prior to microfluidic channel bonding because closing the channel prevents deposition of material from an external source. Alignment of the SERS sensor on glass with a microchannel in PDMS is complicated by microscale dimensions and the deformability of PDMS. The complexity of accurate placement in PDMS microchannels is amplified for designs that include multiple SERS sensors on a single glass substrate. Additional alignment steps limit flexibility of microchannel design,<sup>7</sup> making it less ideal for the production of large numbers of disposable sensors. Fabricating SERS substrates directly into PDMS microchannels before bonding with glass as illustrated by Figure 1 enables the fabrication of complex multisensory, multichannel devices in the absence of rigorous alignment requirements.

In this study, we demonstrated that a ZnO nanowire substrate decorated with e-beam deposited Ag nanoparticles can be simply fabricated within a PDMS microchannel *ex-situ* without requiring an alignment step to complete microchannel fabrication. Furthermore, we demonstrated that trace chemical and biological analytes can be detected through a PDMS microchannel wall by careful optimization of device design and analysis of SERS optical signals.

## Experimental Methods

In order to simplify the fabrication of a SERS-integrated microfluidic channel, Ag-decorated ZnO (Ag/ZnO) nanowires were fabricated directly into the channel such that the nanowires would reside on the “roof” of the channel after bonding with glass, as illustrated by Figure 1. In this orientation, Raman spectra would be acquired through the “roof” of the channel. The first step in accomplishing this is to examine the effect of PDMS thickness on spectral intensity, as crosslinked PDMS polymer is known to scatter light,<sup>27</sup> and Mao *et al.* demonstrated 4× reduced SERS sensitivity when acquiring spectra through a PDMS cap.<sup>28</sup> Next, the applicability of SERS through PDMS must be exemplified through SERS of a relevant analyte. Melamine was chosen for this purpose due to strong Raman peaks in regions where PDMS signal is weak. Melamine is an industrial material primarily used in polymer manufacturing that has also been added to dairy products to produce artificially high readings of protein content. Because melamine can cause kidney failure and even death, the Codex

Alimentarius set a limit of 1 mg/L (7.93 μM) of melamine in powder infant formula.<sup>29</sup> Lastly, using information gained from the previous two experiments, a PDMS channel must be designed and fabricated. The Ag/ZnO nanowire substrate must be constructed within the channel and SERS of crystal violet injected into the channel must be acquired.

### ZnO Seed in PDMS Channel

SERS-active nanostructures were fabricated directly into the channel, such that they would reside on the ‘roof’ of the channel as shown in Figure 1. Substrates and microchannels were fabricated from PDMS via soft lithography with Sylgard 184® (Dow Corning, Batch #H047ICL055) which consists of a liquid PDMS base and a curing agent. A microchannel master was designed in AutoCAD® 2017 as a mold for PDMS microchannels and machined from aluminum, shown in Figure S1. The base and curing agent were mixed at a 10:1 ratio and poured over the base. The solution was then placed in a vacuum chamber at ~25 mmHg until all bubbles were removed. The lid was fitted onto the base before the dish was placed in the oven at 95 °C for two hours to cure the PDMS, after which the dishes were removed and allowed to cool at room temperature. After cooling, the master was cut away from the surrounding PDMS and the microchannels were extracted.

PDMS microchannels were cleaned with the ALD-AMD method<sup>11</sup> which consists of submersion in a 1% Alconox® solution, deionized (DI) water, acetone, methanol, and DI water, sequentially. At each step, the substrates were sonicated for 10 minutes. After this cleaning process was completed, the substrates were dried using nitrogen gas. For each microchannel, Kapton tape was used to mask the PDMS surface containing the channel so that only the channel was exposed. Microchannels were then mounted in a sputter deposition system (Angstrom Amod Multimode Deposition Chamber) which was pumped down to  $5.5 \times 10^{-6}$  Torr, and ZnO was deposited in the channel over the course of 1 hour and 40 minutes. Stylus profilometry (Bruker Dektak 150) was used to measure the thickness of ZnO across the channel. The maximum ZnO thickness was 150 nm at the center of the channel, and dropped off to 0 nm at the corners of the channel. ZnO was sputtered to ensure ZnO deposition on all sides of the channel, thereby minimizing the impact of PDMS hydrophobicity on hydrothermal nanowire growth. The channels were annealed at 100 °C overnight to improve ZnO seed surface morphology and subsequent nanowire growth.

### ZnO Seed on PDMS Substrates

PDMS substrates were fabricated for two purposes in this work. First, it was necessary to explore the effect of PDMS thickness on the quality of Raman signal, since the crosslinked polymeric nature of cured PDMS scatters light.<sup>27</sup> Results of this exploration informed the design of the PDMS channel used in this work. Second, thin PDMS substrates were fabricated to characterize SERS of melamine through PDMS. These substrates were designed to mimic the thickness of the PDMS channel wall through which spectra of crystal violet were acquired.

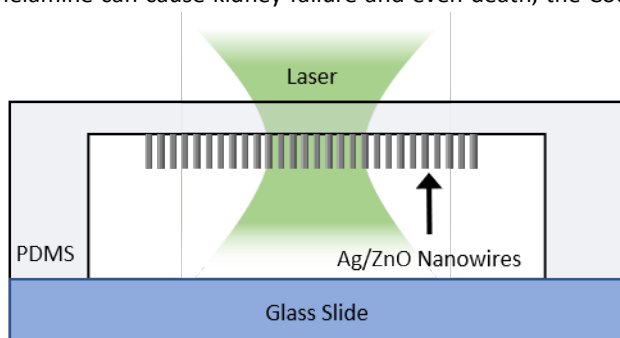


Figure 1: Illustration of the cross-section of a microchannel integrated with an Ag/ZnO nanoprobe fabricated on the PDMS.



To explore the effect of light scattering through PDMS on SERS signal quality, bare ZnO nanowires and Ag nanoparticle-decorated ZnO (Ag/ZnO) nanowires were constructed on thick and thin PDMS substrates, fabricated via soft lithography with Sylgard 184®. Substrate thickness was controlled by varying the PDMS volume placed into Pyrex® petri dishes (95 mm diameter). 7.0 g of PDMS was poured into one petri dish, and 1.4 g of PDMS was poured into another, targeting 1.0 mm and 0.2 mm PDMS thicknesses for thick and thin substrates respectively. After oven-curing, PDMS squares of approximately 1 cm x 1 cm were cut from the center of each petri dish to form substrates for sensor fabrication. The substrates were cleaned via the ALD-AMD method and the thickness of each substrate was determined via stylus profilometry to be ~1.0 mm for the thick substrates and ~0.17 mm for the thin substrates. The discrepancy between the targeted thickness of 0.2 mm and the resultant thickness of 0.17 mm was caused by capillary action drawing PDMS up along the walls of the petri dish. Subsequent substrates fabricated for SERS of melamine were fabricated with controlled thickness by pouring PDMS between two glass slides with a single layer of 0.15-mm thick carbon tape as a spacer. This resulted in 0.15-mm thick PDMS substrates. Cleaned substrates were mounted in an e-beam deposition chamber (Thermionics, 150-0040). The chamber was pumped down to a vacuum of  $5 \times 10^{-6}$  Torr and a 100 nm ZnO seed layer was deposited at a rate of ~0.1 Å/second. PDMS substrates were mounted in a plan configuration throughout ZnO deposition.

#### ZnO Nanowire Growth

The ZnO nanowire growth process is similar to that described in previous work.<sup>11</sup> ZnO nanowires were grown hydrothermally. PDMS channels and substrates were submerged in a 20 mM equimolar solution of zinc acetate dihydrate (Sigma Aldrich, BCMB3068V) and hexamethylenetetramine (Sigma Aldrich, MKBS8102V) in a Teflon reaction chamber. This chamber was placed in a preheated oven at 95 °C for 2.5 hours, after which the chamber was rapidly cooled under running water. The channels and substrates were washed of residual organics with DI water, then placed in the oven at 105 °C for ~10 minutes to dry. Nanowires were grown only where seed layer was deposited.

#### Ag Nanoparticle Formation

ZnO nanowires on PDMS substrates were decorated with Ag nanoparticles via e-beam deposition (Thermionics, 150-0040) as shown in Figure S2. The nanowire substrates were mounted on a glancing-angle deposition apparatus, which rotates azimuthally at an angle during deposition. This angle was calculated by Equation (1) to maximize the area of nanowire sides exposed to deposition while minimizing shadowing from adjacent nanowires.  $L_n$  and  $D_n$ , which are average nanowire length and spacing, were estimated to be 320 and 76 nm, respectively. From these, an angle of  $\theta_{dep} = \sim 13^\circ$  was calculated. The deposition chamber was depressurized to  $\sim 5.0 \times 10^{-6}$ , at which point Ag was deposited at a rate of ~0.1 Å/s to a nominal film thickness of 10 nm while the stage was rotated. This

resulted in an effective film thickness ~2.2 nm on the sides of the nanowires as calculated by Equation (2), where  $t_{nom}$  represents the nominal film thickness and  $\theta_{dep}$  represents the angle of deposition specified above.

$$\theta_{dep} = \tan^{-1}\left(\frac{D_n}{L_n}\right) \quad (1)$$

$$t_{eff} = t_{nom} \sin(\theta_{dep}) \quad (2)$$

Ag nanoparticles were deposited in PDMS channels via e-beam deposition (Angstrom Amod Multimode Deposition System) as shown in Figure S3. The nanowire substrates were mounted with a Kapton-tape mask such that only the channel was exposed on a stage at an angle of approximately 24° from the source crucible. The chamber was pumped down to a pressure of  $\sim 4.0 \times 10^{-6}$  Torr. Ag was deposited at a rate of ~0.1 Å/s to a nominal film thickness of 15 nm while the stage was rotated. This resulted in an effective film thickness ( $t_{eff}$ ) of ~6.1 nm on the sides of the nanowires, and ~13.7 nm on the bottom of the channel. This effective film thickness on the nanowire sides is within the range of 5 – 9 nm film thickness demonstrated in our previous work<sup>30</sup> to maximize SERS acquired with a 532-nm laser. The mask was designed to allow Ag deposition only inside the channel. After deposition, the microchannel was heated to 50 °C for 2 hours to anneal the nanoparticles, which was shown in our previous work to greatly increase surface enhancement.<sup>30</sup>

#### Microfluidic chip Fabrication

After fabrication of Ag-decorated ZnO nanowires inside the microchannels, holes were punched at the inlet and outlet with a 2-mm disposable biopsy punch (Premier® Uni-Punch®) and they were placed in a plasma oxidation chamber (Harrick Plasma PDC-001) for 4 minutes to oxidize the PDMS surface. This enabled bonding to a glass slide (Fisherbrand® 12-550-A3). Lastly, Tygon® tubing (ID: 0.020 in.; OD: 0.060 in.) was inserted at the inlet and outlet and PDMS was used to seal the interface between PDMS and tubing.

#### Characterization Techniques

Scanning electron microscopy images of bare and Ag-decorated ZnO nanowires were acquired with a Zeiss Merlin scanning electron microscope (Jena, Germany) in both plan and 45° configurations. These images were used to visually inspect nanowire and nanoparticle morphology. All image analysis was performed using ImageJ.

Photoluminescence (PL) spectra of ZnO nanowires were acquired to assess nanowire crystallinity using a thermoelectrically cooled (-40 °C) CCD camera in a spectroscopy setup (HORIBA Jobin Yvon LabRAM 800HR). ZnO nanowire emissions were excited using a 325-nm He-Cd laser (Kimmon, 1 K series 200 mW, vertically polarized output measured at the laser head). PL spectra were acquired with a 15×-magnification objective lens (Thorlabs, LMU-15×-NUV, NA = 0.32), and detected in line with the laser normal to the substrate surface. Nanowires were oriented facing incident light. Five locations on



each patch of nanowires were chosen, with a precision of 100  $\mu\text{m}$ . At each location, a PL spectrum was acquired over a wavelength range of 340–700 nm. Each spectrum was the accumulation of 4 background-subtracted spectra, each taken with a 200- $\mu\text{m}$  aperture, and a 600 grooves/mm grating. Exposure time was 0.1 seconds and laser power was between 4.0–5.0 mW, as measured at the lens. The five spectra for each patch were averaged to produce a representative PL spectrum for each patch of nanowires within the channel.

To characterize the effect PDMS-induced scattering on spectral quality, SERS spectra of crystal violet in solution were acquired through Ag/ZnO and bare ZnO nanowires on 1.0-mm and 0.17-mm substrates to compare SERS and non-SERS spectra. These spectra were acquired using a CCD camera on the same spectroscopy setup as the PL measurements with a 532-nm laser (Ventus, 500 mW, horizontally polarized output measured at the laser head) and a 10x-magnification lens (Olympus, MPlan N Achromat, NA = 0.25). Raman scattering was collected in line with the laser normal to the substrate surface. PDMS substrates were affixed face down in a reservoir filled with 25- $\mu\text{M}$  crystal violet, with the Ag-decorated and bare ZnO nanowires oriented away from incoming laser light. Raman spectra were acquired over a range of 100 – 1800  $\text{cm}^{-1}$ , and enhancement factors were estimated from these spectra as described in our previous work.<sup>11</sup> Each Raman spectrum was the accumulation of two background-subtracted spectra, taken with a 20-s exposure time, a 200- $\mu\text{m}$  aperture, and a 1800-grooves/mm grating. Laser power was 10.0 mW, measured at the turret. Raman spectra background was subtracted using a proprietary intelligent fitting algorithm developed by Renishaw.<sup>31</sup> The algorithm used an 11<sup>th</sup> order polynomial and a noise tolerance of 1.50. Spectra were smoothed using a Savitzky-Golay filter. Crystal violet was chosen for this purpose to facilitate detection due to its multiple strong Raman peaks where the PDMS Raman signal is weak. These spectra were intensity normalized using the 687  $\text{cm}^{-1}$  PDMS peak.

There was also concern that the ALD-AMD cleaning method would change the Raman spectrum of the PDMS by introducing solvents into the PDMS. Curling of the substrates was observed after the cleaning process due to the presence of acetone and methanol. To address this concern, nine Raman spectra were acquired of a single PDMS substrate before cleaning and averaged, using the same system and conditions detailed for the spectra acquired through thick and thin PDMS. After cleaning, Raman spectra were acquired at the same locations as before and averaged. These spectra were intensity normalized using the 488  $\text{cm}^{-1}$  PDMS peak.

Raman spectra of melamine through 0.15-mm thick PDMS were acquired with the same system described above. Raman spectra used to quantify SERS were acquired in a range of 200 – 1800  $\text{cm}^{-1}$  for two Ag-decorated ZnO nanowire substrates deposited on 150  $\mu\text{m}$ -thick PDMS, hereafter referred to as S1 and S2. Each Raman spectrum acquired through S1 was the accumulation of four background-subtracted spectra, each taken with a 10-s exposure time. Each Raman spectrum acquired through S2, was the accumulation of 8 background-subtracted spectra, each taken with a 1-s exposure time. All Raman spectra of melamine

were acquired with a 200- $\mu\text{m}$  aperture, and a 600-grooves/mm grating. Laser power was 5 mW, measured at the turret. Raman spectra background was subtracted using an asymmetric least squares method, and smoothed with a Savitzky-Golay filter.

Raman spectra of crystal violet injected into the SERS-integrated PDMS channel were acquired with Thermo Scientific DXR Raman microscope (Waltham, MA, USA). A 532 nm diode-pumped, solid state (DPSS) laser was used with a 50 $\times$  objective (Olympus, MPlan N Achromat, 0.75 NA) at a power of 10 mW as measured at the objective turret. These spectra were intensity normalized using the 488  $\text{cm}^{-1}$  PDMS peak.

Raman spectra were acquired through the PDMS channel “roof” bearing Ag/ZnO nanowires over a range of 100 – 1800  $\text{cm}^{-1}$ . Each Raman spectrum was the accumulation of 4 background-subtracted spectra, each taken with a 60 second exposure time, a 50- $\mu\text{m}$  slit aperture, and 900 grooves/mm grating. Laser power was 10 mW, as measured at the objective and Raman scattering was detected in-line with the laser normal to the surface of the sample. Raman spectra background were subtracted using a 5<sup>th</sup> order polynomial and smoothed with a Savitzky-Golay filter. These spectra were intensity normalized using the 488  $\text{cm}^{-1}$  PDMS peak.

To characterize the plasmonic properties of Ag nanoparticles, ultraviolet-visible-near infrared (UV-vis-NIR) extinction spectra were acquired using a Hitachi U-4100 spectrophotometer with an integrating sphere. Extinction spectra were acquired at a rate of 300 nm/min over a range of 350 – 850 nm, with the nanowire substrate oriented facing oncoming light.

## Results & Discussion

### Effect of Cleaning on PDMS Raman Spectrum

Because SERS-active nanostructures were fabricated on a PDMS surface of the microchannel, SERS will be performed through that PDMS wall. Because PDMS is porous, it is known to absorb multiple solvents used during the ALD-AMD cleaning process.<sup>32,33</sup> Indeed, curling of substrates was observed after cleaning, although subsequent placement of the substrates in a vacuum reduced this curling. It is essential that the Raman spectrum of PDMS be consistent in order to reliably extract signal from dilute analytes, so Raman spectra were acquired before and after the cleaning process to determine whether solvent absorption had an observable effect on the spectrum of PDMS. A comparison of these Raman spectra exhibited only Raman peaks associated with PDMS, as shown in Figure S4. No Raman peaks associated with any of the chemicals used in cleaning were observed. Thus, the cleaning process demonstrably did not affect the Raman spectrum of PDMS.

### ZnO Nanowire Characterization

To be suitable as a platform for SERS enhancements, ZnO nanowires must possess two characteristics: 1) the nanowires must be high quality, which means they grow as single crystals with little to no defects, and 2) Ag/ZnO nanowires must possess uniform dimensional and structural properties, such as crystallinity. SEM images of nanowires (Figure S5) show a dense

bed of hexagonal nanowires, indicating single-crystallinity. A visual comparison of nanowires to remain bare and those to be decorated with Ag in Figure S6 revealed no visible difference in the dimensionality or structure of the nanowires, providing validation for the quantification of SERS enhancements. Furthermore, SEM images revealed nanowires that are long enough to provide large surface area for SERS, but not so long as to induce nesting. Nesting would introduce shadowing during nanoparticle deposition, reducing nanoparticle coverage.

PL spectroscopy was used to assess the crystallinity of the ZnO nanowires. ZnO is a direct bandgap semiconductor with a band-edge emission of  $\sim 3.4$  eV at room temperature,<sup>15</sup> which means that PL spectra of crystalline ZnO nanowires will have a sharp band-edge emission peak around 380 nm. Any native point defects within the crystalline structure, such as vacancies (missing atoms at regular lattice locations), interstitials (extra atoms occupying lattice interstices), or antisites (atoms occupying a lattice site where it doesn't belong) introduce transition levels within the bandgap which induce emissions at wavelengths in the visible region.<sup>34</sup> This defect emission is very broad compared to the band-edge emission, and the ratio of band-edge to defect emission in ZnO nanowires is an indicator of the nanowires' crystallinity.<sup>35</sup> PL spectra of the nanowires in Figure S7 exhibit very little defect emission and very strong band-edge emission, providing further evidence of high crystallinity with few defects. While the band-edge emission peak at 392 nm is shifted slightly for nanowires grown on PDMS versus the band-edge emission of 380 nm previously reported for nanowires similarly grown on fused silica,<sup>35</sup> the ratio of band-edge to defect emission remained similarly large. A comparison of the PL spectra for nanowires to remain bare

(nonSERS) and those to be decorated with nanoparticles (SERS) revealed little variation. 5 PL spectra were acquired of each population and averaged. The band edge and defect emission for nonSERS exhibited a relative standard deviation (RSD) 2.4% and 3.4% respectively, while the SERS nanowires exhibited an RSD of 5.9% and 3.5% for band-edge and defect emission. The average band-edge peak intensity for nonSERS nanowires was within 10% of that for SERS nanowires, indicating that the nanowire populations had similar nanowire density and dimensions. The ratio between band-edge emission and defect emission in the visible region was  $\sim 56.9$  for SERS nanowires and  $\sim 46.4$  for nonSERS nanowires, indicating that both populations were highly crystalline with few defects. These features indicated that light would interact with both nanowire populations similarly, enabling high confidence in the comparison of non-SERS to SERS spectra.

To explore the possibility of patterning ZnO nanowire growth by patterning the ZnO seed layer deposition, a partially shielded PDMS substrate was deposited with a 100-nm seed layer, on which nanowires were hydrothermally grown. UV-Vis-NIR spectra of the seeded and non-seeded portions of the substrate (Figure S8) indicated nanowire growth on the seeded portion of the substrate and negligible nanostructure formation on the unseeded portion.

#### Ag Nanoparticle Deposition Characterization

ImageJ analysis of the SEM images of bare nanowires grown on PDMS substrates revealed an approximate nanowire height of 320 nm and approximate interwire spacing of 76 nm. Plugging these values into Equation (1) resulted in an Ag deposition angle of  $\sim 13^\circ$ . SEM image of the nanowires after nanoparticle

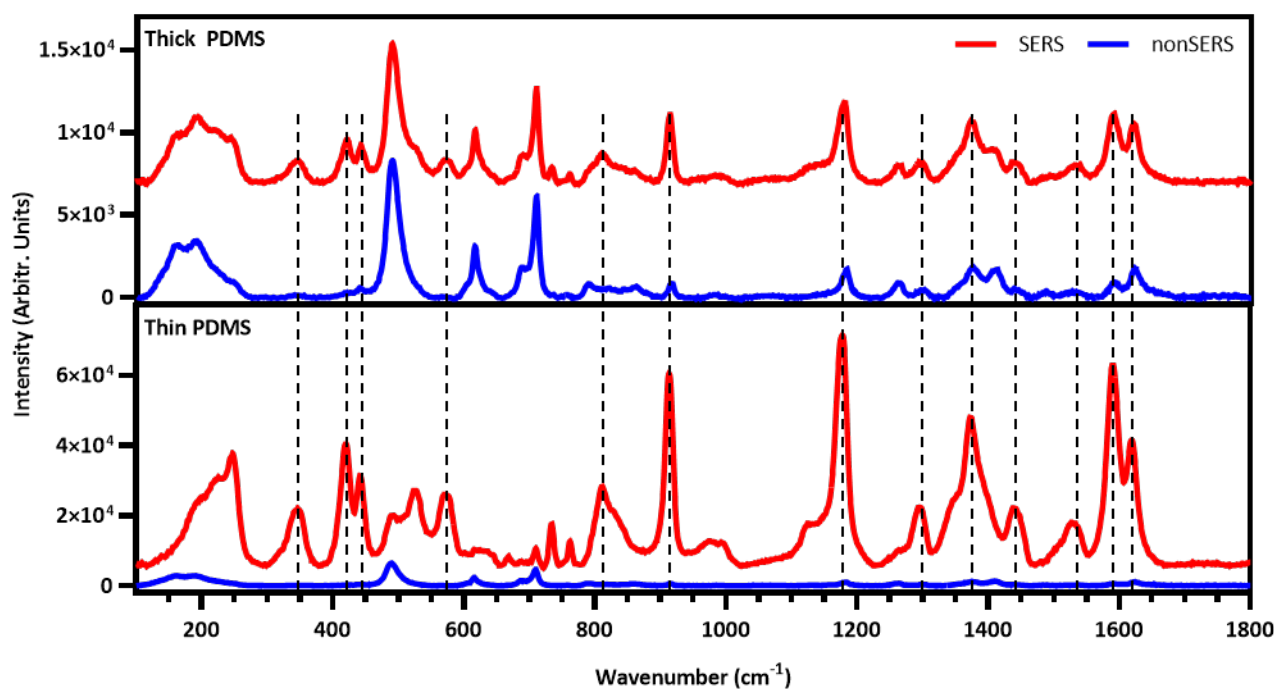


Figure 2: SERS (red) and non-SERS (blue) Raman spectra of crystal violet through (a) thick and (b) thin PDMS, demonstrating the ability to perform SERS spectroscopy through a PDMS wall, as well as the importance of PDMS thickness on the magnitude of enhancement. CV peaks identified by dotted lines.

deposition revealed a dense population of nanoparticles on the nanowire sides (Figure S6). UV-Vis-NIR extinction spectra of Ag/ZnO nanowires before and after Ag deposition revealed a plasmon absorption peak centered at ~450 nm (Figure S9).

### Effect of PDMS Thickness on Surface Enhancement

To quantify SERS, Raman spectra were acquired of a 25- $\mu\text{M}$  solution of crystal violet dye in DI water through both bare ZnO nanowires and Ag/ZnO nanowires for both PDMS thicknesses. Representative examples of these spectra are shown in Figure 2. The SERS intensity was greater for thin PDMS than for thick. This difference was due to increased light scattering through thick PDMS, resulting in less Raman-scattered light reaching the detector. Crystal violet has several strong bands in the fingerprint region of its Raman spectra that can be decoupled from the strong Raman peaks of PDMS, shown in Figure S4. Furthermore, plasmonic nanoparticles used for SERS are separated from PDMS by at least 100 nm, which was the thickness of the ZnO seed layer. This is more than enough to ensure that the PDMS Raman contributions do not experience significant surface enhancements. Enhancement was quantified for 13 individual crystal violet Raman peaks distinguishable from the PDMS background in non-SERS spectra, tabulated with their raw enhancement through thick and thin PDMS in Table 1. Raw enhancement, simply the difference in peak intensity between SERS and non-SERS spectra, ranged from an average of 2.2-fold for spectra taken through thick (~1 mm) PDMS to an average of 130-fold for spectra taken through ~0.17-mm thick PDMS, as shown in Figure 3, demonstrating the impact that PDMS thickness has on the magnitude of enhancement observed. While more PDMS thicknesses would be required to establish a relationship between PDMS thickness and surface enhancement, this data demonstrates that enhancement is inversely related to PDMS thickness. Thus, it is vital to control the thickness of the PDMS cap through which analysis is performed. Multiple parameters must be considered in order to

Table 1: Crystal violet Raman peaks used to compare surface enhancement through thick vs. thin PDMS.

Raman Band ( $\text{cm}^{-1}$ )	Thick PDMS (~1.0 mm)	Thin PDMS (~0.17 mm)
345	2.81	300.17
420	3.63	284.76
441	2.45	74.34
571	2.41	292.79
810	2.17	86.42
915	2.42	111.04
1175	2.47	58.87
1300	1.57	80.21
1374	1.91	43.04
1445	1.55	84.25
1529	1.26	129.17
1592	2.25	116.6
1621	1.95	35.34

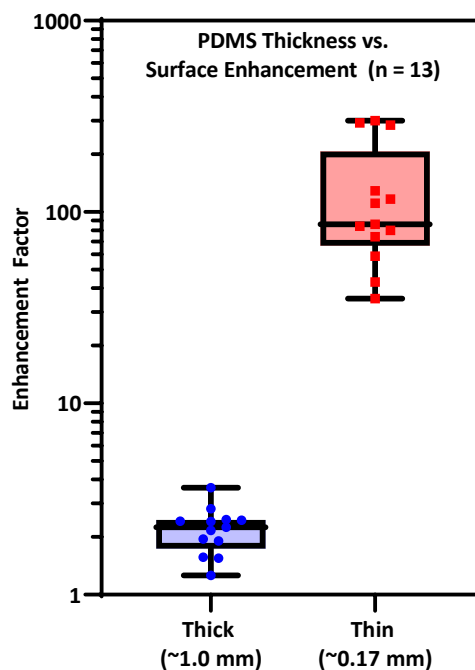


Figure 3: Comparison of the enhancement to selected crystal violet Raman peaks through thick and thin PDMS across  $n = 13$  peaks.

optimize PDMS thickness to maximize sensing reliability. First, PDMS thickness must be counterbalanced by the channel's ability to withstand fluidic pressure without rupturing. The PDMS cap cannot be made so thin that it ruptures when samples are injected. Second, PDMS thickness must be uniform across the sensor area, as well as from sensor to sensor. Uniform thickness is essential to reliable sensing.

A more detailed understanding of the SERS enhancement to the Raman spectra of crystal violet considers the confocal sensing volume of the spectrometer relative to the volume of crystal violet being influenced by SERS. The volume of crystal violet solution being sensed by the laser was orders of magnitude greater than the volume of crystal violet solution sufficiently close to the sensing surfaces to be influenced by SERS, as discussed in previous work.<sup>11</sup> The volume of crystal violet solution being sensed by the spectrometer can be approximated as a cylinder with a diameter equivalent to the laser waist and length equivalent to the confocal range. The beam waist radius was determined to be approximately  $d_w = 12 \mu\text{m}$  via the knife-edge method.<sup>11,36</sup> This was used to calculate the laser's confocal length  $L_c$  via Equation (3).<sup>11,37</sup> This, in turn, was used to calculate the ratio of confocal volume to SERS-influenced volume, defined here as the enhancement factor ( $EF$ ), via Equation (4).

$$L_c = \frac{2\pi(d_w)^2}{\lambda} \quad (1)$$

$$EF = \frac{E_I}{2 \frac{L_n}{L_c} \pi D (d_n d_m + d_m^2)} \quad (2)$$

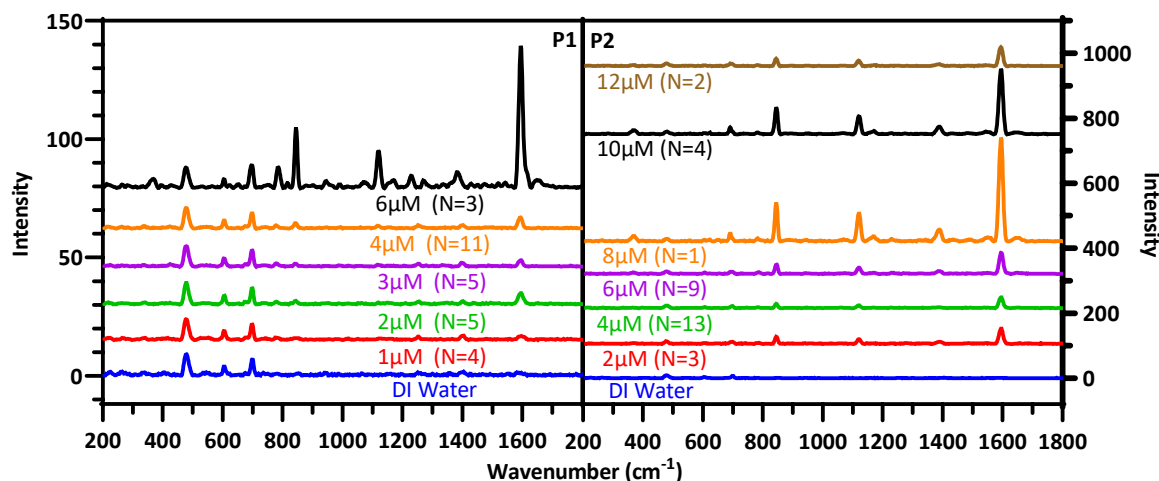


Figure 4: SERS spectra of melamine in DI Water, acquired through P1 on the left and P2 on the right. Number of spectra acquired for each concentration through each substrate in parentheses.

In these equations,  $\lambda$  is the 532-nm laser wavelength,  $E_i$  is the raw enhancement for each peak,  $d_n$  is the average nanowire diameter (nm),  $D$  is the average nanowire density ( $\text{nm}^{-2}$ ), and  $d_m$  is the radius of effect for SERS (nm).  $D$  and  $d_n$  were determined via ImageJ analysis of SEM images of the nanowires to be  $1.96 \times 10^{-4} \text{ nm}^{-2}$  and 29 nm, respectively. Because SERS is extremely local to the sensing surface,<sup>38</sup> a radius of effect of  $d_m = 3 \text{ nm}$  was used.<sup>39</sup> EF was estimated to be an average of  $9.9 \times 10^4$  for crystal violet spectra acquired through thick PDMS and an average of  $5.8 \times 10^6$  for spectra acquired through thin PDMS. The enhancement factors and vibrational modes for each chosen Raman band of crystal violet,<sup>40–47</sup> as well as the vibrational modes for the Raman bands of PDMS<sup>48–52</sup> can be found in Table S1

#### Surface-Enhanced Raman Spectroscopy of Melamine through PDMS Substrates

After demonstrating the viability of SERS through thin PDMS with crystal violet, SERS spectra were acquired of melamine solutions in DI Water using SERS substrates fabricated on  $\sim 0.15$ -mm thick PDMS substrates. Two substrates, hereafter named P1 and P2, were fastened upside down to a reservoir so that Raman spectra were acquired through the PDMS substrate.

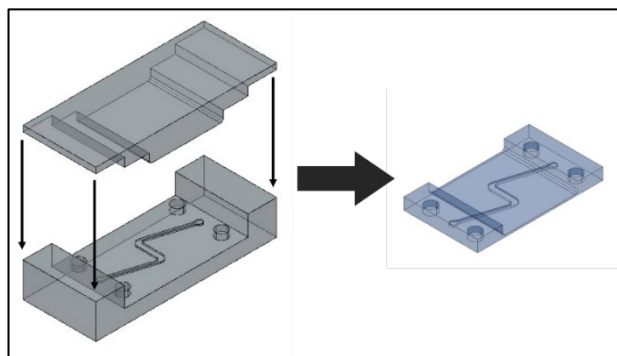


Figure 5: AutoCAD drawing of the microchannel mold designed to enable sensitive SERS through the top channel wall, along with the resultant microchannel.

Raman spectra were acquired of  $\mu\text{M}$  concentrations of melamine in DI water (1, 2, 3, 4, and 6  $\mu\text{M}$  for P1; 2, 4, 6, 8, 10, and 12  $\mu\text{M}$  for P2). While the characteristic peak of melamine at  $691 \text{ cm}^{-1}$  is coincident with the PDMS peak at  $703 \text{ cm}^{-1}$  associated with Si-C symmetric stretching and  $\text{CH}_3$  bending, multiple melamine peaks are visible even at concentrations of 1 and 2  $\mu\text{M}$  for both substrates. 6 melamine peaks other than the  $691 \text{ cm}^{-1}$  peak were identified in the spectra plotted in Figure 4 that could be assigned vibrational modes, as tabulated in Table S2.<sup>53,54</sup> Importantly, the lowest concentrations detected are well below the  $7.93 \mu\text{M}$  limit set by the Codex Alimentarius, demonstrating the efficacy of SERS sensing of melamine through PDMS.

SERS spectra exhibited substrate-to-substrate variation, with spectra from P2 generally having much greater melamine signal than P1, as illustrated by direct comparisons of the signals generated by 2, 4, and 6  $\mu\text{M}$  concentrations of melamine shown in Figure 4. Additionally, signal intensity exhibited point-to-point variability, with some spots on both substrates generating much more melamine signal than other spots. This effect is likely due to variation in nanowire density caused by the hydrophobicity of PDMS inhibiting precursor flow around the ZnO seed during hydrothermal nanowire growth. This variability in nanowire growth would cause variability in effective surface area. The ratios of melamine peak intensity to PDMS peak intensity at  $488 \text{ cm}^{-1}$  shown in Figure S10 were averaged for each melamine peak across all concentrations measured for each substrate. For both substrates, these melamine to PDMS peak ratios followed the same trends with increasing concentration. Furthermore, the ratio of the  $1596$  to  $845 \text{ cm}^{-1}$  melamine peaks, shown in Figure S11, remained consistent between substrates and across melamine concentrations, lending confidence that SERS can be used to reliably and consistently sense melamine through PDMS once device nanowire fabrication is standardized. In addition to variation across substrates, Raman spectra acquired at the same location on a single substrate exhibited varied intensity from measurement to measurement. It was observed that a Raman

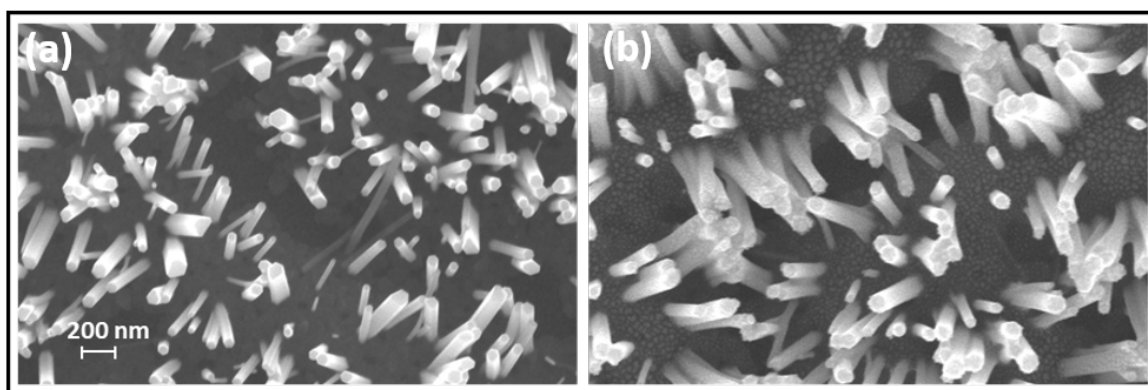


Figure 6: SEM images of ZnO nanowires (a) before and (b) after deposition and anneal of Ag, demonstrating nanowire growth and Ag nanoparticle formation.

spectrum taken immediately after the introduction of a melamine solution would exhibit little-to-no melamine signal. However, after the substrate was manually disturbed, strong melamine signal would appear in subsequent Raman spectra. This phenomenon is likely due to the hydrophobicity of nanowire beds preventing infiltration of the melamine solution. Disturbing the substrates allows melamine solution to infiltrate the bed of nanowires, enabling much stronger melamine signal. However, this infiltration was inconsistent.

#### Microchannel Mold Design and Fabrication

Based on the comparison between surface enhancement through thick and thin PDMS, it became apparent that a thin microchannel wall would be vital for successful SERS detection of trace analytes. Thus, it was necessary to design a microchannel mold that would enable the fabrication of channels able to facilitate such sensitive SERS. The mold was designed with a base and lid as shown in Figure 5, which would be fitted onto the base after PDMS was poured into the mold. The mold was designed such that channels fabricated would be z-shaped channels with a 2-mm width in the center portion to facilitate subsequent nanostructure fabrication. The channel's top wall was designed to be thick enough at the inlet and outlet to support tubing, but thin enough at 0.10 mm to enable sensitive SERS sensing with minimal PDMS interference. The

channel's top wall was also designed such that the thicker portions would be far enough apart to allow high-magnification objectives with short working distances close enough to focus on the SERS-active surface. The channel was designed with the z-shaped structure, ~7 mm long at the center, to enable Raman spectra to be acquired at multiple points along the center portion. The mold was milled from aluminum in the machine shop of the Physics Department at Vanderbilt University. As a function of the milling process, very small ridging occurred on the surface of the mold lid, which could interfere with SERS sensing through the top wall. To combat this, a glass slide was cut to fit the center portion of the lid and affixed with Kapton tape to the mold lid. Glass spacers were also cut and similarly affixed to the ends of the lid, which would rest on the base, in order to maintain the designed thickness of the PDMS cap.

#### Fabricating SERS Substrates Inside PDMS Channels

Several channels were sputtered with a ZnO seed layer and grown with nanowires. PL spectra of the nanowires inside the channels, shown in Figure S12, exhibited a large band-edge emission and minimal visible emission, indicating high crystallinity with few defects. The intensity of the band-edge emission varied from channel to channel as shown in Figure S12, which indicates variability in the amount of ZnO present in the channels. As exhibited by Figure S13, nanowire density and dimensions varied greatly from channel to channels. Nanowire formation was, in general, sparser for sputtered seed layers versus e-beam deposited seed layers, as exemplified by a comparison of nanowire density between Figure S5 and Figure S13. This variability demonstrates that sputtered ZnO does not result in uniform nanowire growth, indicating that another means of combating PDMS hydrophobicity should be explored. One possible way to do so would be to make channels with a copolymer consisting of PDMS and poly(ethylene oxide) (PEO), which has been shown to improve hydrophilicity.<sup>55</sup> Making the channels hydrophilic should improve precursor flow at an e-beam deposited ZnO seed layer, which would make nanowire growth and density more uniform.

Channel 4 in Figure S13 exhibited the most consistent nanowire growth, and was selected for further development. SEM image of the channel taken before (Figure 6(a)) and after Ag deposition (Figure 6(b)) confirmed the growth of highly crystalline nanowires inside the channel. The UV-Vis spectrum

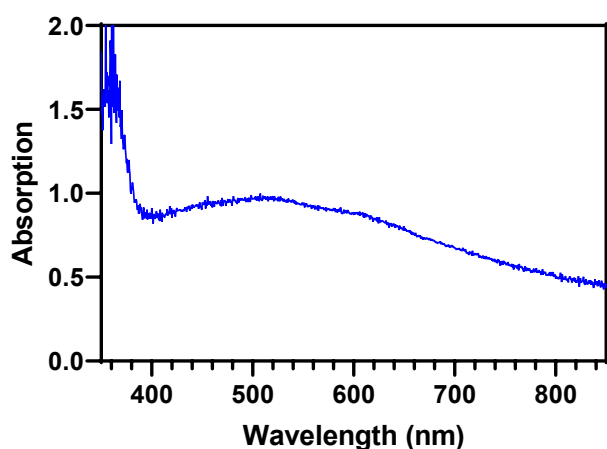


Figure 7: UV-Vis-NIR spectrum of ZnO nanowires decorated with Ag nanoparticles after anneal



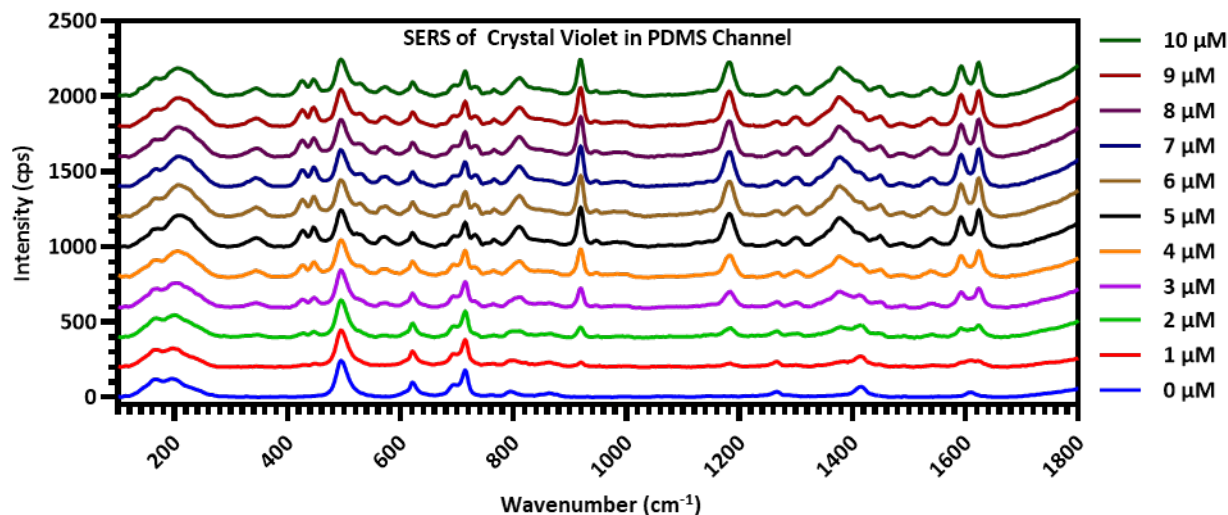


Figure 8: Raman spectra of crystal violet solutions taken inside a fabricated channel, in concentrations ranging from 1 to 10  $\mu\text{M}$  with a DI water control.

of the Ag/ZnO nanowires in the channel (Figure 7) exhibited a clear plasmon peak at  $\sim 515$  nm and shoulder at  $\sim 600$  nm. This is likely because of the dual size populations of Ag nanoparticles deposited on the nanowire sides and the floor of the channel, as is exhibited by SEM of the Ag/ZnO nanowires in Figure 6(b). The plasmon emission peaked at  $\sim 515$  nm, close to the 532 nm laser line, and extended well past the end of the fingerprint region at  $\sim 590$  nm, making the channel suitable for SERS. Subsequently, the channel was completed by binding the PDMS to a glass slide and tubing was inserted at the inlet and outlet.

#### Surface-Enhanced Raman Spectroscopy of Crystal Violet in Channel

Crystal violet was used to characterize a SERS detection in the completed channels, since crystal violet has multiple strong peaks between 900 and 1200  $\text{cm}^{-1}$ , where the Raman of PDMS

is relatively weak. Raman spectra were acquired of 10 crystal violet solutions in DI water ranging from 1  $\mu\text{M}$  to 10  $\mu\text{M}$  concentrations in 1- $\mu\text{M}$  increments, with a DI-water control (Figure 8). Before each solution was syringed through the channel, it was flushed with DI water, and the Raman spectra were all acquired at the same location along the channel. There are two strong crystal violet peaks in particular that are not near any PDMS peaks: the C-C<sub>center</sub>-C bending peak at 917  $\text{cm}^{-1}$  and the C-C<sub>center</sub>-C asymmetric stretching peak at 1175  $\text{cm}^{-1}$ . These peaks were not present in the control spectrum with no crystal violet, but clearly visible at a 1- $\mu\text{M}$  concentration. These crystal violet peaks exhibited a steady increase in intensity through the 5- $\mu\text{M}$  concentration, as illustrated in Figure 9. From 6 – 10  $\mu\text{M}$ , however, the peak intensity reached an asymptotic maximum. Raman spectra taken of the sensing surface after crystal violet solutions were flushed from the channel with DI water exhibited crystal violet peaks, meaning the levelling off of the Raman signal was likely due to accumulation of crystal violet adsorbed on the sensing surface.

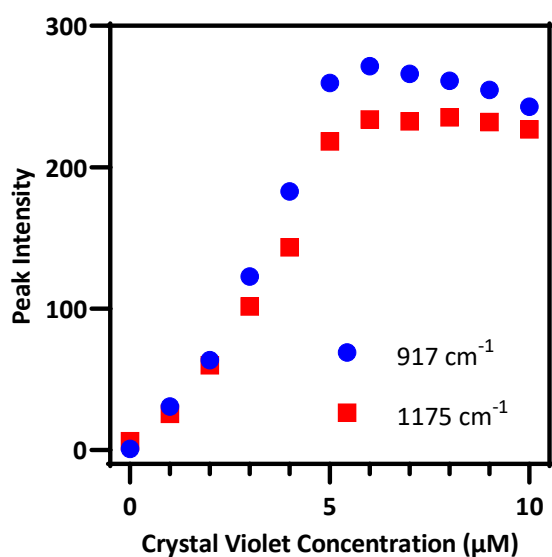


Figure 9: Intensity of two crystal violet peaks as a function of increasing crystal violet concentration

#### Conclusions

This work demonstrated a facile technique to fabricate physically deposited Ag nanoparticle decorated ZnO nanowires inside fluidic channels, allowing microfluidic SERS sensing to benefit from dense Ag nanoparticle formation from e-beam deposition. Through careful design and fabrication of fluidic channels to minimize spectral interference from PDMS,  $\mu\text{M}$  concentrations of crystal violet and melamine were detected, demonstrating the ability of the fluidic device to detect relevant concentrations of melamine. By further improvement on the SERS-active substrate fabrication process, it is expected that this process will provide reliable and sensitive detection of melamine in a SERS-active microfluidic devices.

## Author Contributions

A. L. Cook was responsible for conceptualization, data curation, formal analysis, investigation, methodology, project administration, visualization, writing – original draft preparation, and writing – review & editing. T. D. Giorgio was responsible for funding acquisition, resources, supervision, and writing – reviewing & editing.

## Conflicts of interest

There are no conflicts to declare.

## Acknowledgements

A. L. Cook acknowledges support from the National Science Foundation Graduate Research Fellowship Program (NSF GRFP) 1445197. A. L. Cook and T. D. Giorgio also acknowledge support from the Congressionally Directed Medical Research Program (CDMRP) Peer Reviewed Medical Research Program (PRMRP) W81XWH-18-1-0412. The authors would like to thank Eugene Collins, Ph.D. and Akira Ueda, Ph.D. at Fisk University for the use of their facilities and equipment. The authors would like to thank the Vanderbilt Institute of Nanoscale Science and Engineering (VINSE) for the use of their cleanroom and equipment, and Bill Martinez, Ph.D. for his assistance and training in the use of VINSE equipment. Lastly, the authors would like to thank Andrea Locke, Ph.D. for her input in the development and execution of this work.

## References

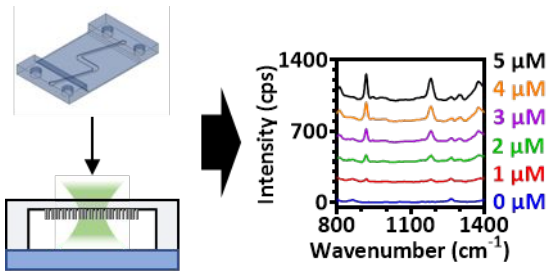
- 1 J. Guo, F. Zeng, J. Guo and X. Ma, *J. Mater. Sci. Technol.*, 2020, **37**, 96–103.
- 2 K. B. Kim, J.-H. Han, H. Choi, H. C. Kim and T. D. Chung, *Small*, 2012, **8**, 378–383.
- 3 H. Hwang, D. Han, Y.-J. Oh, Y.-K. Cho, K.-H. Jeong and J.-K. Park, *Lab Chip*, 2011, **11**, 2518–2525.
- 4 Y.-J. Oh and K.-H. Jeong, *Lab Chip*, 2014, **14**, 865–868.
- 5 H.-Y. Wu and B. T. Cunningham, *Nanoscale*, 2014, **6**, 5162–5171.
- 6 C. Novara, A. Lamberti, A. Chiadò, A. Virga, P. Rivolo, F. Geobaldo and F. Giorgis, *RSC Adv.*, 2016, **6**, 21865–21870.
- 7 H. Pu, W. Xiao and D.-W. Sun, *Trends Food Sci. Technol.*, 2017, **70**, 114–126.
- 8 I. J. Jahn, O. Žukovskaja, X.-S. Zheng, K. Weber, T. W. Bocklitz, D. Cialla-May and J. Popp, *Analyst*, 2017, **142**, 1022–1047.
- 9 J.-A. Huang, Y.-L. Zhang, H. Ding and H.-B. Sun, *Adv. Opt. Mater.*, 2015, **3**, 618–633.
- 10 Y. Xie, S. Yang, Z. Mao, P. Li, C. Zhao, Z. Cohick, P.-H. Huang and T. J. Huang, *ACS Nano*, 2014, **8**, 12175–12184.
- 11 A. L. Cook, C. S. Carson, C. E. Marvinney, T. D. Giorgio and R. R. Mu, *J. Raman Spectrosc.*, 2017, **48**, 1116–1121.
- 12 X. Liu, Q. Hu, Q. Wu, W. Zhang, Z. Fang and Q. Xie, *Colloids Surf. B*, 2009, **74**, 154–158.
- 13 H.-Y. Shin, E.-L. Shim, Y.-J. Choi, J.-H. Park and S. Yoon, *Nanoscale*, 2014, **6**, 14622–14626.
- 14 P. Yang, H. Yan, S. Mao, R. Russo, J. Johnson, R. Saykally, N. Morris, J. Pham, R. He and H.-J. Choi, *Adv. Funct. Mater.*, 2002, **12**, 323–331.
- 15 A. Janotti and C. G. Van de Walle, *Rep. Prog. Phys.*, 2009, **72**, 126501–126530.
- 16 P.-H. Lei and C.-H. Cheng, *Mater. Sci. Semicond. Proc.*, 2017, **57**, 220–226.
- 17 Z. Yi, X. Xu, X. Kang, Y. Zhao, S. Zhang, W. Yao, Y. Yi, J. Luo, C. Wang, Y. Yi and Y. Tang, *Surf. Coat. Tech.*, 2017, **324**, 257–263.
- 18 Y. Wang, W. Ruan, J. Zhang, B. Yang, W. Xu, B. Zhao and J. R. Lombardi, *J. Raman Spectrosc.*, 2009, **40**, 1072–1077.
- 19 Z. Kang, Y. Gu, X. Yan, Z. Bai, Y. Liu, S. Liu, X. Zhang, Z. Zhang, X. Zhang and Y. Zhang, *Biosens. Bioelectron.*, 2015, **64**, 499–504.
- 20 Y. S. Park and J. R. Schneider, *J. Appl. Phys.*, 1968, **39**, 3049–3052.
- 21 G. Barbillon, *Coatings*, 2019, **9**, 86.
- 22 D. C. Mayo, C. E. Marvinney, E. S. Bililign, J. R. McBride, R. R. Mu and R. F. Haglund, *Thin Solid Films*, 2014, **553**, 132–137.
- 23 W. Ji, L. Li, W. Song, X. Wang, B. Zhao and Y. Ozaki, *Angew. Chem.*, 2019, **131**, 14594–14598.
- 24 S. H. Lee, H. J. Lee, D. Oh, S. W. Lee, H. Goto, R. Buckmaster, T. Yasukawa, T. Matsue, S.-K. Hong, Ko, M.-W. Cho and T. Yao, *J. Phys. Chem. B*, 2006, **110**, 3856–3859.
- 25 M. Ladanov, P. Algarin-Amaris, G. Matthews, M. Ram, S. Thomas, A. Kumar and J. Wang, *Nanotechnology*, 2013, **24**, 375301.
- 26 Y. Zhang, B. Walkenfort, J. H. Yoon, S. Schlücker and W. Xie, *Phys. Chem. Chem. Phys.*, 2015, **17**, 21120–21126.
- 27 S. Seiffert, J. Dubbert, W. Richtering and D. A. Weitz, *Lab Chip*, 2011, **11**, 966–968.
- 28 H. Mao, W. Wu, D. She, G. Sun, P. Lv and J. Xu, *Small*, 2014, **10**, 127–134.
- 29 A. M. Giovannozzi, F. Rolle, M. Sega, M. C. Abete, D. Marchis and A. M. Rossi, *Food Chem.*, 2014, **159**, 250–256.
- 30 A. L. Cook, C. P. Haycook, A. K. Locke, R. R. Mu and T. D. Giorgio, *Nanoscale Adv.*, 2021, **3**, 407–417.
- 31 Renishaw, <http://www.renishaw.com/en/automatic-intelligent-background-removal--25934>, (accessed August 9, 2021).
- 32 C. V. Rumens, M. A. Ziai, K. E. Belsey, J. C. Batchelor and S. J. Holder, *J. Mater. Chem. C*, 2015, **3**, 10091–10098.
- 33 T.-M. Durdáková, Z. Hrdlička, M. Dendisová, M. Švecová and O. Vopička, *Polymer*, 2020, **188**, 122140.
- 34 A. Galdámez-Martinez, G. Santana, F. Güell, P. R. Martínez-Alanis and A. Dutt, *Nanomaterials*, 2020, **10**, 857.
- 35 D. C. Mayo, J. R. Nolen, A. Cook, R. R. Mu and R. F. Haglund, in *Proceedings Volume 9737, Synthesis and Photonics of Nanoscale Materials XIII*, SPIE, San Francisco, California, United States, 2016, vol. 9737, p. 973701.
- 36 Y. Suzuki and A. Tachibana, *Appl. Opt.*, 1975, **14**, 2809.
- 37 C. A. Bennett, *Principles of Physical Optics*, John Wiley & Sons, Inc., Hoboken, NJ, USA, 2008.
- 38 A. Sengupta, N. Brar and E. J. Davis, *J. Colloid Interface Sci.*, 2007, **309**, 36–43.
- 39 S. S. Masango, R. A. Hackler, N. Large, A.-I. Henry, M. O. McAnally, G. C. Schatz, P. C. Stair and R. P. Van Duyne, *Nano Lett.*, 2016, **16**, 4251–4259.
- 40 J. Wang, X. Gao, H. Sun, B. Su and C. Gao, *Mater. Lett.*, 2016, **162**, 142–145.
- 41 M. V. Cañamares, C. Chenal, R. L. Birke and J. R. Lombardi, *J. Phys. Chem. C*, 2008, **112**, 20295–20300.
- 42 W. Meng, F. Hu, L.-Y. Zhang, X.-H. Jiang, L.-D. Lu and X. Wang, *J. Mol. Struct.*, 2013, **1035**, 326–331.
- 43 T. Watanabe and B. Pettinger, *Chem. Phys. Lett.*, 1982, **89**, 501–507.

- 44 L. Angeloni, G. Smulevich and M. P. Marzocchi, *J. Raman Spectrosc.*, 1979, **8**, 305–310.
- 45 E. J. Liang, X. L. Ye and W. Kiefer, *J. Phys. Chem. A*, 1997, **101**, 7330–7335.
- 46 F. A. Harraz, A. A. Ismail, H. Bouzid, S. A. Al-Sayari, A. Al-Hajry and M. S. Al-Assiri, *Appl. Surf. Sci.*, 2015, **331**, 241–247.
- 47 M. Alcolea Palafox, *Int. J. Quantum Chem.*, 2000, **77**, 661–684.
- 48 L. A. Leites, S. S. Bukalov, T. S. Yadritzeva, M. K. Mokhov, B. A. Antipova, T. M. Frunze and V. V. Dement'ev, *Macromolecules*, 1992, **25**, 2991–2993.
- 49 M. J. Shenton, H. Herman and G. C. Stevens, *Polym. Int.*, 2000, **49**, 1007–1013.
- 50 R. P. S. de Campos, I. V. P. Yoshida, M. C. Breitreitz, R. J. Poppi and J. A. F. da Silva, *Spectrochim. Acta A Mol. Biomol. Spectrosc.*, 2013, **100**, 67–71.
- 51 L. Bistričić, L. M. Borjanović and V. Dananić, *Vib. Spectrosc.*, 2013, **68**, 1–10.
- 52 L. Jayes, A. P. Hard, C. Séné, S. F. Parker and U. A. Jayasooriya, *Anal. Chem.*, 2003, **75**, 742–746.
- 53 N. E. Mircescu, M. Oltean, V. Chiş and N. Leopold, *Vib. Spectrosc.*, 2012, **62**, 165–171.
- 54 X. Chen, Y. Hu, J. Gao, Y. Zhang and S. Li, *Appl. Spectrosc.*, 2013, **67**, 491–497.
- 55 K. S. Dogbevi, B. K. D. Ngo, C. W. Blake, M. A. Grunlan and G. L. Coté, *ACS Appl. Polym. Mater.*, 2020, **2**, 1731–1738.



## Fabrication of Silver-Decorated Zinc Oxide Nanowire Sensor in Microchannels for Surface-Enhanced Raman Spectroscopy

Andrew L Cook and Todd D Giorgio\*



## Facile Physical Fabrication of Silver-Decorated Zinc Oxide Nanowire Sensor in Microchannels for Surface-Enhanced Raman Spectroscopy

Andrew L. Cook,<sup>a</sup> and Todd D. Giorgio\*<sup>a</sup>

- a. Department of Biomedical Engineering, Vanderbilt University, Nashville TN 37235, USA. E-mail: todd.d.giorgio@vanderbilt.edu

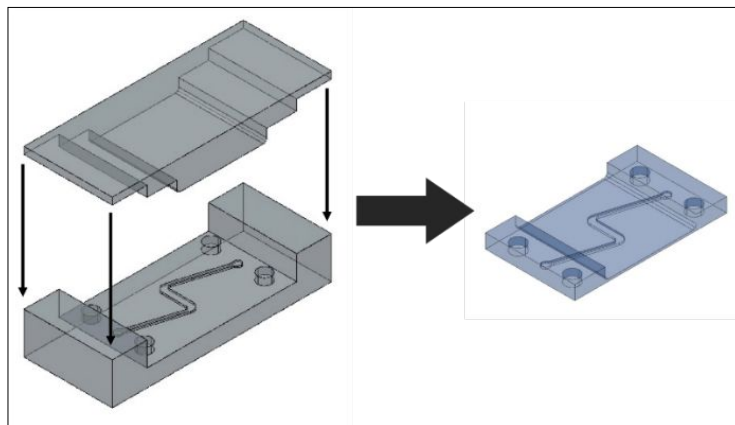


**Figure S1:** Microchannel mold, designed in AutoCAD to minimize PDMS spectral interference.

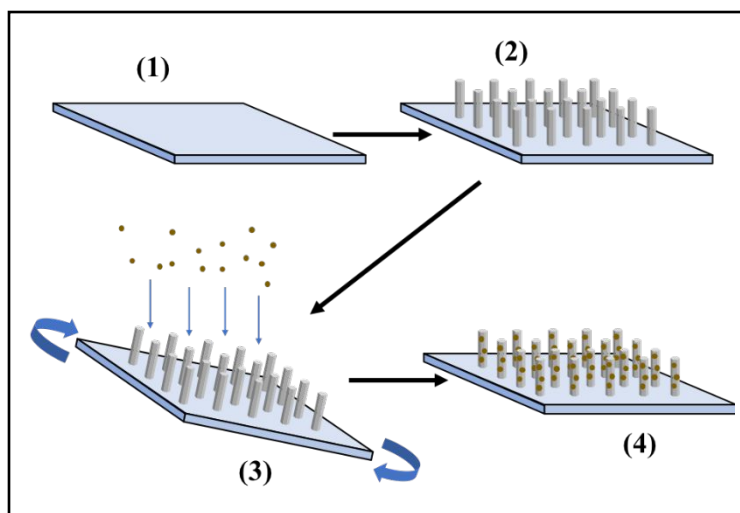


**Figure S2:** Illustration of the Ag/ZnO nanoprobe fabrication process for PDMS substrates: (1) deposit 100-nm ZnO seed layer on PDMS, (2) hydrothermally grow ZnO nanowires, and (3) deposit Ag on the nanowires on an azimuthally rotated sample to get (4) a finished Ag/ZnO nanoprobe.

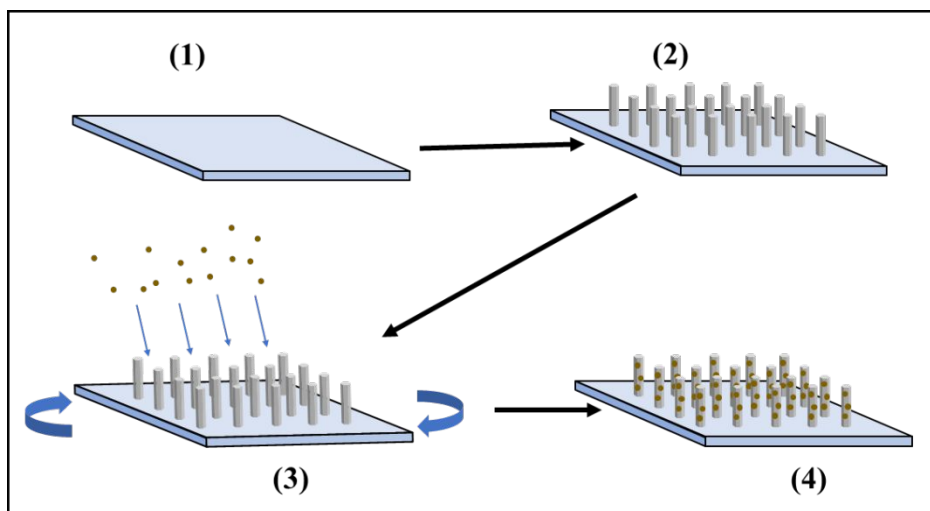


**Figure S3:** Illustration of the Ag/ZnO nanoprobe fabrication process for PDMS channels: (1) deposit 100-nm ZnO seed layer on PDMS, (2) hydrothermally grow ZnO nanowires, and (3) deposit Ag from an angle on the nanowires inside a rotated channel to get (4) a finished Ag/ZnO nanoprobe.

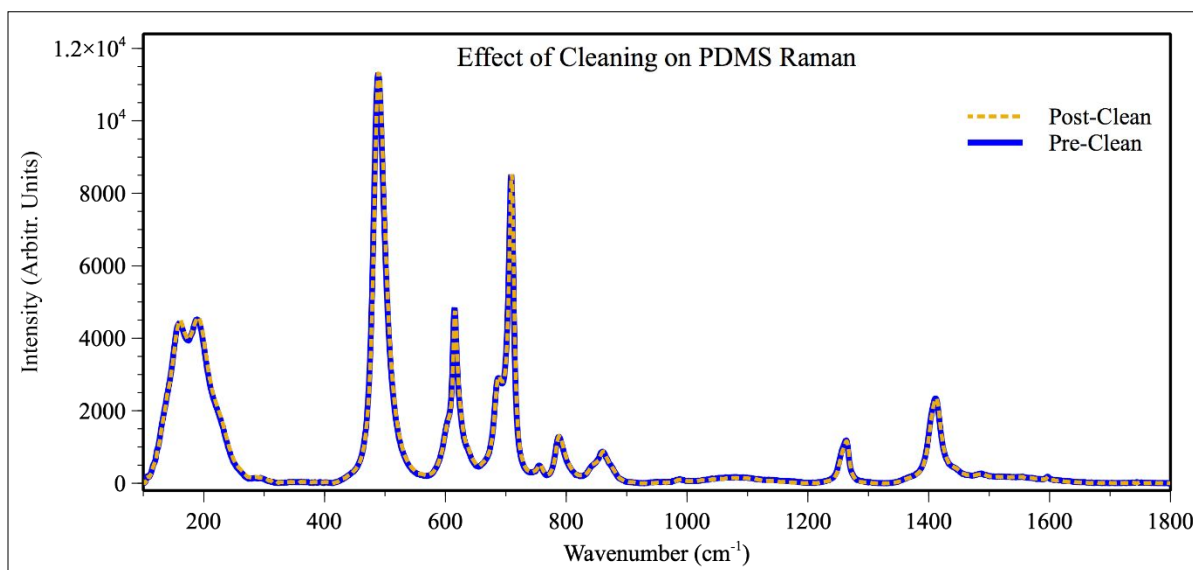


**Figure S4:** Raman spectra of PDMS before and after the ALD-AMD cleaning process, demonstrating no spectral effects due to cleaning.

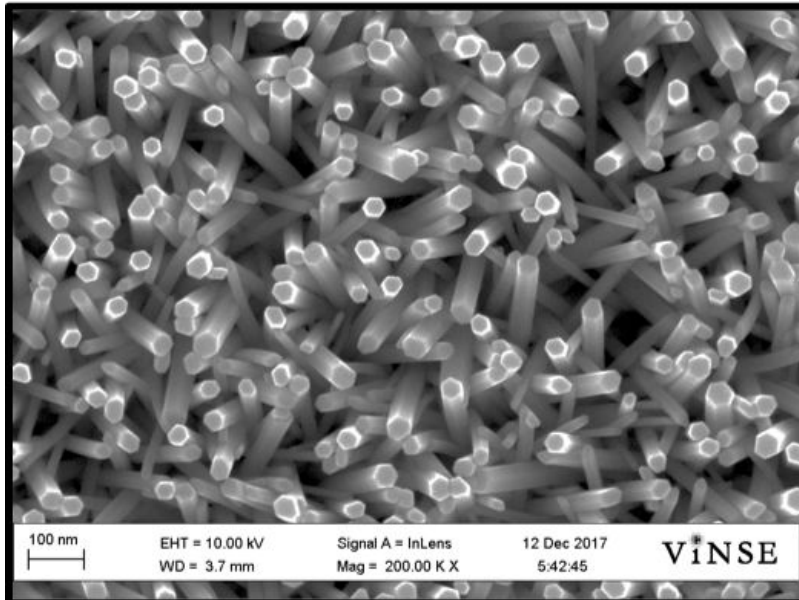


**Figure S5:** SEM image of bare ZnO nanowires, exhibiting highly crystalline nanowires.

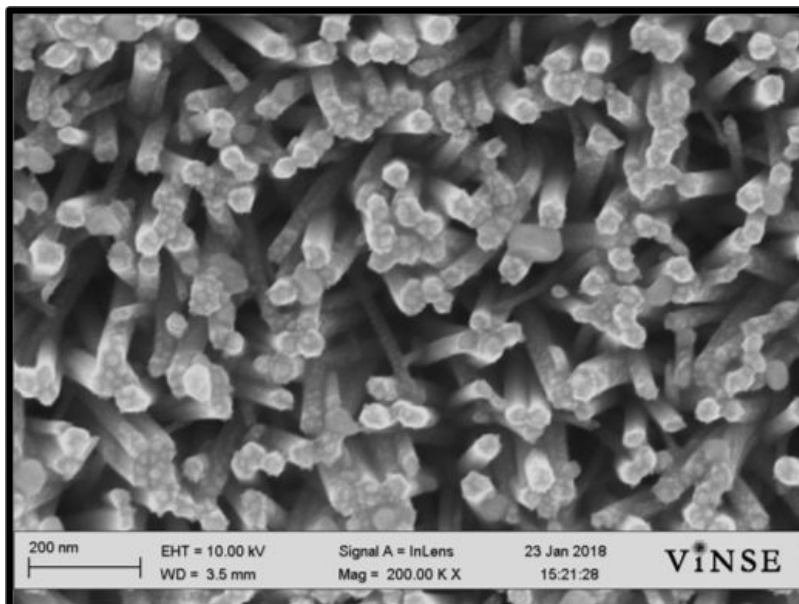


**Figure S6:** SEM image of ZnO nanowires after Ag nanoparticle decoration, demonstrating dense nanoparticle formation on the sides of nanowires.

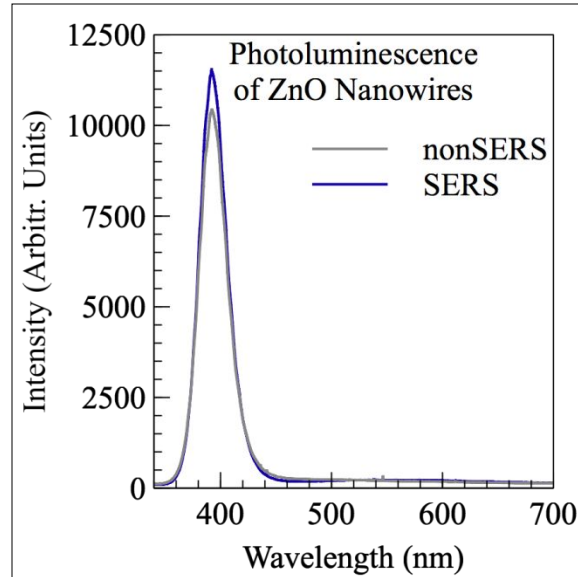


**Figure S7:** PL of ZnO nanowires to be decorated with Ag nanoparticles and those to remain bare, demonstrating highly crystalline nature of the nanowires and the similarity between the two sets of nanowires.

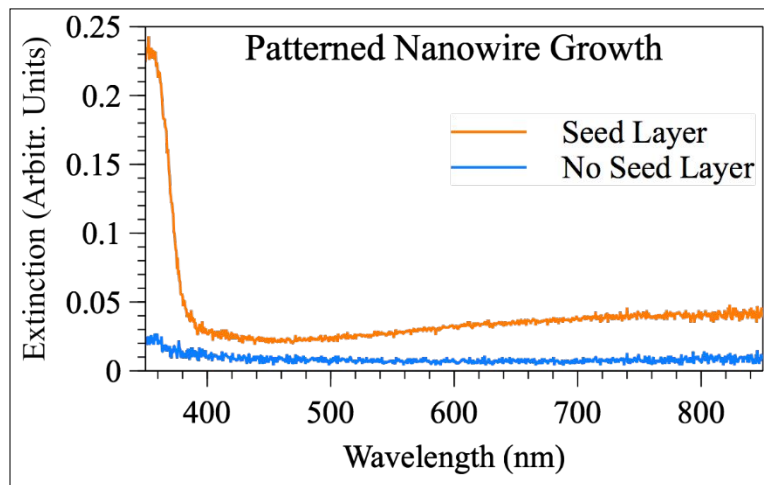


**Figure S8:** UV-Vis-NIR extinction spectra after nanowire growth of the seeded and non-seeded portions of a patterned PDMS substrate, demonstrating the ability to pattern nanowire growth on PDMS by patterning the seed layer.

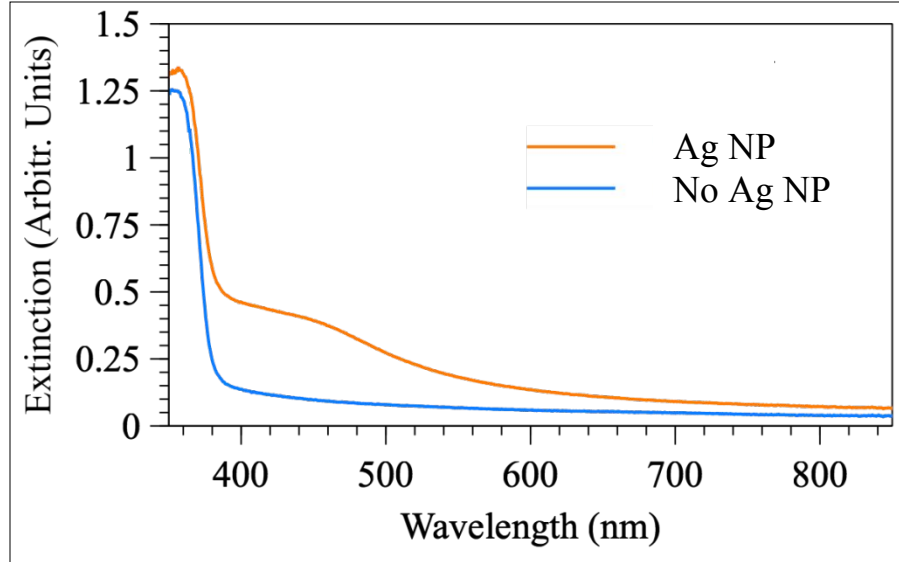


**Figure S9:** UV-Vis-NIR extinction spectra of Ag/ZnO nanoprobe before and after Ag deposition, demonstrating the formation of plasmons, centered at  $\sim 450$  nm.

**Table S1:** Vibrational modes of PDMS in the fingerprint region:  $\gamma$  = torsion,  $\delta$  = bending,  $\nu$  = stretching,  $\sigma$  = scissoring,  $\rho$  = rocking; s = symmetric, as = asymmetric,  $\perp$  = out-of-plane,  $\parallel$  = in-plane

Raman Band ( $\text{cm}^{-1}$ )	Vibrational Modes	Reference
160	$\gamma_{\text{as}}(\text{C-Si-C})$	[1, 2]
188	$\delta(\text{C-Si-C})/\delta(\text{C-Si-O})/\gamma_{\text{s}}(\text{C-Si-C})/\rho(\text{C-Si-C})/\sigma(\text{C-Si-C})$	[1-3]
488	$\nu_{\text{s}}(\text{Si-O-Si})$	[1-5]
615	$\nu(\text{Si-O-Si})/\nu(\text{Si-C})$	[1]
646	$\rho_{\text{as}}(\text{Si-C}_3)$	[4]
687	$\nu(\text{Si-C})/\rho(\text{C-H}_3)$	[1-3]
708	$\nu\text{-s}(\text{Si-C})/\delta(\text{C-H}_3)$	[1, 4, 5]
754	$\rho(\text{C-H}_3)/\rho_{\text{s}}(\text{Si-C}_3)/\nu(\text{Si-C})$	[1, 3, 4]
787	$\rho_{\text{as}}(\text{C-Si-C})/\nu_{\text{as}}(\text{C-Si-C})/\rho(\text{C-H}_3)$	[1, 2, 4, 5]
845	$\rho_{\text{as}}(\text{C-Si-C})$	[4]
859	$\rho(\text{C-Si-C})/\rho(\text{C-H}_3)$	[1, 2, 4, 5]
882	$\rho_{\text{as}}(\text{Si-C}_3)/\rho_{\text{as}}(\text{C-Si-C})$	[4]
1088	$\nu_{\text{as}}(\text{Si-O-Si})$	[4]
1262	$\delta_{\text{s}}(\text{C-H}_3)/\delta(\text{C-H}_2)$	[1, 2, 4, 5]
1411	$\delta_{\text{as}}(\text{C-H}_3)/\delta(\text{C-H}_2)/\sigma(\text{C-H}_2)$	[1-5]

**Table S2:** Selected Vibrational modes of melamine in the fingerprint region:  $\gamma$  = torsion,  $\delta$  = bending,  $\nu$  = stretching,  $\sigma$  = scissoring; s = symmetric,  $\perp$  = out-of-plane

Raman Band ( $\text{cm}^{-1}$ )	Vibrational Modes	Reference
380	$\delta(\text{C-N})$	[6, 7]
691	Ring Breathing	[6, 7]
845	$\delta_{\perp}(\text{Ring})$	[6, 7]
1235	$\delta(\text{N-H})$	[7]
1390	$\sigma(\text{NH}_2)/\nu(\text{C-N})/\delta_s(\text{Ring})$	[7]
1595	$\delta(\text{NH}_2)/\delta(\text{N-C-N})$	[6]

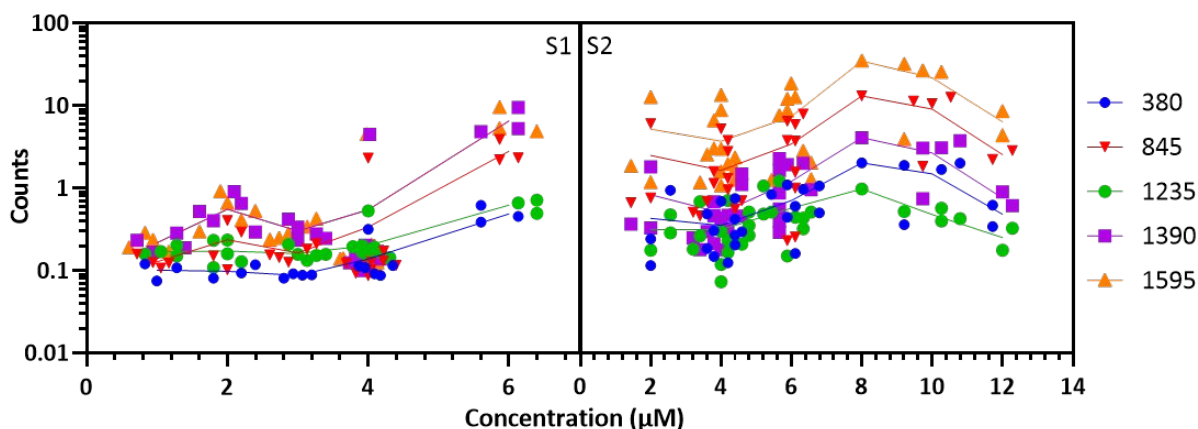


**Figure S10:** Ratios of each melamine peak with the PDMS peak at  $488 \text{ cm}^{-1}$  for each substrate, illustrating the consistency of melamine peak intensities relative to the overall signal intensity for each measurement.

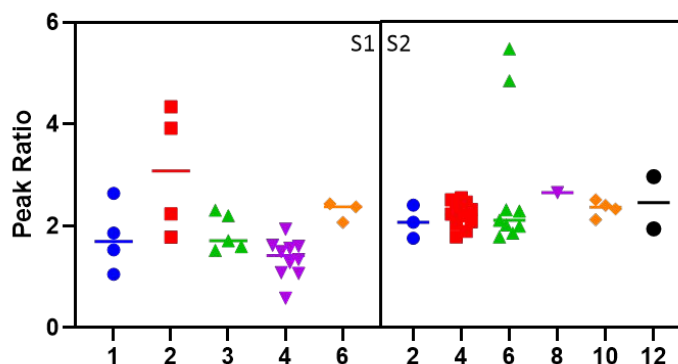


**Figure S11:** Ratios of melamine peaks at  $1595 \text{ cm}^{-1}$  to  $845 \text{ cm}^{-1}$  for each melamine concentration measured for each substrate, illustrating internal signal consistency for all concentrations measured, and across substrates.

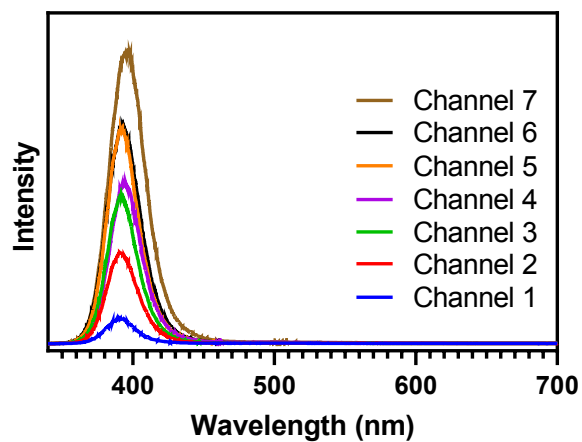


**Figure S12:** Photoluminescence spectra of ZnO nanowires in 7 different PDMS channels, demonstrating variability in ZnO nanowire structure, though each still exhibits high crystallinity with few defects.

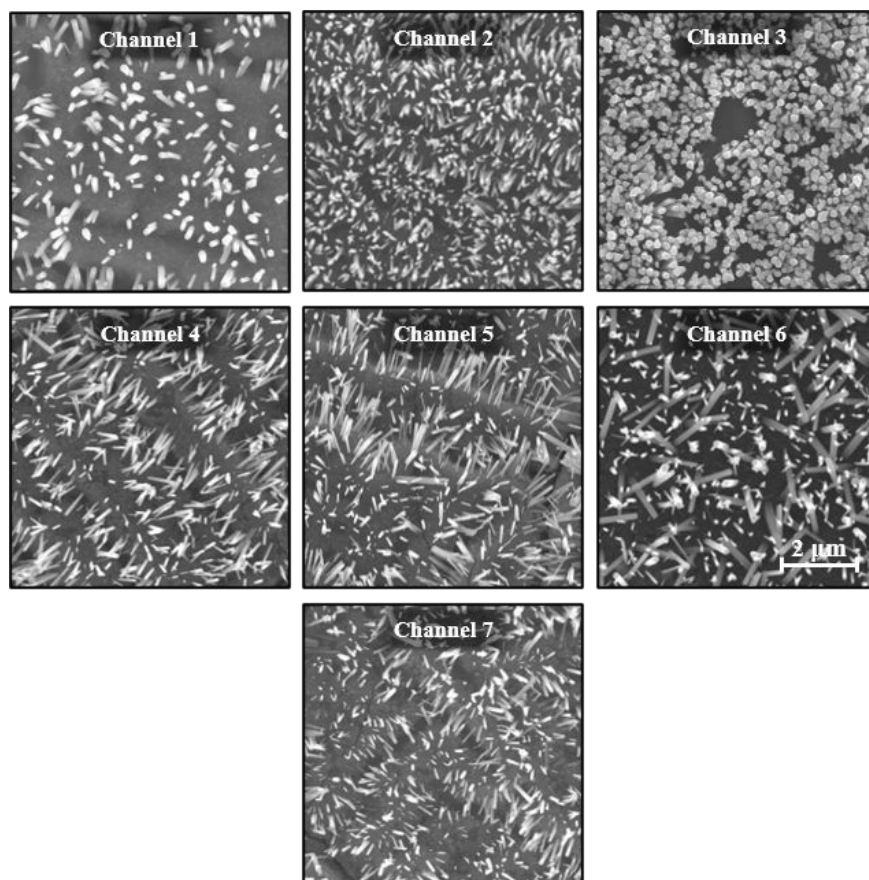


**Figure S13:** SEM images of nanowires within PDMS channels on sputtered ZnO seed layers, illustrating the variability of nanowire growth on sputtered seed layers.



## References

1. Bistričić L, Borjanović V, Mikac L, Dananić V (2013) Vibrational spectroscopic study of poly(dimethylsiloxane)-ZnO nanocomposites. *Vibrational Spectroscopy* 68:1–10. <https://doi.org/10.1016/J.VIBSPEC.2013.05.005>
2. Jayes L, Hard AP, Séné C, et al (2003) Vibrational Spectroscopic Analysis of Silicones: A Fourier Transform-Raman and Inelastic Neutron Scattering Investigation. *Analytical Chemistry* 75:742–746. <https://doi.org/10.1021/ac026012f>
3. Leites LA, Bukalov S, Yadritzeva TS, et al (1992) Vibrational and Electronic Spectra and the Structure of Crystalline Poly(dimethylsilane). *Macromolecules* 25:2991–2993
4. Shenton MJ, Herman H, Stevens GC (2000) Using spectroscopy with chemometrics to measure polymer molar mass. *Polymer International* 49:1007–1013. [https://doi.org/10.1002/1097-0126\(200009\)49:9<1007::AID-PI511>3.0.CO;2-H](https://doi.org/10.1002/1097-0126(200009)49:9<1007::AID-PI511>3.0.CO;2-H)
5. De Campos RPS, Yoshida IVP, Breikreitz MC, et al (2013) Raman imaging spectroscopic characterization of modified poly(dimethylsiloxane) for micro total analysis systems applications. *Spectrochimica Acta Part A: Molecular and Biomolecular Spectroscopy* 100:67–71. <https://doi.org/10.1016/j.saa.2012.03.054>
6. Mircescu NE, Oltean M, Chiş V, Leopold N (2012) FTIR, FT-Raman, SERS and DFT study on melamine. *Vib Spectrosc* 62:165–171. <https://doi.org/10.1016/j.vibspec.2012.04.008>
7. Chen X, Hu Y, Gao J, et al (2013) Interaction of Melamine Molecules with Silver Nanoparticles Explored by Surface-Enhanced Raman Scattering and Density Functional Theory Calculations. *Appl Spectrosc* 67:491–497. <https://doi.org/10.1366/12-06838>

# Toxic Metals Chelation by 18-Crown-6 Ethers in Multiple Solutions and Quantification by Spectroscopic Techniques

Andrew L Cook<sup>1</sup>, Fan Xue<sup>1</sup>, Todd D Giorgio<sup>1</sup>

<sup>1</sup>Department of Biomedical Engineering

Vanderbilt University

2201 West End Avenue, Nashville, TN 37235, United States

Andrew.L.Cook.1@vanderbilt.edu; Fan.Xue@vanderbilt.edu; Todd.D.Giorgio@vanderbilt.edu

**Abstract** - Toxic metals exposure is a significant problem for military personnel, with increasingly prevalent embedded fragments due to improvised explosive devices. Current biomonitoring for military personnel with embedded fragments is centralized, limiting capacity and availability. Importantly, monitoring using this approach begins long after peak exposure, indicating a need for portable, multiplexed toxic metals detection that can be carried out closer to the time of exposure with increased frequency. Small molecule chelators such as crown ethers are known to selectively bind metal cations in solution. Crown ethers possess selective chelation of multiple metal ions and is dependent on molecular structure, solution properties, and other parameters. This selectivity extends to multiple ions and depends on not only molecular structure, but also the solution properties. The goal of this study is to assess the potential for metal sensing in solution as a function of crown ether structure and solution properties with future use for toxic metal sensing from embedded fragments as a potential translational objective.

**Keywords:** Crown Ether, Toxic Metal, UV-vis, Fluorescence, Embedded Fragment, Urine

## 1. Introduction

As of 2017, improvised explosive devices (IEDs) have accounted for almost 75% of all traumatic injuries to U.S. soldiers in recent conflicts in Iraq and Afghanistan [1]. This means that of the more than 50,000 military personnel wounded in action so far in those conflicts [2], almost 40,000 of them could have toxic embedded fragments [3]. In response to this growing need, the United States Department of Veterans Affairs (VA) established the Toxic Embedded Fragment Surveillance Center (TEFSC, Baltimore, MD) in 2008 with the overall mission to 1) identify veterans who may have embedded metal fragments, and 2) conduct long-term medical surveillance of this population [4]. The evaluation process for inclusion into the Embedded Fragments Registry (EFR) is predicated on the individual's knowledge or suspicion of retained fragments [5]. Thus, biomonitoring of toxic embedded fragments begins long after peak exposure and depends on incomplete knowledge concerning exposure and retention toxic fragments from IEDs, making inclusion into the EFR noncomprehensive. As a result, there are currently only around 16,000 veterans enrolled in the EFR [6]. Biomonitoring of these veterans is carried out via centralized urinalysis using inductively-coupled plasma mass spectrometry (ICP-MS)[1], [4], [7]. While ICP-MS is sensitive and precise, it is a large, research-grade instrument that requires significant power and highly trained technicians for operation[8], [9], making it unsuitable for use near locations where military blast injuries occur. Furthermore, there is a lack of information concerning the scope and extent of embedded fragments[10], [11] as well as their long-term health effects[3], [12]. To ensure more comprehensive and complete biomonitoring of embedded fragments, a portable, multiplexed toxic metals sensing strategy is required.

There are many techniques for toxic metals detection that can be implemented in a portable setting, including spectroscopic techniques such as fluorescence, colorimetry, and Raman spectroscopy. Many strategies utilizing these techniques make use of small-molecule chelators known to bind various metal ions in solutions. One common family of chelators are known as crown ethers, small molecules with a characteristic ring made up of carbons and oxygens which are best known for chelating alkali metal cations [13]. While these chelators are moderately selective, they still bind multiple different ions in solution. Small changes in crown ether structure can significantly affect which metals it will bind [14], [15]. Additionally, differences in solution affect crown ether morphology, changing chelation selectivity[16]. The purpose of this

study is to explore how changes in the structure and solution of 18-crown-6 (18C6) ethers can change its selectivity profile for metal ions.

## 2. Experimental

Two different solvents consisting of dimethyl sulfoxide (DMSO) and deionized (DI) water were used for all experiments in this study: 1:1 DMSO/water and 1:3 DMSO/water. 4'-aminobenzo-18-Crown-6 (AB18C6) and benzo-18-Crown-6 (B18C6) and the following 22 metals were examined as a part of this study:  $\text{Al}^{3+}$ ,  $\text{Ag}^+$ ,  $\text{As}^{3+}$ ,  $\text{Ba}^{2+}$ ,  $\text{Ca}^{2+}$ ,  $\text{Cd}^{2+}$ ,  $\text{Co}^{2+}$ ,  $\text{Cr}^{3+}$ ,  $\text{Cu}^{2+}$ ,  $\text{Fe}^{3+}$ ,  $\text{Hg}^{2+}$ ,  $\text{K}^+$ ,  $\text{Li}^+$ ,  $\text{Mg}^{2+}$ ,  $\text{Mn}^{2+}$ ,  $\text{Mo}^{5+}$ ,  $\text{Na}^+$ ,  $\text{Ni}^{2+}$ ,  $\text{Pb}^{2+}$ ,  $\text{UO}_2^{2+}$ ,  $\text{W}^{4+}$ , and  $\text{Zn}^{2+}$ . All metal salts used to obtain these ions were purchased from Sigma Aldrich. All 14 metals in the TEFSC biomonitoring panel [3], [4] are included, as well as metals commonly found in urine, such as  $\text{Ca}^{2+}$ ,  $\text{K}^+$ ,  $\text{Mg}^{2+}$  and  $\text{Na}^+$ . Also included are a number of common metals that could make their way into human urine, such as  $\text{Al}^{3+}$ ,  $\text{Mn}^{2+}$ , and  $\text{Zn}^{2+}$ . 100  $\mu\text{M}$  equimolar solutions of each metal individually with AB18C6 were formed in both 1:1 DMSO/water and 1:3 DMSO/water.

In this study, the chelation of metal ions by two crown ethers was studied in a single solution to explore how a small change in the crown ether's structure might change the crown ether's metal selectivity. Furthermore, chelation of metal ions by one of those crown ethers was examined in two solutions. Chelation of metals by AB18C6 and B18C6 was examined primarily using ultraviolet-visible extinction spectrophotometry. Preliminary examination of the extinction spectrum of using a quartz cuvette in a Varian Cary 50 Bio spectrophotometer. These measurements were acquired at a resolution of 5 nm over a range of 250 – 800 nm to confirm the absorption profile of AB18C6 reported by Sarfo et. al. [15], and to explore differences in chelation of metal ions between AB18C6 and B18C6. For these experiments, the extinctions from 100- $\mu\text{M}$  concentrations of each crown ether in 1:3 DMSO:water were measured without metals. Subsequently, the extinctions of 100- $\mu\text{M}$  equimolar concentrations of each crown ether and selected metal salts in 1:3 DMSO:water were acquired.

Full UV-vis spectrophotometry chelation sweeps of metal ions by AB18C6 were performed using Thermo Scientific™ Nunc™ UV-transparent plastic 96-well plates in a Tecan Infinite M1000 Pro plate reader. These measurements were acquired at a resolution of 1 nm over a range of 250 – 400 nm to determine which metals are chelated by AB18C6. For these measurements, 100- $\mu\text{M}$  concentrations of AB18C6 in both solvents were used without metals, and 100- $\mu\text{M}$  equimolar solutions of AB18C6 and each metal salt in each solvent were used for selectivity assessments. The same instrument was used to acquire fluorescence measurements of AB18C6 in the presence and absence of selected metals were acquired with an excitation wavelength of 295 nm over a range of 300 – 700 nm at a resolution of 2 nm. The same crown ether and metal solution strategy was used for fluorescent measurements, except only two metals known to be chelated from previous experiments were included. UV-vis spectrophotometry with the same spectral parameters described above was performed on 100- $\mu\text{M}$  crown ether solutions with one of the metals known to be chelated in concentrations of 1 nM, 10 nM, 100 nM, 1  $\mu\text{M}$ , 10  $\mu\text{M}$ , and 100  $\mu\text{M}$ . Fluorescence spectroscopy was performed on these same solutions with an excitation wavelength of 295 nm over an emission range of 304 – 500 nm at a resolution of 1 nm.

## 3. Results & Discussion

The first experiment was a comparison via UV-vis spectrophotometry of which metals are chelated by AB18C6 and B18C6. It was reported by Sarfo et. al. [15] that AB18C6 crown ethers possess a strong extinction peak centered at 295 nm. When the crown ether chelates a metal, this peak is quenched and another emerges at  $\sim 280$  nm. For this experiment, 100- $\mu\text{M}$  solutions of AB18C6 and B18C6 by themselves and with equimolar concentrations of 13 selected metal salts prepared in 1:3 DMSO:water. As can be seen in Fig. 1, while AB18C6 has an extinction peak at 295 nm as Sarfo et. al. reported, B18C6 has a peak at  $\sim 275$  nm. No chelation occurred for most of the metals investigated, as evidenced by a lack of quenching of the 295-nm peak for AB18C6 or the 275-nm peak for B18C6, as well as a lack of an additional peak. However, both  $\text{Fe}^{3+}$  and  $\text{Hg}^{2+}$  ions were chelated strongly by AB18C6, evidenced by the quenching of the 295-nm peak and appearance of a peak  $\sim 282$  nm. Benzo-18-Crown-6 chelated none of the metals examined, indicating that even small differences in crown ether structure can lead to big differences in metal chelation.

The second experiment performed was an examination of how different solutions would affect the chelation of metal ions by AB18C6. 100- $\mu$ M solutions of AB18C6 were prepared in 1:1 DMSO:water and 1:3 DMSO:water, without and with equimolar concentrations of 22 metals. UV-vis spectra were acquired of each solution and plotted in Fig. 2. While the chelation profile for AB18C6 was very similar in both solutions, there were some significant differences. AB18C6 chelated

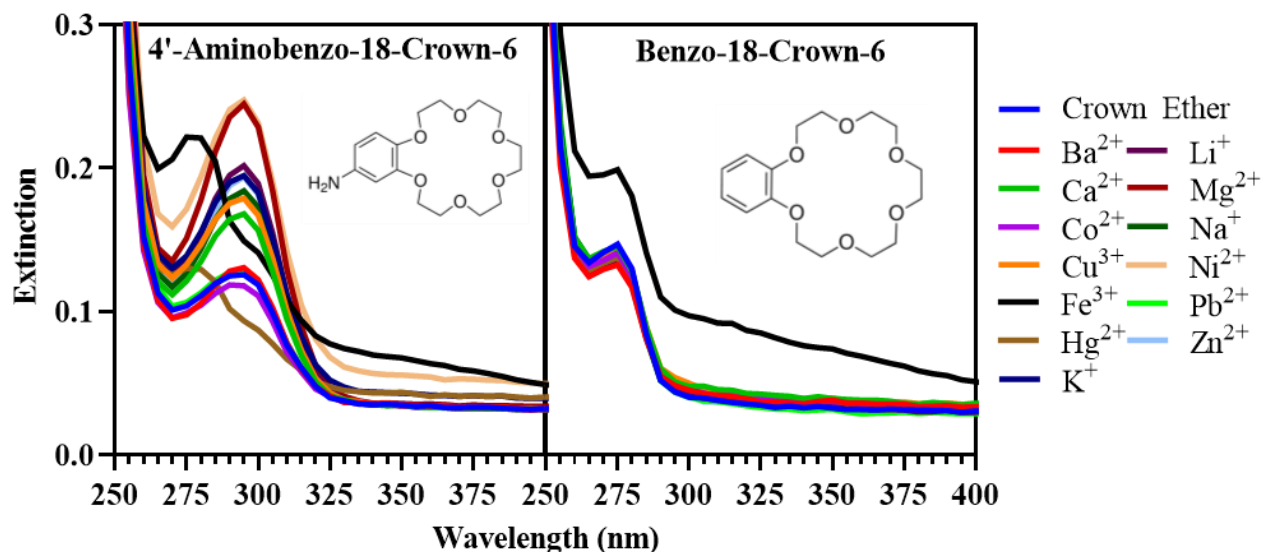


Fig. 1: UV-vis extinction spectra of 100- $\mu$ M AB18C6 and B18C6 in 1:3 DMSO:water without and with equimolar concentrations of selected metals.

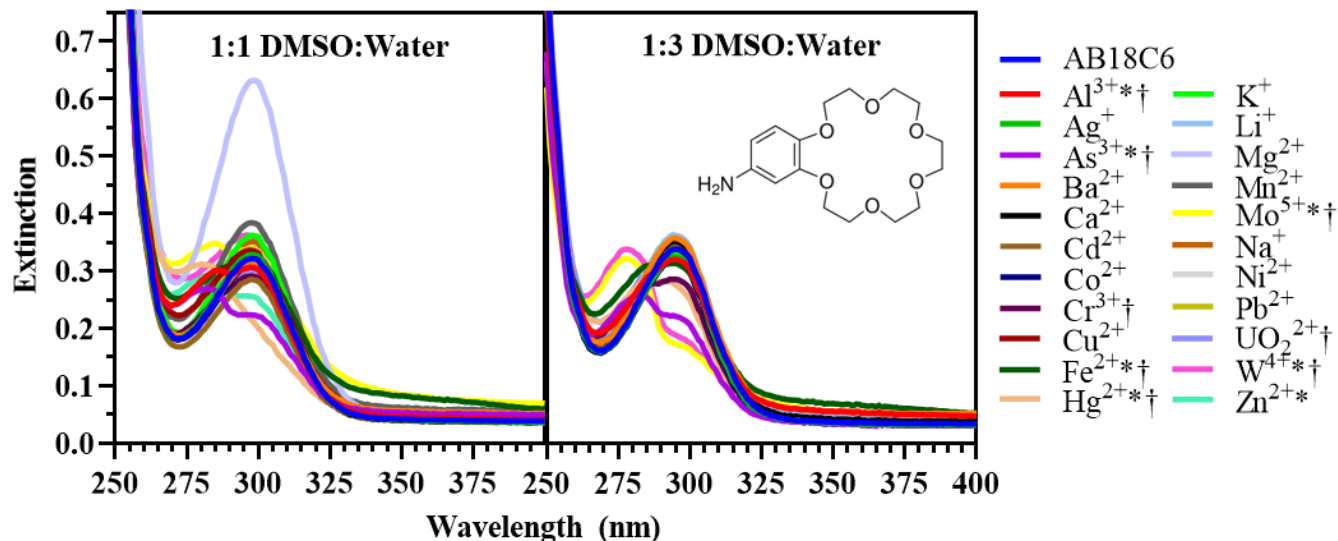


Fig. 2: UV-vis extinction spectra of 100- $\mu$ M AB18C6 alone and with equimolar concentrations of 22 metal salts in two different solutions. Metals chelated by AB18C6 in 1:1 DMSO:water are denoted with “\*”, while metals chelated by AB18C6 in 1:3 DMSO:water are denoted with “†”.

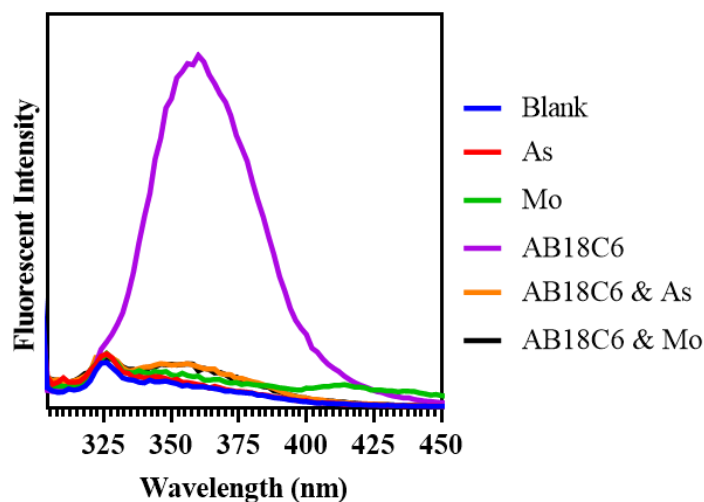


Fig. 3: Fluorescence spectra of 100- $\mu$ M AB18C6 without and with equimolar concentrations of As and Mo in 1:3 DMSO:water.

Al, As, Fe, Hg, Mo, and W in both solutions, while it chelated U in only 1:1 DMSO:water and Zn in only 1:3 DMSO:water. Even among metals chelated in both solutions, there were differences in the strength of chelation. Notably, Al is more strongly chelated in 1:1 DMSO:water while Hg is more strongly chelated in 1:3 DMSO:water. Interestingly, while Sarfo et al. reported that AB18C6 chelates  $\text{Pb}^{2+}$  [15], these experiments demonstrate a lack of  $\text{Pb}^{2+}$  chelation in either solution. Because of the dependence chelation has on solution, it is likely that this discrepancy with reported results result from an unreported difference in solution.

While UV-vis is excellent for qualitatively determining whether a crown ether is chelating a metal ion, it is difficult to extract any meaningful quantitative information on the amount of chelation taking place in a given solution. However, Sarfo et al. reported that AB18C6 possesses a fluorescence peak at  $\sim 370$  nm that gets quenched in the presence of chelated metals [15]. To confirm this, fluorescence measurements of 100- $\mu$ M solutions of AB18C6 without and with equimolar concentrations of  $\text{As}^{3+}$  and  $\text{Mo}^{5+}$  (known to be strongly chelated from Fig. 2) in 1:3 DMSO:water were acquired. As can be seen in Fig. 3, AB18C6 with no metal ions present fluoresces as Sarfo et al. reported. This fluorescence was strongly quenched when As and Mo were present. However, even at equimolar concentrations of metal ions, this fluorescence was not quenched completely, indicating that fluorescence can be used for quantification of toxic metals chelation by AB18C6.

An initial survey of the changes in optical absorbance and fluorescence resulting from AB18C6 chelation of a range of molybdenum concentrations between 1 nM and 100  $\mu$ M, as shown in Fig. 4. Mo was selected for this assessment based on the quenching of extinction at 295 nm and the presence of another extinction peak at  $\sim 280$  nm (Fig. 2). Mo concentrations of 1 nM, 10 nM, 100 nM, 1  $\mu$ M, 10  $\mu$ M and 100  $\mu$ M were prepared with 100- $\mu$ M solutions of AB18C6 in 1:3 DMSO:water. UV-vis spectrophotometry was performed at a resolution of 1 nm over a range of 250 – 400 nm (Fig. 4), and spectra of each concentration of Mo were subtracted from their corresponding spectra of mixed AB18C6 and Mo. Fluorescence used an excitation wavelength of 295 nm over a range of 304 – 450 nm at a resolution of 1 nm. A clear peak shift from  $\sim 295$  to  $\sim 275$  nm at 100  $\mu$ M Mo concentration was evident in addition to a small peak shift at 10  $\mu$ M. Large fluorescence quenching occurred at 100  $\mu$ M at  $\sim 360$  nm with additional, slight quenching at 10  $\mu$ M Mo concentration. Other concentrations of Mo did not produce evident changes in either UV-vis or fluorescence (Fig. 4).

To expand the characterization of Mo chelation by AB18C6, the same experiment was performed using Mo concentrations (in  $\mu$ M) of 6.25, 12.5, 25, 50, 100, and 200. UV-vis spectrophotometry and fluorescence spectroscopy used

the same resolution and range, as shown in Fig. 5. The extinction peak at  $\sim 295$  nm steadily decreased with increasing Mo concentration between  $6.25 \mu\text{M}$  and  $50 \mu\text{M}$ . This decrease reached a minimum at  $50 \mu\text{M}$  and did not continue to decrease for  $100$  or  $200 \mu\text{M}$ . The extinction peak at  $\sim 277$  nm increased in conjunction with the decrease of the  $295$ -nm peak, steadily intensifying between  $6.25 \mu\text{M}$  and  $50 \mu\text{M}$  and remaining steady for  $100$  and  $200 \mu\text{M}$ . Gradual quenching of AB18C6's

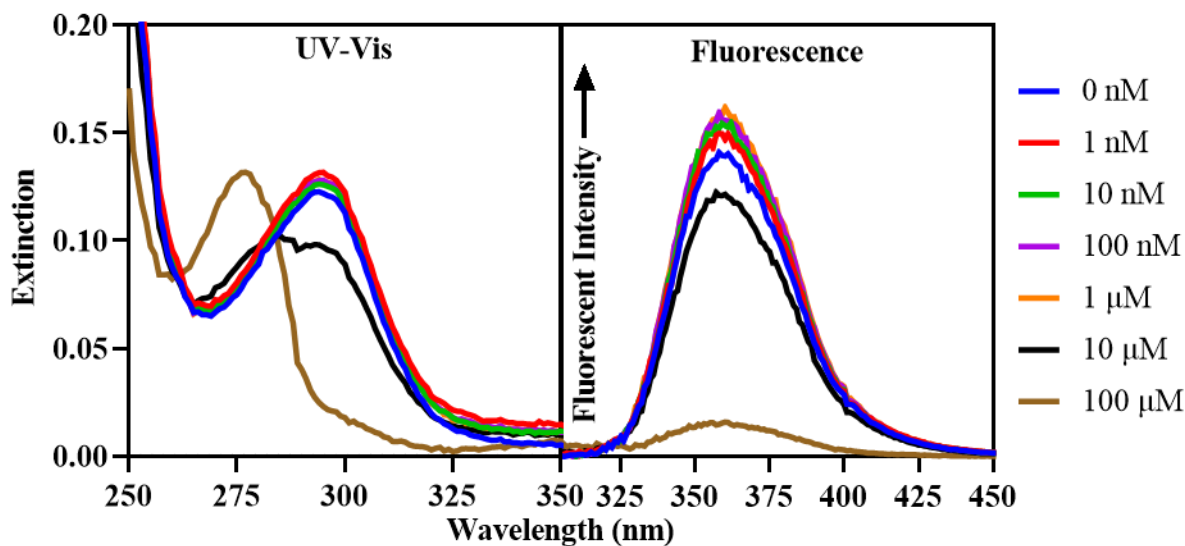


Fig. 4: UV-Vis and fluorescence spectra of  $100\text{-}\mu\text{M}$  AB18C6 with concentrations of Mo between  $1$  nM and  $100 \mu\text{M}$ , with a control solution of  $100\text{-}\mu\text{M}$  AB18C6 unmixed with Mo.

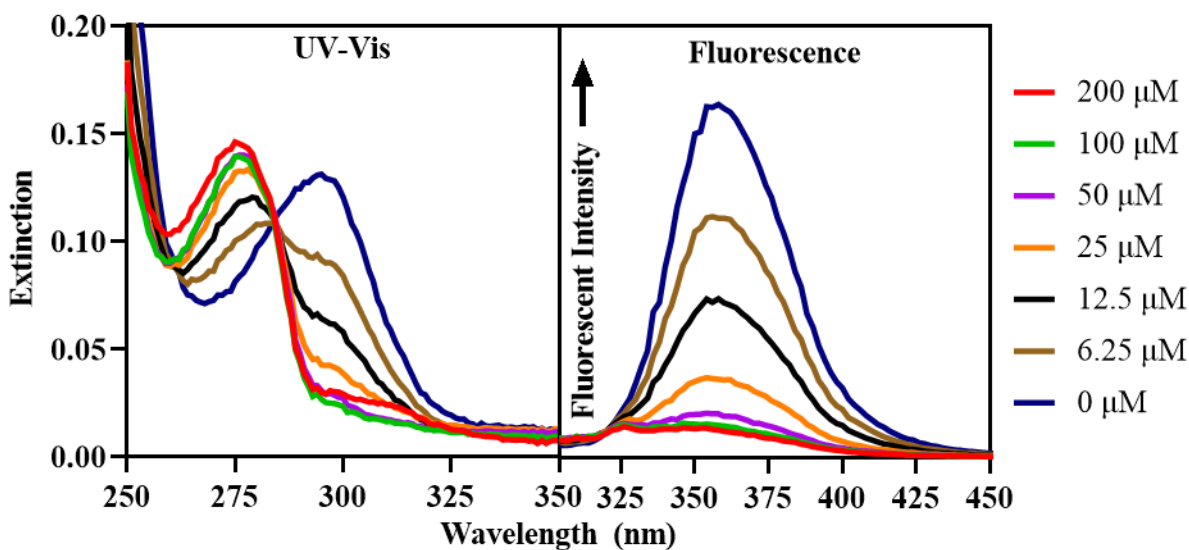


Fig. 5: UV-Vis and fluorescence spectra of  $100\text{-}\mu\text{M}$  AB18C6 with concentrations of Mo between  $6.25$  and  $200 \mu\text{M}$ , with a control solution of  $100\text{-}\mu\text{M}$  AB18C6 unmixed with Mo.

fluorescence peak at ~360 nm was observed under increasing Mo concentrations, as shown in Fig. 5. Full quenching of this fluorescence peak occurred at the 100  $\mu$ M concentration of Mo, indicating greater range of chelation quantification for fluorescence than for UV-vis. The absorption decrease at ~295 nm or increase at ~277 nm did not directly correlate with the increase in Mo concentration, suggesting that absorbance may be a complicated indicator of concentration for this metal. However, these experiments indicate that a quantitative relationship between AB18C6's extinction profile and Mo concentration exists. Furthermore, fluorescence quenching is directly correlated with increasing Mo concentration, that demonstrates the quantitative potential for fluorescent detection of Mo through crown ether chelation.

#### 4. Conclusions

This study demonstrated that minor structural changes in 18C6 ethers modulate metal ion chelation with crown ethers. Furthermore, solution characteristics influence crown ether morphology and the strength of metal ion chelations. Crown ether structure and the solvent environment determine metal chelation characteristics. Optimal quantitation of metal ion concentrations will require additional studies of crown ether chelation under various conditions. The quantitative spectroscopic response of single metal ion species with crown ethers, as demonstrated here, can also be expanded to include multi-composition solutions characterized by suitable mathematical analysis. This study demonstrated the potential for UV-vis and fluorescence spectroscopy to quantify chelation of toxic metal ions by crown ethers. These results inform the design of future portable detection and quantification techniques for toxic metal ions in solution.

#### Acknowledgements

A.L. Cook would like to acknowledge financial support from the National Science Foundation Graduate Research Fellowship Program (NSF GRF) 1445197. A.L. Cook and T.D. Giorgio would like to acknowledge support from the Congressionally Directed Medical Research Program (CDMRP) Peer-Reviewed Medical Research Program (PRMRP) W81XWH-18-1-0412. A.L. Cook would like to thank the Fisk-Vanderbilt Masters-to-PhD Bridge Program for their support of this research. The authors would also like to thank the Vanderbilt Institute of Nanoscale Science and Engineering (VINSE) for the use of their instrumentation.

#### References

- [1] J. M. Gaitens, M. Condon, K. S. Squibb, J. A. Centeno, and M. A. McDiarmid, "Metal Exposure in Veterans With Embedded Fragments From War-Related Injuries: Early Findings From Surveillance Efforts," *Journal of Occupational & Environmental Medicine*, vol. 59, no. 11, pp. 1056–1062, 2017, doi: 10.1097/JOM.0000000000001119.
- [2] H. Fischer, "A Guide to U.S. Military Casualty Statistics: Operation Freedom's Sentinel, Operation Inherent Resolve, Operation New Dawn, Operation Iraqi Freedom, and Operation Enduring Freedom," 2015.
- [3] J. F. Kalinich, E. A. Vane, J. A. Centeno, J. M. Gaitens, K. S. Squibb, M. A. McDiarmid, and C. E. Kasper, "Embedded Metal Fragments," in *Annual Review of Nursing Research, Volume 32, 2014: Military and Veteran Innovations of Care*, P. W. Kelley, Ed. New York, NY: Springer Publishing Co., 2014, pp. 63–78.
- [4] J. M. Gaitens and M. A. McDiarmid, "Toxic Embedded Fragments Registry: Lessons Learned," in *Airborne Hazards Related to Deployment*, Borden Institute, C. P. Baird, and D. K. Harkins, Eds. Government Printing Office, 2015, pp. 245–251.
- [5] J. M. Gaitens, C. D. Dorsey, and M. A. McDiarmid, "Using a Public Health Registry to Conduct Medical Sureillance: The Case of Toxic Embedded Fragments in U.S. Military Veterans," *European Journal of Oncology*, vol. 15, no. 2, pp. 77–90, Jun. 2010.
- [6] K. Cavanaugh, "Personal Communication." 2018.

- [7] S. Skaik, N. Abu-Shaban, N. Abu-Shaban, M. Barbieri, M. Barbieri, U. Giani, and P. Manduca, "Metals detected by ICP/MS in wound tissue of war injuries without fragments in Gaza," *BMC International Health and Human Rights*, vol. 10, no. 1, p. 17, Dec. 2010, doi: 10.1186/1472-698X-10-17.
- [8] H. T. Temiz, I. H. Boyaci, I. Grabchev, and U. Tamer, "Surface enhanced Raman spectroscopy as a new spectral technique for quantitative detection of metal ions," *Spectrochimica Acta Part A: Molecular and Biomolecular Spectroscopy*, vol. 116, pp. 339–347, 2013, doi: 10.1016/j.saa.2013.07.071.
- [9] O. O. Soldatkin, I. S. Kucherenko, V. M. Pyeshkova, A. L. Kukla, N. Jaffrezic-Renault, A. V. El'skaya, S. V. Dzyadevych, and A. P. Soldatkin, "Novel conductometric biosensor based on three-enzyme system for selective determination of heavy metal ions," *Bioelectrochemistry*, vol. 83, pp. 25–30, Feb. 2012, doi: 10.1016/J.BIOELECTROCHEM.2011.08.001.
- [10] C. P. Baird, "Considerations Regarding a Burn Pit Registry," *The Army Medical Department Journal*, pp. 46–52, 2013.
- [11] C. Rose, J. Abraham, D. Harkins, R. Miller, M. Morris, L. Zacher, R. Meehan, A. Szema, J. Tolle, M. King, D. Jackson, J. Lewis, A. Stahl, M. B. Lyles, M. Hodgson, R. Teichman, W. Salihi, G. Matwiyoff, G. Meeker, S. Mormon, K. Bird, and C. Baird, "Overview and Recommendations for Medical Screening and Diagnostic Evaluation for Postdeployment Lung Disease in Returning US Warfighters," *Journal of Occupational and Environmental Medicine*, vol. 54, no. 6, pp. 746–751, Jun. 2012, doi: 10.1097/JOM.0b013e31825297ba.
- [12] M. A. Kane, C. E. Kasper, and J. F. Kalinich, "Protocol for the Assessment of Potential Health Effects From Embedded Metal Fragments," *Military Medicine*, vol. 174, no. 3, pp. 265–269, 2009.
- [13] J. W. Steed, "First- and second-sphere coordination chemistry of alkali metal crown ether complexes," *Coordination Chemistry Reviews*, vol. 215, no. 1, pp. 171–221, May 2001, doi: 10.1016/S0010-8545(01)00317-4.
- [14] D. K. Sarfo, A. Sivanesan, E. L. Izake, and G. A. Ayoko, "Rapid detection of mercury contamination in water by surface enhanced Raman spectroscopy," *RSC Adv.*, vol. 7, pp. 21567–21575, 2017, doi: 10.1039/C7RA02209C.
- [15] D. K. Sarfo, E. L. Izake, A. P. O'Mullane, and G. A. Ayoko, "Molecular recognition and detection of Pb(II) ions in water by aminobenzo-18-crown-6 immobilised onto a nanostructured SERS substrate," *Sensors and Actuators B: Chemical*, vol. 255, pp. 1945–1952, Feb. 2018, doi: 10.1016/j.snb.2017.08.223.
- [16] Y. K. Agrawal, P. Shrivastav, and S. K. Menon, "Solvent extraction, separation of uranium (VI) with crown ether," *Separation and Purification Technology*, vol. 20, no. 2–3, pp. 177–183, Sep. 2000, doi: 10.1016/S1383-5866(00)00110-6.



## PAPER

Cite this: *Nanoscale Adv.*, 2021, 3, 407

# Optimization of electron beam-deposited silver nanoparticles on zinc oxide for maximally surface enhanced Raman spectroscopy†

Andrew L. Cook,<sup>a</sup> Christopher P. Haycook,<sup>a</sup> Andrea K. Locke,<sup>a</sup> Richard R. Mu<sup>b</sup> and Todd D. Giorgio<sup>\*a</sup>

Surface enhanced Raman spectroscopy enables robust, rapid analysis on highly dilute samples. To be useful, the technique needs sensing substrates that will enhance intrinsically weak Raman signals of trace analytes. In particular, three-dimensional substrates such as zinc oxide nanowires decorated with electron-beam deposited silver nanoparticles are easily fabricated and serve the dual need of structural stability and detection sensitivity. However, little has been done to optimize electron beam-deposited silver nanoparticles for maximal surface enhancement in the unique dielectric environment of the zinc oxide substrate. Herein, fabrication and anneal parameters of electron beam-deposited silver nanoparticles were examined for the purpose of maximizing surface enhancement. Specifically, this work explored the effect of changing film thickness, deposition rate, anneal temperature, and anneal time on the surface plasmon resonance of Ag nanoparticles. In this study, multiple sets of fabrication and annealing parameters were discovered that optimized surface plasmon resonance for maximal enhancement to Raman signals acquired with a 532 nm laser. This work represents the first characterization of the fabrication and annealing parameters for electron beam-deposited silver nanoparticles on zinc oxide.

Received 8th July 2020  
Accepted 28th October 2020

DOI: 10.1039/d0na00563k

rsc.li/nanoscale-advances

## Introduction

There is an unmet multidisciplinary need for bioanalytical techniques that can perform analyses on small volumes of highly diluted specimens with minimum sample preparation. Applications such as the detection of toxic metals,<sup>1–4</sup> other pollutants or contaminants,<sup>5–8</sup> circulating tumor cells,<sup>9</sup> bacteria,<sup>10</sup> or viruses<sup>11</sup> benefit from fast and reliable molecular sensing. State-of-the-art tools used for these purposes such as high-performance liquid chromatography, mass spectrometry, and enzyme-linked immunosorbent assays commonly involve expensive reagents, large sample volumes, skilled technicians and frequently have low throughput rates. In addition, such tools are often plagued by limited differentiation among chemically or biologically similar analytes.<sup>12–14</sup> Raman spectroscopy is an attractive technique that addresses some of the limitations of other approaches because it provides a unique spectroscopic “fingerprint” of the biomolecular and biochemical composition of specimens, potentially offering effective detection of analytes

in minutes or seconds.<sup>15–17</sup> Raman also exhibits portability and facile function, as demonstrated by its use in forensic fields such as explosives identification.<sup>18</sup> However, Raman scattering has a small optical cross-section, with only one in  $10^6$  to  $10^8$  photons being Raman scattered, limiting its usefulness for trace analyte sensing. Surface-enhanced Raman spectroscopy (SERS), however, can significantly enhance intrinsically weak Raman signals, enabling reliable, efficient, and non-destructive detection of highly dilute analytes.

It is well-known that there are two mechanisms principally responsible for the enhancement effects in SERS: an electromagnetic mechanism resulting from localized surface plasmon resonance (LSPR) and a chemical mechanism resulting from charge transfer between analyte and metallic nanostructure.<sup>19–21</sup> To take full advantage of the dominant electromagnetic mechanism of surface enhancement, it is necessary that the nanoparticles be spatially dense, to make use of “hotspots” in the gaps between nanoparticles.<sup>22,23</sup> For these reasons, much attention has been devoted to the use of metallic nanoparticles for incorporating SERS into various sensing system solutions. However, the expansive parameter space controlling SERS performance requires further investigation to effectively design sensors that provide optimal surface enhancement of intrinsically weak Raman signals.

Silver (Ag) is among the most commonly used metals for SERS-based sensing, due to strong Ag plasmon resonance in the

<sup>a</sup>Department of Biomedical Engineering, Vanderbilt University, Nashville, TN 37235, USA. E-mail: todd.d.giorgio@vanderbilt.edu

<sup>b</sup>TSU Interdisciplinary Graduate Engineering Research (TIGER) Institute, Tennessee State University, Nashville, TN 37209, USA

† Electronic supplementary information (ESI) available. See DOI: 10.1039/d0na00563k

visible region<sup>24,25</sup> and facile synthesis.<sup>26</sup> Many Ag nanostructures have been explored for SERS-based sensing, which fall into two basic categories: (1) colloidal nanostructures and (2) nanostructures on solid surfaces.<sup>27</sup> Colloidal nanostructures offer high sensitivity due to the ability to easily generate a large sensing surface area. However, due to random suspension of particles in free solution, colloidal nanostructures lack stability, and thus can affect measurement reproducibility. Conversely, nanostructures fabricated onto solid surfaces can possess great structural stability, resulting in greater measurement reliability. However, this stability comes at the cost of reduced sensitivity compared to colloidal paradigms due to lower surface area. This cost can be mitigated by fabricating inherently three-dimensional (3D) sensing substrates, as described in our previous work.<sup>28</sup> There are several methods of fabricating metallic nanoparticles onto a solid substrate that generally fall into two categories: chemical fabrication and physical deposition. Physical deposition techniques such as electron beam (e-beam) deposition facilitate formation of densely arranged Ag nanoparticles, enabling use of “hot-spots” between nanoparticles.<sup>29</sup> However, these techniques do not easily lend themselves to control of nanoparticle properties that affect LSPR. In the case of chemical fabrication, techniques such as hydrothermal growth are used to fabricate nanoparticles directly on the sensing surface.<sup>30</sup> While these techniques are more easily implemented and easier to control than physical deposition, they usually result in lower surface coverage by nanoparticles, reducing the impact of inter-particle hotspots. Therefore, by exploring the fabrication parameters that affect nanoparticle formation in physical deposition paradigms, greater control over nanoparticle formation can be implemented.

Recent research has illuminated multiple strategies for realizing 3D templates for SERS-active substrates, including anodized aluminum oxide,<sup>31</sup> porous silicon,<sup>32</sup> electrospun polymers,<sup>33</sup> silicon nanowires,<sup>34</sup> and zinc oxide (ZnO) nanowires,<sup>30</sup> among others. ZnO, in particular, is an attractive material for fabricating 3D SERS substrates. ZnO is a biocompatible<sup>35</sup> wide direct-bandgap semiconductor with a band-edge emission of 3.3 eV and a high exciton binding energy of 60 meV, making it electronically stable at room temperature.<sup>36,37</sup> The semiconducting nature of ZnO also enables charge transfer between the ZnO and Ag,<sup>38</sup> increasing surface enhancement over strategies that rely solely on the electromagnetic mechanism. Crystalline ZnO is also transparent to visible light,<sup>39</sup> which reduces absorptive loss of light when acquiring spectra through the substrate as we did in our previous work.<sup>28</sup> Additionally, ZnO possesses a large refractive index of approximately 2.0 in the visible region, which aids in the confinement of light.<sup>40,41</sup> Combining these characteristics with the atomically smooth and highly faceted hexagonal single-crystal structure of the nanowires allows for waveguiding of light, which can reduce signal loss due to light scattered away from the detector.<sup>42</sup>

Previously, we prepared ZnO nanowires decorated with Ag nanoparticles for sensing soluble analytes. This sensing paradigm yielded an estimated six orders of magnitude surface enhancement of the Raman signal for crystal violet (CV, CCDC # 137090), melamine, and adenine.<sup>28</sup> Performance of this sensor

was likely reduced because the Ag nanoparticles, with a plasmon peak at  $\sim 460$  nm, were not optimal for SERS with the 532 nm laser used. We also did not explore the sensor performance as a function of Ag deposition parameters that are likely to influence SERS amplification mechanisms. Through this study, Ag-decorated ZnO nanowires demonstrated potential for effective sensing of trace analytes, which can be realized by examining the effect of fabrication and anneal parameters on surface plasmon resonance.

Parameters that can be manipulated during e-beam deposition of Ag and significantly impact the Raman enhancement include film thickness and deposition rate. Film thickness, in general, changes the shape and surface coverage of metallic nanostructures which changes LSPR characteristics of the film. By consequence, these changes modulate the magnitude of surface enhancement. Other research groups have explored how Ag nanoparticle plasmon resonance changes with film thickness in e-beam deposited<sup>43</sup> and sputtered<sup>44</sup> systems, but in neither of these works were nanoparticles deposited on a ZnO layer, which can significantly impact plasmon resonance as part of the dielectric environment of the nanoparticles. Also, while the effects of Ag film thickness on LSPR has been explored in some way, little attention has been devoted to the effects of Ag film deposition rate on plasmon resonance, even though deposition rate has a known effect on the structural properties of metallic films.<sup>45</sup> Furthermore, thermal annealing following deposition changes the nanoparticle size and shape through Ostwald ripening.<sup>46</sup> Since nanoparticle geometry and dimensions are important drivers of plasmon resonance, thermal annealing offers an additional strategy for optimization of SERS sensing. Thermal annealing occurs as a result of two independent parameters: anneal temperature and anneal time.

In this work, four independently selectable parameters that influence Ag nanoparticle formation and presentation on ZnO were quantitatively controlled. These parameters, namely film thickness, deposition rate, anneal temperature, and anneal time were examined to assess their impact in modulating surface plasmon resonance. The functional consequences of these fabrication parameters were comparatively assessed using surface-enhanced Raman spectra that were acquired from crystal violet deposited onto each substrate. We aim to discover fundamental fabrication principles and sensor characteristics that will advance the design of maximally sensitive SERS devices based upon e-beam deposited Ag nanoparticles on a ZnO substrate.

## Experimental

### Substrate preparation

Glass slides (Fisherbrand® Plain Microscope Slides) were cut into 80 1 cm<sup>2</sup> substrates with a diamond saw and cleaned by sonication sequentially for 10 minutes each in 1% aqueous Alconox® solution, deionized (DI) water, acetone, methanol, and again in DI water. Onto these substrates, a 100 nm ZnO layer was deposited *via* e-beam deposition at a rate of approximately 0.1 Å s<sup>-1</sup> to ensure even deposition of Zn and O. As demonstrated by Fig. S1,† Masks were cut from aluminum foil

large enough to completely cover the substrates, with a square cutout  $\sim 0.2$  cm to a side, allowing a Ag film to be deposited on only a small portion of each substrate. After each film was deposited, the masks were shifted so that the cutouts exposed a new portion of each substrate, and a new film was deposited. This process was repeated nine times, for nine different Ag film thicknesses fit on each substrate, as illustrated by Fig. S1.† Ag thin films were deposited over a range of 1 nm to 9 nm film thicknesses, in 1 nm increments, hereafter referred to as T1–T9. The 62 substrates were divided into two groups of 31 substrates, as shown in Fig. 1. In each group, 30 substrates would be annealed and 1 would remain unannealed. These two groups, hereafter referred to as group A and group B, were deposited with Ag thin films at rates of  $0.1$  and  $0.3 \text{ \AA s}^{-1}$ , respectively. All Ag films in group A were deposited at rates of  $0.1 \pm 0.002 \text{ \AA s}^{-1}$  and all Ag films in group B were deposited at rates of  $0.3 \pm 0.018 \text{ \AA s}^{-1}$ . It is well known that when material from a point source is deposited onto substrates affixed to a flat plate, deposition rates fall off with axial distance from the source. This results in varying film thickness as a function of axial distance, defined by eqn (1):

$$t_d = \left[ 1 + \left( \frac{d}{R_0} \right)^2 \right]^{-3/2} \quad (1)$$

In this equation,  $t_d$  represents the film thickness at distance  $d$  from the axis defined by the point source and  $R_0$  represents the distance from the source to the plane of deposition.  $R_0$  was measured to be 27 cm and the axial distance  $d$  of substrates farthest from the source was measured to be  $\sim 4.5$  cm. Thus, the largest variation in film thickness was  $\sim 4\%$  of the target thickness. All e-beam depositions were performed at pressures below 6.7 mPa.

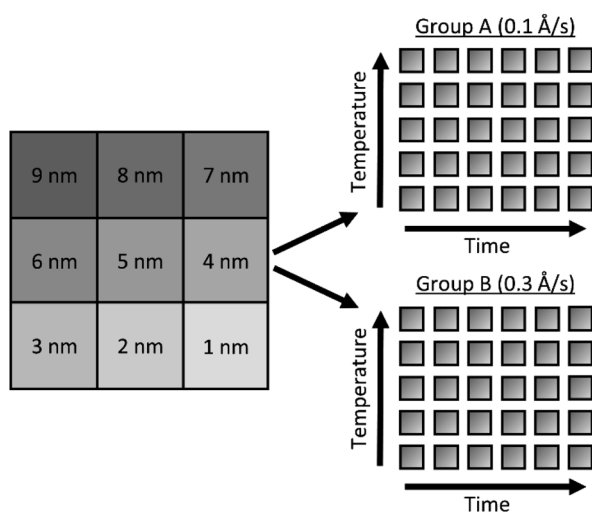


Fig. 1 Schematic of substrates used for parameter exploration. Substrates deposited with 9 different Ag film thicknesses and separated into two rate groups (A and B). In each group, substrates are annealed over a range of times (15–150 min) and temperatures (50–400 °C).

Following the deposition of silver, the substrates were annealed at various temperatures: 50, 100, 200, 300 and 400 °C. At each temperature, different substrates were annealed at times: 15, 30, 60, 90, 120, and 150 minutes, providing a substrate from each deposition rate group (2 groups) with every anneal temperature (5) and time (6), producing  $2 \times 5 \times 6 = 60$  uniquely fabricated and annealed substrates and 1 unannealed control per group, each presenting T1 through T9 film thicknesses for a total of 558 different substrates.

### Optical characterization techniques

Scanning electron microscopy (SEM) images, before annealing, were acquired of each Ag film thickness from a random substrate to get a visual perspective on the changing Ag nanostructure morphology as a result of changing film thickness. These images were acquired using a Zeiss Merlin scanning electron microscope (Jena, Germany) in a plan configuration with a 10 kV electron beam at a magnification of  $400\,000\times$  and a working distance of 2.8 mm. The average size of nanostructures was determined using Fiji image analysis of acquired SEM images.<sup>47,48</sup> The images were first converted to black-and-white *via* the Make Binary function and noise was removed *via* the Despeckle function, in which each pixel is given the median value of its  $3 \times 3$  neighborhood. The area of the nanostructures were acquired *via* the Analyze Particles function and area values that didn't correspond to single nanostructures were removed.

Extinction spectra were acquired of each film thickness, on each substrate before and after annealing, using a Hitachi U-4100 spectrophotometer integrating sphere to determine peak surface plasmon resonance wavelength. Extinction spectra were obtained at a rate of  $3 \text{ nm s}^{-1}$  over a range of 350–850 nm, with each substrate oriented facing away from oncoming light.

Raman spectra were acquired using a Thermo Scientific DXR Raman microscope (Waltham, MA, USA). A 532 nm diode-pumped, solid state (DPSS) laser was used with a  $10\times$  objective (Olympus, MPlan N Achromat, 0.25 NA) at a power of 10 mW as measured at the objective turret. Focal plane was adjusted before each acquisition to maximize spectral intensity. All substrates were placed in contact with a  $25 \text{ }\mu\text{M}$  aqueous solution of crystal violet (CV) overnight. The substrates were then removed from the CV solution and air-dried. Five Raman spectra were acquired from each substrate (T1–T9), along with five spectra of a portion on each substrate without Ag, hereafter referred to as T0. Each Raman spectrum was the accumulation of four background-subtracted spectra acquired over a range of  $200\text{--}1800 \text{ cm}^{-1}$ , each taken with a 5 s exposure time. All Raman spectra were acquired with a  $50 \text{ }\mu\text{m}$  pinhole aperture and a 900 grooves per mm grating.

### Spectral processing

UV-Vis spectra of the Ag films deposited on ZnO layers exhibit extinction from both Ag and ZnO. While ZnO is largely transparent in the visible region, light extinction due to the ZnO band edge occurs below approximately 380 nm. In order to accurately obtain Ag plasmon peak information, absorptive

contributions from ZnO were approximated and subtracted as illustrated in Fig. S2.† This method was chosen to minimize variation in ZnO signal induced by the fabrication and anneal process, as illustrated by Fig. S3.† To approximate ZnO absorptive contributions, UV-Vis spectra from the T1 portions of each substrate were fitted to a tri-gaussian equation, shown in eqn (2). In this fit, the first gaussian approximated the ZnO band-edge contribution, the second approximated the ZnO visible contribution, and the third approximated the Ag plasmon peak. T1 spectra were chosen for this task because of minimal overlap between the Ag plasmon peak and the ZnO band-edge and because the plasmon peak could be accurately approximated by a gaussian curve. Once fits to these spectra were successfully obtained, the third gaussian was subtracted from the fit to arrive at an approximation of the ZnO contribution to the spectra. This ZnO contribution for each substrate was then subtracted from the UV-Vis spectra for T1–T9 for each substrate. Finally, a cubic smoothing spline, where eqn (3) is minimized, was fit to the resultant plasmon peaks to remove noise, enabling accurate extraction of plasmon peak extinction, wavelength, and spread.

$$F_g(x) = a_b e^{-\frac{(x-\mu_b)^2}{2\sigma_b^2}} + a_v e^{-\frac{(x-\mu_v)^2}{2\sigma_v^2}} + a_p e^{-\frac{(x-\mu_p)^2}{2\sigma_p^2}} \quad (2)$$

$$\lambda \sum_i [y_i - s(x_i)]^2 + (1 - \lambda) \int_{x_{\min}}^{x_{\max}} \left( \frac{d^2 s(x)}{dx^2} \right)^2 dx \quad (3)$$

In eqn (2),  $F_g$  is the gaussian fit,  $a$  is an arbitrary fit parameter, and  $\mu$  &  $\sigma$  represent the peak and root-mean-square width of the gaussian, respectively. Subscripts b, v, and p denote the gaussian fitting of the ZnO band-edge, ZnO visible, and Ag plasmon contributions to the spectrum, respectively. In eqn (3)  $\lambda$  represents the smoothing parameter,  $y$  is the set of observed extinctions at each wavelength,  $x$  is the set of wavelengths at which extinction is measured,  $s$  is the smoothed function output of the equation, and  $x_{\min}$  &  $x_{\max}$  are the minimum and maximum wavelengths of the spectrum, respectively. For this work, a smoothing parameter  $\lambda = 0.003$  was used. A smoothing spline was used to approximate the plasmon rather than a gaussian because, while the plasmon peaks of thinner films

could be accurately approximated by a gaussian fit, the plasmon peaks of thicker films could not due to increasing asymmetry in the peak. Spread was measured at the full width-half maximum (FWHM) of each plasmon peak where possible. For several spectra, particularly of thicker Ag, the FWHM was sufficiently broad to extend beyond the measured wavelength range and could not be determined. All processing of UV-Vis spectra was performed in MATLAB.<sup>49</sup> Energy dispersive X-ray spectroscopy had been previously performed on similarly prepared SERS-active substrates, confirming the presence of ZnO and Ag.<sup>28</sup> Raman spectra were subtracted of their fluorescent background, estimated using 5<sup>th</sup>-degree polynomial fit. These spectra were then smoothed using a Savitzky–Golay filter. Each of the five spectra acquired from each film thickness (T0–T9) on each substrate were averaged to find a representative spectrum. Three CV Raman peaks at 420, 915, and 1592  $\text{cm}^{-1}$ , tabulated in Table 1 with their associated vibrational modes and the CV molecular structure, were selected to provide specific, characteristic features for the estimation of enhancement factors (EFs). These peaks were selected to interrogate EFs from each end of the measured spectra and one feature near the middle of the spectra. The intensities of these peaks in the spectra for T1–T9 on each substrate were divided by the intensities of the same peaks in the spectrum of T0 on the same substrate to arrive at EFs for each peak.

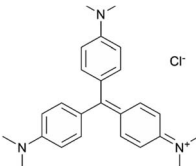
### Statistical analysis

All error bars represent standard deviation unless otherwise stated. Two-way analysis of variance followed by Tukey's and Sidak's multiple comparison tests was performed for data presented here as indicated, and statistical significance was defined as  $p < 0.05$ . Statistical analyses were performed using Prism 7.04 (GraphPad Software).

## Results & discussion

The surface plasmon peak of a distribution of Ag nanoparticles possesses three characteristics that affect the level of enhancement: peak intensity, peak wavelength, and peak breadth. Because surface plasmons enhance both incident light from the laser and Raman-scattered light, surface enhancement is most effective when high plasmon extinction occurs at both the laser line and across the range of wavelengths at which light is scattered. Thus, the surface plasmon peak should be located near the laser line to maximize enhancement to incident light, and the peak should be sufficiently broad to provide significant enhancement to Raman-scattered light across the wavelength range of interest. In addition, plasmon intensity correlates with enhancement factor, with higher plasmon intensities generally producing greater enhancement for non-colloidal sensing substrates.<sup>50</sup> Surface plasmon peak intensity, wavelength, and breadth are all influenced by nanoparticle size, size distribution, crystal composition, proximity, and shape. These nanoparticle properties are modulated by deposition thickness and deposition rate, and by anneal temperature and time, post-deposition. In this study, we explore the combinatorial effect

**Table 1** The benzene and non-benzene vibrational modes of the CV peaks selected for analysis, with the CV molecular structure for reference

Raman band ( $\text{cm}^{-1}$ )	Non-benzene vibrational modes	Benzene modes	Molecular structure
420	$\delta(\text{C-C}_{\text{center}}-\text{C})/\delta(\text{C-N-C})_{\parallel}$	16a	
915	$\delta(\text{C-C}_{\text{center}}-\text{C})$	12,17a	
1592		8a	



of these fabrication parameters on the surface plasmon peak characteristics of Ag nanoparticle arrays and correlate these effects to changes in enhancement of intrinsic Raman spectral intensity of CV. By doing so, we aim to facilitate the development of optimized sensing substrates for maximally surface-enhanced Raman spectroscopy.

### Effect of film thickness on surface enhanced Raman spectroscopy

Increasing Ag film thickness was anticipated to intensify, broaden, and red-shift the plasmon extinction peak due to increasing Ag surface coverage, increasing particle diameter, and decreasing interparticle distance. However, the quantitative relationships that describe these effects as a function of film thickness have not been previously described. Furthermore, while increasing intensity is correlated with increasing surface enhancement, for solid substrates, maximizing enhancement requires proximity of the peak wavelength with the incident laser. In addition, broadening the plasmon peak is only effective insofar as it maximizes plasmon extinction across the wavelengths of interest. Therefore, we examined the relationships between Ag film thickness and maximized surface enhancement through changes to nanostructure morphology and plasmon peak extinction characteristics. SEM images were acquired from group A before annealing to explore the relationship between film thickness and nanostructure morphology. These images, shown in Fig. 2, reveal that Ag was deposited as small islands that grow with increasing film thicknesses from 1 nm (T1) to approximately 5 nm (T5) and become more film-like for depositions of 6 nm (T6) and greater. This change is likely due to surface coverage approaching 100% as a result of increasing Ag mass per area. Extinction spectra are superimposed on each

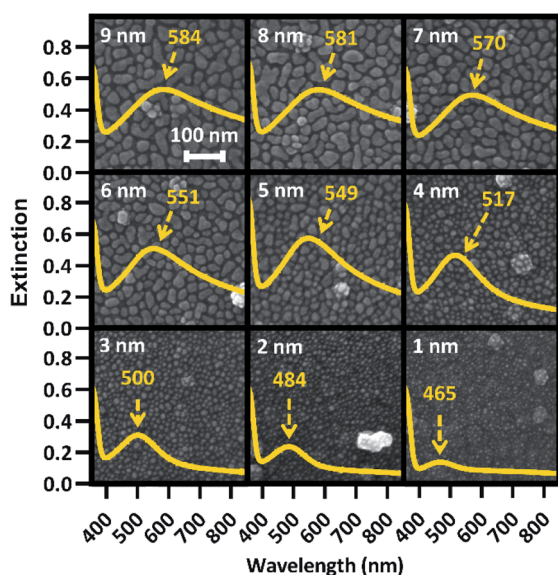


Fig. 2 SEM images of all film thicknesses (identified in white) for a random substrate, with associated extinction spectra displaying peak plasmon wavelength overlaid. The plasmon peak wavelength is identified in yellow for each extinction spectrum.

SEM image in Fig. 2, confirming intensified and red-shifted extinction with increasing film thickness. The symmetrical plasmon peaks observed among the lowest Ag depositions (T1–T4) are consistent with individual, spherical Ag nanoparticles. The transition toward nanostructured thin films (T5–T9) was accompanied by increasingly exotic nanostructure shapes, associated with increasing asymmetry in the plasmon peaks.

The UV-Vis spectra for all 9 film thicknesses on each of 40 substrates in group A were processed as described in the Experimental section above to find peak extinction intensity, wavelength, and breadth in each case. Plasmon extinction intensity increased with Ag film thickness, as shown in Fig. 3(a). Intensity increases approximately linearly for T1–T5, but begins to approach an asymptotic maximum for T6–T9. The reduction in differential extinction for high film thicknesses is confirmed by the lack of statistically significant differences between T7 & T8 and T8 & T9 as compared to T1–T6 in which each thickness group was significantly different from every other thickness group. This change in behavior between thin and thick films correlates with proximity-induced hotspots. When adjacent nanoparticles are within a few nanometers of each other plasmonic coupling results in a hotspot between them, greatly increasing plasmon extinction.<sup>22</sup> For T1–T5, plasmonic coupling between nanoparticles drove the growth in plasmon extinction intensity as interparticle distances decreased, exhibited by Fig. 2. Beginning at T6 however, interparticle gaps ceased to decrease as Ag was deposited. At that point, plasmon extinction intensity began to plateau, which is consistent with Ag accumulation becoming the primary driver for increasing plasmon extinction.

Plasmon peak wavelength red-shifted with increasing Ag film thickness, shown in Fig. 3(b), from well below the laser line at an average of  $\sim 464$  nm for 1 nm films, to well past the laser line at an average of  $\sim 584$  nm for 9 nm films. This redshift was likely due primarily to increasing nanostructure size, which correlated with increasing film thickness (Fig. 2). Nanostructures increased in size from an average of  $\sim 30$  nm<sup>2</sup> for 1 nm films to an average of  $\sim 970$  nm<sup>2</sup> for 9 nm films, as shown in Fig. S4.† Unlike intensity, maximizing surface enhancements requires proximity of the plasmon extinction peak and the laser wavelength, illustrated by the green line in Fig. 3(b). The wavelength of peak plasmon extinction also influences surface enhancement, as the efficiency of optical coupling is enhanced when the laser line is near the plasmon peak. The closest alignment between peak extinction and the laser line was at 517 nm for T4 and 548 nm for T5. Additionally, variability in peak wavelength generally increased as films thickened, with standard deviation growing from 4.2 nm for 1 nm films to as much as 17.3 nm for 8 nm films. We speculate that this behavior is associated with the increasingly exotic nanostructure shapes associated with increasing film thickness.

Maximal surface enhancement requires LSPR with both incident laser light and wave-shifted scattered light. While enhancement is improved when the plasmon extinction peak is close to the laser wavelength, the peak should also be sufficiently broad to enhance wave-shifted scattered light across the fingerprint region which, for organic molecules, usually

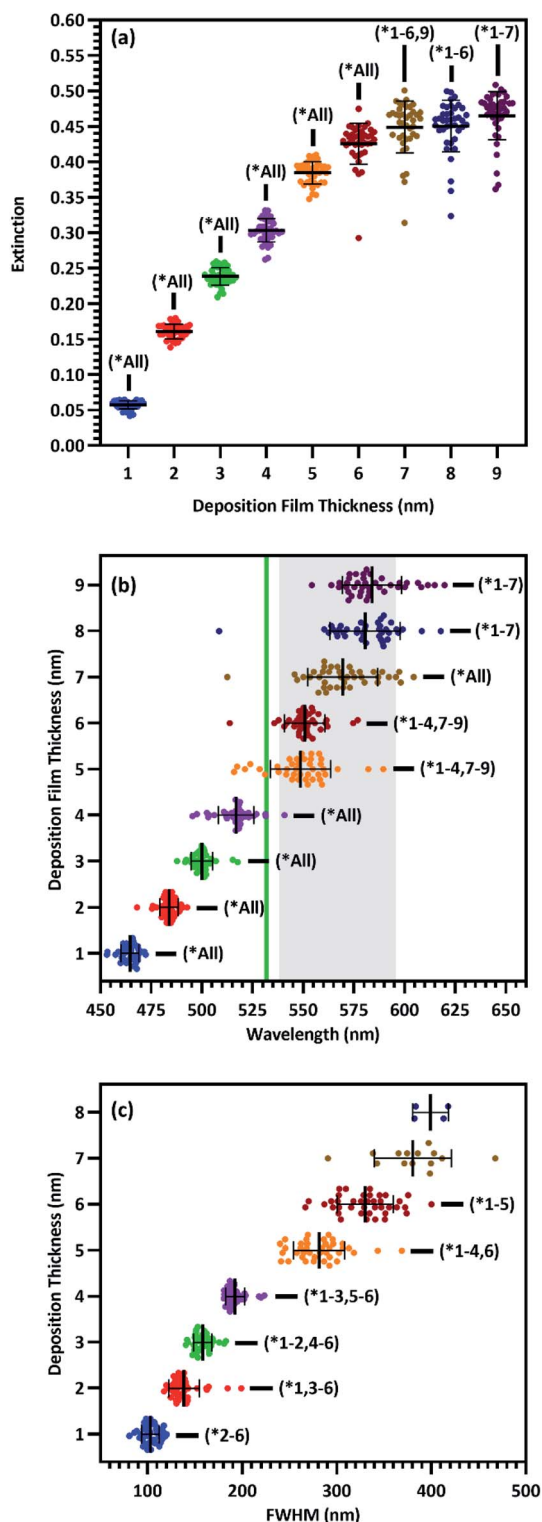


Fig. 3 Scatterplots of plasmon peak (a) intensity ( $n = 40$ ), (b) wavelength ( $n = 40$ ), and (c) FWHM (T1–T4:  $n = 40$ , T5–T6:  $n = 39$ , T7:  $n = 14$ , T8:  $n = 4$ ) for each film thickness of substrates in group A. Green line and shaded region in (b) represent the laser line and fingerprint region, respectively. All data shown with mean and standard deviation of each group. \* $p < 0.05$  two-way ANOVA. Statistical significance of the FWHM of 7 and 8 nm films as compared to other films not shown due to an insufficient number of data points to use a parametric test.

consists of some portion of the region between 200 and  $2000 \text{ cm}^{-1}$ . When a 532 nm laser is used to acquire Raman spectra, this fingerprint region translates to 537.7–595.3 nm, illustrated by the shaded region in Fig. 3(b).<sup>51–54</sup> Thus, the sensing approach aims for a plasmon wavelength range that usefully overlaps with the entire spectral region of interest. To estimate breadth of the plasmon peak, the FWHM was determined where possible. FWHM of the plasmon peaks correlate with film thickness and range from  $\sim 104 \text{ nm}$  for 1 nm films to more than 400 nm for 8 nm films, as shown in Fig. 3(c). While this phenomenon provides a greater wavelength range with the potential for useful sensing at the largest deposition thicknesses, it complicated our ability to accurately characterize the FWHM. For substrates with T5 and T6 film thickness, a FWHM could be calculated for 39/40 spectrums. For T7, a FWHM could only be calculated for 14/40 spectra. For T8, a FWHM could only be calculated for 4/40 spectra, and for T9, no FWHM's could be calculated. This phenomenon correlated with the increasing asymmetry of the plasmon peaks as films transitioned from individual nanoparticles to nanostructured films, shown in Fig. 2. This increasing asymmetry was beneficial for maximizing surface enhancement due to greater plasmon resonance across the fingerprint region.

Analyses of individual plasmon characteristics indicated that the film thickness required to produce maximal surface enhancement would optimize the balance among plasmon extinction intensity, peak proximity to the laser line, and extinction intensity across the fingerprint region. Because these plasmon extinction characteristics interact in non-obvious ways to influence the overall Raman spectra enhancement, SERS spectra of CV adsorbed onto the Ag films were acquired and shown in Fig. 4(a) to characterize the role of film thickness on surface enhancement. CV possesses multiple strong Raman peaks, tabulated in Table S1† with their associated vibrational modes, across a large portion of the fingerprint region.<sup>55</sup> Very little enhancement was observed for T1–T4, with the T4 film resulting in less than 5-fold enhancement across the fingerprint region as compared to the T0 spectrum. This inconsequential enhancement likely resulted from a combination of low plasmon intensity (Fig. 3(a)), inefficient coupling between the plasmon peak and the laser line (Fig. 3(b)), and insufficient peak breadth to enhance wave-shifted light across the fingerprint region. However, enhancement notably increased starting at T5, with up to 15.8-fold enhancement as compared to the T0 spectrum at  $1592 \text{ cm}^{-1}$ . Maximal enhancement was found to occur for the T7 film, with up to 25.7-fold enhancement across the fingerprint region at  $1592 \text{ cm}^{-1}$ , before decreasing with T8 and T9 films. The diminished enhancement for the thickest Ag films is correlated with an increasing departure from the laser line due to red-shifting peak plasmon extinction (Fig. 3(b)) accompanied by decreasing rate of plasmon extinction intensification (Fig. 3(a)). These results are non-obvious when assessing plasmon peak characteristics individually, illustrating the value in analyzing relationships between these characteristics in light of how they influence surface enhancement. These results demonstrate that film thicknesses of 5 nm or greater provide the best surface enhancement, peaking with

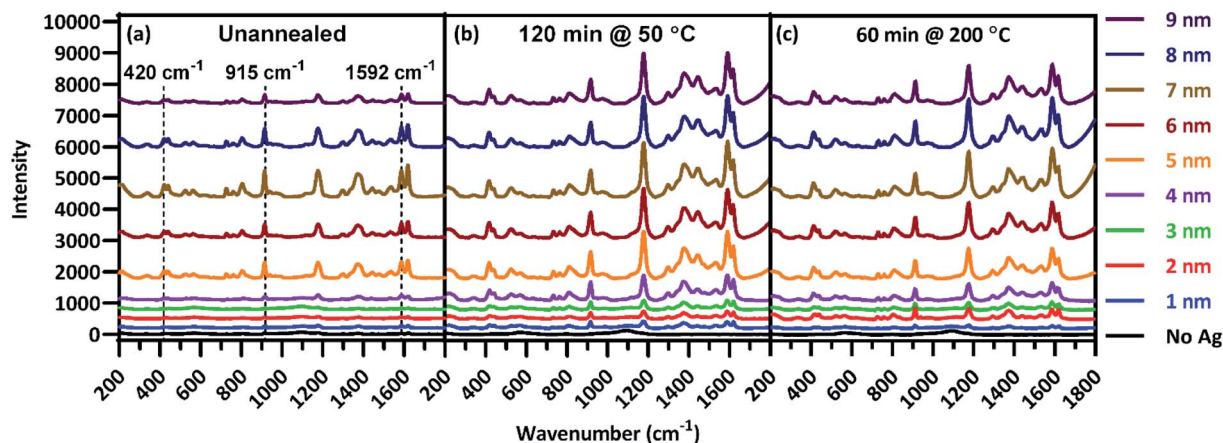


Fig. 4 Raman spectra of CV deposited on each film thickness for substrates (a) unannealed, (b) annealed at 50 °C for 60 min, and (c) annealed at 200 °C for 60 min.

7 nm film thickness. Thus, continued analysis focused on thicker films of 5 nm and above.

#### Effect of annealing on surface enhanced Raman spectroscopy

Following the analysis of deposition thickness, substrates were annealed to explore the effect of annealing temperature and time on plasmon extinction characteristics, toward additionally maximizing surface enhancement. From group A, 31 substrates from group A were chosen for this analysis, with the remaining 9 held in reserve should they be needed. Of the 31 substrates, one was set aside as an unannealed control and the remaining 30 were annealed at five temperatures in the range of 50–400 °C for six anneal times in the range of 15–150 min. Raman spectra were acquired of CV adsorbed onto Ag films after annealing,

examples of which are presented in Fig. 4(b and c). As with the pre-anneal spectra in Fig. 4(a), film thicknesses of 5–9 nm provided the best surface enhancement for both annealed substrates presented in Fig. 4(b and c), peaking at 7 nm. However, the difference in surface enhancement between 7 nm and 5 or 9 nm films is much less pronounced for the annealed substrates than the unannealed substrate. Thus, annealing can be used to obtain near-maximum surface enhancement over a range of film thicknesses. Such flexibility in deposition thickness may be especially useful for three-dimensional sensing substrates such as ZnO nanowires. In such cases, thicker films may over-fill interwire gaps, reducing effective surface area. Because maximal surface enhancement results in part from enhancement of Raman-scattered light across the

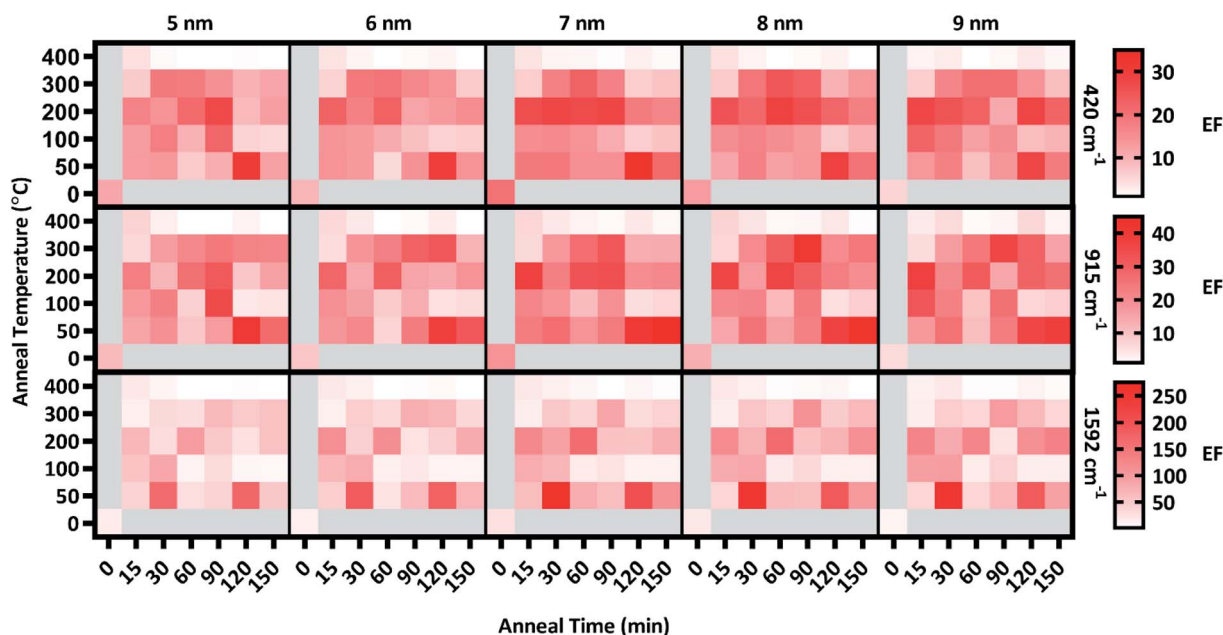


Fig. 5 Heat map of the enhancement factors of T5–T9 for 420, 915, & 1592  $\text{cm}^{-1}$  peaks across all anneal temperatures & times along with the unannealed control.



fingerprint region, three CV peaks at 420, 915, and 1592  $\text{cm}^{-1}$  as identified in Fig. 4(a) were chosen to quantitatively assess enhancement at multiple points that span the fingerprint region. The enhancement of these peaks was calculated for T5–T9 at each anneal temperature and time. These enhancements appear as a heat map in Fig. 5, where red shading indicates increased enhancement. Annealing produced substantial impact to surface enhancement, but in ways that are nonlinear with respect to time and temperature. Annealing conditions generated changes to surface enhancements ranging from less than 3% to almost 3000% of the unannealed surface enhancement. Clearly, the selection of annealing parameters measurably impacts the performance of these sensors. Fig. 5 reveals that annealing at 400 °C for even a short time drastically reduced surface enhancement across the board, indicating an upper temperature limit for this sensing paradigm well below 400 °C. Further examination of Fig. 5 reveals that in general, the anneal time required to maximize surface enhancement decreased as anneal temperature increased. At 50 °C, maximizing enhancement required 120 min while at 100 °C, enhancement dropped off significantly after annealing 90 min. At 200 °C, enhancement was strongest when annealed from 15–60 min. Two of these anneal temperatures, 50 °C and 200 °C, produced particularly strong results toward maximizing surface enhancement, motivating closer examination.

Enhancement factors for the five film thicknesses were averaged for each anneal time at each temperature and plotted in Fig. 6. The relative strength of enhancement between the two anneal temperatures varies across the three CV peaks, indicating the necessity of investigating enhancement across the entire fingerprint region. For instance, annealing at 30 °C resulted in opposing enhancement trends for the two anneal temperatures. Relative enhancement decreased farther away from the laser wavelength when annealed at 200 °C while it increased away from the laser wavelength when annealed at 50 °C. Among this variability, two anneal times produced consistently strong surface enhancement at these temperatures: 60 min at 200 °C and 120 min at 50 °C.

This study seeks to not only describe the deposition and annealing parameters that result in maximal surface enhancement, but also relate these results to changes in plasmon extinction characteristics effected by those fabrication parameters. To this end, changes to plasmon extinction characteristics for all five effective film thicknesses (T5–T9) due to annealing at 50 and 200 °C were plotted in Fig. 7. Annealing at 200 °C caused the plasmon intensity of all five film thicknesses to decrease steadily with increasing anneal time. In addition, annealing for 15 min or more at 200 °C blue-shifted the plasmon peaks. Annealing for 60 min slightly red-shifted the peaks, which blue-shifted again at higher anneal times (>90 min). This blue-shifting behavior is consistent with increasing nanostructure uniformity due to Ostwald ripening, reducing the exotic nature of nanostructure shapes. FWHMs followed a similar behavior as peak wavelengths, with a short anneal time narrowing the plasmon peaks. These plasmon peaks widened slightly when annealed for 60 min before narrowing again beyond 90 min. These observations agree with the results

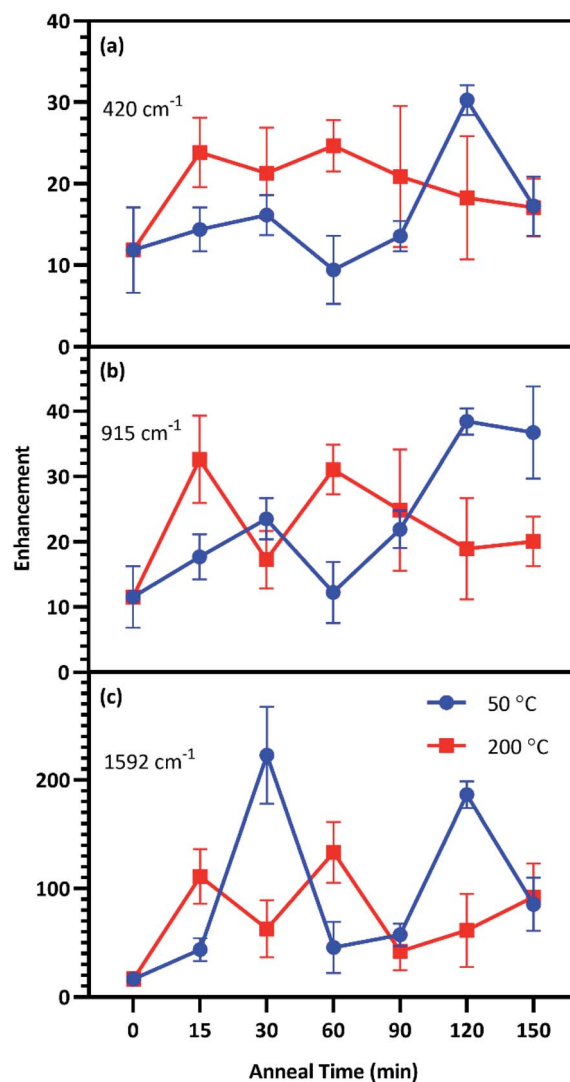


Fig. 6 SERS EFs of substrates annealed at 50 °C (blue) and 200 °C (red) for up to 150 min, along with the unannealed control for the (a) 420  $\text{cm}^{-1}$ , (b) 915  $\text{cm}^{-1}$ , and (c) 1592  $\text{cm}^{-1}$  peaks. Each point in the figure exhibits the mean and standard deviation of the EFs for T5–T9.

in Fig. 6, indicating that annealing at 200 °C generated the best combination of plasmon intensity, peak wavelength, and peak width at 60 min of anneal time.

Annealing at 50 °C for less than 60 min reduced peak intensity that rebounded for anneal times of 60–120 min. Peak wavelength blue-shifted slightly following annealing for less than 60 min at 50 °C before subsequent red-shifting for annealing times of 60–120 min. FWHMs for 5 and 6 nm films were increased with increasing anneal time. These results agree with the results in Fig. 6 that indicate an optimum anneal time of 120 min at 50 °C. We anticipate that deposition and dewetting kinetics differ between the ZnO films used in this work and ZnO nanowires often utilized in 3D SERS substrates. However, this work expedites future nanoparticle optimization by narrowing the window of parameters values to explore in future works involving ZnO nanowires.



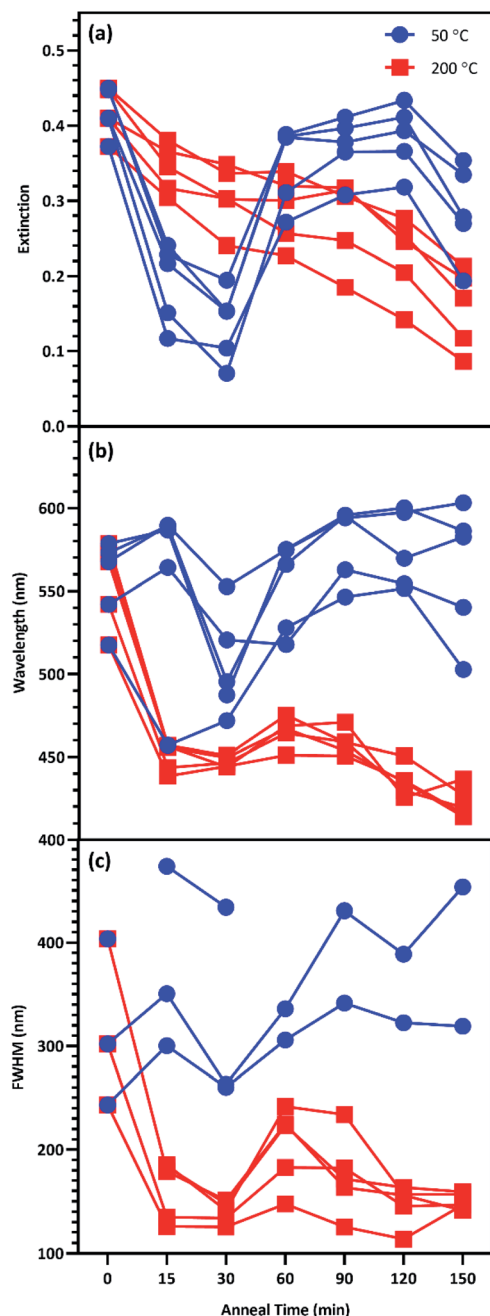


Fig. 7 Change to the plasmon peak (a) intensity, (b) wavelength, and (c) FWHM due to anneal time at 50 °C (blue) and 200 °C (red) for T5T9.

### Effect of deposition rate on surface enhanced Raman spectroscopy

Deposition rate had a significant impact on plasmon peak wavelengths, with films deposited at  $0.3 \text{ \AA s}^{-1}$  exhibiting significantly red-shifted peaks compared to a deposition rate of  $0.1 \text{ \AA s}^{-1}$  for each film thickness examined, excepting 7 nm, as shown in Fig. S5(b).<sup>†</sup> We hypothesize that this behavior can be explained by rate-induced differences in the crystal structure of Ag nanoparticles, as deposition rate has been shown to effect such crystal properties as grain size, dislocation density, and twin boundary density in metallic nanostructures.<sup>45</sup> These

results suggest that the plasmon characteristics of e-beam deposited Ag films are sensitive to deposition rates, as small changes can have a significant impact on important physical characteristics of the nanoparticles. These results also clearly indicate the trade-off between degraded sensor performance and the reduced deposition time achieved at elevated deposition rate.

While there was no significant difference in terms of enhancement in the unannealed controls between groups A ( $0.1 \text{ \AA s}^{-1}$ ) and B ( $0.3 \text{ \AA s}^{-1}$ ), Fig. S6<sup>†</sup> demonstrates that annealing the substrates in group A generally produced more surface enhancement than group B, across all film thicknesses, and anneal temperatures/times. This suggests that rate-induced differences in the crystal structure of Ag nanoparticles impacts annealing-induced effects on surface enhancement. This observation further emphasizes the important impact of deposition rate on the physical characteristics of Ag nanoparticles and the resulting surface enhancement of the structure.

Several combinations of fabrication and anneal parameters maximize surface enhancement by optimizing plasmon extinction. This study substantially improves the potential for fabricating high-performance sensors through elimination of fabrication parameters that yield low-enhancement materials. Importantly, these results demonstrate that maximal surface enhancement can be achieved by multiple different fabrication strategies. For instance, 2D sensing surfaces where film thickness does not impact device function have the best enhancement with a 7 nm thick surface deposited at  $0.1 \text{ \AA s}^{-1}$  and annealed at 200 °C for 60 min. However, for 3D sensing surfaces such as the ZnO nanowire-based structure described in our previous work,<sup>28</sup> a thicker sensing surface could reduce device functionality by over-filling the spaces between nanowires, thereby reducing effective surface area. In such cases, a film approximately 5 nm thick, deposited at  $0.1 \text{ \AA s}^{-1}$  and annealed at 200 °C for an hour is predicted to provide near-maximal surface enhancement without sacrificing sensing surface area. Another consideration is the substrate on which such nanostructures are fabricated. Many sensing strategies utilize substrates with high melting points such as glass or fused silica. In such cases, annealing at 200 °C is not problematic. However, increasing attention has been devoted in recent years toward fabricating SERS-active structures on flexible substrates made of materials like polyvinyl alcohol (PVA),<sup>56,57</sup> poly(dimethylsiloxane) (PDMS),<sup>58</sup> or polyvinylidene fluoride (PVDF).<sup>59</sup> In such cases substrates, even temperatures as low as 100 °C can have an undesirable effect on the substrate itself, such as increasing brittleness. For such device designs, excellent surface enhancement can be achieved by annealing substrates at 50 °C for 120 min.

## Conclusions

This study provides guidance for the fabrication of sensors with maximal SERS enhancement excited with a 532 nm laser through e-beam deposited Ag nanoparticles on ZnO. 7 nm Ag films possess the optimal combination of plasmon peak intensity, wavelength, and breadth for maximal surface

enhancement with a 532 nm laser. When 7 nm films are untenable, films as thin as 5 nm still provide near-maximal surface enhancement. We demonstrated that annealing at temperatures up to 200 °C for one to two hours further improved surface enhancement, but annealing at 200 °C for one hour or 50 °C for two hours resulted in the greatest increase to surface enhancement. Lastly, we discovered that Ag deposition rate significantly influences surface plasmon extinction peak characteristics. Increasing deposition rate from 0.1 to 0.3 Å s<sup>-1</sup> resulted in decreased surface enhancement at all anneal times and temperatures, making 0.1 Å s<sup>-1</sup> the clearly preferable deposition rate. The results presented in this study fill a vital need for guidance in determining fabrication and annealing parameters for maximal SERS with e-beam deposited Ag nanoparticles with a 532 nm laser. We presume that similar fabrication relationships control the performance of other SERS substrates based on metal nanoparticles. This is the first report to begin to explore the impact of fabrication choices on the performance of a specific SERS sensor, but lays the groundwork for the assessment of similar phenomena in other Raman sensing approaches.

## Conflicts of interest

There are no conflicts of interest to declare.

## Acknowledgements

A. L. Cook acknowledges support from the National Science Foundation Graduate Research Fellowship Program (NSF GRFP) 1445197. A. L. Cook and T. D. Giorgio also acknowledge support from the Congressionally Directed Medical Research Program (CDMRP) Peer Reviewed Medical Research Program (PRMRP) W81XWH-18-1-0412. C. P. Haycock acknowledges support from the National Heart Lung and Blood Institute (NHLBI) T32HL144446. R. R. Mu acknowledges support from the NSF Historically Black Colleges and Universities Research Infrastructure for Science and Engineering (HBCU-RISE) 1924241. The authors would like to thank Eugene Collins, PhD and Akira Ueda, PhD at Fisk University for the use of their facilities and equipment. Lastly, the authors would like to thank Dmitry Koktysh, PhD for his assistance and the Vanderbilt Institute of Nanoscale Science and Engineering (VINSE) for the use of their facilities and equipment in the course of this study.

## References

- 1 D. K. Sarfo, A. Sivanesan, E. L. Izake and G. A. Ayoko, *RSC Adv.*, 2017, **7**, 21567–21575.
- 2 S. Jayabal, A. Pandikumar, H. N. Lim, R. Ramaraj, T. Sun and N. M. Huang, *Analyst*, 2015, **140**, 2540–2555.
- 3 M. S. Frost, M. J. Dempsey and D. E. Whitehead, *Sens. Actuators, B*, 2015, **221**, 1003–1008.
- 4 Y. Zeng, J. Ren, A. Shen and J. Hu, *ACS Appl. Mater. Interfaces*, 2016, **8**, 27772–27778.
- 5 C. Rosman, J. Prasad, A. Neiser, A. Henkel, J. Edgar and C. Sönnichsen, *Nano Lett.*, 2013, **13**, 3243–3247.
- 6 R. A. Halvorson and P. J. Vikesland, *Environ. Sci. Technol.*, 2010, **44**, 7749–7755.
- 7 W. F. Pearman, S. M. Angel, J. L. Ferry and S. Hall, *Appl. Spectrosc.*, 2008, **62**, 727–732.
- 8 N. E. Mircescu, M. Oltean, V. Chiş and N. Leopold, *Vib. Spectrosc.*, 2012, **62**, 165–171.
- 9 X. Wang, X. Qian, J. J. Beitler, Z. Chen, F. R. Khuri, M. M. Lewis, H. J.-C. Shin, S. Nie and D. M. Shin, *Cancer Res.*, 2011, **71**, 1526–1532.
- 10 R. M. Jarvis and R. Goodacre, *Anal. Chem.*, 2004, **76**, 40–47.
- 11 A. A. Yanik, M. Huang, O. Kamohara, A. Artar, T. W. Geisbert, J. H. Connor and H. Altug, *Nano Lett.*, 2010, **10**, 4962–4969.
- 12 J. D. Driskell, K. M. Kwarta, R. J. Lipert, M. D. Porter, J. D. Neill and J. F. Ridpath, *Anal. Chem.*, 2005, **77**, 6147–6154.
- 13 H. Zhou, D. Yang, N. P. Ivleva, N. E. Mircescu, R. Niessner and C. Haisch, *Anal. Chem.*, 2014, **86**, 1525–1533.
- 14 T. T. X. Ong, E. W. Blanch and O. A. H. Jones, *Sci. Total Environ.*, 2020, **720**, 137601.
- 15 A. Sivanesan, E. Witkowska, W. Adamkiewicz, Ł. Dziewit, A. Kamińska and J. Waluk, *Analyst*, 2014, **139**, 1037–1043.
- 16 A. Kamińska, E. Witkowska, K. Winkler, I. Dzieścielewski, J. L. Weyher and J. Waluk, *Biosens. Bioelectron.*, 2015, **66**, 461–467.
- 17 A. M. Giovannozzi, F. Rolle, M. Sega, M. C. Abete, D. Marchis and A. M. Rossi, *Food Chem.*, 2014, **159**, 250–256.
- 18 D. S. Moore and R. J. Scharff, *Anal. Bioanal. Chem.*, 2009, **393**, 1571–1578.
- 19 A. Campion and P. Kambhampati, *Chem. Soc. Rev.*, 1998, **27**, 241–250.
- 20 K. Kneipp, H. Kneipp, I. Itzkan, R. R. Dasari and M. S. Feld, *J. Phys.: Condens. Matter*, 2002, **14**, R597–R624.
- 21 T. Vo-Dinh, *Trends Anal. Chem.*, 1998, **17**, 557–582.
- 22 J. D. Caldwell, O. J. Glembocki, F. J. Bezares, M. I. Kariniemi, J. T. Niinistö, T. T. Hatanpää, R. W. Rendell, M. Ukaegbu, M. K. Ritala, S. M. Prokes, C. M. Hosten, M. A. Leskelä and R. Kasica, *Opt. Express*, 2011, **19**, 26056–26064.
- 23 K. Kneipp, H. Kneipp and J. Kneipp, *Acc. Chem. Res.*, 2006, **39**, 443–450.
- 24 D. Graham, K. Faulds and W. E. Smith, *Chem. Commun.*, 2006, 4363–4371.
- 25 R. Pilot, R. Signorini, C. Durante, L. Orian, M. Bhamidipati and L. Fabris, *Biosens*, 2019, **9**, 57–156.
- 26 Y. Zhang, B. Walkenfort, J. H. Yoon, S. Schlücker and W. Xie, *Phys. Chem. Chem. Phys.*, 2015, **17**, 21120–21126.
- 27 P. A. Mosier-Boss, *Nanomaterials*, 2017, **7**, 142–172.
- 28 A. L. Cook, C. S. Carson, C. E. Marvinney, T. D. Giorgio and R. R. Mu, *J. Raman Spectrosc.*, 2017, **48**, 1116–1121.
- 29 B. H. Nguyen, V. H. Nguyen and H. N. Tran, *Adv. Nat. Sci.: Nanosci. Nanotechnol.*, 2016, **7**, 033001–033012.
- 30 Y. Xie, S. Yang, Z. Mao, P. Li, C. Zhao, Z. Cohick, P.-H. Huang and T. J. Huang, *ACS Nano*, 2014, **8**, 12175–12184.
- 31 X. Wang, S. Xu, H. Li, J. Tao, B. Zhao and W. Xu, *J. Raman Spectrosc.*, 2012, **43**, 459–463.
- 32 A. Yu. Panarin, S. N. Terekhov, K. I. Kholostov and V. P. Bondarenko, *Appl. Surf. Sci.*, 2010, **256**, 6969–6976.

- 33 T. Szymborski, E. Witkowska, W. Adamkiewicz, J. Waluk and A. Kamińska, *Analyst*, 2014, **139**, 5061–5064.
- 34 Y. He, S. Su, T. Xu, Y. Zhong, J. A. Zapien, J. Li, C. Fan and S.-T. Lee, *Nano Today*, 2011, **6**, 122–130.
- 35 X. Liu, Q. Hu, Q. Wu, W. Zhang, Z. Fang and Q. Xie, *Colloids Surf., B*, 2009, **74**, 154–158.
- 36 P. Yang, H. Yan, S. Mao, R. Russo, J. Johnson, R. Saykally, N. Morris, J. Pham, R. He and H.-J. Choi, *Adv. Funct. Mater.*, 2002, **12**, 323–331.
- 37 A. Janotti and C. G. Van de Walle, *Rep. Prog. Phys.*, 2009, **72**, 126501–126530.
- 38 Z. Yi, X. Xu, X. Kang, Y. Zhao, S. Zhang, W. Yao, Y. Yi, J. Luo, C. Wang, Y. Yi and Y. Tang, *Surf. Coat. Technol.*, 2017, **324**, 257–263.
- 39 P.-H. Lei and C.-H. Cheng, *Mater. Sci. Semicond. Process.*, 2017, **57**, 220–226.
- 40 Y. S. Park and J. R. Schneider, *J. Appl. Phys.*, 1968, **39**, 3049–3052.
- 41 G. Barbillon, *Coatings*, 2019, **9**, 86.
- 42 D. C. Mayo, C. E. Marvinney, E. S. Bililign, J. R. McBride, R. R. Mu and R. F. Haglund, *Thin Solid Films*, 2014, **553**, 132–137.
- 43 E. Thouti, N. Chander, V. Dutta and V. K. Komarala, *Journal of Optics*, 2013, **15**, 035005–035012.
- 44 S. Rezaee, *Results Phys.*, 2018, **9**, 1521–1524.
- 45 B. Amin-Ahmadi, H. Idrissi, M. Galceran, M. S. Colla, J. P. Raskin, T. Pardoen, S. Godet and D. Schryvers, *Thin Solid Films*, 2013, **539**, 145–150.
- 46 M. Bechelany, X. Maeder, J. Riesterer, J. Hankache, D. Lerosé, S. Christiansen, J. Michler and L. Philippe, *Cryst. Growth Des.*, 2010, **10**, 587–596.
- 47 J. Schindelin, I. Arganda-Carreras, E. Frise, V. Kaynig, M. Longair, T. Pietzsch, S. Preibisch, C. Rueden, S. Saalfeld, B. Schmid, J.-Y. Tinevez, D. J. White, V. Hartenstein, K. Eliceiri, P. Tomancak and A. Cardona, *Nat. Methods*, 2012, **9**, 676–682.
- 48 C. A. Schneider, W. S. Rasband and K. W. Eliceiri, *Nat. Methods*, 2012, **9**, 671–675.
- 49 *MATLAB R2019a*, The Mathworks, Inc., Natick, Massachusetts, United States.
- 50 Y. Nishijima, Y. Hashimoto, L. Rosa, J. B. Khurgin and S. Juodkazis, *Adv. Opt. Mater.*, 2014, **2**, 382–388.
- 51 J. Dunkers and H. Ishida, *Spectrochim. Acta, Part A*, 1995, **51**, 855–867.
- 52 A. Krylov, A. Vtyurin, P. Petkov, I. Senkovska, M. Maliuta, V. Bon, T. Heine, S. Kaskel and E. Slyusareva, *Phys. Chem. Chem. Phys.*, 2017, **19**, 32099–32104.
- 53 C. A. Patil, I. J. Pence, C. A. Lieber and A. Mahadevan-Jansen, *Opt. Lett.*, 2014, **39**, 303–306.
- 54 H. Sato, H. Chiba, H. Tashiro and Y. Ozaki, *J. Biomed. Opt.*, 2001, **6**, 366.
- 55 S. J. Cho, Y.-H. Ahn, K. K. Maiti, U. S. Dinish, C. Y. Fu, P. Thoniyot, M. Olivo and Y.-T. Chang, *ChemComm*, 2010, **46**, 722–724.
- 56 D. He, B. Hu, Q.-F. Yao, K. Wang and S.-H. Yu, *ACS Nano*, 2009, **3**, 3993–4002.
- 57 C.-L. Zhang, K.-P. Lv, H.-P. Cong and S.-H. Yu, *Small*, 2012, **8**, 648–653.
- 58 A. J. Chung, Y. Suk Huh and D. Erickson, *Nanoscale*, 2011, **3**, 2903–2908.
- 59 T. K. Sinha, S. K. Ghosh, R. Maiti, S. Jana, B. Adhikari, D. Mandal and S. K. Ray, *ACS Appl. Mater. Interfaces*, 2016, **8**, 14986–14993.

## Optimization of Electron Beam-Deposited Silver Nanoparticles on Zinc Oxide for Maximally Surface Enhanced Raman Spectroscopy

Andrew L Cook, Christopher P Haycock, Richard R Mu, Andrea K Locke, and Todd D Giorgio

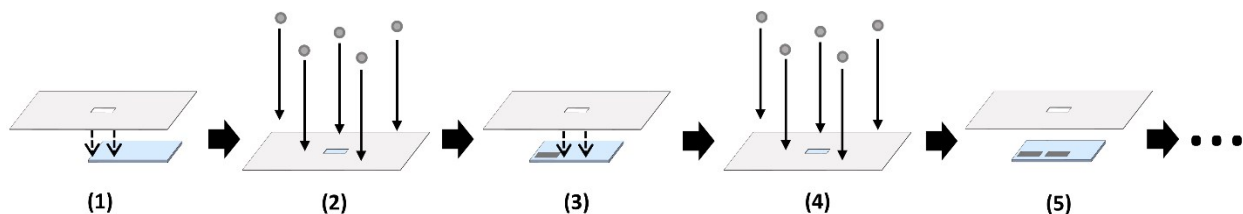


Figure S1: Illustration of the Ag deposition process. Masks cut from aluminum foil were placed on top of each substrate in step (1) such that only a small portion of the substrates was exposed. Ag was then e-beam deposited in step (2), after which the masks were moved to expose a new portion of each substrate in step (3). Ag was again deposited in step (4), and the process was repeated from step (5) onward until 9 Ag films of different thicknesses were deposited on each substrate.

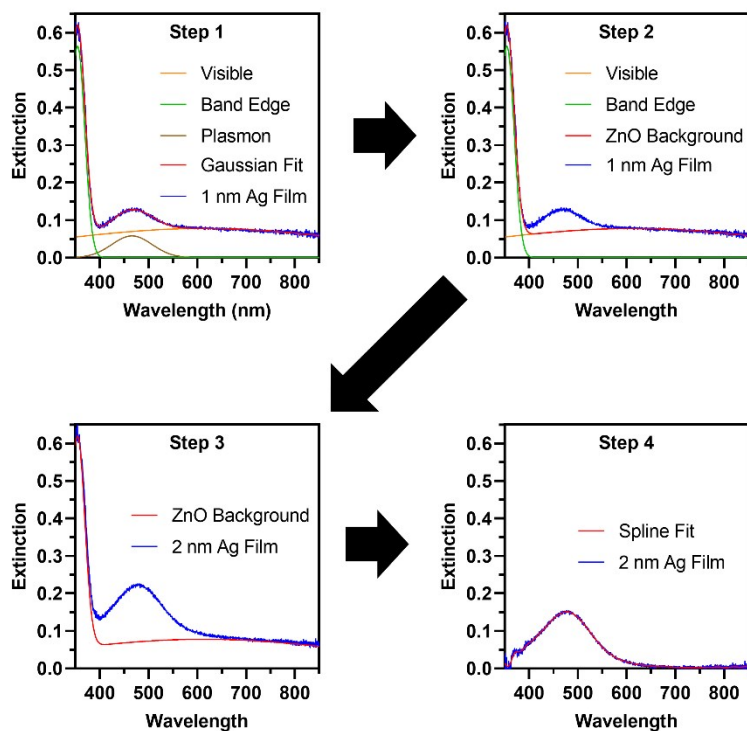


Figure S2: Process for isolating Ag nanoparticle plasmon extinction, in which (Step 1) extinction spectra for 1-nm Ag films on each substrate were approximated with a tri-gaussian fit, (Step 2) the gaussian peaks associated with ZnO background were determined and summed, then (Step 3) subtracted from each film thickness on each substrate. The resultant plasmon peak was (Step 4) approximated with a spline fit to determine peak information.

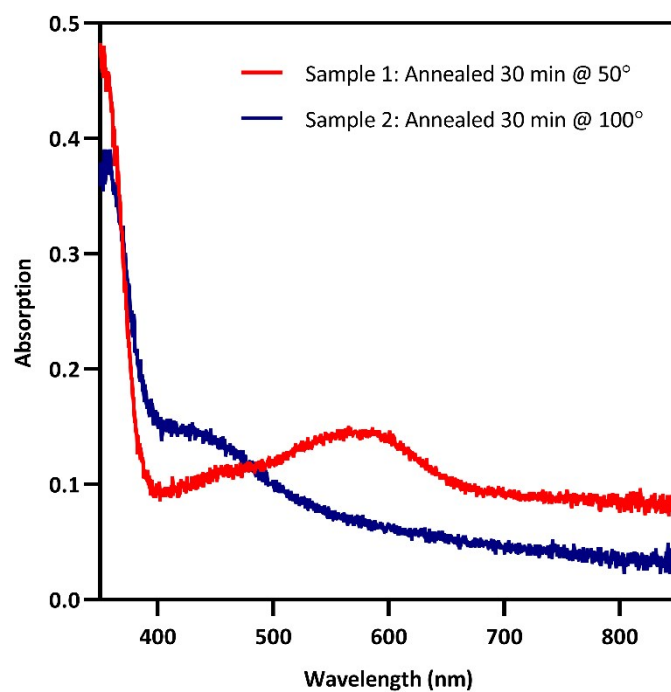


Figure S3: UV-Vis of two Ag-decorated ZnO samples, illustrating the variability in ZnO absorptive background induced by the fabrication and anneal process

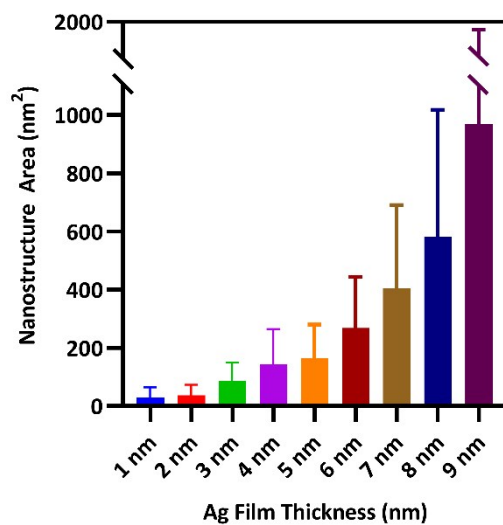


Figure S4: Average area of nanostructures for each Ag film thickness, demonstrating increasing nanostructure size with increasing film thickness.

Table S1: Benzene and non-benzene vibrational modes associated with crystal violet Raman peaks.  $\gamma$  = torsion,  $\delta$  = bending,  $\nu$  = stretching,  $\sigma$  = scissoring,  $\rho$  = rocking; *s* = symmetric, *as* = asymmetric

Raman Band (cm <sup>-1</sup> )	Non-Benzene Vibrational Modes	Benzene Modes	Reference
208	$\gamma(\text{C-H})/\text{whole molecule breathing}$		[1]
225	$\nu_s(\text{C-C}_{\text{center-C}})$		[2]
345	$\gamma(\text{C-N-C})/\delta(\text{C-C}_{\text{center-C}})$		[1–5]
420	$\delta(\text{C-C}_{\text{center-C}})/\delta(\text{C-N-C})$	16a	[1–4, 6]
441	$\delta(\text{C-C-C})_{\text{ring},\perp}/\delta(\text{C-N-C})/\delta_{\text{as}}(\text{C-C}_{\text{center-C}})_{\perp}$	16a	[1, 4–6]
525	$\delta(\text{C-N-C})$	16b,6b	[1, 3, 4]
571	$\delta(\text{C-C-C})_{\perp}/\delta(\text{C-N-C})/\delta(\text{C-C}_{\text{center-C}})$	6a	[1, 3, 4]
605	$\delta(\text{C-C-C})/\delta(\text{C-N-C})/\nu_s(\text{C-C}_{\text{center-C}})$	6a	[1, 4]
623		6b	[1]
730	$\nu_s(\text{C-N-C})$	4,17b	[1, 2, 4]
761	$\nu_s(\text{C-C}_{\text{center-C}})/\nu(\text{C-N-C})$	6a,17a	[1, 2, 4]
810		10a	[1–4, 6, 7]
825		10b,17b	[1, 3, 4]
915	$\delta(\text{C-C}_{\text{center-C}})$	12,17a	[1, 3, 4, 6]
980		17a,18a	[1, 4]
990	$\delta(\text{C-C-C})$	1	[1, 4]
1130	$\delta(\text{C-C}_{\text{center-C}})/\nu(\text{C-N})$	15	[1, 2]
1175	$\nu_{\text{as}}(\text{C-C}_{\text{center-C}})$	9a,9b	[1–7]
1300	$\nu(\text{C-C-C})/\delta(\text{C-C-C})_{\text{ring}}/\delta(\text{C-H})$		[1, 2, 7]
1345	$\delta(\text{C-N})/\delta(\text{C-C-C})_{\text{ring}}/\nu_{\text{as}}(\text{C-C}_{\text{center-C}})/\delta(\text{C-H})$		[1]
1374	$\nu(\text{C-N})/\nu_{\text{as}}(\text{C-C}_{\text{center-C}})/\delta(\text{C-H})$		[1–7]
1445	$\delta_{\text{as}}(\text{C-H}_3)$	19b	[1–4]
1490	$\delta_{\text{as}}(\text{C-H}_3)$	19a	[1, 3, 4]
1529	$\nu(\text{C}_{\text{ring-N}})/\delta_s(\text{C-H}_3)$	8b	[1, 2, 5–7]
1592		8a	[1, 2, 4–7]
1621		8a	[1, 2, 4–7]



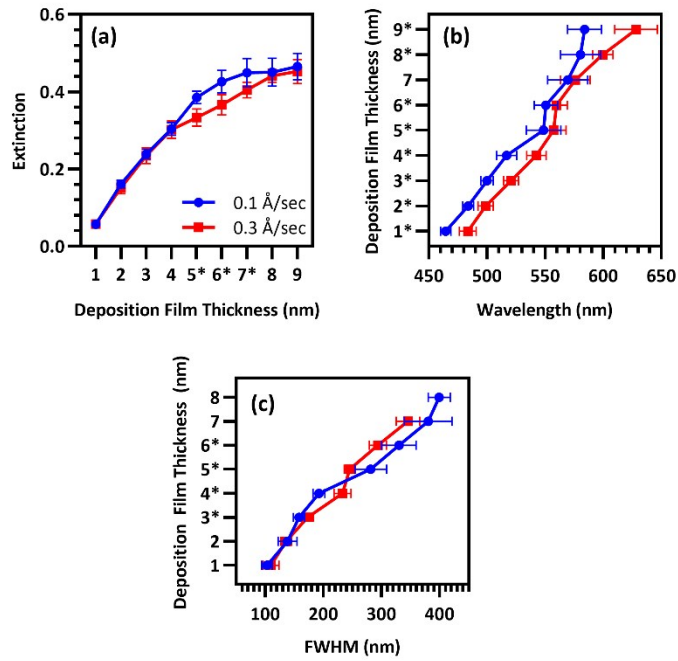


Figure S5: Means of (a) peak intensity ( $n = 40$ ), (b) plasmon peak wavelength ( $n = 40$ ), and (c) plasmon peak FWHM for each film thickness of Group A (blue) and Group B (red). Statistical testing performed with two-way ANOVA,  $*p = 0.05$ .

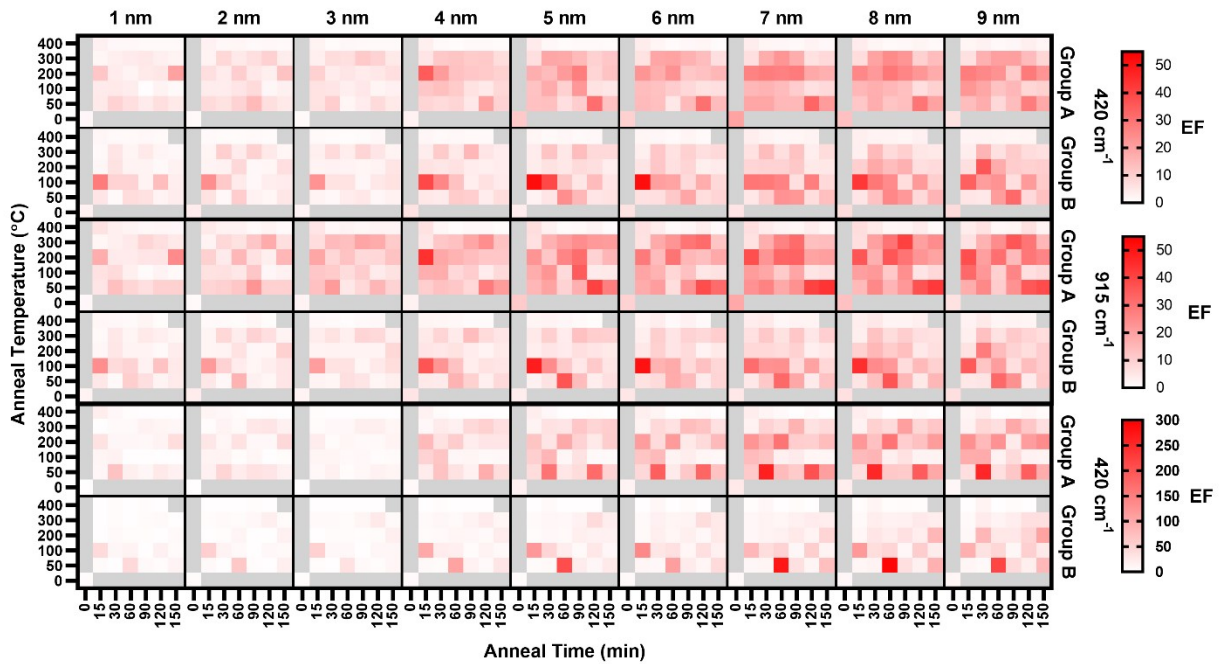


Figure S6: Enhancement Factors for three analyzed peaks of the CV SERS spectra of each film thickness on each annealed substrate and the unannealed control for each rate group.

## References

1. Cañamares MV, Chenal C, Birke RL, Lombardi JR (2008) DFT, SERS, and Single-Molecule SERS of Crystal Violet. *J Phys Chem C* 112:20295–20300. <https://doi.org/10.1021/jp807807j>
2. Liang EJ, Ye XL, Kiefer W (1997) Surface-Enhanced Raman Spectroscopy of Crystal Violet in the Presence of Halide and Halate Ions with Near-Infrared Wavelength Excitation. *J Phys Chem A* 101:7330–7335. <https://doi.org/10.1021/jp971960j>
3. Watanabe T, Pettinger B (1982) Surface-enhanced Raman scattering from crystal violet adsorbed on a silver electrode. *Chemical Physics Letters* 89:501–507. [https://doi.org/10.1016/0009-2614\(82\)83054-6](https://doi.org/10.1016/0009-2614(82)83054-6)
4. Angeloni L, Smulevich G, Marzocchi MP (1979) Resonance Raman spectrum of crystal violet. *J Raman Spectrosc* 8:305–310. <https://doi.org/10.1002/jrs.1250080603>
5. Harraz FA, Ismail AA, Bouzid H, et al (2015) Surface-enhanced Raman scattering (SERS)-active substrates from silver plated-porous silicon for detection of crystal violet. *Applied Surface Science* 331:241–247. <https://doi.org/10.1016/j.apsusc.2015.01.042>
6. Meng W, Hu F, Zhang L-Y, et al (2013) SERS and DFT study of crystal violet. *Journal of Molecular Structure* 1035:326–331. <https://doi.org/10.1016/j.molstruc.2012.10.066>
7. Wang J, Gao X, Sun H, et al (2016) Monodispersed graphene quantum dots encapsulated Ag nanoparticles for surface-enhanced Raman scattering. *Materials Letters* 162:142–145. <https://doi.org/10.1016/j.matlet.2015.09.127>



Surface Enhanced Raman Spectroscopy-Based Sensor for Portable, Multiplexed  
Detection of Toxic Metals in Urine

By

Andrew Luis Cook, M.A.

Dissertation

Submitted to the Faculty of the  
Graduate School of Vanderbilt University  
in partial fulfillment of the requirements

for the degree of

DOCTOR OF PHILOSOPHY

in

Biomedical Engineering

July 14<sup>th</sup>, 2021

Nashville, TN

**Approved:**

**Date:**

---

Todd Giorgio, Ph.D., Chair, Dissertation Advisor

---

Richard Mu, Ph.D.

---

Joshua Caldwell, Ph.D.

---

Anita Mahadevan-Jansen, Ph.D.

---

Kerri Cavanaugh, M.D.

To my wife, Kaitlin, without whose support I would never have finished.

## ACKNOWLEDGEMENTS

As with most worthwhile endeavors, I could not have gotten to my doctoral defense without a great deal of help, mentoring, support, and education from a multitude of people. I would first like to thank my parents for the time, thought, and effort they put into educating me, engaging my curiosity, and helping me from a young age to pursue my dream of becoming a scientist.

I'd like to thank those who educated me and mentored me at the University of North Texas as I pursued my bachelor's degree. In particular, I appreciate the time and effort Dr. Usha Philipose put into mentoring and advising me through the development of my undergraduate thesis, teaching me about nanomaterials and allowing me to take part in her research. I'd also like to thank the McNair Scholars Program at the University of North Texas for preparing me to undertake the rigors of graduate school. In particular, I'd like to thank Dr. Diana Elrod for her mentorship of me throughout my time at the University of North Texas.

I'd like to thank the Fisk-Vanderbilt Masters-to-Ph.D. Program for taking a chance on me and giving me the opportunity to transition from physics to biomedical engineering. There were many in the Bridge program who took a great deal of time to mentor and educate me during my pursuit of my master's degree at Fisk. In particular, I'd like to thank Dr. Dina Stroud for her continued encouragement and support. I'd like to thank Dr. Richard Mu, who advised me excellently in research during my time at Fisk and has continued to mentor me during my pursuit of a Ph.D, including sitting on my dissertation committee. I'd also like to thank Drs. Daniel Mayo, Claire Marvinney, and Jennifer Jones for taking me under their wings, mentoring me and showing me the ropes. They all took a great deal of time to aid me in my pursuit of a master's

degree and I am ever grateful to them. I'd like thank Anthony Mayo and Dr. Akira Ueda for helping me use and maintain the equipment instrumental to my research. I'd like to thank Dr. Deyu Li for allowing me to spend time in his lab using his instruments and materials, taking the time to sit on my master's thesis committee.

I'd like to thank everyone at Vanderbilt University who has mentored and supported me throughout my pursuit of a Ph.D. in biomedical engineering, including those in the Bridge program who continued their support of me beyond the completion my master's degree. First and foremost, I'd like to thank Dr. Todd Giorgio, who worked with Dr. Mu and me to devise a master's research project that would facilitate my transition to biomedical engineering, sat on my master's thesis committee, and mentored & advised me during my pursuit of a Ph.D. I'd like to thank those who, along with Dr. Giorgio, sat on my mentoring committee during my early years at Vanderbilt, Drs. Anita Mahadevan-Jansen and Craig Duvall. I'd also like to thank Drs. Mahadevan-Jansen, Kerri Cavanaugh, and Joshua Caldwell for sitting on my dissertation committee, lending their expertise and support as I performed the research presented here. In addition, there are a number of current and former doctoral and post-doctoral students who took time to mentor and support me, both in my own research group and others. I'd like to thank Dr. Stephanie Dudzinski, Dr. Sinead Miller, Dr. Charleson Bell, Dr. Shirin Masjedi, Dr. Meredith Jackson, Dr. Andrea Locke, Evan Glass, Chris Haycook, Mary Dockery, Carcia Carson, along with many others. I'd like to thank those in the Vanderbilt Institute of Nanoscale Science and Engineering who taught me use the Institute's instrumentation vital to my research, including Drs. Anthony Hmelo, Dmitry Koktysh, and Bill Martinez.

I would be remiss to ignore the significant contribution of my wife, Kaitlin, toward my education since we got married during my time at the University of North Texas. She married me

knowing I wanted to pursue a doctorate and never wavered in her support of me during the intervening years. She has put her all into caring for me and our boys, taking point on their education and therapies, allowing me to focus more on my own education. She has always been honest with me about the hardships she has experienced during this time, but has never held resentment toward me for choosing such a difficult career path. I would never have gotten to this point without her encouragement will always be grateful to her for her support and love. Lastly, I would like to thank God and my savior, Jesus Christ, for giving me the ability and inclination to become a scientist, and for opening the doors I needed to be successful, making me a better person during this time. Without Him, I would not be where I am today.

## TABLE OF CONTENTS

	Page
ACKNOWLEDGEMENTS .....	iii
LIST OF TABLES .....	viii
LIST OF FIGURES .....	ix
LIST OF ABBREVIATIONS .....	xiii
I. INTRODUCTION .....	1
Background and Significance .....	1
Need for Toxic Metals Biomonitoring.....	1
Need for Portable Analyte Sensing.....	3
Toxic Metal Ion Detection Strategies .....	4
Surface Enhanced Raman Spectroscopy for Trace Analyte Sensing.....	6
Surface-Enhanced Raman Sensing of Toxic Metals.....	8
Zinc Oxide Nanowire-Based Surface Enhanced Raman Spectroscopy.....	10
Chelating Toxic Metals with Crown Ethers.....	11
Spectral Processing and Analysis .....	12
Specific Aims.....	14
II. OPTIMIZATION OF SILVER NANOPARTICLE FORMATION FOR SURFACE- ENHANCED RAMAN SPECTROSCOPY WITH A 532-NM LASER .....	19
Abstract.....	19
Introduction.....	20
Experimental .....	24
Substrate Preparation .....	24
Optical Characterization Techniques .....	26
Spectral Processing .....	27
Statistical Analysis.....	29
Results & Discussion .....	30
Effect of Film Thickness on Surface Enhanced Raman Spectroscopy.....	30
Effect of Annealing on Surface-Enhanced Raman Spectroscopy.....	36
Effect of Deposition Rate on Surface Enhanced Raman Spectroscopy.....	41
Conclusions.....	43
III. A FACILE METHOD TO FABRICATE SILVER-DECORATED ZINC OXIDE NANOWIRES INSIDE MICROFLUIDIC CHANNELS FOR SURFACE ENHANCED RAMAN SPECTROSCOPY .....	45
Abstract.....	45
Introduction.....	45
Experimental .....	48
Zinc Oxide Seed in PDMS Channel .....	48

Zinc Oxide Seed on PDMS Substrates .....	49
Zinc Oxide Nanowire Growth .....	51
Ag Nanoparticle Fabrication.....	52
Microfluidic Chip Fabrication .....	53
Characterization Techniques.....	53
Results & Discussion .....	55
Effect of Cleaning on PDMS Raman Spectrum .....	55
ZnO Nanowire Characterization .....	56
Ag Nanoparticle Deposition Characterization .....	57
Effect of PDMS Thickness on Surface Enhancement .....	58
Microchannel Mold Design and Fabrication .....	61
Fabricating SERS Substrates Inside PDMS Channels.....	62
Surface-Enhanced Raman Spectroscopy of Crystal Violet in Channel .....	65
Surface-Enhanced Raman Spectroscopy of Melamine through PDMS .....	65
Conclusions.....	69
IV. TOXIC METALS CHELATION BY 18-CROWN-6 ETHERS IN MULTIPLE SOLUTIONS AND QUANTIFICATION BY SPECTROSCOPIC TECHNIQUES.....	70
Abstract.....	70
Introduction.....	71
Experimental.....	72
Results & Discussion .....	74
Conclusions.....	79
V. CONCLUSIONS.....	80
Chapter Summaries & Impact.....	80
Shortcomings .....	84
Significant Aim 1 .....	84
Significant Aim 2.....	86
Significant Aim 3.....	87
Future Work & Potential Applications .....	87
Conclusion .....	89
APPENDIX A.....	91
APPENDIX B.....	95
APPENDIX C.....	102
REFERENCES .....	104

## LIST OF TABLES

<b>Table I.1:</b> Metals Included in the TEFSC Biomonitoring Panel [3], [4] .....	3
<b>Table II.1:</b> The benzene and non-benzene vibrational modes of the CV peaks selected for analysis, with the CV molecular structure for reference.....	29
<b>Table III.1:</b> Crystal violet Raman peaks used to compare surface enhancement through thick vs. thin PDMS.....	59
<b>Table A.1:</b> Benzene and non-benzene vibrational modes associated with crystal violet Raman peaks. $\gamma$ = torsion, $\delta$ = bending, $\nu$ = stretching, $\sigma$ = scissoring, $\rho$ = rocking; $s$ = symmetric, $as$ = asymmetric .....	93
<b>Table B.1:</b> Vibrational modes of PDMS in the fingerprint region: $\gamma$ = torsion, $\delta$ = bending, $\nu$ = stretching, $\sigma$ = scissoring, $\rho$ = rocking; $s$ = symmetric, $as$ = asymmetric, $\perp$ = out-of-plane, $\parallel$ = in-plane .....	99
<b>Table B.2:</b> Vibrational modes of melamine in the fingerprint region: $\gamma$ = torsion, $\delta$ = bending, $\nu$ = stretching, $\sigma$ = scissoring; $s$ = symmetric, $\perp$ = out-of-plane .....	101



## LIST OF FIGURES

<b>Figure I.1:</b> Ratio of wounded to dead in major U.S. conflicts, illustrating the rising need for toxic metals biomonitoring <sup>4</sup> .....	2
<b>Figure I.2:</b> (a) A Jablonski diagram of Rayleigh, Stokes Raman, and anti-Stokes Raman scattering; <sup>47</sup> (b) An illustration of plasmons caused by incident light. <sup>50</sup> .....	7
<b>Figure I.3:</b> Breakdown of techniques used for SERS detection of toxic metal ions .....	9
<b>Figure I.4:</b> Effects of size and shape on the wavelength of plasmonic resonance for silver nanoparticles <sup>76</sup> .....	12
<b>Figure I.5:</b> Chemical structure of 4'-aminobenzo-18-crown-6 .....	14
<b>Figure I.6:</b> Illustration of the proposed advanced sensor. ZnO nanowires decorated with silver nanoparticles amplify the changes in Raman spectra resulting from metal binding to crown ethers functionalized to the silver .....	15
<b>Figure II.1:</b> Schematic of substrates used for parameter exploration. Substrates deposited with 9 different Ag film thicknesses and separated into two rate groups (A and B). In each group, substrates are annealed over a range of times (15 – 150 min) and temperatures (50 – 400 °C) .....	25
<b>Figure II.2:</b> SEM images of all film thicknesses (identified in white) for a random substrate, with associated extinction spectra displaying peak plasmon wavelength overlaid. The plasmon peak wavelength is identified in yellow for each extinction spectrum. ....	31
<b>Figure II.3:</b> Scatterplots of plasmon peak (a) intensity (n = 40), (b) wavelength (n = 40), and (c) FWHM (T1 – T4: n = 40, T5 – T6: n = 39, T7: n = 14, T8: n = 4) for each film thickness of substrates in Group A. Green line and shaded region in (b) represent the laser line and fingerprint region, respectively. All data shown with mean and standard deviation of each group, *p < 0.05 two-way ANOVA. Statistical significance of the FWHM of 7- and 8-nm films as compared to other films not shown due to an insufficient number of data points to use a parametric test. ....	33
<b>Figure II.4:</b> Raman spectra of CV deposited on each film thickness for substrates (a) unannealed, (b) annealed at 50 °C for 60 min, and (c) annealed at 200 °C for 60 min. ....	35
<b>Figure II.5:</b> Heat map of the enhancement factors of T5 – T9 for 420, 915, & 1592 cm <sup>-1</sup> peaks across all anneal temperatures & times along with the unannealed control. ....	37
<b>Figure II.6:</b> SERS EFs of substrates annealed at 50 °C (blue) and 200 °C (red) for up to 150 min, along with the unannealed control for the (a) 420 cm <sup>-1</sup> , (b) 915 cm <sup>-1</sup> , and (c) 1592 cm <sup>-1</sup> peaks. Each point in the figure exhibits the mean and standard deviation of the EFs for T5 – T9. ....	39

<b>Figure II.7:</b> Change to the plasmon peak (a)intensity, (b)wavelength, and (c)FWHM due to anneal time at 50 °C (blue) and 200 °C (red) for T5 – T9.....	40
<b>Figure III.1:</b> Illustration of the cross-section of a microchannel integrated with an Ag/ZnO nanoprobe fabricated on the PDMS.....	48
<b>Figure III.2:</b> SERS (blue) and non-SERS (grey) Raman spectra of crystal violet through (a) thick and (b) thin PDMS, demonstrating the ability to perform SERS spectroscopy through a PDMS wall, as well as the importance of PDMS thickness on the magnitude of enhancement. .	58
<b>Figure III.3:</b> Comparison of the enhancement to selected crystal violet Raman peaks through thick and thin PDMS.....	60
<b>Figure III.4:</b> AutoCAD drawing of the microchannel mold designed to enable sensitive SERS through the top channel wall, along with the resultant microchannel.....	62
<b>Figure III.5:</b> SEM images of ZnO nanowires before and after deposition and anneal of Ag, demonstrating nanowire growth and Ag nanoparticle formation. ....	63
<b>Figure III.6:</b> UV-Vis spectrum of ZnO nanowires decorated with Ag nanoparticels after anneal .....	64
<b>Figure III.7:</b> Raman spectra of crystal violet solutions taken inside a fabricated channel, in concentrations ranging from 1 to 10 $\mu$ M with a DI water control.....	66
<b>Figure III.8:</b> Intensity of two crystal violet peaks as a function of increasing crystal violet concentration.....	67
<b>Figure III.9:</b> SERS spectra of melamine in DI Water, acquired through S1 on the left and S2 on the right. Number of spectra acquired for each concentration through each substrate in parentheses.....	68
<b>Figure IV.1:</b> UV-Vis extinction spectra of 100- $\mu$ M AB18C6 and B18C6 in 1:3 DMSO:water without and with equimolar concentrations of selected metals. ....	74
<b>Figure IV.2:</b> UV-Vis extinction spectra of 100- $\mu$ M AB18C6 alone and with equimolar concentrations of 22 metal salts in two different solutions. Metals chelated by AB18C6 in 1:1 DMSO:water are denoted with “*”, while metals chelated by AB18C6 in 1:3 DMSO:water are denoted with “†”. ....	75
<b>Figure IV.3:</b> Fluorescent Spectra of AB18C6 by itself and with As and Mo separately in 1:3 DMSO:DI Water, demonstrating fluorescent quenching when of the crown ether when chelating both metals. ....	76
<b>Figure IV.4:</b> UV-Vis and fluorescence spectra of 100- $\mu$ M AB18C6 with concentrations of Mo between 1 nM and 100 $\mu$ M, with a control solution of 100- $\mu$ M AB18C6 unmixed with Mo. ....	77

<b>Figure IV.5:</b> UV-Vis and fluorescence spectra of 100- $\mu$ M AB18C6 with concentrations of Mo between 6.25 and 200 $\mu$ M, with a control solution of 100- $\mu$ M AB18C6 unmixed with Mo.....	78
<b>Figure A.1:</b> Illustration of the Ag deposition process. Masks cut from aluminum foil were placed on top of each substrate in step (1) such that only a small portion of the substrates was exposed. Ag was then e-beam deposited in step (2), after which the masks were moved to expose a new portion of each substrate in step (3). Ag was again deposited in step (4), and the process was repeated from step (5) onward until 9 Ag films of different thicknesses were deposited on each substrate.....	91
<b>Figure A.2:</b> Process for isolating Ag nanoparticle plasmon extinction, in which (Step 1) extinction spectra for 1-nm Ag films on each substrate were approximated with a tri-gaussian fit, (Step 2) the gaussian peaks associated with ZnO background were determined and summed, then (Step 3) subtracted from each film thickness on each substrate. The resultant plasmon peak was (Step 4) approximated with a spline fit to determine peak information. ....	91
<b>Figure A.3:</b> UV-Vis of two Ag-decorated ZnO samples, illustrating the variability in ZnO absorptive background induced by the fabrication and anneal process .....	92
<b>Figure A.4:</b> Average area of nanostructures for each Ag film thickness, demonstrating increasing nanostructure size with increasing film thickness. ....	92
<b>Figure A.5:</b> Means of (a)peak intensity (n = 40), (b)plasmon peak wavelength (n = 40), and (c)plasmon peak FWHM for each film thickness of Group A (blue) and Group B (red). Statistical testing performed with two-way ANOVA, *p = 0.05.....	94
<b>Figure A.6:</b> Enhancement Factors for three analyzed peaks of the CV SERS spectra of each film thickness on each annealed substrate and the unannealed control for each rate group.....	94
<b>Figure B.1:</b> Illustration of the Ag/ZnO nanoprobe fabrication process for PDMS substrates: (1) deposit 100-nm ZnO seed layer on PDMS, (2) hydrothermally grow ZnO nanowires, and (3) deposit Ag on the nanowires on an azimuthally rotated sample to get (4) a finished Ag/ZnO nanoprobe. ....	95
<b>Figure B.2:</b> Illustration of the Ag/ZnO nanoprobe fabrication process for PDMS channels: (1) deposit 100-nm ZnO seed layer on PDMS, (2) hydrothermally grow ZnO nanowires, and (3) deposit Ag from an angle on the nanowires inside a rotated channel to get (4) a finished Ag/ZnO nanoprobe. ....	95
<b>Figure B.3:</b> Raman spectra of PDMS before and after the ALD-AMD cleaning process, demonstrating no spectral effects due to cleaning. ....	96
<b>Figure B.4:</b> SEM image of bare ZnO nanowires, exhibiting highly crystalline nanowires.....	96
<b>Figure B.5:</b> SEM image of ZnO nanowires after Ag nanoparticle decoration, demonstrating dense nanoparticle formation on the sides of nanowires. ....	97

<b>Figure B.6:</b> PL of ZnO nanowires to be decorated with Ag nanoparticles and those to remain bare, demonstrating highly crystalline nature of the nanowires and the similarity between the two sets of nanowires. ....	97
<b>Figure B.7:</b> UV-Vis extinction spectra after nanowire growth of the seeded and non-seeded portions of a patterned PDMS substrate, demonstrating the ability to pattern nanowire growth on PDMS by patterning the seed layer. ....	98
<b>Figure B.8:</b> UV-Vis extinction spectra of Ag/ZnO nanoprobe before and after Ag deposition, demonstrating the formation of plasmons, centered at ~450 nm. ....	98
<b>Figure B.9:</b> Photoluminescence spectra of ZnO nanowires in 7 different PDMS channels, demonstrating variability in ZnO nanowire structure, though each still exhibits high crystallinity with few defects. ....	99
<b>Figure B.10:</b> SEM images of nanowires within PDMS channels on sputtered ZnO seed layers, illustrating the variability of nanowire growth on sputtered seed layers. ....	100
<b>Figure B.11:</b> Ratios of each melamine peak with the PDMS peak at 488 cm <sup>-1</sup> for each substrate, illustrating the consistency of melamine peak intensities relative to the overall signal intensity for each measurement. ....	101
<b>Figure B.12:</b> Ratios of melamine peaks at 1595 cm <sup>-1</sup> to 845 cm <sup>-1</sup> for each melamine concentration measured for each substrate, illustrating internal signal consistency for all concentrations measured, and across substrates. ....	101
<b>Figure C.1:</b> UV-vis spectra of the 100 μM AB18C6 solution in 1:3 DMSO:DI water before and after incubation with an Ag-decorated ZnO nanowire substrate, with a spectrum of the solvent as a negative control .....	102
<b>Figure C.2:</b> UV-vis spectra of the 100 μM AB18C6 solution in 1:3 DMSO:DI water before and after incubation with an Ag-decorated ZnO nanowire substrate, with a spectrum of the solvent as a negative control .....	103

## LIST OF ABBREVIATIONS

AB18C6	4'-Aminobenzo-18-Crown 6
3D	Three-Dimensional
Ag	Silver
Ag/ZnO	Silver Nanoparticle-Decorated Zinc Oxide
Au	Gold
B18C6	Benzo-18-Crown-6
CE	Capillary Electrophoresis
CV	Crystal Violet
DI	Deionized
DMSO	Dimethylsulfoxide
DOD	United States Department of Defense
DPSS	Diode-Pumped, Solid State
DU	Depleted Uranium
e-beam	Electron Beam
EF	Enhancement Factor
EFR	Embedded Fragments Registry
FWHM	Full Width-Half Maximum
HPLC	High-Performance Liquid Chromatography
ICP-MS	Inductively-Coupled Plasma Mass Spectrometry
IED	Improvised Explosive Device
LSPR	Localized Surface Plasmon Resonance
PDMS	Poly(Dimethylsiloxane)
PEO	Poly(Ethylene Oxide)
PL	Photoluminescence
PVA	Polyvinyl Alcohol
SEM	Scanning Electron Microscopy
SERS	Surface-Enhanced Raman Scattering
TEFSC	Toxic Embedded Fragment Surveillance Center
UV-vis	Ultraviolet-Visible
UV-vis-NIR	Ultraviolet-Visible-Near Infrared
VA	United States Department of Veterans Affairs
ZnO	Zinc Oxide

## CHAPTER I

### INTRODUCTION

#### BACKGROUND AND SIGNIFICANCE

##### **Need for Toxic Metals Biomonitoring**

Personnel in modern conflicts, such as those in Iran and Afghanistan, are exposed to toxic metals from sources such as burn pits<sup>1</sup> and injuries resultant from explosive devices.<sup>2</sup> Indeed, most injuries that have occurred in those conflicts are results of explosions from improvised explosive devices (IEDs).<sup>3</sup> Not only are wounded military personnel surviving in much greater numbers than ever before (**Figure I.1**<sup>4</sup>), but such exposures can also have significant adverse long-term health effects for those exposed.<sup>2</sup>

It was once thought that metal fragments imbedded in the body were inert.<sup>2</sup> For this reason, accepted practice was to leave embedded fragments undisturbed unless they presented acute health concerns. It was commonly believed that the trauma associated with surgical removal of those fragments outweighed the presumed negligible long-term health effects of leaving those fragments embedded. Very little was done to actually examine the long-term health effects of such metals.<sup>5</sup> The advent of depleted uranium (DU) in munitions<sup>6</sup> during the Gulf War and increasing evidence demonstrating mobilization of embedded fragments have raised concerns about long-term adverse health effects from embedded fragments.<sup>7-9</sup> Health toxicity from embedded fragments, however, is not limited to DU. There is a range of military-relevant metals, particularly soluble metals, that can cause systemic adverse health effects.<sup>10</sup> Many of

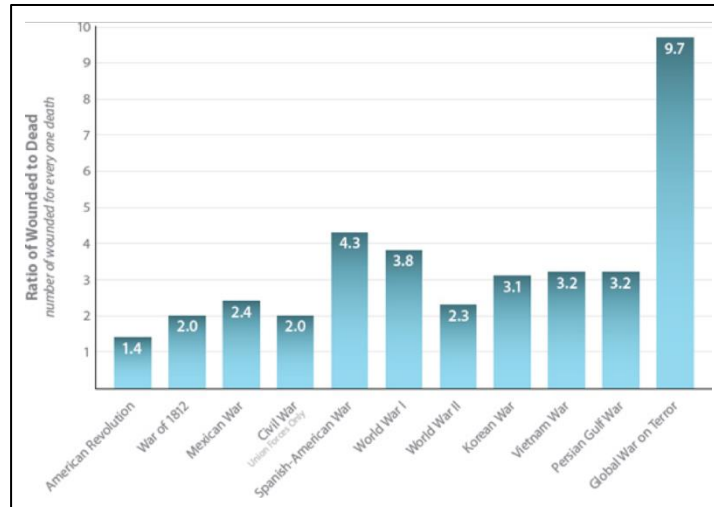


**Figure I.1:** Ratio of wounded to dead in major U.S. conflicts, illustrating the rising need for toxic metals biomonitoring<sup>4</sup>

these metals are excreted in urine, making urinalysis an important approach for identifying and monitoring embedded toxic metal fragments.<sup>11</sup>

A second significant source for metals toxicity is burn pit exposure. Burn pits are a common method of waste disposal in deployed settings<sup>12</sup>. In such situations, waste includes a wide variety of materials, including flammables, plastics, ammunition, and bulk metals<sup>13-15</sup>. Adverse health effects have been associated with burn pit exposure<sup>16-19</sup> and relevant metals have been found in lung tissue after inhalation<sup>20</sup>. However, other reports conflict with this association<sup>21-23</sup>, and the relationship between burn pit exposure and these health effects is not well understood<sup>24</sup>. Indeed, one report explicitly concluded that there is insufficient data to concretely associate adverse health effects with burn pit exposure<sup>25</sup>. This inadequacy is resultant, in large part, from a lack of post-deployment medical surveillance<sup>25</sup>. Thus, toxic metals biomonitoring for personnel exposed to burn pits can potentially help elucidate the relationship between burn pit exposure, toxic metal inhalation, and associated adverse health outcomes.

**Table I.1:** Metals Included in the TEFSC Biomonitoring Panel<sup>26, 28</sup>

Aluminum (Al)	Copper (Cu)	Nickel (Ni)
Arsenic (As)	Iron (Fe)	Tungsten (W)
Cadmium (Cd)	Lead (Pb)	Uranium (U)
Chromium (Cr)	Manganese (Mn)	Zinc (Zn)
Cobalt (Co)	Molybdenum (Mo)	

### Need for Portable Analyte Sensing

Currently, biomonitoring of military members known or suspected of having embedded toxic metal fragments takes the form of urinalysis, with urine samples sent to the Toxic Embedded Fragment Surveillance Center (TEFSC, Baltimore, MD).<sup>26</sup> Analysis is carried out using inductively-coupled plasma mass spectrometry (ICP-MS),<sup>8,27</sup> and the list of metals in the biomonitoring panel includes uranium, cobalt, aluminum, and lead among 14 toxic or potentially toxic metals (**Table I.1**<sup>26,28</sup>). All of these metals have either been found in fragments that have been surgically removed from service members or have well-known toxicological effects<sup>29</sup> Importantly, this program does not include veterans who may have retained metals less-readily detected by contemporary imaging evaluation, such as metal particles embedded in the lung after inhalational exposure from burn pits.<sup>26</sup>

While ICP-MS is sensitive and precise, it is a large, research-grade instrument that requires significant power and highly trained technicians for operation<sup>30,31</sup> making it unsuitable for use near the locations where military blast injuries occur. For this reason, such monitoring is initiated long after the acute exposure at the time of the blast injury. There is still much uncertainty concerning long-term health effects of embedded metal fragments<sup>5,28</sup> and of particulate metal from burn pit exposure,<sup>25</sup> yet ICP-MS precludes sample analysis at or near the



time of exposure. No commercial instrument combines sensitivity and selectivity for metals associated with military-related exposures with the portable, rugged, self-powered characteristics necessary for use at the site of blast or inhalational injuries. Furthermore, there is a lack of information concerning the scope and extent of both burn pit exposure<sup>15,32</sup> and embedded fragments<sup>3,26</sup>. Thus, a device that enables portable toxic metals detection can enable the collection of information concerning composition and acute exposure levels, which may significantly strengthen correlations of health outcomes with toxic metal exposure from embedded fragments or burn pit inhalation.

### **Toxic Metal Ion Detection Strategies**

There are multiple methods available to detect toxic metal ions in an aqueous or organic environment. Some of these are instrumental approaches, such as mass spectrometry, while others are molecular approaches, such as fluorescence and colorimetry, which still require sophisticated dedicated instrumentation. ICP-MS is the method currently used for monitoring embedded fragments in military personnel.<sup>27</sup> ICP-MS is an analysis method that relies on ionizing a sample into an inductively coupled plasma that is characterized by mass spectrometry. The ions are identified based on their mass-to-charge ratios. ICP-MS is very sensitive, being able to detect ng/L concentration,<sup>33</sup> and offers multiplexed detection of toxic metals. However, ICP-MS requires significant sample preparation, often involving dissolution of particulate matter, preconcentration of trace analytes,<sup>34</sup> and sample aerosolization.<sup>35</sup> In addition, highly trained personnel and sophisticated instrumentation is required, making ICP-MS unsuitable for portable toxic metals sensing, as discussed above. Similarly, other instrumental approaches used for metal ion detection, such as inductively coupled plasma optical emission spectrometry (ICP-OES),

atomic absorption spectrometry (AAS), and gas chromatography suffer from the same disadvantages.<sup>36</sup> Some studies have combined chromophores with techniques such as high-performance liquid chromatography (HPLC) and capillary electrophoresis (CE) as alternative detection approaches to toxic metals detection. Detection limits in the ng/L range have been achieved with HPLC and  $\mu\text{g/L}$  for CE.<sup>36</sup> Both techniques reduce sample preparation difficulty in that they test liquid samples. However, HPLC requires complex instrumentation and CE can require preconcentration steps and suffers from false positives.

Electrochemical techniques are another prevalent class of methodologies for detecting toxic metal ions in urine. The basic setup consists of an electrolytic cell with an ionic conductor and an electronic conductor. In the case of toxic metal ions, an aqueous solution of the toxic metal ions in question acts as the electrolytic cell. Electrochemical ion detection relies on changes induced by the presence of toxic metal ions to electrical parameters such as current, voltage, impedance, and charge. The most sensitive electrochemical techniques have limits of detection on the order of ng/L,<sup>37,38</sup> though detection limits on the order of  $\mu\text{g/L}$  are more common.<sup>39-41</sup> Although high sensitivity has been achieved for certain electrochemical techniques, miniaturization remains an issue, making portability problematic. Additionally, most electrochemical techniques suffer from poor reproducibility and stability. These drawbacks coupled with an inability to selectively detect toxic metals in complex samples<sup>42</sup> limit the usefulness of electrochemical techniques for toxic metals detection in the field. There are other optical, electrochemical, or even biological sensing techniques for metal ions, but much work still needs to be done to overcome challenges in sensitivity, selectivity, robustness, field deployability, and cost-effectiveness, among others.<sup>43</sup>

## Surface Enhanced Raman Spectroscopy for Trace Analyte Sensing

Raman spectroscopy has attracted much attention in recent years as technique to identify analytes because it is non-destructive to the sample, label-free,<sup>44</sup> and not subject to photobleaching,<sup>45</sup> relying on exciting vibrational modes in molecular bonds. Raman scattering, first discovered in the 1920s,<sup>46</sup> occurs when light illuminates a sample. Most photons are elastically scattered via Rayleigh scattering, but a small portion of incident photons (on the order of one in a million) are inelastically Raman scattered. In Raman scattering, the energy of the photon changes, either losing energy to induce molecular vibrations or (rarely) gaining energy from already vibrating bonds (Stokes and anti-Stokes scattering, respectively; see **Figure I.2(a)**<sup>47</sup>). The change in photonic energy is dependent on the structure of the molecule in question, and is constant, irrespective of incoming light frequency,<sup>48</sup>

Because Raman scattering is so rare relative to Rayleigh scattering, Raman spectroscopy suffers from low sensitivity, hampering the detection and identification of trace analytes. The effect of Raman's low optical cross-section can be greatly mitigated through surface-enhanced Raman scattering (SERS). First observed in 1974,<sup>49</sup> SERS is the result of two distinct mechanisms. The first is electromagnetic in nature. Light incident on the surface of a conductor causes the excitation of the electron gas within the conductor, called a "plasmon" (**Figure I.2(b)**<sup>50</sup>) When excitation is confined near the surface of the conductor, it is called a "surface plasmon." Importantly, the excitation of surface plasmons requires surface roughness or curvature, as in the case of metal nanoparticles. In the case of nanoparticles, surface plasmons have a "natural frequency," which is dependent on the size and shape of the nanoparticle, the dielectric environment of the nanoparticle, and the metal composition of the nanoparticle. As the frequency of incident light approaches the plasmon's natural frequency, a resonance condition occurs, which vastly increases the field local to the nanoparticle. In the case of Raman

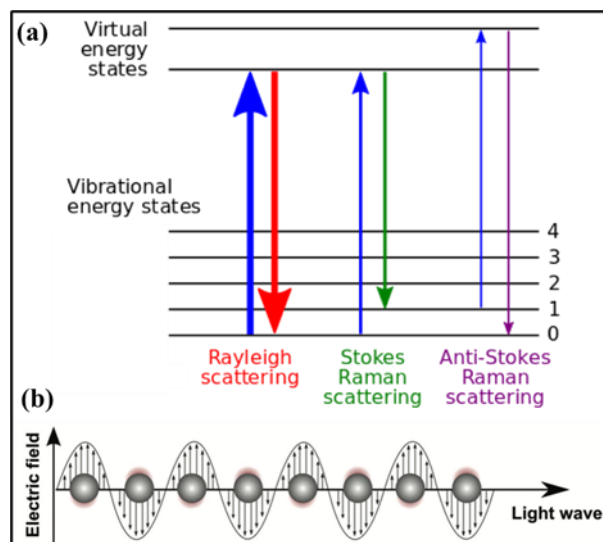


**Figure I.2:** (a) A Jablonski diagram of Rayleigh, Stokes Raman, and anti-Stokes Raman scattering;<sup>47</sup> (b) An illustration of plasmons caused by incident light.<sup>50</sup>

spectroscopy, this means that not only incident light is enhanced, but also scattered light, causing even greater enhancement to the Raman spectra of analytes local to the nanoparticle.<sup>51</sup>

Theoretical estimates show that enhancement factors can be as large as  $10^{12}$ , which can enable single-molecule detection.<sup>52</sup>

While the electromagnetic mechanism is well understood and explains the majority of surface enhancements, the second mechanism is not so clear. There has long been observed, in some cases, an additional one to three orders of magnitude enhancement to the Raman spectra of certain chemisorbed analytes that cannot be explained by the electromagnetic theory.<sup>51-53</sup> This additional enhancement is difficult to isolate from electromagnetic enhancement, but is believed to be chemical in nature, and three different mechanisms have been proposed to contribute to this additional enhancement. The first is chemical interaction between the nanoparticle and the analyte in the ground state. It is suggested that for analytes not covalently bound to the nanoparticle surface, the presence of the metal can induce a slight change in the electronic distribution of the analyte.<sup>50</sup> The second is commonly referred to as the charge-transfer model, in

which charge transfer can occur between the molecule and the metal.<sup>50</sup> Charge transfer can occur when the Fermi level of the metal allows charge transfer excitations from the highest occupied molecular orbital to the lowest unoccupied molecular orbital in the analyte.<sup>51-53</sup> The third mechanism is resonance Raman enhancement in chemically bound analytes.<sup>50</sup> While chemical enhancements are not as large as electromagnetic enhancements, they may still be significant.

### **Surface-Enhanced Raman Sensing of Toxic Metals**

SERS-based techniques for sensing toxic metal ions can be divided into three major types based on changes to the SERS reporter signal: SERS signal decrease (or turn-off), SERS signal increase (or turn-on), and SERS signal modification (**Figure I.3**). The most common mechanisms for turn-off SERS sensing are reporter detachment<sup>54,55</sup> and nanoparticle de-aggregation<sup>56,57</sup> in the presence of the metal ion, either from direct interaction between the reporter and the ion or SERS surface, or from ion interaction with a DNAzyme. While these techniques are often very sensitive, they are difficult to multiplex. Furthermore, these techniques have been developed for few metal ions, further complicating the development of a multiplexed toxic metal SERS sensor. The most common mechanisms for turn-on SERS sensing of toxic metals are reporter attachment (or juxtaposition),<sup>58</sup> and controlled nanoparticle aggregation<sup>59-61</sup> in the presence of the metal ion. By far the most common method of accomplishing both mechanisms is aptamer or DNAzyme functionalization of the SERS substrate. DNAzymes, in particular, have been developed for the selective coordination of a variety of metal ions,<sup>62</sup> and biomolecule-based techniques are often very sensitive. However, biomolecules are susceptible to denaturation in suboptimal storage conditions,<sup>63</sup> making them unsuitable for the development of a portable toxic metals sensing platform. Turn-on mechanisms that are not based on aptamers are

limited in variety of metal ions able to be sensed, limiting their usefulness for multiplexed toxic metal ion sensing.

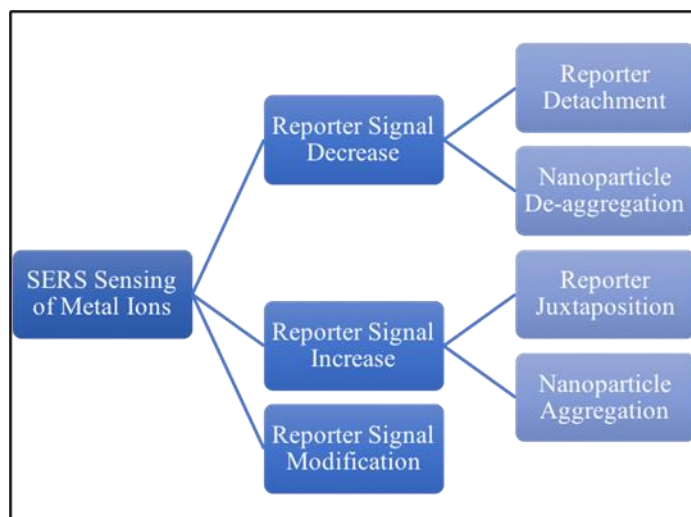


**Figure I.3:** Breakdown of techniques used for SERS detection of toxic metal ions

Reporter modification techniques for SERS sensing of toxic metal ions rely on changing the SERS signal of the reporter molecule upon coordination with metal ions, rather than change in SERS intensity.<sup>30,64–67</sup> These techniques do not rely on colloidal SERS substrates, as aggregation and de-aggregation strategies do, nor do they require biomolecules, as aptamer and DNzyme-based strategies do. Because these techniques rely on signal modification, multiplexation is easier than for turn-on and turn-off strategies. It has been shown that reporter SERS signals will change differently depending on the metal ion being coordinated.<sup>30</sup> This reduces the need for highly specific binding, facilitating multiplexed metal ion sensing on the same SERS substrate. These advantages make SERS reporter signal modification the optimal strategy for portable, multiplexed detection of toxic metals.

## Zinc Oxide Nanowire-Based Surface Enhanced Raman Spectroscopy

A number of SERS-active substrates have been designed for use with fluid samples, which can be broadly categorized as “in-solution” or “stationary.” In-solution SERS nanoprob­es have attracted much recent attention for analyte detection, especially for continuous-flow strategies, due to several advantages. These include freedom to manipulate flow, ease of integration with microfluidics, and highly sensitive sensing.<sup>50</sup> However, colloidal nanoprob­es suffer from a lack of stability<sup>68</sup> and spectral reproducibility,<sup>69,70</sup> as well as contamination.<sup>71–73</sup> In contrast, stationary SERS-active substrates are much more stable than colloids and result in more reproducible spectra, due to a lack of uncontrolled dynamic colloid motion.<sup>71</sup> On the other hand, stationary substrates are less sensitive than colloidal nanoprob­es since stationary substrates don’t mix with sample fluids.<sup>50</sup> Integration of stationary substrates also increases the complexity of microfluidic channel fabrication by requiring extra fabrication steps. For portable SERS sensing applications, the approach must possess sufficient stability and ruggedness to survive in suboptimal conditions, but must also be sensitive enough for trace detection with portable equipment.

A bed of nanowires offers a potential approach for the design of a toxic metals sensor in this application for portable SERS. Nanowires possess the stability of stationary substrates, but also an increased surface area, which simultaneously allows for more plasmonic “hotspots” and increased analyte adsorption.<sup>68</sup> Zinc oxide (ZnO) nanowires, in particular, are advantageous for SERS sensing due to numerous electronic characteristics, such as electronic stability at room temperature.<sup>74</sup> and a large direct bandgap.<sup>75</sup> More importantly for Raman spectroscopy, ZnO is transparent in the visible and near-infrared regions, reducing adsorption of Raman-scattered photons. Single-crystal ZnO nanowires have a hexagonal crystal structure, which can allow the nanowires to form Fabry-Perot or whispering gallery optical cavity modes. This can result in

waveguiding of light, if the diameter of the nanowires is large enough for the chosen wavelength of light, reducing loss due to scattering.<sup>75</sup>

The metal chosen for SERS applications plays a large part in the range of wavelengths for which enhancements can occur. While there is a multitude of metals that can be used for SERS, such as gold, platinum, copper, and palladium, silver (Ag) is among the most common metals used for SERS sensing in the visible region.<sup>50</sup> Surface plasmon resonances (SPRs) from Ag nanoparticles generally have wavelengths of 400-500 nm, although nanoparticles with sharp edges or corners can push SPRs towards 800 nm, as shown in **Figure I.4**.<sup>76</sup> Ag nanoparticle strongly enhance Raman spectra by virtue of strong plasmon resonance. By decorating ZnO nanowires with Au or Ag nanoparticles, the advantage of a three-dimensional nanowire structure can be realized.

### **Chelating Toxic Metals with Crown Ethers**

To detect toxic metal ions by SERS reporter signal modification, chelating ligands are required to bind the ions local to the sensing surfaces. These ligands serve the dual purpose of bringing metal ions close to sensing surfaces and reporting the presence of metal ions through changes to the ligands' Raman spectra, since metal ions alone have little to no Raman signal. Specifically, crown ethers are an attractive option for this purpose. Crown ethers are cyclic compounds consisting of a number of ether groups. The most common crown ethers consist of repeating ethyleneoxy units. Variations of these include benzo- or dibenzo-crown ethers which have one or two benzene rings appended to the crown, aza-crown ethers which have nitrogen atoms substituted for oxygen atoms, and thia-crown ethers which have sulfur atoms substituted for oxygen atoms.



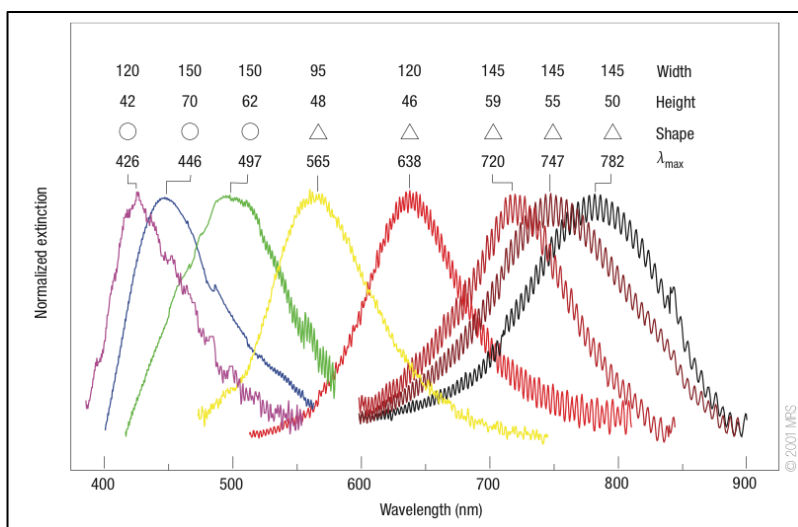


**Figure I.4:** Effects of size and shape on the wavelength of plasmonic resonance for silver nanoparticles<sup>76</sup>

Crown ethers are best-known for selective coordination of alkali metal cations,<sup>77</sup> but have been studied for coordination with multiple toxic or potentially toxic metals. In particular, 4'-aminobenzo-18-Crown-6 (AB18C6, shown in **Figure I.5**), which has a crown radius of 2.2 – 3.2 Å has been reported to bind  $Pb^{2+}$ , which has a radius of 2.4 Å.<sup>78,79</sup> However, crown ethers are known to chelate multiple different cations based on size fit and coordination chemistry.<sup>77</sup> There is evidence that crown ethers with different structures will chelate metal ions differently.<sup>78,80</sup> In addition, solvent affects metal chelation by crown ethers.<sup>81</sup>

### Spectral Processing and Analysis

Before Raman spectra can be used in any sort of quantitative analysis, they must be pre-processed, which includes noise removal, background subtraction, and normalization. Noise removal is required to reveal or clarify spectral features due to the small optical cross-section of Raman scattering. Shot noise, which is random in nature and high frequency,<sup>82</sup> can be removed or reduced by a variety of methodologies. Perhaps the simplest is smoothing by a moving

average, which relies on the randomness and high frequency of noise. The moving average technique averages each point on a spectrum with a specified number of adjacent points.<sup>83</sup> With this technique, spectral points at the ends of the spectrum are lost due to an inability to average them. Additionally, increasing the number of points to be averaged also increases spectral distortion in the smoothed spectrum. Smoothing by the Savitzky-Golay polynomial technique<sup>84</sup> can alleviate spectral distortion, as each point in the spectrum is fit to a polynomial function derived from adjacent points. The order of the polynomial is dependent on the number of adjacent points used, with an  $n$ th-order polynomial requires  $2n+1$  points. Low-order polynomials significantly reduce noise, with an increased risk of spectral distortion. High-order polynomials reduce signal distortion at the cost of reduced noise removal. If the signal-to-noise ratio is extremely small, noise can be removed by discrete frequency analysis accomplished by applying the fast Fourier transform to the spectrum. By this technique, high-frequency spectral components can be separated from mid- and low-frequency components. However, difficulty lies in choosing the frequencies to remove, as Raman bands can have similar frequencies to noise. Cosmic rays are another common source of noise, causing significant but random spikes during measurement.<sup>85</sup> These, being random, are extremely unlikely to occur at the same wavenumber over multiple measurements, can be easily removed by repeat measurements.<sup>86</sup>

A major component of Raman spectra, particularly of organic materials (including crown ethers), is broad background signal due to fluorescence that can alter acquired Raman spectra. Although several methods exist to remove background from spectra, perhaps the most common is polynomial curve fitting.<sup>86</sup> This technique fits the purpose well, as fluorescence background is broadband with few features. Polynomial fitting also lends itself well to Raman analysis because it largely preserves Raman band shape and intensity, if performed correctly. However, a major

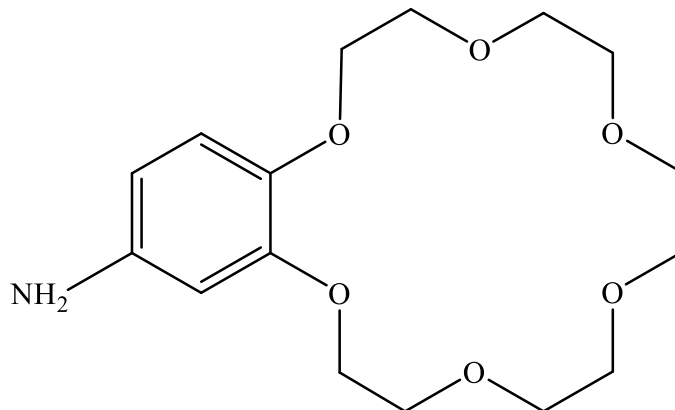


**Figure I.5:** Chemical structure of 4'-aminobenzo-18-crown-6

drawback of this technique has been the need for extensive manual and subjective processing to exclude Raman bands from the curve-fitting process. This drawback has been significantly alleviated by the development of an automated polynomial function developed by Lieber and Mahadevan-Jansen,<sup>87</sup> This function iteratively examines spectral data points, conserving those that are lower in intensity than the corresponding point on the fitted polynomial curve. This process effectively retains Raman bands while eliminating broadband fluorescence, even for spectra with weak Raman bands respective to fluorescence.<sup>88</sup>

### SPECIFIC AIMS

As of 2017, improvised explosive devices (IEDs) have accounted for almost 75% of all traumatic injuries to U.S. soldiers in recent conflicts in Iraq and Afghanistan.<sup>27</sup> This means that of the more than 50,000 military personnel wounded in action so far in those conflicts,<sup>89</sup> almost 40,000 of them could have toxic embedded fragments.<sup>28</sup> In response to this growing need, the United States Department of Veterans Affairs (VA) established the Toxic Embedded Fragment Surveillance Center (TEFSC, Baltimore, MD) in 2008 with the overall mission to 1) identify veterans who may have embedded metal fragments, and 2) conduct long-term medical surveillance of this population.<sup>26</sup> The evaluation process for inclusion into the Embedded

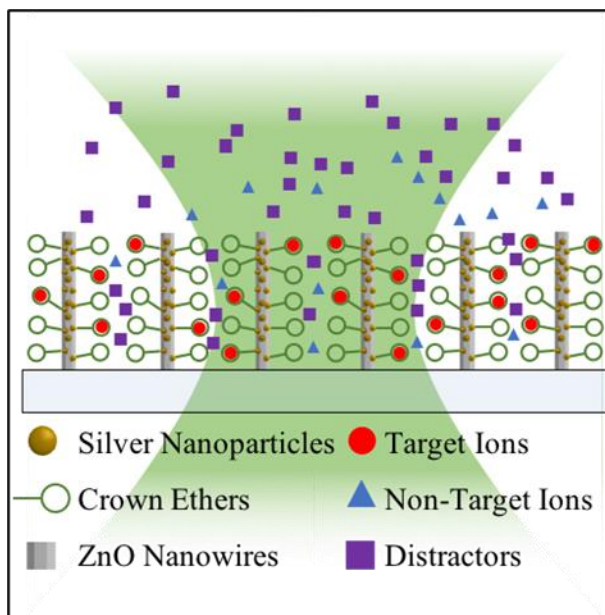


**Figure I.6:** Illustration of the proposed advanced sensor. ZnO nanowires decorated with silver nanoparticles amplify the changes in Raman spectra resulting from metal binding to crown ethers functionalized to the silver

Fragments Registry (EFR) is predicated on the individual's knowledge or suspicion of retained fragments.<sup>29</sup> Thus, biomonitoring of toxic embedded fragments begins long after peak exposure and depends on incomplete knowledge concerning exposure and retention toxic fragments from IEDs, making inclusion into the EFR noncomprehensive. As a result, there are currently only around 16,000 Veterans enrolled in the EFR.<sup>90</sup> The development of a portable toxic metals sensor would allow military personnel to be screened for toxic metal ions associated with embedded fragments near the time of exposure, enabling more comprehensive biomonitoring of veterans exposed to toxic metals, as well as potential early intervention.

The overall goal of this work is to develop an inexpensive, disposable sensor that can reproducibly characterize the presence of analytes such as toxic metals in biological and environmental samples using portable equipment. This work will develop a microfluidic device integrated with an inherently three-dimensional surface-enhanced Raman scattering (SERS) substrate using a novel fabrication procedure. In preparation to functionalize this SERS-active

substrate with the chelating ligand 4'-aminobenzo-18-crown-6, this work will identify which toxic metals are selectively chelated by this crown ether in solution (**Figure I.6**).

**Specific Aim 1: Optimize silver nanoparticle formation for surface enhanced Raman spectroscopy with 532-nm laser.**

To maximize the sensitivity of the sensor, Ag nanoparticles' shape and dimensions must be modified to align their plasmon peak with the fingerprint region of the analyte. To accomplish this, the effects of Ag nanoparticles' deposition and anneal parameters on their plasmon peak will be examined. Ag film thicknesses of ranging from 1 – 9 nm will be deposited on a ZnO layer via electron beam deposition at rates of 0.1 and 0.3 Å/s. These films will be examined via SEM imaging to examine their shape and distribution. UV-Vis spectrophotometry will be performed to ascertain their plasmon peak properties and Raman spectra will be acquired using a 532-nm laser from crystal violet (CV) deposited on the substrates to determine which thicknesses afford the most spectral enhancement. These substrates will be annealed at temperatures ranging from 50 – 400 °C for times ranging from 15 – 150 min, with UV-Vis being performed as above to discover how their plasmon properties change due to annealing. Likewise, Raman spectroscopy will be performed on annealed substrates to determine how annealing changes affects the nanoparticles' surface enhancement at each thickness. An optimal nanoparticle fabrication and anneal parameters will be determined from these results, maximizing device sensitivity.

### **Specific Aim 2: Design and Fabricate Microfluidic Channel with Integrated Silver-Decorated Zinc Oxide Nanowires for Surface Enhanced Raman Spectroscopy.**

Surface-enhanced Raman scattering (SERS) detection of selected analytes will be characterized within a microfluidic channel. The SERS-active substrate will consist of high quality, single-crystal zinc oxide (ZnO) nanowires and silver (Ag) nanoparticles decorating the nanowire sides. A microfluidic channel master will be fabricated and will be used to embed the channel in poly(dimethylsiloxane) (PDMS). A ZnO seed layer will be patterned inside the microfluidic channel and ZnO nanowires will be grown from this seed layer. ZnO nanowires will be characterized for crystallinity, defects, and dimensionality. Ag nanoparticles will be deposited on the nanowires and characterized for plasmonic resonance. Subsequently, the PDMS will be irreversibly bonded to glass and a solutions of crystal violet and melamine, a Raman-reporter and contaminant of dairy products respectively, will be injected into the channel. Label-free SERS sensing of crystal violet at various concentrations will demonstrate efficacy of the SERS-active substrate within a microfluidic channel.

### **Specific Aim 3: Explore Chelation of Toxic Metals by 4'-Aminobenzo-18-Crown-6**

Once device utility for SERS sensing has been demonstrated, the chelation of toxic metals will be explored in multiple solutions. The metal ions which crown ether 4'-aminobenzo-18-crown-6 (AB18C6) binds in both 1:1 dimethylsulfoxide (DMSO):DI water and 1:3 DMSO:DI water will be determined using UV-Vis spectrophotometry. Metals will be selected for further study based on how well they are chelated by AB18C6. Fluorescence spectroscopy will be performed on AB18C6 chelating selected metals, and concentration-dependent studies will be performed with both UV-Vis spectrophotometry to explore the possibility of using fluorescence

and UV-Vis to inform SERS quantification of toxic metals, or as possible dual sensing strategies in conjunction with SERS.

## CHAPTER II

### OPTIMIZATION OF SILVER NANOPARTICLE FORMATION FOR SURFACE- ENHANCED RAMAN SPECTROSCOPY WITH A 532-NM LASER

Text for Chapter II taken from:

**Cook AL**, Haycook CP, Locke AK, Mu RR, Giorgio TD. Optimization of Electron Beam-Deposited Silver Nanoparticles on Zinc Oxide for Maximally Surface Enhanced Raman Spectroscopy. *Nanoscale Advances*. 2021. **3**. 407-417. DOI: 10.1039/D0NA00563K<sup>91</sup>

#### ABSTRACT

Surface enhanced Raman spectroscopy enables robust, rapid analysis on highly dilute samples. To be useful, the technique needs sensing substrates that will enhance intrinsically weak Raman signals of trace analytes. In particular, three-dimensional substrates such as zinc oxide nanowires decorated with electron-beam deposited silver nanoparticles are easily fabricated and serve the dual need of structural stability and detection sensitivity. However, little has been done to optimize e-beam deposited silver nanoparticles for maximal surface enhancement in the unique dielectric environment of the zinc oxide substrate. Herein, fabrication and anneal parameters of electron beam-deposited silver nanoparticles were examined for the purpose of maximizing surface enhancement. Specifically, this work explored the effect of changing film thickness, deposition rate, anneal temperature, and anneal time on the surface plasmon resonance of Ag nanoparticles. In this study, multiple sets of fabrication and annealing parameters were discovered that optimized surface plasmon resonance for maximal enhancement to Raman signals acquired with a 532-nm laser. This work represents the first characterization of the fabrication and annealing parameters for electron beam-deposited silver nanoparticles on zinc oxide.



## INTRODUCTION

There is an unmet multidisciplinary need for bioanalytical techniques that can perform analyses on small volumes of highly diluted specimens with minimum sample preparation. Applications such as the detection of toxic metals,<sup>80,92-94</sup> other pollutants or contaminants,<sup>95-98</sup> circulating tumor cells,<sup>99</sup> bacteria,<sup>100</sup> or viruses<sup>101</sup> benefit from fast and reliable molecular sensing. State-of-the-art tools used for these purposes such as high-performance liquid chromatography, mass spectrometry, and enzyme-linked immunosorbent assays commonly involve expensive reagents, large sample volumes, skilled technicians and frequently have low throughput rates. In addition, such tools are often plagued by limited differentiation among chemically or biologically similar analytes.<sup>102-104</sup> Raman spectroscopy is an attractive technique that addresses some of the limitations of other approaches because it provides a unique spectroscopic “fingerprint” of the biomolecular and biochemical composition of specimens, potentially offering effective detection of analytes in minutes or seconds.<sup>105-107</sup> Raman also exhibits portability and facile function, as demonstrated by its use in forensic fields such as explosives identification.<sup>108</sup> However, Raman scattering has a small optical cross-section, with only one in  $10^6 - 10^8$  photons being Raman scattered, limiting its usefulness for trace analyte sensing. Surface-enhanced Raman spectroscopy (SERS), however, can significantly enhance intrinsically weak Raman signals, enabling reliable, efficient, and non-destructive detection of highly dilute analytes.

It is well-known that there are two mechanisms principally responsible for the enhancement effects in SERS: an electromagnetic mechanism resulting from localized surface plasmon resonance (LSPR) and a chemical mechanism resulting from charge transfer between analyte and metallic nanostructure.<sup>109-111</sup> To take full advantage of the dominant electromagnetic mechanism of surface enhancement, it is necessary that the nanoparticles be spatially dense, to

make use of “hotspots” in the gaps between nanoparticles.<sup>112,113</sup> For these reasons, much attention has been devoted to the use of metallic nanoparticles for incorporating SERS into various sensing system solutions. However, the expansive parameter space controlling SERS performance requires further investigation to effectively design sensors that provide optimal surface enhancement of intrinsically weak Raman signals.

Silver (Ag) is among the most commonly used metals for SERS-based sensing, due to strong Ag plasmon resonance in the visible region<sup>114,115</sup> and facile synthesis.<sup>116</sup> Many Ag nanostructures have been explored for SERS-based sensing, which fall into two basic categories: (1) colloidal nanostructures and (2) nanostructures on solid surfaces.<sup>117</sup> Colloidal nanostructures offer high sensitivity due to the ability to easily generate a large sensing surface area. However, due to random suspension of particles in free solution, colloidal nanostructures lack stability, and thus can affect measurement reproducibility. Conversely, nanostructures fabricated onto solid surfaces can possess great structural stability, resulting in greater measurement reliability. However, this stability comes at the cost of reduced sensitivity compared to colloidal paradigms due to lower surface area. This cost can be mitigated by fabricating inherently three-dimensional (3D) sensing substrates, as described in our previous work.<sup>118</sup> There are several methods of fabricating metallic nanoparticles onto a solid substrate that generally fall into two categories: chemical fabrication and physical deposition. Physical deposition techniques such as electron beam (e-beam) deposition facilitate formation of densely arranged Ag nanoparticles, enabling use of “hot-spots” between nanoparticles.<sup>119</sup> However, these techniques do not easily lend themselves to control of nanoparticle properties that affect LSPR. In the case of chemical fabrication, techniques such as hydrothermal growth are used to fabricate nanoparticles directly on the sensing surface.<sup>120</sup> While these techniques are more easily implemented and easier to

control than physical deposition, they usually result in lower surface coverage by nanoparticles, reducing the impact of inter-particle hotspots. Therefore, by exploring the fabrication parameters that affect nanoparticle formation in physical deposition paradigms, greater control over nanoparticle formation can be implemented.

Recent research has illuminated multiple strategies for realizing 3D templates for SERS-active substrates, including anodized aluminum oxide,<sup>121</sup> porous silicon,<sup>122</sup> electrospun polymers,<sup>123</sup> silicon nanowires,<sup>124</sup> and zinc oxide (ZnO) nanowires,<sup>120</sup> among others. ZnO, in particular, is an attractive material for fabricating 3D SERS substrates. ZnO is a biocompatible<sup>125</sup> wide direct-bandgap semiconductor with a band-edge emission of 3.3 eV and a high exciton binding energy of 60 meV, making it electronically stable at room temperature.<sup>74,126</sup> The semiconducting nature of ZnO also enables charge transfer between the ZnO and Ag,<sup>127</sup> increasing surface enhancement over strategies that rely solely on the electromagnetic mechanism. Crystalline ZnO is also transparent to visible light,<sup>128</sup> which reduces absorptive loss of light when acquiring spectra through the substrate as we did in our previous work.<sup>118</sup> Additionally, ZnO possesses a large refractive index of approximately 2.0 in the visible region, which aids in the confinement of light.<sup>129,130</sup> Combining these characteristics with the atomically smooth and highly faceted hexagonal single-crystal structure of the nanowires allows for waveguiding of light, which can reduce signal loss due to light scattered away from the detector.<sup>131</sup>

Previously, we prepared ZnO nanowires decorated with Ag nanoparticles for sensing soluble analytes. This sensing paradigm yielded an estimated six orders of magnitude surface enhancement of the Raman signal for crystal violet (CV, CCDC # 137090), melamine, and adenine.<sup>118</sup> Performance of this sensor was likely reduced because the Ag nanoparticles, with a plasmon peak at ~460 nm, were not optimal for SERS with the 532-nm laser used. We also did

not explore the sensor performance as a function of Ag deposition parameters that are likely to influence SERS amplification mechanisms. Through this study, Ag-decorated ZnO nanowires demonstrated potential for effective sensing of trace analytes, which can be realized by examining the effect of fabrication and anneal parameters on surface plasmon resonance.

Parameters that can be manipulated during e-beam deposition of Ag and significantly impact the Raman enhancement include film thickness and deposition rate. Film thickness, in general, changes the shape and surface coverage of metallic nanostructures which changes LSPR characteristics of the film. By consequence, these changes modulate the magnitude of surface enhancement. Other research groups have explored how Ag nanoparticle plasmon resonance changes with film thickness in e-beam deposited<sup>132</sup> and sputtered<sup>133</sup> systems, but in neither of these works were nanoparticles deposited on a ZnO layer, which can significantly impact plasmon resonance as part of the dielectric environment of the nanoparticles. Also, while the effects of Ag film thickness on LSPR has been explored in some way, little attention has been devoted to the effects of Ag film deposition rate on plasmon resonance, even though deposition rate has a known effect on the structural properties of metallic films.<sup>134</sup> Furthermore, thermal annealing following deposition changes the nanoparticle size and shape through Ostwald ripening.<sup>135</sup> Since nanoparticle geometry and dimension are important drivers of plasmon resonance, thermal annealing offers an additional strategy for optimization of SERS sensing. Thermal annealing occurs as a result of two independent parameters: anneal temperature and anneal time.

In this work, four independently selectable parameters that influence Ag nanoparticle formation and presentation on ZnO were quantitatively controlled. These parameters, namely film thickness, deposition rate, anneal temperature, and anneal time were examined to assess

their impact in modulating surface plasmon resonance. The functional consequences of these fabrication parameters were comparatively assessed using surface-enhanced Raman spectra that were acquired from crystal violet deposited onto each substrate. We aim to discover fundamental fabrication principles and sensor characteristics that will advance the design of maximally sensitive SERS devices based upon e-beam deposited Ag nanoparticles on a ZnO substrate.

## EXPERIMENTAL

### Substrate Preparation

Glass slides (Fisherbrand® Plain Microscope Slides) were cut into 80 1-cm<sup>2</sup> substrates with a diamond saw and cleaned by sonication sequentially for 10 minutes each in 1% aqueous Alconox® solution, deionized (DI) water, acetone, methanol, and again in DI water. Onto these substrates, a 100 nm ZnO layer was deposited via e-beam deposition at a rate of approximately 0.1 Å/s to ensure even deposition of Zn and O. As demonstrated by **Figure A.1**. Masks were cut from aluminum foil large enough to completely cover the substrates, with a square cutout ~0.2 cm to a side, allowing a Ag film to be deposited on only a small portion of each substrate. After each film was deposited, the masks were shifted so that the cutouts exposed a new portion of each substrate, and a new film was deposited. This process was repeated nine times, for nine different Ag film thicknesses fit on each substrate, as illustrated by **Figure A.1**. Ag thin films were deposited over a range of 1 nm to 9 nm film thicknesses, in 1 nm increments, hereafter referred to as T1 – T9. The 80 substrates were divided into two groups of 40 substrates, as shown in **Figure II.1**. These two groups, hereafter referred to as Group A and Group B, were deposited with Ag thin films at rates of 0.1 and 0.3 Å/s, respectively. All Ag films in Group A were

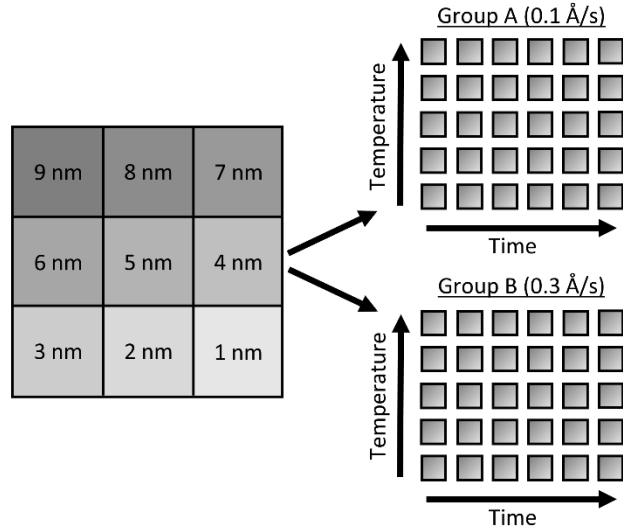


**Figure II.1:** Schematic of substrates used for parameter exploration. Substrates deposited with 9 different Ag film thicknesses and separated into two rate groups (A and B). In each group, substrates are annealed over a range of times (15 – 150 min) and temperatures (50 – 400 °C)

deposited at rates of  $0.1 \pm 0.002 \text{ \AA/s}$  and all Ag films in Group B were deposited at rates of  $0.3 \pm 0.018 \text{ \AA/s}$ . It is well known that when material from a point source is deposited onto substrates affixed to a flat plate, deposition rates fall off with axial distance from the source. This results in varying film thickness as a function of axial distance, defined by **Equation (II.1)**:

$$t_d = \left[ 1 + \left( \frac{d}{R_0} \right)^2 \right]^{-3/2} \quad (\text{II.1})$$

In this equation,  $t_d$  represents the film thickness at distance  $d$  from the axis defined by the point source and  $R_0$  represents the distance from the source to the plane of deposition.  $R_0$  was measured to be 27 cm and the axial distance  $d$  of substrates farthest from the source was measured to be ~4.5 cm. Thus, the largest variation in film thickness was ~4% of the target thickness. All e-beam depositions were performed at pressures below 6.7 mPa.

Following the deposition of silver, the substrates were annealed at various temperatures: 50, 100, 200, 300 and 400 °C. At each temperature, different substrates were annealed at times: 15, 30, 60, 90, 120, and 150 minutes, providing a substrate from each deposition rate group (2

groups) with every anneal temperature (5) and time (6), producing  $2 \times 5 \times 6 = 60$  uniquely fabricated and annealed substrates and 1 unannealed control, each presenting T1 through T9 film thicknesses for a total of 549 different substrates.

### **Optical Characterization Techniques**

Scanning electron microscopy (SEM) images, before annealing, were acquired of each Ag film thickness from a random substrate to get a visual perspective on the changing Ag nanostructure morphology as a result of changing film thickness. These images were acquired using a Zeiss Merlin scanning electron microscope (Jena, Germany) in a plan configuration with a 10 kV electron beam at a magnification of  $400,000\times$  and a working distance of 2.8 mm. The average size of nanostructures was determined using Fiji image analysis of acquired SEM images.<sup>136,137</sup> The images were first converted to black-and-white via the Make Binary function and noise was removed via the Despeckle function, in which each pixel is given the median value of its  $3\times 3$  neighborhood. The area of the nanostructures were acquired via the Analyze Particles function and area values that didn't correspond to single nanostructures were removed.

Extinction spectra were acquired of each film thickness, on each substrate before and after annealing, using a Hitachi U-4100 spectrophotometer integrating sphere to determine peak surface plasmon resonance wavelength. Extinction spectra were obtained at a rate of 3 nm/s over a range of 350 – 850 nm, with each substrate oriented facing away from oncoming light.

Raman spectra were acquired using a Thermo Scientific DXR Raman microscope (Waltham, MA, USA). A 532 nm diode-pumped, solid state (DPSS) laser was used with a 10x objective (Olympus, MPlan N Achromat, 0.25 NA) at a power of 10 mW as measured at the objective turret. Focal plane was adjusted before each acquisition to maximize spectral intensity.

All substrates were placed in contact with a 25  $\mu\text{M}$  aqueous solution of crystal violet (CV) overnight. The substrates were then removed from the CV solution and air-dried. Five Raman spectra were acquired from each substrate (T1-T9), along with five spectra of a portion on each substrate without Ag, hereafter referred to as T0. Each Raman spectrum was the accumulation of four background-subtracted spectra acquired over a range of 200-1800  $\text{cm}^{-1}$ , each taken with a 5 s exposure time. All Raman spectra were acquired with a 50  $\mu\text{m}$  pinhole aperture and a 900 grooves/mm grating.

### **Spectral Processing**

UV-Vis spectra of the Ag films deposited on ZnO layers exhibit extinction from both Ag and ZnO. While ZnO is largely transparent in the visible region, light extinction due to the ZnO band edge occurs below approximately 380 nm. In order to accurately obtain Ag plasmon peak information, absorptive contributions from ZnO were approximated and subtracted as illustrated in **Figure A.2**. This method was chosen to minimize variation in ZnO signal induced by the fabrication and anneal process, as illustrated by **Figure A.3**. To approximate ZnO absorptive contributions, UV-Vis spectra from the T1 portions of each substrate were fitted to a tri-gaussian equation, shown in **Equation (II.2)**. In this fit, the first gaussian approximated the ZnO band-edge contribution, the second approximated the ZnO visible contribution, and the third approximated the Ag plasmon peak. T1 spectra were chosen for this task because of minimal overlap between the Ag plasmon peak and the ZnO band-edge and because the plasmon peak could be accurately approximated by a gaussian curve. Once fits to these spectra were successfully obtained, the third gaussian was subtracted from the fit to arrive at an approximation of the ZnO contribution to the spectra. This ZnO contribution for each substrate was then



subtracted from the UV-Vis spectra for T1-T9 for each substrate. Finally, a cubic smoothing spline, where **Equation (II.3)**, is minimized, was fit to the resultant plasmon peaks to remove noise, enabling accurate extraction of plasmon peak extinction, wavelength, and spread.

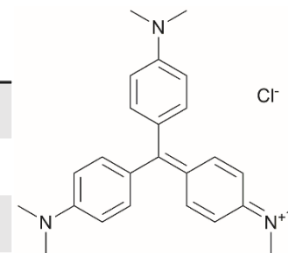
$$F_g(x) = a_b e^{-\frac{(x-\mu_b)^2}{2\sigma_b^2}} + a_v e^{-\frac{(x-\mu_v)^2}{2\sigma_v^2}} + a_p e^{-\frac{(x-\mu_p)^2}{2\sigma_p^2}} \quad (\text{II.2})$$

$$\lambda \sum_i [y_i - s(x_i)]^2 + (1 - \lambda) \int_{x_{min}}^{x_{max}} \left( \frac{d^2 s(x)}{dx^2} \right)^2 dx \quad (\text{II.3})$$

In **Equation (II.2)**,  $F_g$  is the gaussian fit,  $a$  is an arbitrary fit parameter, and  $\mu$  &  $\sigma$  represent the peak and root-mean-square width of the gaussian, respectively. Subscripts  $b$ ,  $v$ , and  $p$  denote the gaussian fitting of the ZnO band-edge, ZnO visible, and Ag plasmon contributions to the spectrum, respectively. In **Equation (II.3)**  $\lambda$  represents the smoothing parameter,  $y$  is the set of observed extinctions at each wavelength,  $x$  is the set of wavelengths at which extinction is measured,  $s$  is the smoothed function output of the equation, and  $x_{min}$  &  $x_{max}$  are the minimum and maximum wavelengths of the spectrum, respectively. For this work, a smoothing parameter  $\lambda = 0.003$  was used. A smoothing spline was used to approximate the plasmon rather than a gaussian because, while the plasmon peaks of thinner films could be accurately approximated by a gaussian fit, the plasmon peaks of thicker films could not due to increasing asymmetry in the peak. Spread was measured at the full width-half maximum (FWHM) of each plasmon peak where possible. For several spectra, particularly of thicker Ag, the FWHM was sufficiently broad to extend beyond the measured wavelength range and could not be determined. All processing of UV-Vis spectra was performed in MATLAB.<sup>42</sup> Energy dispersive x-ray spectroscopy had been previously performed on similarly prepared SERS-active substrates, confirming the presence of ZnO and Ag.<sup>118</sup>

**Table II.1:** The benzene and non-benzene vibrational modes of the CV peaks selected for analysis, with the CV molecular structure for reference

Raman Band (cm <sup>-1</sup> )	Non-Benzene Vibrational Modes	Benzene Modes
420	$\delta(C-C_{\text{center}}-C)/\delta(C-N-C)_l$	16a
915	$\delta(C-C_{\text{center}}-C)$	12,17a
1592		8a



Raman spectra were subtracted of their fluorescent background, estimated using 5<sup>th</sup>-degree polynomial fit. These spectra were then smoothed using a Savitzky-Golay filter. Each of the five spectra acquired from each film thickness (T0-T9) on each substrate were averaged to find a representative spectrum. Three CV Raman peaks at 420, 915, and 1592 cm<sup>-1</sup>, tabulated in **Table II.1** with their associated vibrational modes and the CV molecular structure, were selected to provide specific, characteristic features for the estimation of enhancement factors (EFs). These peaks were selected to interrogate EFs from each end of the measured spectra and one feature near the middle of the spectra. The intensities of these peaks in the spectra for T1-T9 on each substrate were divided by the intensities of the same peaks in the spectrum of T0 on the same substrate to arrive at EFs for each peak.

### Statistical Analysis

All error bars represent standard deviation unless otherwise stated. Two-way analysis of variance followed by Tukey's and Sidak's multiple comparison tests was performed for data presented here as indicated, and statistical significance was defined as  $p < 0.05$ . Statistical analyses were performed using Prism 7.04 (GraphPad Software).

## RESULTS & DISCUSSION

The surface plasmon peak of a distribution of Ag nanoparticles possesses three characteristics that affect the level of enhancement: peak intensity, peak wavelength, and peak breadth. Because surface plasmons enhance both incident light from the laser and Raman-scattered light, surface enhancement is most effective when high plasmon extinction occurs at both the laser line and across the range of wavelengths at which light is scattered. Thus, the surface plasmon peak should be located near the laser line to maximize enhancement to incident light, and the peak should be sufficiently broad to provide significant enhancement to Raman-scattered light across the wavelength range of interest. In addition, plasmon intensity correlates with enhancement factor, with higher plasmon intensities generally producing greater enhancement for non-colloidal sensing substrates.<sup>139</sup> Surface plasmon peak intensity, wavelength, and breadth are all influenced by nanoparticle size, size distribution, crystal composition, proximity, and shape. These nanoparticle properties are modulated by deposition thickness and deposition rate, and by anneal temperature and time, post-deposition. In this study, we explore the combinatorial effect of these fabrication parameters on the surface plasmon peak characteristics of Ag nanoparticle arrays and correlate these effects to changes in enhancement of intrinsic Raman spectral intensity of CV. By doing so, we aim to facilitate the development of optimized sensing substrates for maximally surface-enhanced Raman spectroscopy.

### **Effect of Film Thickness on Surface Enhanced Raman Spectroscopy**

Increasing Ag film thickness was anticipated to intensify, broaden, and red-shift the plasmon extinction peak due to increasing Ag surface coverage, increasing particle diameter, and decreasing interparticle distance. However, the quantitative relationships that describe these

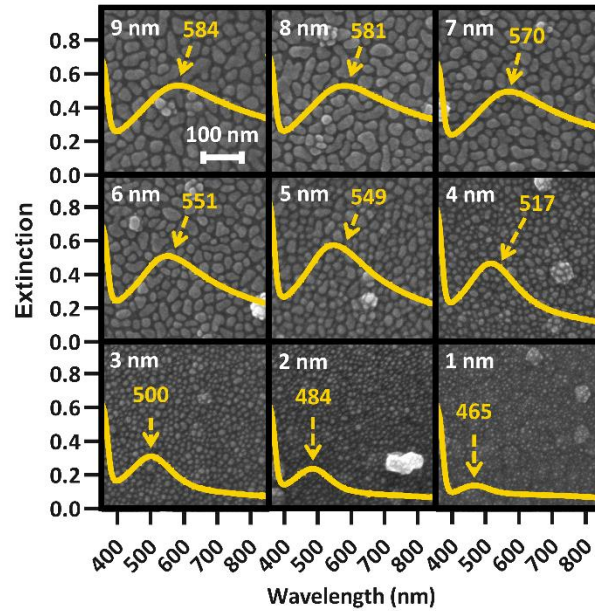


**Figure II.2:** SEM images of all film thicknesses (identified in white) for a random substrate, with associated extinction spectra displaying peak plasmon wavelength overlaid. The plasmon peak wavelength is identified in yellow for each extinction spectrum.

effects as a function of film thickness have not been previously described. Furthermore, while increasing intensity is correlated with increasing surface enhancement, for solid substrates, maximizing enhancement requires proximity of the peak wavelength with the incident laser. In addition, broadening the plasmon peak is only effective insofar as it maximizes plasmon extinction across the wavelengths of interest. Therefore, we examined the relationships between Ag film thickness and maximized surface enhancement through changes to nanostructure morphology and plasmon peak extinction characteristics. SEM images were acquired from Group A before annealing to explore the relationship between film thickness and nanostructure morphology. These images, shown in **Figure II.2**, reveal that Ag was deposited as small islands that grow with increasing film thicknesses from 1 nm (T1) to approximately 5 nm (T5) and become more film-like for depositions of 6 nm (T6) and greater. This change is likely due to surface coverage approaching 100% as a result of increasing Ag mass per area. Extinction

spectra are superimposed on each SEM image in **Figure II.2**, confirming intensified and red-shifted extinction with increasing film thickness. The symmetrical plasmon peaks observed among the lowest Ag depositions (T1 – T4) are consistent with individual, spherical Ag nanoparticles. The transition toward nanostructured thin films (T5 – T9) was accompanied by increasingly exotic nanostructure shapes, associated with increasing asymmetry in the plasmon peaks.

The UV-Vis spectra for all 9 film thicknesses on each of 40 substrates in Group A were processed as described in the Experimental Section above to find peak extinction intensity, wavelength, and breadth in each case. Plasmon extinction intensity increased with Ag film thickness, as shown in **Figure II.3(a)**. Intensity increases approximately linearly for T1 – T5, but begins to approach an asymptotic maximum for T6 – T9. The reduction in differential extinction for high film thicknesses is confirmed by the lack of statistically significant differences between T7 & T8 and T8 & T9 as compared to T1 – T6 in which each thickness group was significantly different from every other thickness group. This change in behavior between thin and thick films correlates with proximity-induced hotspots. When adjacent nanoparticles are within a few nanometers of each other plasmonic coupling results in a hotspot between them, greatly increasing plasmon extinction.<sup>112</sup> For T1 – T5, plasmonic coupling between nanoparticles drove the growth in plasmon extinction intensity as interparticle distances decreased, exhibited by **Figure II.2**. Beginning at T6 however, interparticle gaps ceased to decrease as Ag was deposited. At that point, plasmon extinction intensity began to plateau, which is consistent with Ag accumulation becoming the primary driver for increasing plasmon extinction.

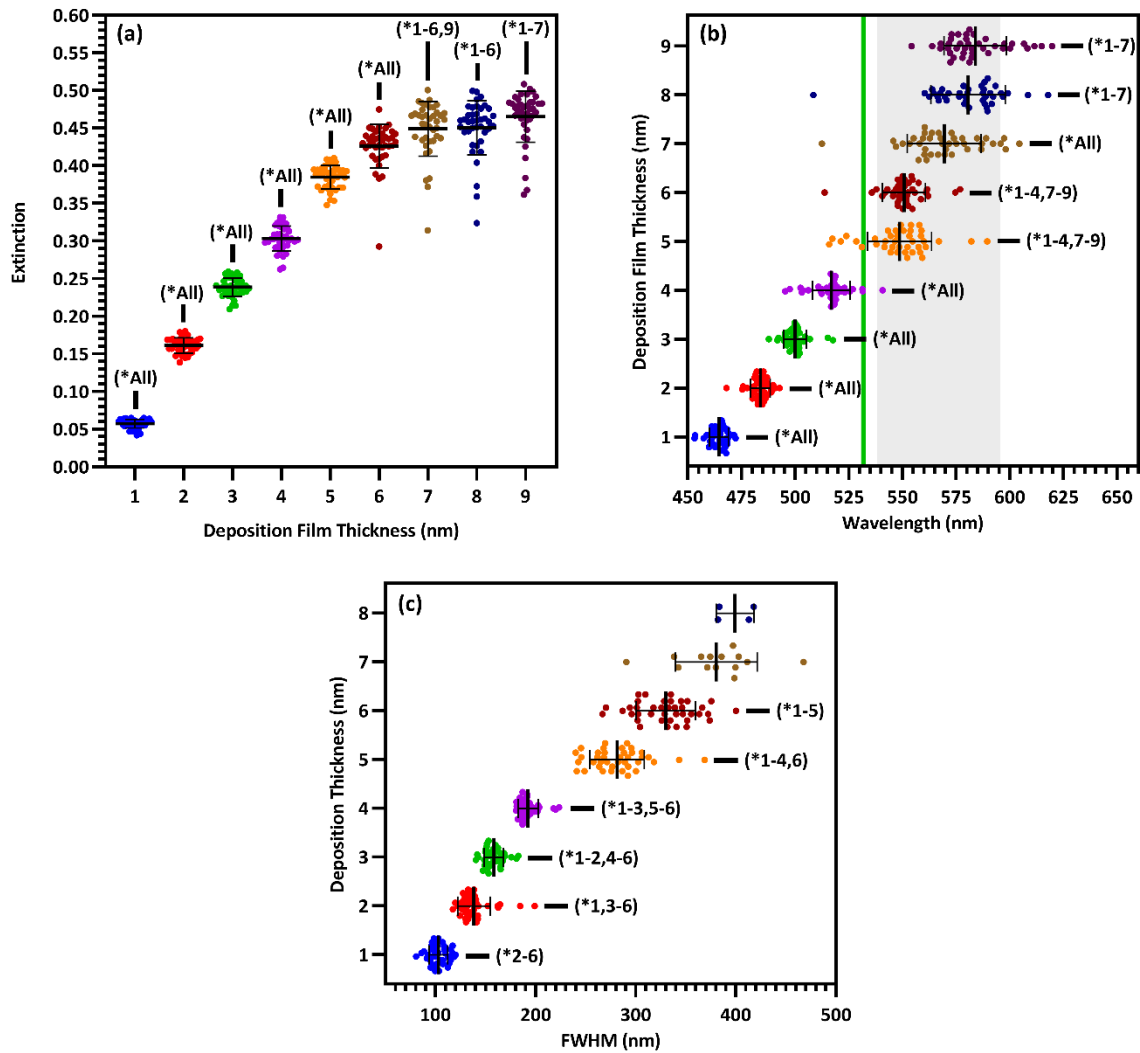


**Figure II.3:** Scatterplots of plasmon peak (a) intensity ( $n = 40$ ), (b) wavelength ( $n = 40$ ), and (c) FWHM (T1 – T4:  $n = 40$ , T5 – T6:  $n = 39$ , T7:  $n = 14$ , T8:  $n = 4$ ) for each film thickness of substrates in Group A. Green line and shaded region in (b) represent the laser line and fingerprint region, respectively. All data shown with mean and standard deviation of each group, \* $p < 0.05$  two-way ANOVA. Statistical significance of the FWHM of 7- and 8-nm films as compared to other films not shown due to an insufficient number of data points to use a parametric test.

Plasmon peak wavelength red-shifted with increasing Ag film thickness, shown in **Figure II.3(b)**, from well below the laser line at an average of  $\sim 464$  nm for 1-nm films, to well past the laser line at an average of  $\sim 584$  nm for 9-nm films. This redshift was likely due primarily to increasing nanostructure size, which correlated with increasing film thickness (**Figure II.2**).

Nanostructures increased in size from an average of  $\sim 30 \text{ nm}^2$  for 1-nm films to an average of  $\sim 970 \text{ nm}^2$  for 9-nm films, as shown in **Figure A.4**. Unlike intensity, maximizing surface enhancements requires proximity of the plasmon extinction peak and the laser wavelength, illustrated by the green line in **Figure II.3(b)**. The wavelength of peak plasmon extinction also influences surface enhancement, as the efficiency of optical coupling is enhanced when the laser line is near the plasmon peak. The closest alignment between peak extinction and the laser line was at 517 nm for T4 and 548 nm for T5. Additionally, variability in peak wavelength generally increased as films thickened, with standard deviation growing from 4.2 nm for 1-nm films to as much as 17.3 nm for 8-nm films. We speculate that this behavior is associated with the increasingly exotic nanostructure shapes associated with increasing film thickness.

Maximal surface enhancement requires LSPR with both incident laser light and wave-shifted scattered light. While enhancement is improved when the plasmon extinction peak is close to the laser wavelength, the peak should also be sufficiently broad to enhance wave-shifted scattered light across the fingerprint region which, for organic molecules, usually consists of some portion of the region between 200 and 2000  $\text{cm}^{-1}$ . When a 532-nm laser is used to acquire Raman spectra, this fingerprint region translates to 537.7 – 595.3 nm, illustrated by the shaded region in **Figure II.3(b)**.<sup>140–143</sup> Thus, the sensing approach aims for a plasmon wavelength range that usefully overlaps with the entire spectral region of interest. To estimate breadth of the plasmon peak, the FWHM was determined where possible. FWHM of the plasmon peaks correlate with film thickness and range from  $\sim 104 \text{ nm}$  for 1-nm films to more than 400 nm for 8-nm films, as shown in **Figure II.3(c)**. While this phenomenon provides a greater wavelength range with the potential for useful sensing at the largest deposition thicknesses, it complicated our ability to accurately characterize the FWHM. For substrates with T5 and T6 film thickness, a

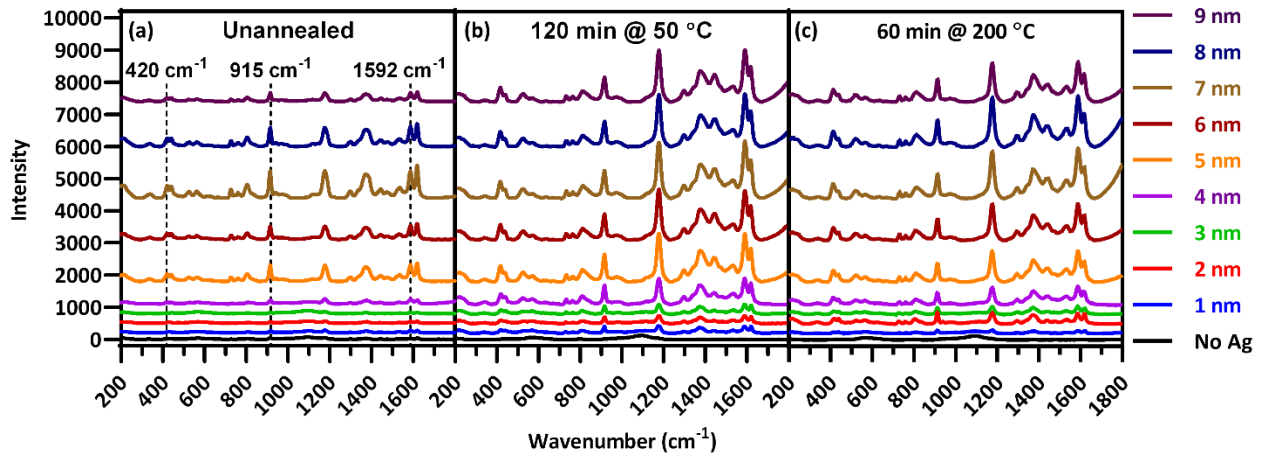


**Figure II.4:** Raman spectra of CV deposited on each film thickness for substrates (a) unannealed, (b) annealed at 50 °C for 60 min, and (c) annealed at 200 °C for 60 min.

FWHM could be calculated for 39/40 spectrums. For T7, a FWHM could only be calculated for 14/40 spectra. For T8, a FWHM could only be calculated for 4/40 spectra, and for T9, no FWHM's could be calculated. This phenomenon correlated with the increasing asymmetry of the plasmon peaks as films transitioned from individual nanoparticles to nanostructured films, shown in **Figure II.2**. This increasing asymmetry was beneficial for maximizing surface enhancement due to greater plasmon resonance across the fingerprint region.

Analyses of individual plasmon characteristics indicated that the film thickness required to produce maximal surface enhancement would optimize the balance among plasmon extinction intensity, peak proximity to the laser line, and extinction intensity across the fingerprint region. Because these plasmon extinction characteristics interact in non-obvious ways to influence the overall Raman spectra enhancement, SERS spectra of CV adsorbed onto the Ag films were acquired and shown in **Figure II.4(a)** to characterize the role of film thickness on surface enhancement. CV possesses multiple strong Raman peaks, tabulated in **Table A.1** with their associated vibrational modes, across a large portion of the fingerprint region,<sup>144</sup> Very little enhancement was observed for T1 – T4, with the T4 film resulting in less than 5-fold



enhancement across the fingerprint region as compared to the T0 spectrum. This inconsequential enhancement likely resulted from a combination of low plasmon intensity (**Figure II.3(a)**), inefficient coupling between the plasmon peak and the laser line (**Figure II.3(b)**), and insufficient peak breadth to enhance wave-shifted light across the fingerprint region. However, enhancement notably increased starting at T5, with up to 15.8-fold enhancement as compared to the T0 spectrum at  $1592\text{ cm}^{-1}$ . Maximal enhancement was found to occur for the T7 film, with up to 25.7-fold enhancement across the fingerprint region at  $1592\text{ cm}^{-1}$ , before decreasing with T8 and T9 films. The diminished enhancement for the thickest Ag films is correlated with an increasing departure from the laser line due to red-shifting peak plasmon extinction (**Figure II.3(b)**) accompanied by decreasing rate of plasmon extinction intensification (**Figure II.3(a)**). These results are non-obvious when assessing plasmon peak characteristics individually, illustrating the value in analyzing relationships between these characteristics in light of how they influence surface enhancement. These results demonstrate that film thicknesses of 5 nm or greater provide the best surface enhancement, peaking with 7 nm film thickness. Thus, continued analysis focused on thicker films of 5 nm and above.

### **Effect of Annealing on Surface-Enhanced Raman Spectroscopy**

Following the analysis of deposition thickness, substrates were annealed to explore the effect of annealing temperature and time on plasmon extinction characteristics, toward additionally maximizing surface enhancement. From Group A, 31 substrates from Group A were chosen for this analysis, with the remaining 9 held in reserve should they be needed. Of the 31 substrates, one was set aside as an unannealed control and the remaining 30 were annealed at five temperatures in the range of  $50 - 400\text{ }^{\circ}\text{C}$  for six anneal times in the range of  $15 - 150\text{ min}$ .

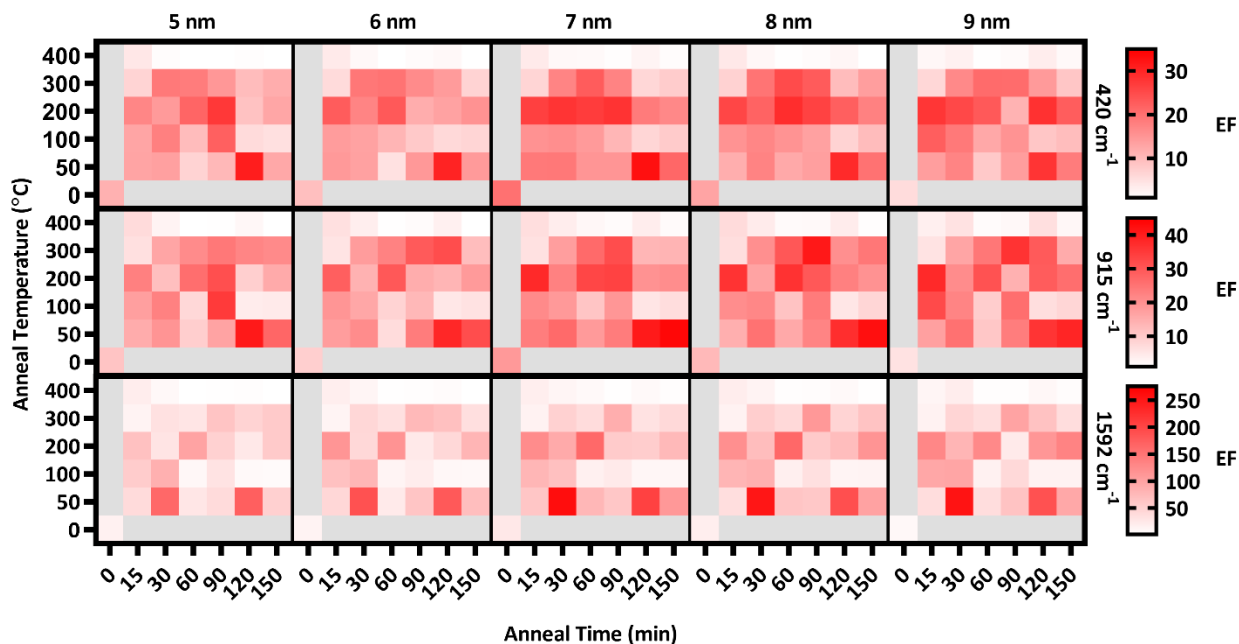


**Figure II.5:** Heat map of the enhancement factors of T5 – T9 for 420, 915, & 1592  $\text{cm}^{-1}$  peaks across all anneal temperatures & times along with the unannealed control.

Raman spectra were acquired of CV adsorbed onto Ag films after annealing, examples of which are presented in **Figure II.4(b,c)**. As with the pre-anneal spectra in **Figure II.4(a)**, film thicknesses of 5 – 9 nm provided the best surface enhancement for both annealed substrates presented in **Figure II.4(b,c)**, peaking at 7 nm. However, the difference in surface enhancement between 7 nm and 5 or 9 nm films is much less pronounced for the annealed substrates than the unannealed substrate. Thus, annealing can be used to obtain near-maximum surface enhancement over a range of film thicknesses. Such flexibility in deposition thickness may be especially useful for three-dimensional sensing substrates such as ZnO nanowires. In such cases, thicker films may over-fill interwire gaps, reducing effective surface area. Because maximal surface enhancement results in part from enhancement of Raman-scattered light across the fingerprint region, three CV peaks at 420, 915, and 1592  $\text{cm}^{-1}$  as identified in **Figure II.4(a)** were chosen to quantitatively assess enhancement at multiple points that span the fingerprint region. The enhancement of these peaks was calculated for T5 – T9 at each anneal temperature and time.

These enhancements appear as a heat map in **Figure II.5**, where red shading indicates increased enhancement. Annealing produced substantial impact to surface enhancement, but in ways that are nonlinear with respect to time and temperature. Annealing conditions generated changes to surface enhancements ranging from less than 3% to almost 3000% of the unannealed surface enhancement. Clearly, the selection of annealing parameters measurably impacts the performance of these sensors. **Figure II.5** reveals that annealing at 400 °C for even a short time drastically reduced surface enhancement across the board, indicating an upper temperature limit for this sensing paradigm well below 400 °C. Further examination of **Figure II.5** reveals that in general, the anneal time required to maximize surface enhancement decreased as anneal temperature increased. At 50 °C, maximizing enhancement required 120 min while at 100 °C, enhancement dropped off significantly after annealing 90 min. At 200 °C, enhancement was strongest when annealed from 15 – 60 min. Two of these anneal temperatures, 50 °C and 200 °C, produced particularly strong results toward maximizing surface enhancement, motivating closer examination.

Enhancement factors for the five film thicknesses were averaged for each anneal time at each temperature and plotted in **Figure II.6**. The relative strength of enhancement between the two anneal temperatures varies across the three CV peaks, indicating the necessity of investigating enhancement across the entire fingerprint region. For instance, annealing at 30 °C resulted in opposing enhancement trends for the two anneal temperatures. Relative enhancement decreased farther away from the laser wavelength when annealed at 200 °C while it increased away from the laser wavelength when annealed at 50 °C. Among this variability, two anneal times produced consistently strong surface enhancement at these temperatures: 60 min at 200 °C and 120 min at 50 °C.

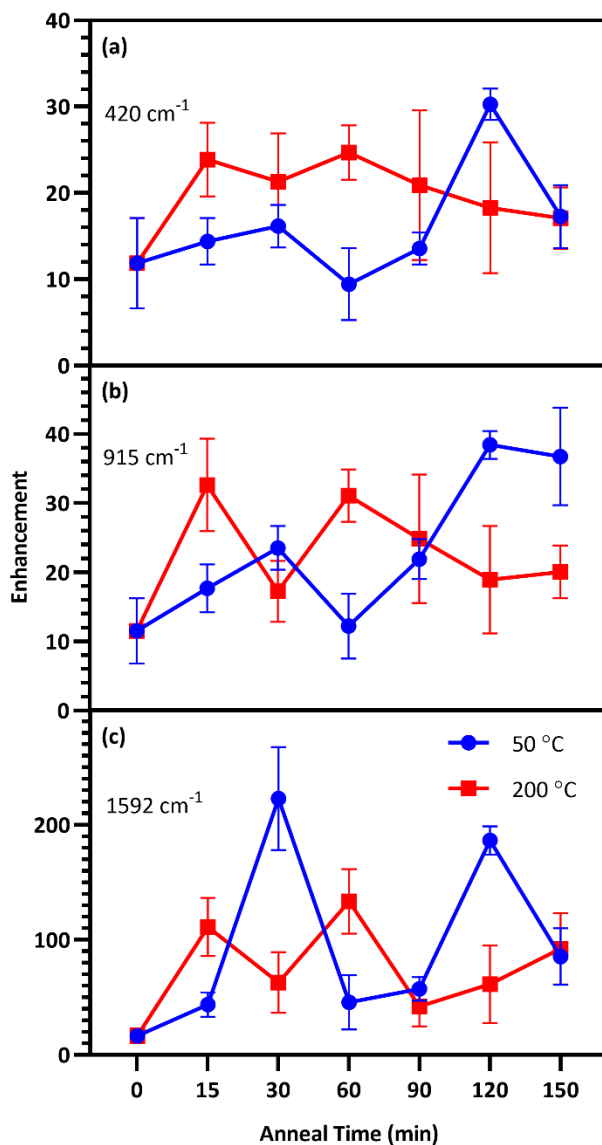


**Figure II.6:** SERS EFs of substrates annealed at 50 °C (blue) and 200 °C (red) for up to 150 min, along with the unannealed control for the (a) 420 cm<sup>-1</sup>, (b) 915 cm<sup>-1</sup>, and (c) 1592 cm<sup>-1</sup> peaks. Each point in the figure exhibits the mean and standard deviation of the EFs for T5 – T9.

This study seeks to not only describe the deposition and annealing parameters that result in maximal surface enhancement, but also relate these results to changes in plasmon extinction characteristics effected by those fabrication parameters. To this end, changes to plasmon extinction characteristics for all five effective film thicknesses (T5 – T9) due to annealing at 50 and 200 °C were plotted in **Figure II.7**. Annealing at 200 °C caused the plasmon intensity of all

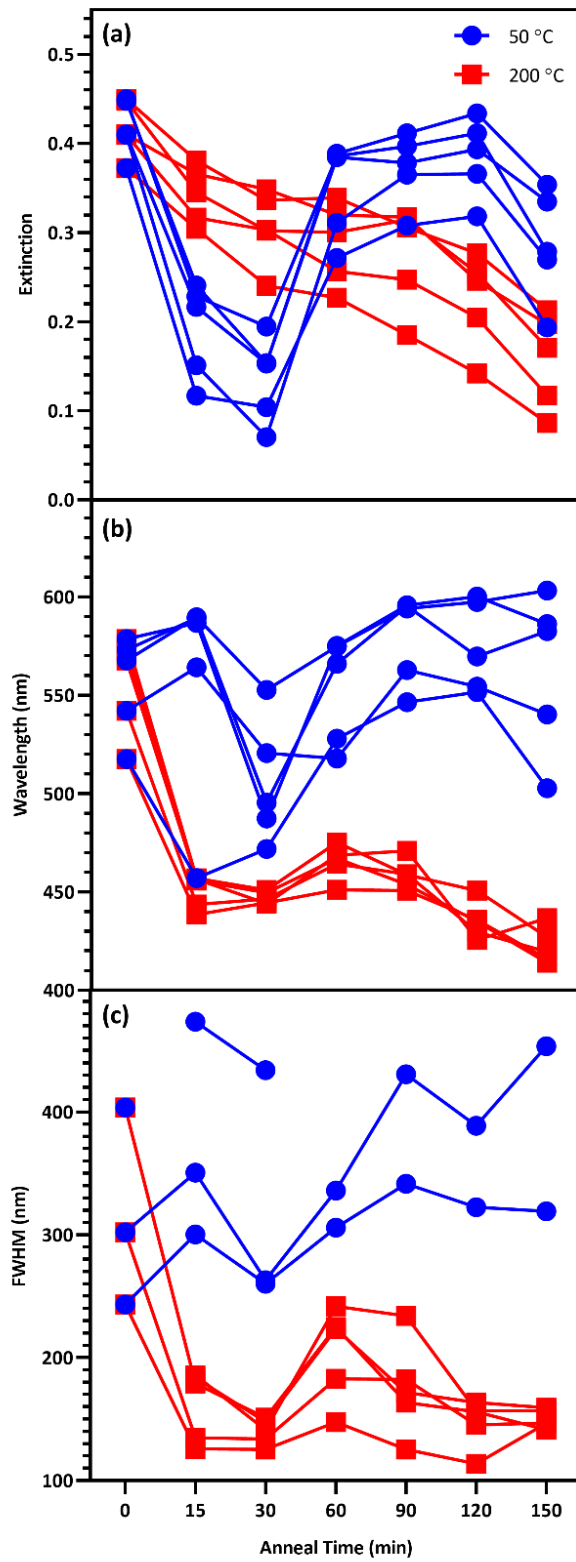


**Figure II.7:** Change to the plasmon peak (a)intensity, (b)wavelength, and (c)FWHM due to anneal time at 50 °C (blue) and 200 °C (red) for T5 – T9.

five film thicknesses to decrease steadily with increasing anneal time. In addition, annealing for 15 min or more at 200 °C blue-shifted the plasmon peaks. Annealing for 60 min slightly red-shifted the peaks, which blue-shifted again at higher anneal times (> 90 min). This blue-shifting behavior is consistent with increasing nanostructure uniformity due to Ostwald ripening, reducing the exotic nature of nanostructure shapes. FWHMs followed a similar behavior as peak wavelengths, with a short anneal time narrowing the plasmon peaks. These plasmon peaks widened slightly when annealed for 60 min before narrowing again beyond 90 min. These observations agree with the results in **Figure II.6**, indicating that annealing at 200 °C generated the best combination of plasmon intensity, peak wavelength, and peak width at 60 min of anneal time.

Annealing at 50 °C for less than 60 min reduced peak intensity that rebounded for anneal times of 60 – 120 min. Peak wavelength blue-shifted slightly following annealing for less than 60 min at 50 °C before subsequent red-shifting for annealing times of 60 – 120 min. FWHMs for 5- and 6-nm films were increased with increasing anneal time. These results agree with the results in **Figure II.6** that indicate an optimum anneal time of 120 min at 50 °C. We anticipate that deposition and dewetting kinetics differ between the ZnO films used in this work and ZnO nanowires often utilized in 3D SERS substrates. However, this work expedites future nanoparticle optimization by narrowing the window of parameters values to explore in future works involving ZnO nanowires.

### **Effect of Deposition Rate on Surface Enhanced Raman Spectroscopy**

Deposition rate had a significant impact on plasmon peak wavelengths, with films deposited at 0.3 Å/s exhibiting significantly red-shifted peaks compared to a deposition rate of

0.1 Å/s for each film thickness examined, excepting 7 nm, as shown in **Figure A.5(b)**. We hypothesize that this behavior can be explained by rate-induced differences in the crystal structure of Ag nanoparticles, as deposition rate has been shown to effect such crystal properties as grain size, dislocation density, and twin boundary density in metallic nanostructures.<sup>134</sup> These results suggest that the plasmon characteristics of e-beam deposited Ag films are sensitive to deposition rates, as small changes can have a significant impact on important physical characteristics of the nanoparticles. These results also clearly indicate the trade-off between degraded sensor performance and the reduced deposition time achieved at elevated deposition rate.

While there was no significant difference in terms of enhancement in the unannealed controls between Groups A (0.1 Å/s) and B (0.3 Å/s), **Figure A.6** demonstrates that annealing the substrates in Group A generally produced more surface enhancement than Group B, across all film thicknesses, and anneal temperatures/times. This suggests that rate-induced differences in the crystal structure of Ag nanoparticles impacts annealing-induced effects on surface enhancement. This observation further emphasizes the important impact of deposition rate on the physical characteristics of Ag nanoparticles and the resulting surface enhancement of the structure.

Several combinations of fabrication and anneal parameters maximize surface enhancement by optimizing plasmon extinction. This study substantially improves the potential for fabricating high-performance sensors through elimination of fabrication parameters that yield low-enhancement materials. Importantly, these results demonstrate that maximal surface enhancement can be achieved by multiple different fabrication strategies. For instance, 2D sensing surfaces where film thickness does not impact device function have the best

enhancement with a 7 nm thick surface deposited at 0.1 Å/s and annealed at 200 °C for 60 min. However, for 3D sensing surfaces such as the ZnO nanowire-based structure described in our previous work,<sup>118</sup> a thicker sensing surface could reduce device functionality by over-filling the spaces between nanowires, thereby reducing effective surface area. In such cases, a film approximately 5 nm thick, deposited at 0.1 Å/s and annealed at 200 °C for an hour is predicted to provide near-maximal surface enhancement without sacrificing sensing surface area. Another consideration is the substrate on which such nanostructures are fabricated. Many sensing strategies utilize substrates with high melting points such as glass or fused silica. In such cases, annealing at 200 °C is not problematic. However, increasing attention has been devoted in recent years toward fabricating SERS-active structures on flexible substrates made of materials like polyvinyl alcohol (PVA),<sup>145,146</sup> poly(dimethylsiloxane) (PDMS),<sup>147</sup> or polyvinylidene fluoride (PVDF).<sup>148</sup> In such cases substrates, even temperatures as low as 100 °C can have an undesirable effect on the substrate itself, such as increasing brittleness. For such device designs, excellent surface enhancement can be achieved by annealing substrates at 50 °C for 120 min.

## CONCLUSIONS

This study provides guidance for the fabrication of sensors with maximal SERS enhancement excited with a 532-nm laser through e-beam deposited Ag nanoparticles on ZnO. 7-nm Ag films possess the optimal combination of plasmon peak intensity, wavelength, and breadth for maximal surface enhancement with a 532-nm laser. When 7-nm films are untenable, films as thin as 5 nm still provide near-maximal surface enhancement. We demonstrated that annealing at temperatures up to 200 °C for one to two hours further improved surface enhancement, but annealing at 200 °C for one hour or 50 °C for two hours resulted in the greatest



increase to surface enhancement. Lastly, we discovered that Ag deposition rate significantly influences surface plasmon extinction peak characteristics. Increasing deposition rate from 0.1 to 0.3 Å/s resulted in decreased surface enhancement at all anneal times and temperatures, making 0.1 Å/s the clearly preferable deposition rate. The results presented in this study fill a vital need for guidance in determining fabrication and annealing parameters for maximal SERS with e-beam deposited Ag nanoparticles with a 532-nm laser. We presume that similar fabrication relationships control the performance of other SERS substrates based on metal nanoparticles. This is the first report to begin to explore the impact of fabrication choices on the performance of a specific SERS sensor, but lays the groundwork for the assessment of similar phenomena in other Raman sensing approaches.

## CHAPTER III

### A FACILE METHOD TO FABRICATE SILVER-DECORATED ZINC OXIDE NANOWIRES INSIDE MICROFLUIDIC CHANNELS FOR SURFACE ENHANCED RAMAN SPECTROSCOPY

#### ABSTRACT

Surface-enhanced Raman spectroscopy (SERS) performed in microfluidic technology offers multiple benefits to sensitive and reliable detection of dilute analytes. Physical deposition of metallic nanoparticles by techniques such as electron beam deposition result in dense populations of nanoparticles and hotspots between nanoparticles for sensitive detection, but complicate channel fabrication. This work demonstrated a simplified approach to physical fabrication of a SERS-active substrates inside a poly(dimethylsiloxane) (PDMS) microfluidic channel. Direct growth of zinc oxide nanowires on the inner PDMS wall and e-beam deposition of silver to coat the nanowires, before bonding to glass, allowed for label-free SERS sensing of analytes within a fluid through a thin PDMS wall, as successfully demonstrated for micromolar concentrations of crystal violet and melamine with minimal spectral interference from the PDMS-based channel.

#### INTRODUCTION

Surface-enhanced Raman spectroscopy (SERS) integrated with microfluidic technology offers reduced sample consumption and reaction time, high detection efficiency, and portability as compared to state-of-the-art detection paradigms.<sup>149</sup> This integration is primarily pursued through either colloidal solutions<sup>72,150</sup> or stationary substrates.<sup>151–153</sup> Injection of SERS-active colloids can provide efficient sensing and heat-dissipation, although this technique often suffers

from random aggregation, resulting in reduced reproducibility and poor mixing due to predominantly laminar flow in microfluidic channels.<sup>154</sup> Stationary substrates offer greater stability and reproducibility, although they are often less efficient than colloidal strategies because stationary substrates cannot be dispersed within sample fluids.<sup>50,71</sup>

SERS-active substrates based on nanowires decorated with metal nanoparticles such as silver (Ag) or gold (Au), can minimize the drawbacks associated with both strategies described above when fabricated within a microfluidic channel. They offer stability and reproducibility similar to stationary substrates, but can also offer the sensing efficiency of colloidal strategies due to their inherent 3-dimensional architecture.<sup>118,120</sup> Metal-decorated zinc oxide (ZnO) nanowires are an attractive platform for SERS sensing. ZnO is a biocompatible<sup>125</sup> wide direct-bandgap semiconductor with a band-edge emission of 3.3 eV and a high exciton binding energy of 60 meV,<sup>74,126</sup> making ZnO nanowires electronically stable at room temperature.<sup>74</sup> In addition, ZnO has been demonstrated to increase surface enhancement due to charge transfer between ZnO and Ag.<sup>127</sup> ZnO nanowires are also transparent to visible light,<sup>128</sup> allowing propagation of light through the wires. This is ideal for Raman spectra acquired through the substrate as is necessitated by microfluidic technology. Additionally, ZnO possesses high electron mobility<sup>155</sup> and a large refractive index of approximately 2.0 in the visible region.<sup>129,130</sup> Combining these characteristics with the atomically smooth and highly faceted hexagonal single-crystal structure of ZnO nanowires can reduce signal loss to scattering through waveguiding light.<sup>75</sup>

During the fabrication of SERS-active microchannels, stationary substrates such as the Ag-decorated ZnO nanowires are During the fabrication of SERS-active microchannels, stationary substrates such as the Ag-decorated ZnO nanowires are usually fabricated on the glass wall of the channel. This is done to avoid spectroscopic interference by commonly used

polymers such as poly(dimethylsiloxane) (PDMS), which has its own strong Raman spectrum. ZnO nanowire fabrication on glass lends itself to *in situ* fabrication techniques like hydrothermal growth and electroplating after microchannel fabrication. In particular, metal-decorated ZnO nanowires can be easily fabricated *in situ* hydrothermally,<sup>156–158</sup> however hydrothermal fabrication typically results in sparse metal nanoparticle formation.<sup>156</sup> In contrast, electron beam (e-beam) deposition as a physical technique forms denser nanoparticle distributions,<sup>75,118</sup> resulting in higher surface enhancement due to proximity-induced hotspots between nanoparticles.<sup>159</sup> However, one major drawback is that physical deposition of nanoparticles necessitates *ex-situ* SERS substrate fabrication on glass, prior to microfluidic channel bonding. Thus, requiring additional fabrication steps such as the careful alignment of the PDMS microchannel with the glass to ensure proper positioning of SERS substrates. Additional alignment steps limit flexibility of microchannel design,<sup>154</sup> making it less ideal for the production of large numbers of disposable sensors. Fabricating SERS substrates directly into PDMS microchannels before bonding with glass as illustrated by **Figure III.1** eliminates the need to align glass with the PDMS microchannel during bonding, simplifying the microchannel fabrication process and facilitating production of sensitive SERS-based microfluidic sensing devices.

In this study, we demonstrated that a ZnO nanowire substrate decorated with e-beam deposited Ag nanoparticles can be simply fabricated within a PDMS microchannel *ex-situ* without requiring an alignment step to complete microchannel fabrication. Furthermore, we demonstrated that trace chemical and biological analytes can be detected through a PDMS microchannel wall through careful optimization of device design and analysis of SERS optical signals.

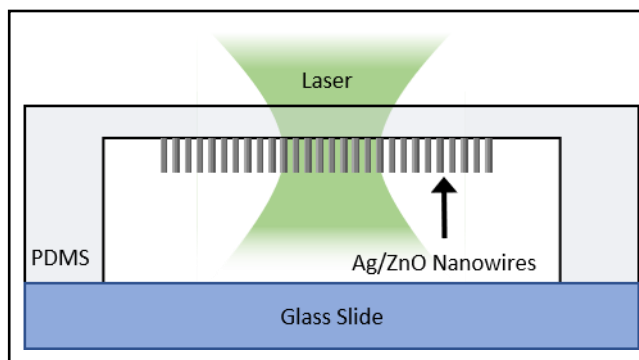


**Figure III.1:** Illustration of the cross-section of a microchannel integrated with an Ag/ZnO nanoprobe fabricated on the PDMS.

In this study, we demonstrate that a ZnO nanowire substrate decorated with e-beam deposited Ag nanoparticles can be simply fabricated within a PDMS microchannel *ex-situ* without requiring an alignment step to complete microchannel fabrication. Furthermore, we demonstrate that trace chemical and biological analytes can be detected through a PDMS microchannel wall through careful optimization of device design and analysis of SERS optical signals.

## EXPERIMENTAL

Physical deposition of silver on ZnO nanowires were performed using the e-beam deposition parameters identified in our previous work.<sup>91</sup> First ZnO seeds were deposited on PDMS substrates and channels prior to nanowire growth and Ag e-beam deposition as described below.

### Zinc Oxide Seed in PDMS Channel

SERS-active nanostructures were fabricated directly into the channel, such that they would reside on the roof of the channel as shown in **Figure III.1**. Like PDMS substrates, microchannels were fabricated from PDMS via soft lithography with Sylgard 184® (Dow

Corning, Batch #H047ICL055) which consists of a liquid PDMS base and a curing agent. A microchannel master was designed in AutoCAD® 2017 as a mold for PDMS microchannels and machined from aluminum. The base and curing agent were mixed at a 10:1 ratio and poured over the base. After which, the solution was placed in a vacuum chamber at ~25 mmHg until all bubbles were removed from the solution. The lid was fitted onto the base before the dish was placed in the oven at 90 °C for two hours to cure the PDMS, after which the dishes were removed and allowed to cool at room temperature. After cooling, the master was cut away from the surrounding PDMS and the microchannels were extracted.

PDMS microchannels were cleaned with the ALD-AMD method<sup>118</sup> which consists of submerging it in a 1% Alconox® solution, deionized (DI) water, acetone methanol, and DI water, sequentially. At each step, the substrates were sonicated for 10 minutes. After this cleaning process was completed, the substrates were dried using nitrogen gas. For each microchannel, Kapton tape was used to mask the PDMS surface containing the channel so that only the channel was exposed. Microchannels were then mounted in a sputter deposition system (Angstrom Amod Multimode Deposition Chamber) and ZnO was deposited in the channel. ZnO was sputtered to ensure ZnO deposition on all sides of the channel, thereby preventing the hydrophobicity of PDMS from impacting hydrothermal nanowire growth. The channels were annealed at 100 °C overnight to improve ZnO seed surface morphology to improve nanowire growth.

### **Zinc Oxide Seed on PDMS Substrates**

PDMS substrates were fabricated for two purposes in this work. Firstly, it was necessary to explore the effect of PDMS thickness on the Raman surface enhancement in order to inform

the design of the PDMS channel used in this work. Secondly, thin PDMS substrates were fabricated to demonstrate effective SERS of melamine through PDMS. These substrates were designed to mimic the thickness of the PDMS channel wall through which spectra of crystal violet were acquired.

To explore the effect of PDMS thickness on Raman surface enhancement, bare ZnO nanowires and Ag nanoparticle-decorated ZnO (Ag/ZnO) nanowires were fabricated on thick and thin PDMS substrates, measured after fabrication to be ~1.0 mm and ~0.17 mm thick, respectively. The PDMS substrates were fabricated via soft lithography with Sylgard 184®. Two different volumes of PDMS were poured into petri dishes to obtain thick and thin substrates. The dishes were placed in an oven. The PDMS was cut into squares of approximately 1 cm x 1 cm. The substrates were cleaned via the ALD-AMD method.<sup>118</sup> Cleaned substrates were mounted in an e-beam deposition chamber. The chamber was pumped down to a vacuum of  $5 \times 10^{-6}$  Torr and a 100 nm ZnO seed layer was deposited at a rate of ~0.1 Å/second. PDMS substrates were mounted in a plan configuration throughout ZnO deposition.

For each PDMS substrate thickness, Raman spectra of crystal violet were acquired through Ag/ZnO and bare ZnO nanowires, to compare SERS and non-SERS spectra. From these spectra enhancement factors were calculated as described in our previous work.<sup>118</sup> Crystal violet was chosen for this purpose to facilitate detection due to its multiple strong Raman peaks where the PDMS Raman signal is weak. Based on the results acquired by this interaction study, a microchannel master was designed to minimize PDMS influence upon SERS detection of analytes. With this master, microchannels were fabricated with soft lithography and Ag/ZnO nanowires were fabricated inside the microchannel. Comparative studies were performed

between SERS and non-SERS spectra for crystal violet to assess enhancement of crystal violet's Raman signal.

To demonstrate SERS through PDMS, substrates were fabricated with controlled thickness by pouring PDMS between two glass slides with a single layer of 0.15-mm thick carbon tape as a spacer. The same soft lithography process was followed as for channels, and a ZnO seed was deposited via e-beam as discussed above.

There was also concern that the ALD-AMD cleaning method would change the Raman spectrum of the PDMS by introducing solvents into the PDMS. Curling of the substrates was observed after the cleaning process due to the presence of acetone and methanol. To address this concern, nine Raman spectra were acquired of a single PDMS substrate before cleaning and averaged. After cleaning, Raman spectra were acquired at the same locations as before and averaged

### **Zinc Oxide Nanowire Growth**

The ZnO nanowire growth process is similar to that described in previous work.<sup>160</sup> ZnO nanowires were grown hydrothermally. PDMS channels and substrates were submerged in a 20 mM equimolar solution of zinc acetate dihydrate (Sigma Aldrich, BCBM3068V) and hexamethylenetetramine (Sigma Aldrich, MKBS8102V) in a Teflon reaction chamber. This chamber was placed in a preheated oven at 95 °C for 2.5 hours, after which the chamber was rapidly cooled under running water. The channels and substrates were washed of residual organics with DI water, then placed in the oven at 105 °C for ~10 minutes to dry. Nanowires were grown only where seed layer was deposited.



## Ag Nanoparticle Fabrication

ZnO nanowires on PDMS substrates were decorated with Ag nanoparticles via e-beam deposition (Thermionics, 150-0040) as shown in **Figure B.1**. The nanowire substrates were mounted on a glancing-angle deposition apparatus, which rotates azimuthally at an angle during deposition. This angle was calculated by **Equation (III.1)** to maximize the area of nanowire sides exposed to deposition while minimizing shadowing from adjacent nanowires.  $L_n$  and  $D_n$ , which are average nanowire length and spacing, were estimated to be 320 and 76 nm, respectively. From these, an angle of  $\theta_{dep} = \sim 13^\circ$  was calculated. The deposition chamber was depressurized to  $\sim 5.0 \times 10^{-6}$ , at which point Ag was deposited at a rate of  $\sim 0.1 \text{ \AA/s}$  to a nominal film thickness of 10 nm while the stage was rotated. This resulted in an effective film thickness  $\sim 2.2$  nm on the sides of the nanowires as calculated by **Equation (III.2)**, where  $t_{nom}$  represents the nominal film thickness and  $\theta_{dep}$  represents the angle of deposition specified above.

$$\theta_{dep} = \text{TAN}^{-1} \left( \frac{D_n}{L_n} \right) \quad \text{(III.1)}$$

$$t_{eff} = t_{nom} \sin(\theta_{dep}) \quad \text{(III.2)}$$

Due to equipment failures, Ag nanoparticles were deposited in PDMS channels via e-beam deposition (Angstrom Amod Multimode Deposition System) as shown in **Figure B.2**. The nanowire substrates were mounted with a Kapton-tape mask such that only the channel was exposed on a stage at an angle of approximately  $24^\circ$  from the source crucible. The chamber was pumped to a pressure of  $\sim 4.0 \times 10^{-6}$  Torr. Ag was deposited at a rate of  $\sim 0.1 \text{ \AA/s}$  to a nominal film thickness of 15 nm while the stage was rotated. This resulted in an effective film thickness ( $t_{eff}$ ) of  $\sim 6.1$  nm. This effective film thickness is within the range of 5 – 9 nm film thickness demonstrated in our previous work<sup>91</sup> to maximize SERS acquired with a 532-nm laser. The mask was designed to allow Ag deposition only inside the channel. After deposition, the microchannel

was heated to 50 °C for 2 hours to anneal the nanoparticles, which was shown in Chapter II to greatly increase surface enhancement.

### **Microfluidic Chip Fabrication**

After fabrication of Ag-decorated ZnO nanowires inside the microchannels, holes were punched at the inlet and outlet with a 2-mm disposable biopsy punch (Premier® Uni-Punch®) and they were placed in a plasma oxidation chamber (Harrick Plasma PDC-001) for 4 minutes to oxidize the PDMS surface. This enabled bonding to a glass slide (Fisherbrand® 12-550-A3). Lastly, Tygon® tubing (ID: 0.020 in.; OD: 0.060 in.) was inserted at the inlet and outlet and PDMS was used to seal the interface between PDMS and tubing.

### **Characterization Techniques**

Scanning electron microscopy images of bare and Ag-decorated ZnO nanowires were acquired with a Zeiss Merlin scanning electron microscope (Jena, Germany) in both plan and 45° configurations. These images were used to visually inspect nanowire and nanoparticle morphology. All image analysis was performed using ImageJ.

Photoluminescence (PL) spectra of ZnO nanowires were acquired to assess nanowire crystallinity using a thermoelectrically cooled (-40 °C) CCD camera in a spectroscopy setup (HORIBA Jobin Yvon LabRAM 800HR). ZnO nanowire emissions were excited using a 325-nm He-Cd laser (Kimmon, 1 K series 200 mW, vertically polarized output measured at the laser head). PL spectra were acquired with a 15×-magnification objective lens (Thorlabs, LMU-15×-NUV, NA = 0.32), and detected in line with the laser normal to the substrate surface. Nanowires were oriented facing incident light. Five locations on each patch of nanowires were chosen, with

a precision of 100  $\mu\text{m}$ . At each location, a PL spectrum was acquired over a wavelength range of 340-700 nm. Each spectrum was the accumulation of 4 background-subtracted spectra, each taken with a 200- $\mu\text{m}$  aperture, and a 600 grooves/mm grating. Exposure time was 0.1 seconds and laser power was between 4.0 – 5.0 mW, as measured at the lens. The five spectra for each patch were averaged to produce a representative PL spectrum for each patch of nanowires within the channel.

Raman spectra of crystal violet within the channel were acquired using a CCD camera on the same spectroscopy setup as the PL measurements with a 532-nm laser (Ventus, 500 mW, horizontally polarized output measured at the laser head) and a 100x-magnification lens (Olympus, MPlan N Achromat, NA = 0.90). Raman scattering was collected in line with the laser normal to the substrate surface. 25- $\mu\text{M}$  crystal violet solution was syringed through the channel and Raman spectra were acquired through the PDMS channel wall at both patches of nanowires. Raman spectra were acquired in a range of 100 – 1800  $\text{cm}^{-1}$ . Each Raman spectrum was the accumulation of 4 background-subtracted spectra, each taken with a 60 second exposure time, a 50- $\mu\text{m}$  slit aperture, and 900 grooves/mm grating. Laser power was 10 mW, as measured at the objective. Raman spectra background were subtracted using a 5<sup>th</sup> order polynomial and smoothed with a Savitzky-Golay filter. Raman spectra of melamine were acquired using a CCD camera in a spectroscopy instrument (HORIBA Jobin Yvon LabRAM 800HR) and a 532-nm laser (Ventus, 500 mW, horizontally polarized output measured at the laser head) with a 10 $\times$  magnification lens (Olympus, MPlan N Achromat, NA = 0.25). Raman scattering was detected in line with the laser normal to the surface of the sample. ZnO nanowire samples were oriented face down in a reservoir of a melamine solutions, with the nanowires facing away from incoming laser light. Raman spectra used to quantify SERS were acquired in a range of 200– 1800  $\text{cm}^{-1}$  for

two Ag-decorated ZnO nanowire substrates deposited on 150  $\mu\text{m}$ -thick PDMS, hereafter referred to as S1 and S2. Each Raman spectrum acquired through S1 was the accumulation of four background-subtracted spectra, each taken with a 10-s exposure time. Each Raman spectrum acquired through S2, was the accumulation of 8 background-subtracted spectra, each taken with a 1-s exposure time. All Raman spectra of melamine were acquired with a 200- $\mu\text{m}$  aperture, and a 600-grooves/mm grating. Laser power was 5 mW, measured at the turret. Raman spectra background was subtracted using an asymmetric least squares method, and smoothed with a Savitzky-Golay filter. All crystal violet and melamine spectra were intensity normalized with the PDMS Raman peak at 488  $\text{cm}^{-1}$ .

To characterize the plasmonic properties of Ag nanoparticles, ultraviolet-visible-near infrared (UV-vis-NIR) extinction spectra were acquired using a Hitachi U-4100 spectrophotometer with an integrating sphere. Extinction spectra were acquired at a rate of 300 nm/min over a range of 350 – 850 nm, with the nanowire substrate oriented facing oncoming light.

## RESULTS & DISCUSSION

### **Effect of Cleaning on PDMS Raman Spectrum**

Because SERS-active nanostructures are fabricated on a PDMS surface of the microchannel, SERS will be performed through that PDMS wall. This necessitates exploration of how the thickness of that PDMS wall affect spectral intensity of analytes within the channel. For this reason, PDMS substrates of two different thicknesses were fabricated via soft lithography. These were measured to be  $\sim 1.0$  mm and  $\sim 0.17$  mm via stylus profilometry (Bruker Dektak 150).

On these substrates, bare and Ag-decorated ZnO nanowires were deposited using the same growth and deposition parameters. Before nanostructure fabrication, these substrates were cleaned via the ALD-AMD method. A comparison of the Raman spectra acquired of PDMS before and after cleaning showed no change to the Raman spectra, shown in **Figure B.3**. Thus, the cleaning process demonstrably did not affect the Raman spectrum of PDMS.

### **ZnO Nanowire Characterization**

To be suitable as a platform for SERS enhancements, ZnO nanowires must possess two characteristics: 1) the nanowires must be high quality, which means they grow as single crystals with little to no defects, and 2) Ag/ZnO nanowires must possess uniform dimensional and structural properties, such as crystallinity. SEM images of nanowires after growth (**Figure B.4**) show a dense bed of hexagonal nanowires, indicating single-crystallinity. A visual comparison of nanowires to remain bare and those to be decorated with Ag in **Figure B.5** revealed no difference in the dimensionality or structure of the nanowires, providing validation for the quantification of SERS enhancements. Furthermore, SEM images revealed nanowires that are neither short and stubby nor so long and thin as to induce nesting. Stubbiness would reduce the surface area available for nanoparticles, negating one of the primary advantages of this 3D architecture. Nesting would introduce shadowing during nanoparticle deposition, reducing nanoparticle coverage.

PL spectroscopy was used to assess the crystallinity of the ZnO nanowires. ZnO is a direct bandgap semiconductor with a band-edge emission of  $\sim 3.4$  eV at room temperature,<sup>161</sup> which means that PL spectra of crystalline ZnO nanowires will have a sharp band-edge emission peak around 380 nm. Any native point defects within the crystalline structure, such as vacancies

(missing atoms at regular lattice locations), interstitials (extra atoms occupying lattice interstices), or antisites (atoms occupying a lattice site where it doesn't belong) introduce transition levels within the bandgap which induce emissions at wavelengths in the visible region.<sup>162</sup> This defect emission is very broad compared to the band-edge emission, and the intensity of defect emission relative to band-edge emission is an indicator of the crystallinity of the sample. Thus, the ratio of band-edge to defect emission in ZnO nanowires is an indicator of the nanowires' crystallinity. PL spectra of the nanowires in **Figure B.6** exhibit very little defect emission and very strong band-edge emission, providing further evidence of high crystallinity with few defects. A comparison of the PL spectra for nanowires to remain bare and those to be decorated with nanoparticles revealed little variation, which enables high confidence in the comparison of non-SERS to SERS spectra.

To explore the possibility of patterning ZnO nanowire growth by patterning ZnO seed layer deposition, a partially shielded PDMS substrate was deposited with a 100-nm seed layer, on which nanowires were hydrothermally grown. UV-Vis-NIR spectra of the seeded and non-seeded portions of the substrate (**Figure B.7**) indicated nanowire growth on the seeded portion of the substrate and negligible nanostructure formation on the unseeded portion.

### **Ag Nanoparticle Deposition Characterization**

ImageJ analysis of the SEM images of bare nanowires grown on PDMS substrates revealed an approximate nanowire height of 320 nm and approximate interwire spacing of 76 nm. Plugging these values into **Equation (III.4)** resulted in a Ag deposition angle of  $\sim 13^\circ$ . SEM image of the nanowires after nanoparticle deposition revealed a dense population of resulted in an Ag deposition angle of  $\sim 13^\circ$ . SEM image of the nanowires after nanoparticle deposition

revealed a dense population of nanoparticles on the nanowire sides (**Figure B.5**). UV-Vis-NIR extinction spectra of Ag/ZnO nanowires before and after Ag deposition revealed a plasmon absorption peak centered at ~450 nm (**Figure B.8**).

### Effect of PDMS Thickness on Surface Enhancement

To quantify SERS, Raman spectra were acquired of a 25- $\mu$ M solution of crystal violet in DI water through both bare ZnO nanowires and Ag/ZnO nanowires for both PDMS thicknesses. These spectra are shown in **Figure III.2**. Crystal violet has several strong Raman bands in the fingerprint region of its Raman spectra. While PDMS has several strong Raman peaks, crystal violet has many Raman peaks that can be decoupled from the PDMS background (see **Figure B.3**). Furthermore, plasmonic nanoparticles used for SERS are separated from

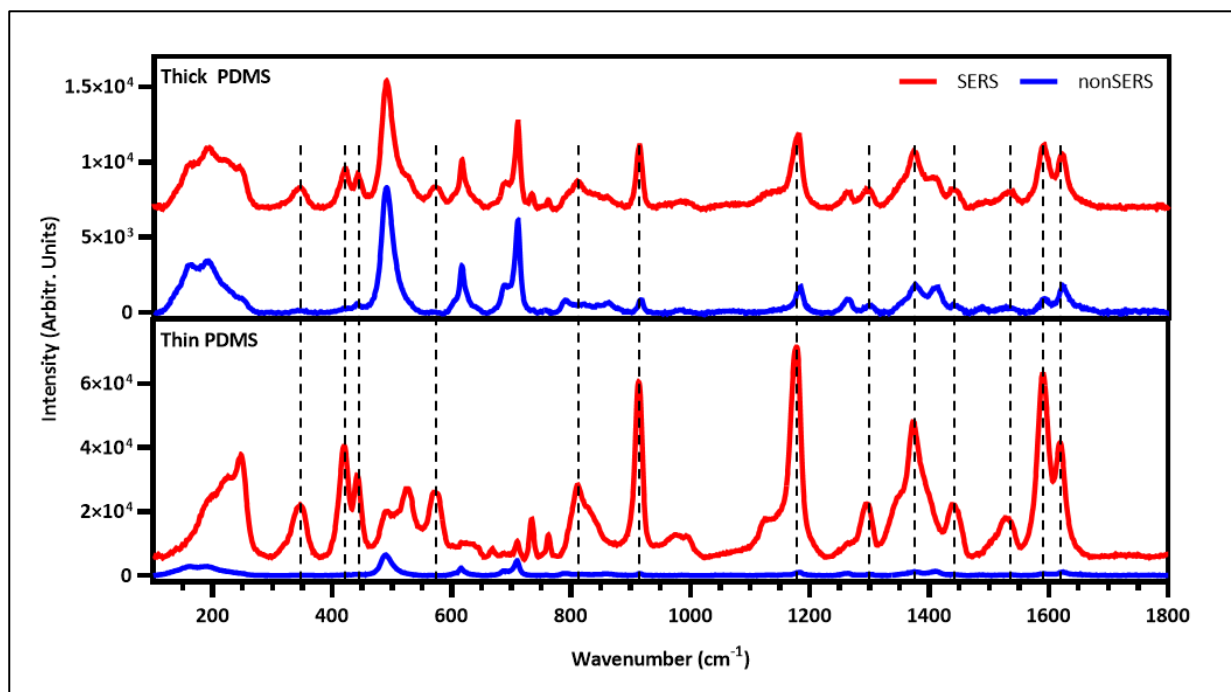


**Figure III.2:** SERS (blue) and non-SERS (grey) Raman spectra of crystal violet through (a) thick and (b) thin PDMS, demonstrating the ability to perform SERS spectroscopy through a PDMS wall, as well as the importance of PDMS thickness on the magnitude of enhancement.

PDMS by a 100-nm ZnO layer, which is more than enough to ensure that the PDMS Raman contributions do not experience significant surface enhancements. Enhancement was quantified for 13 individual crystal violet Raman peaks distinguishable from the PDMS background in non-SERS spectra, tabulated with their raw enhancement through thick and thin PDMS in **Table III.1**. Raw enhancement, simply the difference in peak intensity between SERS and non-SERS spectra, ranged from an average of 2.2-fold for spectra taken through thick (~1 mm) PDMS to an average of 130-fold for spectra taken through ~0.17-mm thick PDMS, as shown in **Figure III.3**, demonstrating the impact that PDMS thickness has on the magnitude of enhancement observed. The thinner the PDMS, the greater is the enhancement to the analyte's Raman spectrum. Thus, it is vital to control the PDMS wall thickness through which analysis is performed.

**Table III.1:** Crystal violet Raman peaks used to compare surface enhancement through thick vs. thin PDMS.

Raman Band (cm <sup>-1</sup> )	Thick (~1.0 mm)	Thin (~0.17 mm)
345	2.81	300.17
420	3.63	284.76
441	2.45	74.34
571	2.41	292.79
810	2.17	86.42
915	2.42	111.04
1175	2.47	58.87
1300	1.57	80.21
1374	1.91	43.04
1445	1.55	84.25
1529	1.26	129.17
1592	2.25	116.60
1621	1.95	35.34



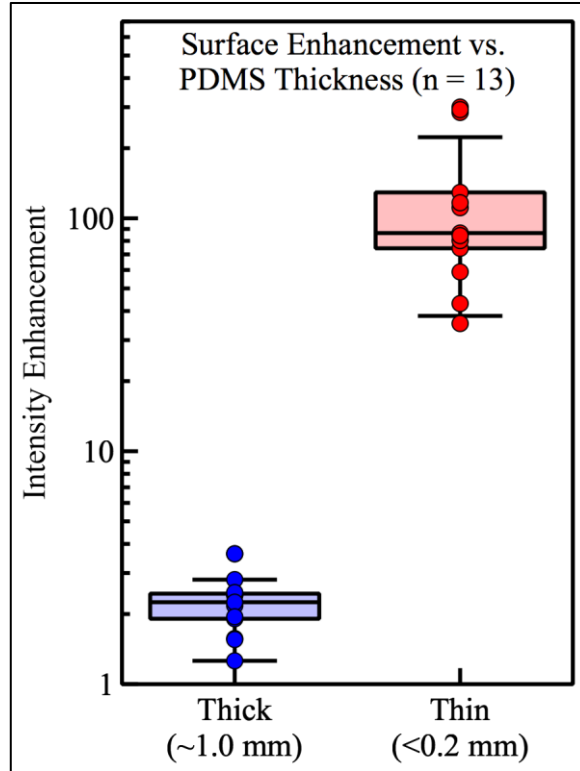


**Figure III.3:** Comparison of the enhancement to selected crystal violet Raman peaks through thick and thin PDMS.

A more detailed understanding of the SERS enhancement to the Raman spectra of crystal violet considers the confocal volume of the spectrometer relative to the volume of crystal violet being influenced by SERS. The volume of crystal violet solution being sensed by the laser was orders of magnitude greater than the volume of crystal violet solution sufficiently close to the sensing surfaces to be influenced by SERS, as discussed in previous work.<sup>118</sup> The volume of crystal violet solution being sensed by the spectrometer can be approximated as a cylinder with a diameter equivalent to the laser waist and length equivalent to the confocal range. The beam waist radius was determined to be approximately  $d_w = 12 \mu\text{m}$  via the knife-edge method.<sup>160,163</sup> This was used to calculate the laser's confocal length  $L_c$  via **Equation (III.3)**.<sup>160,164</sup> This, in turn, was used to calculate the ratio of confocal volume to SERS-influenced volume, defined here as the enhancement factor ( $EF$ ), via **Equation (III.4)**.

$$L_c = \frac{2\pi(d_w)^2}{\frac{\lambda}{10^3}} \quad (\text{III.3})$$

$$EF = \frac{E_I}{2 \frac{L_n}{L_c} \pi D (d_n d_m + d_m^2)} \quad (\text{III.4})$$

In these equations,  $\lambda$  is the 532-nm laser wavelength,  $E_I$  is the raw enhancement for each peak,  $d_n$  is the average nanowire diameter (nm),  $D$  is the average nanowire density (nm<sup>-2</sup>), and  $d_m$  is the radius of effect for SERS (nm).  $D$  and  $d_n$  were determined via ImageJ analysis of SEM images of the nanowires to be  $1.96 \times 10^{-4}$  nm<sup>-2</sup> and 29 nm, respectively. Because SERS is extremely local to the sensing surface,<sup>165</sup> a radius of effect of  $d_m = 3$  nm was used.<sup>166</sup> EF was estimated to be an average of  $9.9 \times 10^4$  for crystal violet spectra acquired through thick PDMS and an average of  $5.8 \times 10^6$  for spectra acquired through thin PDMS. The enhancement factors and vibrational modes for each chosen Raman band of crystal violet,<sup>167–174</sup> as well as the vibrational modes for the Raman bands of PDMS<sup>175–179</sup> can be found in **Table B.1**.

### Microchannel Mold Design and Fabrication

Based on the comparison between surface enhancement through thick and thin PDMS, it became apparent that a thin microchannel wall would be vital for successful SERS detection of trace analytes. Thus, it was necessary to design a microchannel mold that would enable the fabrication of channels able to facilitate such sensitive SERS. The mold was designed with a base and lid as shown in **Figure III.4**, which would be fitted onto the base after PDMS was poured into the mold. The mold was designed such that channels fabricated would be z-shaped channels with a 2-mm width in the center portion to facilitate subsequent nanostructure fabrication. The channel's top wall was designed to be thick enough at the inlet and outlet to

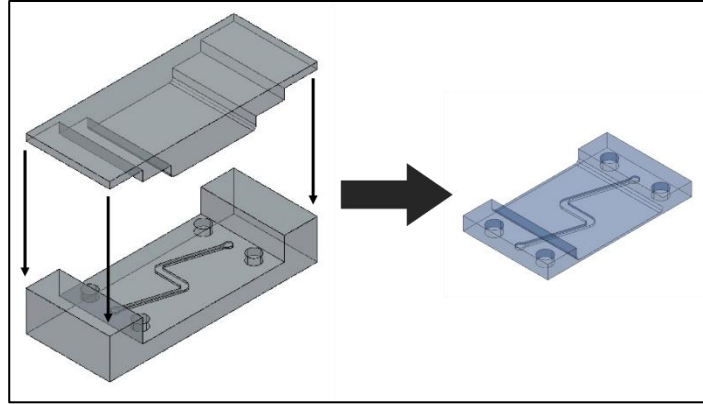


**Figure III.4:** AutoCAD drawing of the microchannel mold designed to enable sensitive SERS through the top channel wall, along with the resultant microchannel.

support tubing, but thin enough at 0.10 mm to enable sensitive SERS sensing with minimal PDMS interference. The channel's top wall was also designed such that the thicker portions would be far enough apart to allow high-magnification objectives with short working distances close enough to focus on the SERS-active surface. The channel was designed with the z-shaped structure, ~7 mm long at the center, to enable Raman spectra to be acquired at multiple points along the center portion. The mold was milled from aluminum in the machine shop of the Physics Department at Vanderbilt University. As a function of the milling process, very small ridging occurred on the surface of the mold lid, which could interfere with SERS sensing through the top wall. To combat this, a glass slide was cut to fit the center portion of the lid and affixed with Kapton tape to the mold lid. Glass spacers were also cut and similarly affixed to the ends of the lid, which would rest on the base, in order to maintain channel integrity.

### **Fabricating SERS Substrates Inside PDMS Channels**

Fluidic channels were fabricated using the aluminum mold above and a 100-nm ZnO seed was deposited inside the channels. The channel was masked with Kapton tape such that

only the channel itself was exposed to deposition. The seed was annealed overnight at 100 °C, after which ZnO nanowires were grown hydrothermally. PL spectra of the nanowires inside the channel, shown in **Figure B.9**, exhibited a large band-edge emission and minimal visible emission, indicating high crystallinity with few defects. The intensity of the band-edge emission varied from channel to channel as shown in **Figure B.9**, which could indicate variability in nanowire density or size between channels. An SEM image of the channel in **Figure III.5(a)** confirmed the growth of highly crystalline nanowires inside the channel. SEM images of the channels of which PL spectra were acquired also exhibited channel-to-channel variability in nanowire formation and density (**Figure B.10**). The nanowires in some channels, like channel 2, were thin and long while in other channels like channel 6, were short and extremely thick. Nanowire formation was, in general, sparser for sputtered seed layers versus e-beam deposited seed layers, as exemplified by a comparison of nanowire density between **Figure B.4** and **Figure B.10**. The nanowires in some channels, like channel 2, were thin and long while in other channels like channel 6, were short and extremely thick.

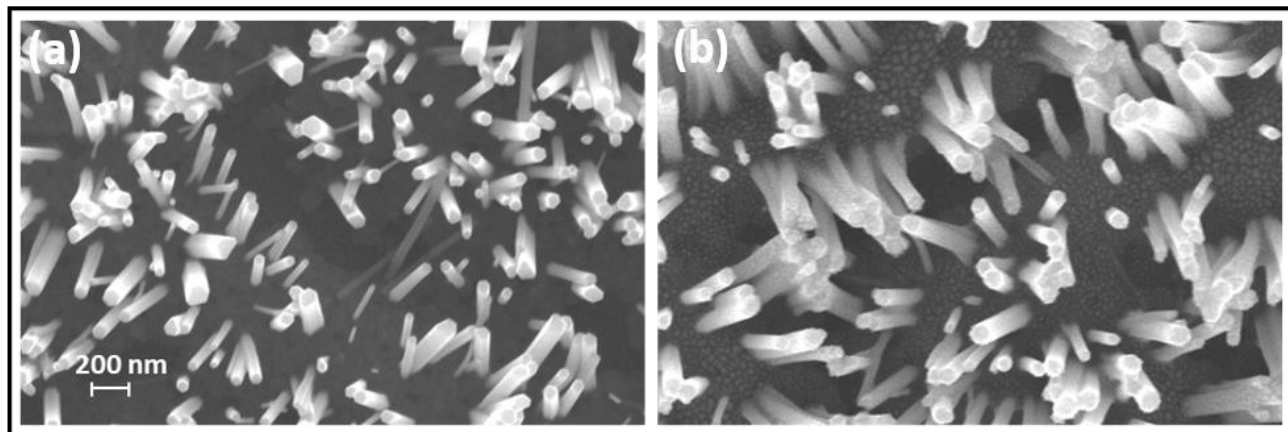


**Figure III.5:** SEM images of ZnO nanowires before and after deposition and anneal of Ag, demonstrating nanowire growth and Ag nanoparticle formation.

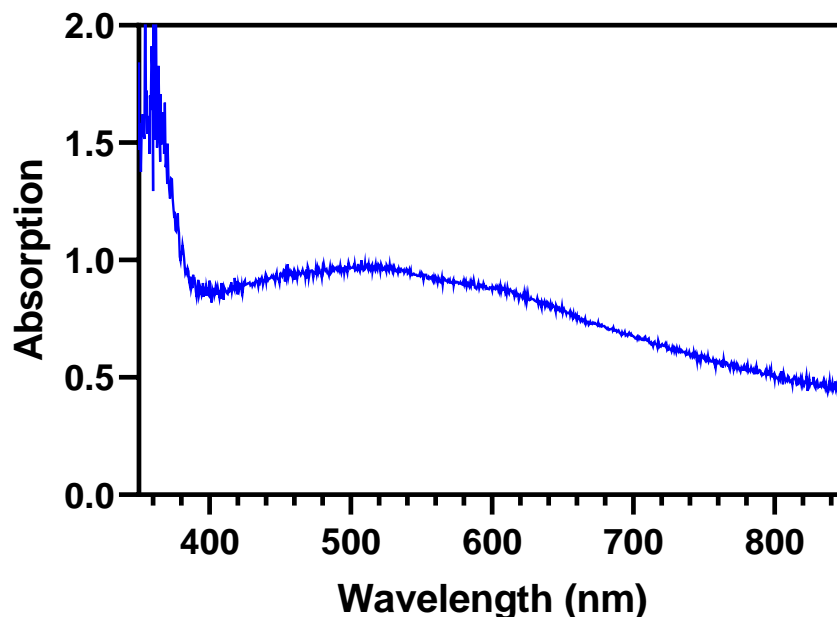


**Figure III.6:** UV-Vis spectrum of ZnO nanowires decorated with Ag nanoparticles after anneal

After nanowire growth, Ag nanoparticles were deposited onto the beds of nanowires at an angle of  $\sim 24^\circ$ . As before, the channels were masked with Kapton tape so that only the channel itself was exposed to deposition and the channels were rotated about a central axis. 15 nm of Ag was deposited at a rate of  $\sim 0.1 \text{ \AA/s}$ . At the specified angle of deposition, this resulted in  $\sim 6 \text{ nm}$  of Ag deposited on the nanowire sides, and 13.7 nm deposited on the bottom of the channel. After deposition, the channel was annealed at  $50^\circ \text{C}$  for 2 hours, as indicated by the results discussed in our previous work,<sup>91</sup> in order to optimize nanoparticle formation for SERS with a 532-nm laser. A UV-Vis spectrum was then acquired of the Ag/ZnO nanowires within the channel, shown in **Figure III.6**. The UV-Vis spectrum of the channel exhibited a clear plasmon peak at  $\sim 515 \text{ nm}$  and shoulder at  $\sim 600 \text{ nm}$ . This is likely because of the dual size populations of Ag nanoparticles deposited on the nanowire sides and the floor of the channel, as is exhibited by SEM of the Ag-decorated ZnO nanowires in **Figure III.5**: SEM images of ZnO nanowires before and after deposition and anneal of Ag, demonstrating nanowire growth and Ag

nanoparticle formation.. The plasmon emission peaked at ~515 nm, close to the 532 nm laser line, and extended well past the end of the fingerprint region at ~590 nm, making the channel suitable for SERS. Subsequently, the channel was completed by binding the PDMS to a glass slide and tubing was inserted at the inlet and outlet.

### **Surface-Enhanced Raman Spectroscopy of Crystal Violet in Channel**

Crystal violet was used to characterize a SERS detection for the completed channels, since crystal violet has multiple strong peaks between 900 and 1200  $\text{cm}^{-1}$ , where there's little PDMS signal. Raman spectra were acquired of 10 crystal violet solutions in DI water ranging from 1  $\mu\text{M}$  to 10  $\mu\text{M}$  concentrations in 1- $\mu\text{M}$  increments, with a DI-water control. These spectra are shown in **Figure III.7**. Before each solution was syringed through the channel, it was flushed with DI water, and the Raman spectra were all acquired at the same location along the channel. Once acquired, the spectra were processed as discussed in Experimental Methods and normalized using the Si-O-Si symmetric stretching peak at 488  $\text{cm}^{-1}$ . Two strong crystal violet peaks; the C-C<sub>center</sub>-C bending peak at 917  $\text{cm}^{-1}$  and the C-C<sub>center</sub>-C asymmetric stretching peak at 1175  $\text{cm}^{-1}$ , which are not near any PDMS peaks. These peaks were clearly visible at a 1- $\mu\text{M}$  concentration, and experienced a steady increase in intensity through the 5- $\mu\text{M}$  concentration, as illustrated in **Figure III.8**. From 6 – 10  $\mu\text{M}$ , however, the peak intensity levelled off. Raman spectra taken of the sensing after crystal violet solutions were evacuated from the channel exhibited crystal violet peaks, meaning the levelling off of the Raman signal was likely due to accumulation of crystal violet adsorbed on the sensing surface.

### **Surface-Enhanced Raman Spectroscopy of Melamine through PDMS**

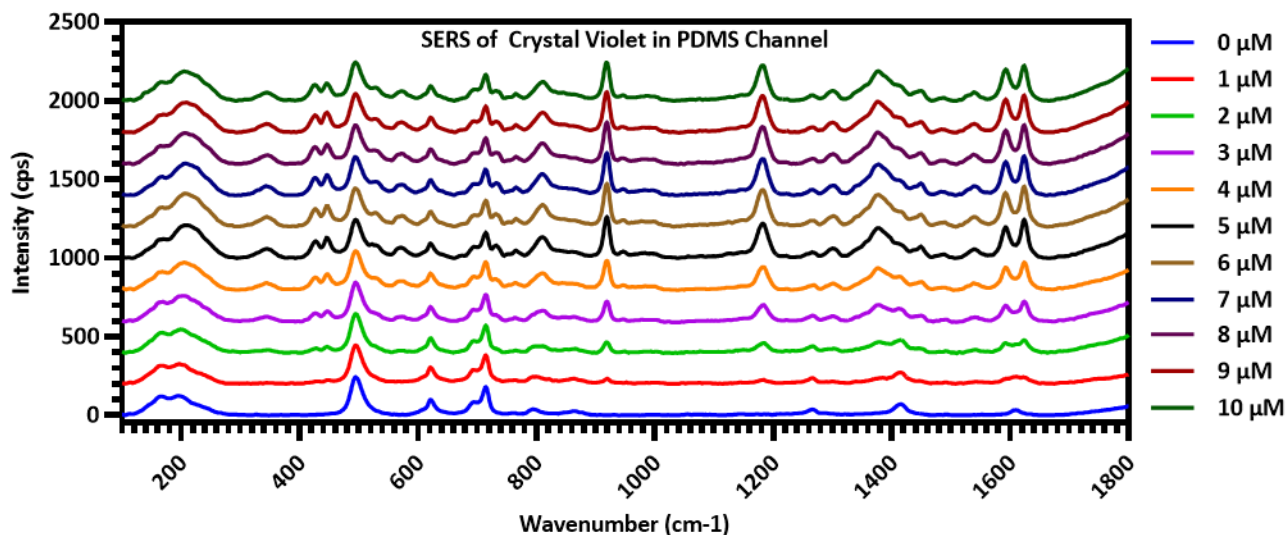


**Figure III.7:** Raman spectra of crystal violet solutions taken inside a fabricated channel, in concentrations ranging from 1 to 10  $\mu\text{M}$  with a DI water control.

After demonstrating the viability of SERS through a PDMS wall of a channel with crystal violet, SERS spectra were acquired of Melamine solutions in DI Water using SERS substrates fabricated on  $\sim 150\text{-}\mu\text{m}$  thick PDMS substrates. Melamine is an industrial material primarily used in polymer manufacturing that has also been added to dairy products to produce artificially high readings of protein content. Because melamine can cause kidney failure and even death, the Codex Alimentarius set a limit of 1 mg/L (7.93  $\mu\text{M}$ ) of melamine in powder infant formula.<sup>107</sup>

Two substrates, hereafter named P1 and P2, were fastened upside down to a reservoir so that Raman spectra were acquired through the PDMS substrate. Raman spectra were acquired of  $\mu\text{M}$  concentrations of melamine in DI water (1, 2, 3, 4, and 6  $\mu\text{M}$  for P1 and 2, 4, 6, 8, 10, and 12  $\mu\text{M}$  for P2). Spectra were first smoothed with a Savitzky-Golay filter and the fluorescent background was subtracted using an asymmetric least squares technique. Spectral intensity was normalized with the PDMS Si-O-Si symmetric stretching peak at  $488\text{ cm}^{-1}$ . While the characteristic peak of melamine at  $691\text{ cm}^{-1}$  is coincident with the PDMS peak at  $703\text{ cm}^{-1}$  associated with Si-C symmetric stretching and  $\text{CH}_3$  bending, multiple melamine peaks are visible

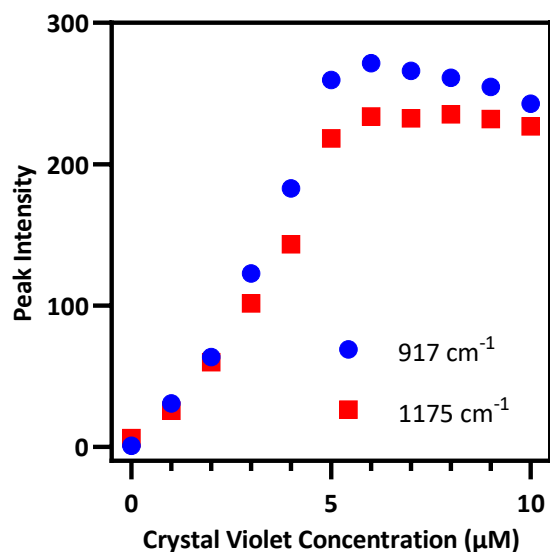


**Figure III.8:** Intensity of two crystal violet peaks as a function of increasing crystal violet concentration.

even at concentrations of 1 and 2  $\mu\text{M}$  for both substrates. 6 melamine peaks other than the 691  $\text{cm}^{-1}$  peak were identified in the spectra plotted in **Figure III.9** that could be assigned vibrational modes, as tabulated in **Table B.2**.<sup>180,181</sup> Importantly, these concentrations are well below the 7.93  $\mu\text{M}$  limit set by the Codex Alimentarius, demonstrating the efficacy of the fluidic device designed and fabricated here for sensing melamine.

Raman spectra acquired exhibited substrate-to-substrate variation, with spectra from P2 generally having much greater melamine signal than P1, as illustrated by direct comparisons of the signals generated by 2, 4, and 6  $\mu\text{M}$  concentrations of melamine shown in **Figure III.9**. Additionally, signal intensity exhibited point-to-point variability, with some spots on both substrates generating much more melamine signal than other spots. This effect is likely due to variation in nanowire density caused by the hydrophobicity of PDMS inhibiting precursor flow around the ZnO seed during hydrothermal nanowire growth which would cause variability in effective surface area, similar to the variation of nanowire growth exhibited by SEM images of channels in **Figure B.10**. The ratios of melamine peak intensity to PDMS peak intensity at 488



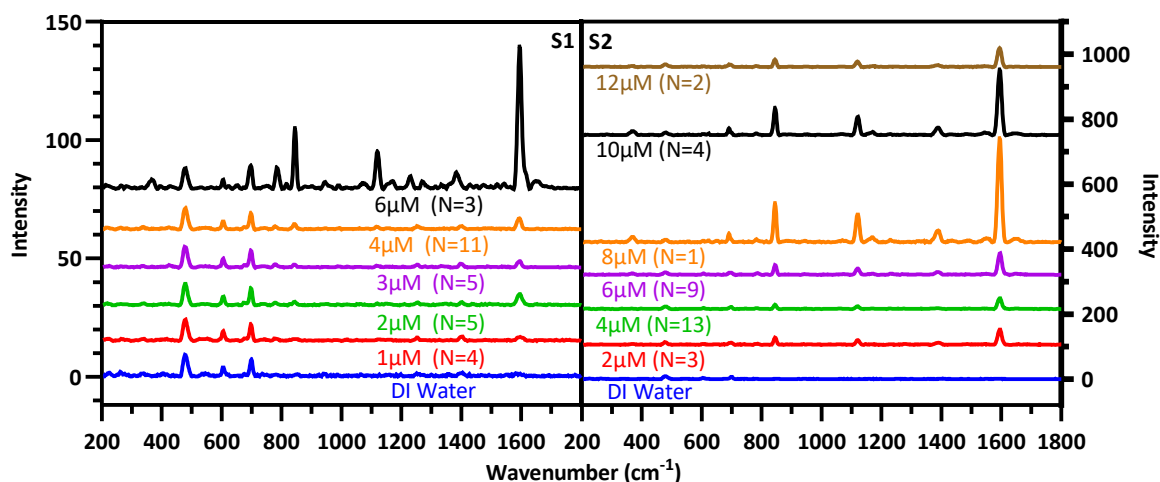


**Figure III.9:** SERS spectra of melamine in DI Water, acquired through S1 on the left and S2 on the right. Number of spectra acquired for each concentration through each substrate in parentheses.

$\text{cm}^{-1}$  shown in **Figure B.11** were averaged for each melamine peak across all concentrations measured for each substrate. For both substrates, these melamine to PDMS peak ratios followed the same trends with increasing concentration. Furthermore, the ratio of the 1596 to 845  $\text{cm}^{-1}$  melamine peaks, shown in **Figure B.12**, remained consistent between substrates and across melamine concentrations, lending confidence to device's ability to reliably and consistently sense melamine once device fabrication is optimized. To combat the variation, channels could be made with a copolymer consisting of PDMS and poly(ethylene oxide) (PEO), which has been shown to improve hydrophilicity.<sup>182</sup> Making the channels hydrophilic should improve precursor flow at the ZnO seed layer, making nanowire growth and density more uniform. In addition to variation across substrates, Raman spectra acquired at the same location on a single substrate exhibited varied intensity from measurement to measurement. It was observed that a Raman spectrum taken immediately after the introduction of a melamine solutions would exhibit little-to-no melamine signal. However, after the substrate was manually disturbed, strong melamine signal would appear in subsequent Raman spectra. This phenomenon is likely due to the

hydrophobicity of nanowire beds preventing infiltration of the melamine solution. Disturbing the substrates allows melamine solution to infiltrate the bed of nanowires, enabling much stronger melamine signal. However, this infiltration was inconsistent. It is expected that sensing within a copolymer PDMS/PEO microfluidic channel will overcome this challenge.

## CONCLUSIONS

This work demonstrated a facile technique to fabricate physically deposited Ag nanoparticle decorated ZnO nanowires inside fluidic channels, allowing microfluidic SERS sensing to benefit from dense Ag nanoparticle formation from e-beam deposition. Through careful design and fabrication of fluidic channels to minimize spectral interference from PDMS,  $\mu\text{M}$  concentrations of crystal violet and melamine were detected, demonstrating the ability of the fluidic device to detect relevant concentrations of melamine. By further improvement on the SERS-active substrate fabrication process, it is expected that this process can provide a reliable and sensitive detection of melamine in a SERS-active microfluidic devices.

## CHAPTER IV

### TOXIC METALS CHELATION BY 18-CROWN-6 ETHERS IN MULTIPLE SOLUTIONS AND QUANTIFICATION BY SPECTROSCOPIC TECHNIQUES

Text for Chapter IV taken from:

**Cook AL**, Xue F, Giorgio TD. Toxic Metals Chelation by 18-Crown-6 Ethers in Multiple Solutions and Quantification by Spectroscopic Techniques. *Proceedings of the 6<sup>th</sup> World Congress on Recent Advances in Nanotechnology*. 2021. DOI: 10.11159/nddte21.lx.202<sup>183</sup>

#### ABSTRACT

Toxic metals exposure is a significant problem for military personnel, with increasingly prevalent embedded fragments due to improvised explosive devices. Current biomonitoring for military personnel with embedded fragments is centralized, limiting capacity and availability. Importantly, monitoring using this approach begins long after peak exposure, indicating a need for portable, multiplexed toxic metals detection that can be carried out closer to the time of exposure with increased frequency. Small molecule chelators such as crown ethers are known to selectively bind metal cations in solution. Crown ethers possess selective chelation of multiple metal ions and is dependent on molecular structure, solution properties, and other parameters. This selectivity extends to multiple ions and depends on not only molecular structure, but also the solution properties. The goal of this study is to assess the potential for metal sensing in solution as a function of crown ether structure and solution properties with future use for toxic metal sensing from embedded fragments as a potential translational objective.

## INTRODUCTION

As of 2017, improvised explosive devices (IEDs) have accounted for almost 75% of all traumatic injuries to U.S. soldiers in recent conflicts in Iraq and Afghanistan.<sup>27</sup> This means that of the more than 50,000 military personnel wounded in action so far in those conflicts,<sup>89</sup> almost 40,000 of them could have toxic embedded fragments.<sup>28</sup> In response to this growing need, the United States Department of Veterans Affairs (VA) established the Toxic Embedded Fragment Surveillance Center (TEFSC, Baltimore, MD) in 2008 with the overall mission to 1) identify veterans who may have embedded metal fragments, and 2) conduct long-term medical surveillance of this population.<sup>26</sup> The evaluation process for inclusion into the Embedded Fragments Registry (EFR) is predicated on the individual's knowledge or suspicion of retained fragments,<sup>29</sup> Thus, biomonitoring of toxic embedded fragments begins long after peak exposure and depends on incomplete knowledge concerning exposure and retention toxic fragments from IEDs, making inclusion into the EFR noncomprehensive. As a result, there are currently only around 16,000 veterans enrolled in the EFR.<sup>90</sup> Biomonitoring of these veterans is carried out via centralized urinalysis using inductively-coupled plasma mass spectrometry (ICP-MS).<sup>8,26,27</sup> While ICP-MS is sensitive and precise, it is a large, research-grade instrument that requires significant power and highly trained technicians for operation,<sup>30,31</sup> making it unsuitable for use near locations where military blast injuries occur. Furthermore, there is a lack of information concerning the scope and extent of embedded fragments<sup>15,32</sup> as well as their long-term health effects.<sup>5,28</sup> To ensure more comprehensive and complete biomonitoring of embedded fragments, a portable, multiplexed toxic metals sensing strategy is required.

There are many techniques for toxic metals detection that can be implemented in a portable setting, including spectroscopic techniques such as fluorescence, colorimetry, and Raman spectroscopy. Many strategies utilizing these techniques make use of small-molecule

chelators known to bind various metal ions in solutions. One common family of chelators are known as crown ethers, small molecules with a characteristic ring made up of carbons and oxygens which are best known for chelating alkali metal cations.<sup>184</sup> While these chelators are moderately selective, they still bind multiple different ions in solution. Small changes in crown ether structure can significantly affect which metals it will bind.<sup>78,80</sup> Additionally, differences in solution affect crown ether morphology, changing chelation selectivity.<sup>185</sup> The purpose of this study is to explore how changes in the structure and solution of 18-crown-6 (18C6) ethers can change its selectivity profile for metal ions.

## EXPERIMENTAL

Two different solvents consisting of dimethyl sulfoxide (DMSO) and deionized (DI) water were used for all experiments in this study: 1:1 DMSO/water and 1:3 DMSO/water. 4'-aminobenzo-18-Crown-6 (AB18C6) and benzo-18-Crown-6 (B18C6) and the following 22 metals were examined as a part of this study: Al<sup>3+</sup>, Ag<sup>+</sup>, As<sup>3+</sup>, Ba<sup>2+</sup>, Ca<sup>2+</sup>, Cd<sup>2+</sup>, Co<sup>2+</sup>, Cr<sup>3+</sup>, Cu<sup>2+</sup>, Fe<sup>3+</sup>, Hg<sup>2+</sup>, K<sup>+</sup>, Li<sup>+</sup>, Mg<sup>2+</sup>, Mn<sup>2+</sup>, Mo<sup>5+</sup>, Na<sup>+</sup>, Ni<sup>2+</sup>, Pb<sup>2+</sup>, UO<sub>2</sub><sup>2+</sup>, W<sup>4+</sup>, and Zn<sup>2+</sup>. All metal salts used to obtain these ions

were purchased from Sigma Aldrich. All 14 metals in the TEFSC biomonitoring panel<sup>26,28</sup> are included, as well as metals commonly found in urine, such as Ca<sup>2+</sup>, K<sup>+</sup>, Mg<sup>2+</sup> and Na<sup>+</sup>. Also included are a number of common metals that could make their way into human urine, such as Al<sup>3+</sup>, Mn<sup>2+</sup>, and Zn<sup>2+</sup>. 100 μM equimolar solutions of each metal individually with AB18C6 were formed in both 1:1 DMSO/water and 1:3 DMSO/water.

In this study, the chelation of metal ions by two crown ethers was studied in a single solution to explore how a small change in the crown ether's structure might change the crown

ether's metal selectivity. Furthermore, chelation by chelation of metal ions by one of those crown ethers was examined in two solutions. Chelation of metals by AB18C6 and B18C6 was examined primarily using ultraviolet-visible extinction spectrophotometry. Preliminary examination of the extinction spectrum of using a quartz cuvette in a Varian Cary 50 Bio spectrophotometer. These measurements were acquired at a resolution of 5 nm over a range of 250 – 800 nm to confirm the absorption profile of AB18C6 reported by Sarfo et. al.,<sup>78</sup> and to explore differences in chelation of metal ions between AB18C6 and B18C6. For these experiments, the extinctions from 100- $\mu$ M concentrations of each crown ether in 1:3 DMSO:water were measured without metals. Subsequently, the extinctions of 100- $\mu$ M equimolar concentrations of each crown ether and selected metal salts in 1:3 DMSO:water were acquired.

Full UV-vis spectrophotometry chelation sweeps of metal ions by AB18C6 were performed using Thermo Scientific<sup>TM</sup> Nunc<sup>TM</sup> UV-transparent plastic 96-well plates in a Tecan Infinite M1000 Pro plate reader. These measurements were acquired at a resolution of 1 nm over a range of 250 – 400 nm to determine which metals are chelated by AB18C6. For these measurements, 100- $\mu$ M concentrations of AB18C6 in both solvents were used without metals, and 100- $\mu$ M equimolar solutions of AB18C6 and each metal salt in each solvent were used for selectivity assessments. The same instrument was used to acquire fluorescence measurements of AB18C6 in the presence and absence of selected metals were acquired with an excitation wavelength of 295 nm over a range of 300 – 700 nm at a resolution of 2 nm. The same crown ether and metal solution strategy was used for fluorescent measurements, except only two metals known to be chelated from previous experiments were included. UV-vis spectrophotometry with the same spectral parameters described above was performed on 100- $\mu$ M crown ether solutions with one of the metals known to be chelated in concentrations of 1 nM, 10 nM, 100 nM, 1 $\mu$ M, 10

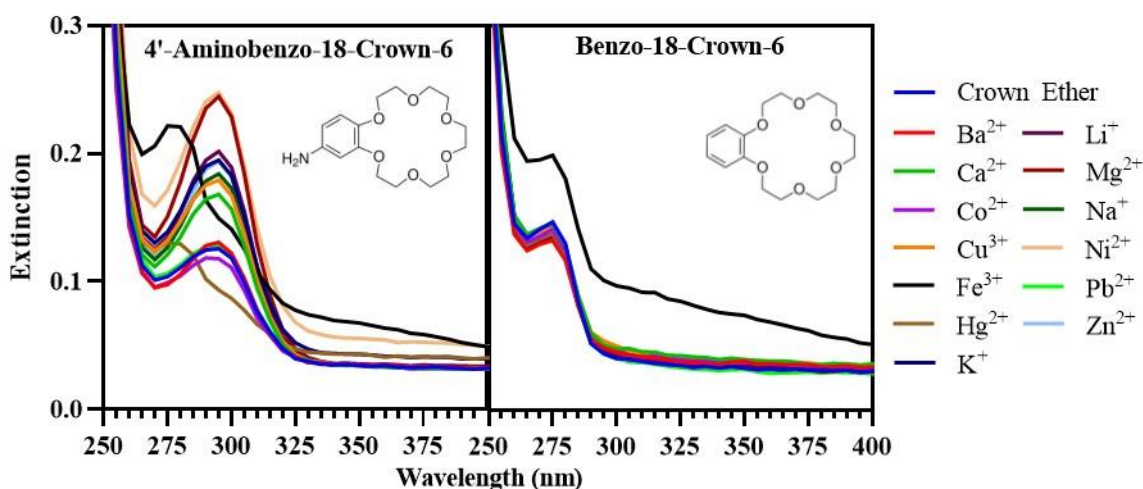


**Figure IV.1:** UV-Vis extinction spectra of 100- $\mu$ M AB18C6 and B18C6 in 1:3 DMSO:water without and with equimolar concentrations of selected metals.

$\mu$ M, and 100  $\mu$ M. Fluorescence spectroscopy was performed on these same solutions with an excitation wavelength of 295 nm over an emission range of 304 – 500 nm at a resolution of 1 nm.

## RESULTS & DISCUSSION

The first experiment was a comparison via UV-vis spectrophotometry of which metals are chelated by AB18C6 and B18C6. It was reported by Sarfo et. al.<sup>78</sup> that AB18C6 crown ethers possess a strong extinction peak centered at 295 nm. When the crown ether chelates a metal, this peak is quenched and another emerges at  $\sim$ 280 nm. For this experiment, 100- $\mu$ M solutions of AB18C6 and B18C6 by themselves and with equimolar concentrations of 13 selected metal salts prepared in 1:3 DMSO:water. As can be seen in **Figure IV.1**, while AB18C6 has an extinction peak at 295 nm as Sarfo et. al. reported, B18C6 has a peak at  $\sim$ 275 nm. No chelation occurred for most of the metals investigated, as evidenced by a lack of quenching of the 295-nm peak for AB18C6 or the 275-nm peak for B18C6, as well as a lack of an additional peak. However, both

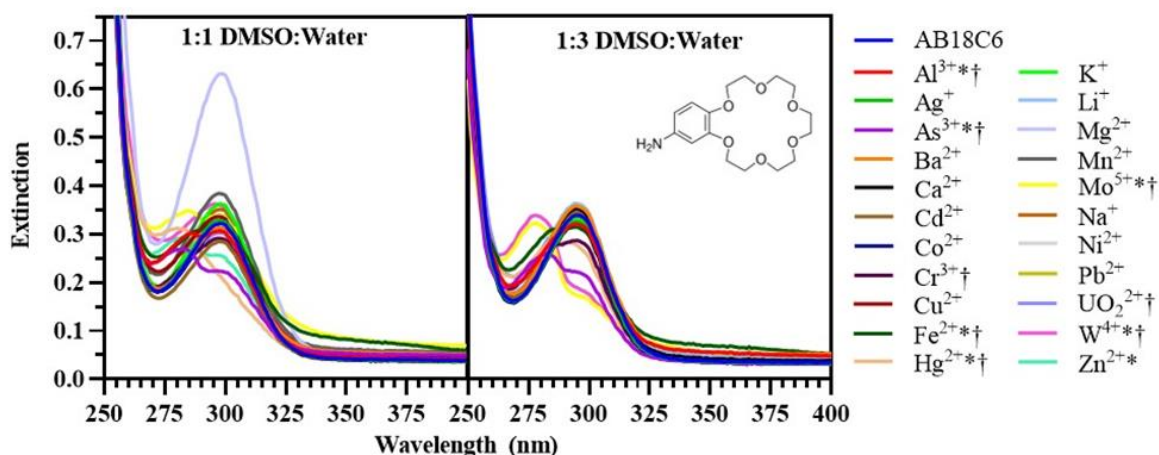


**Figure IV.2:** UV-Vis extinction spectra of 100- $\mu$ M AB18C6 alone and with equimolar concentrations of 22 metal salts in two different solutions. Metals chelated by AB18C6 in 1:1 DMSO:water are denoted with “\*”, while metals chelated by AB18C6 in 1:3 DMSO:water are denoted with “†”.

$\text{Fe}^{3+}$  and  $\text{Hg}^{2+}$  ions were chelated strongly by AB18C6, evidenced by the quenching of the 295-nm peak and appearance of a peak  $\sim$ 282 nm. Benzo-18-Crown-6 chelated none of the metals examined, indicating that even small differences in crown ether structure can lead to big differences in metal chelation.

The second experiment performed was an examination of how different solutions would affect the chelation of metal ions by AB18C6. 100- $\mu$ M solutions of AB18C6 were prepared in 1:1 DMSO:water and 1:3 DMSO:water, without and with equimolar concentrations of 22 metals. UV-vis spectra were acquired of each solution and plotted in **Figure IV.2**. While the chelation profile for AB18C6 was very similar in both solutions, there were some significant differences. AB18C6 chelated Al, As, Fe, Hg, Mo, and W in both solutions, while it chelated U in only 1:1 DMSO:water and Zn in only 1:3 DMSO:water. Even among metals chelated in both solutions, there were differences in the strength of chelation. Notably, Al is more strongly chelated in 1:1 DMSO:water while Hg is more strongly chelated in 1:3 DMSO:water. Interestingly, while Sarfo et. al. reported that AB18C6 chelates  $\text{Pb}^{2+}$ ,<sup>78</sup> these experiments demonstrate a lack of  $\text{Pb}^{2+}$



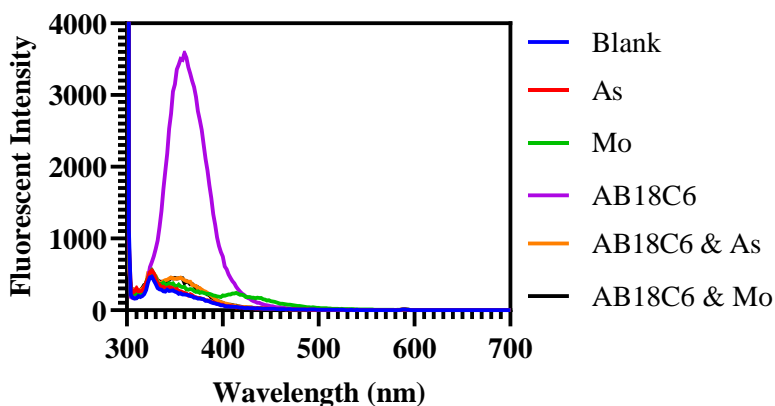


**Figure IV.3:** Fluorescent Spectra of AB18C6 by itself and with As and Mo separately in 1:3 DMSO:DI Water, demonstrating fluorescent quenching when of the crown ether when chelating both metals.

chelation in either solution. Because of the dependence chelation has on solution, it is likely that this discrepancy with reported results result from an unreported difference in solution.

While UV-vis is excellent for qualitatively determining whether a crown ether is chelating a metal ion, it is difficult to extract any meaningful quantitative information on the amount of chelation taking place in a given solution. However, Sarfo et al. reported that AB18C6 possesses a fluorescence peak at ~370 nm that gets quenched in the presence of chelated metals.<sup>78</sup> To confirm this, fluorescence measurements of 100- $\mu$ M solutions of AB18C6 without and with equimolar concentrations of  $\text{As}^{3+}$  and  $\text{Mo}^{5+}$  (known to be strongly chelated from **Figure IV.2**) in 1:3 DMSO:water were acquired. As can be seen in **Figure IV.3**, AB18C6 with no metal ions present fluoresces as Sarfo et. al. reported. This fluorescence was strongly quenched when As and Mo were present. However, even at equimolar concentrations of metal ions, this fluorescence was not quenched completely, indicating that fluorescence can be used for quantification of toxic metals chelation by AB18C6.

An initial survey of the changes in optical absorbance and fluorescence resulting from AB18C6 chelation of a range of molybdenum concentrations between 1 nM and 100  $\mu$ M, as

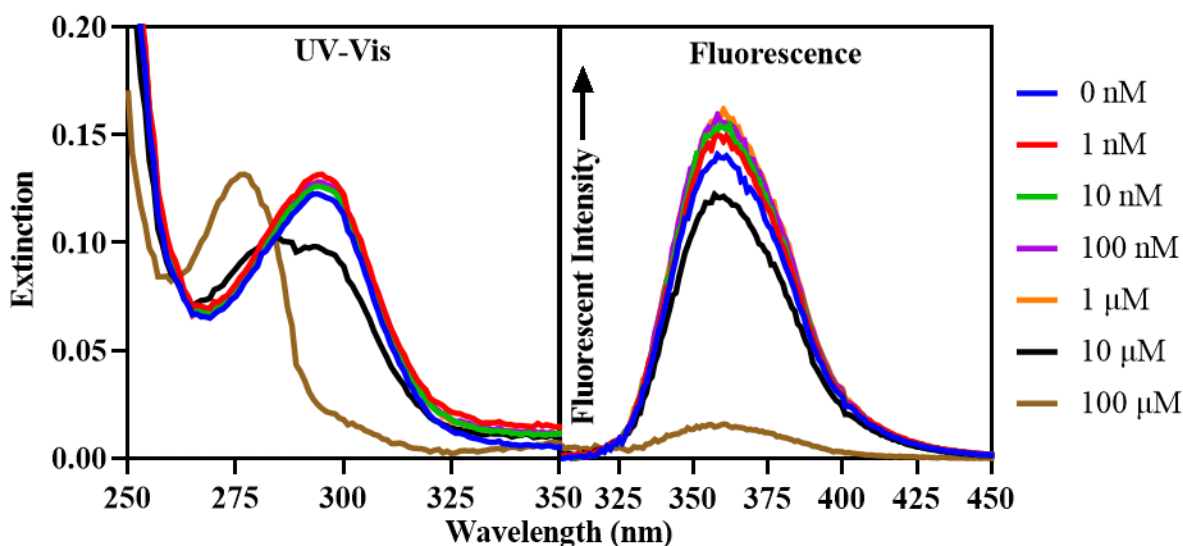


**Figure IV.4:** UV-Vis and fluorescence spectra of 100- $\mu$ M AB18C6 with concentrations of Mo between 1 nM and 100  $\mu$ M, with a control solution of 100- $\mu$ M AB18C6 unmixed with Mo.

shown in **Figure IV.4**. Mo was selected for this assessment based on the quenching of extinction at 295 nm and the presence of another extinction peak at  $\sim$ 280nm (**Figure IV.2**). Mo concentrations of 1 nM, 10 nM, 100 nM, 1  $\mu$ M, 10  $\mu$ M and 100  $\mu$ M were prepared with 100- $\mu$ M solutions of AB18C6 in 1:3 DMSO:water. UV-vis spectrophotometry was performed at a resolution of 1 nm over a range of 250 – 400 nm (**Figure IV.4**), and spectra of each concentration of Mo were subtracted from their corresponding spectra of mixed AB18C6 and Mo. Fluorescence used an excitation wavelength of 295 nm over a range of 304 – 450 nm at a resolution of 1 nm. A clear peak shift from  $\sim$ 295 to  $\sim$ 275 nm at 100  $\mu$ M Mo concentration was evident in addition to a small peak shift at 10  $\mu$ M. Large fluorescence quenching occurred at 100  $\mu$ M at  $\sim$ 360 nm with additional, slight quenching at 10  $\mu$ M Mo concentration. Other concentrations of Mo did not produce evident changes in either UV-vis or fluorescence (**Figure IV.4**).

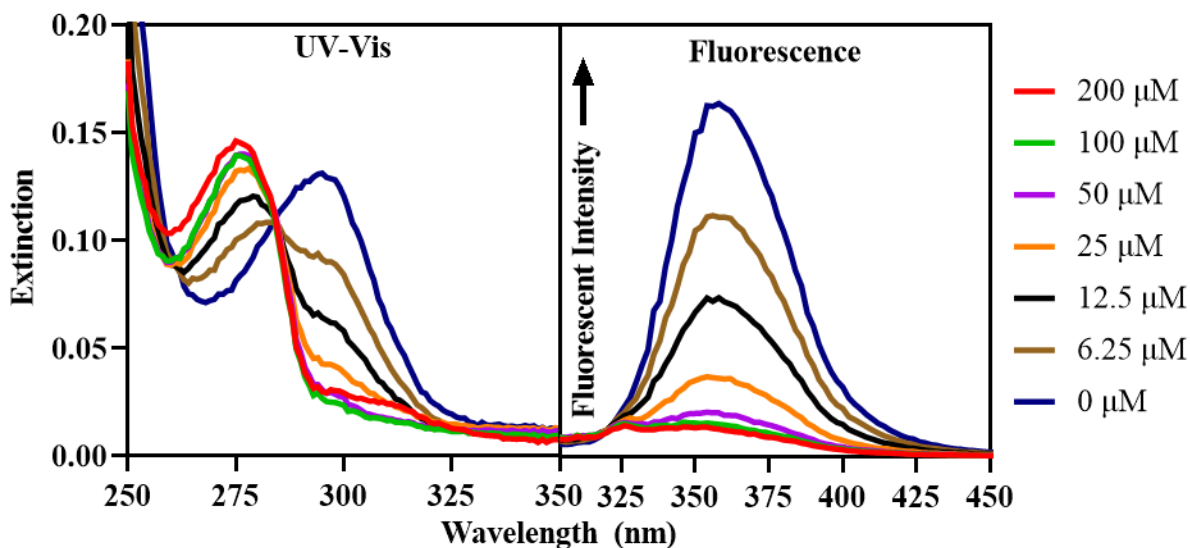


**Figure IV.5:** UV-Vis and fluorescence spectra of 100- $\mu\text{M}$  AB18C6 with concentrations of Mo between 6.25 and 200  $\mu\text{M}$ , with a control solution of 100- $\mu\text{M}$  AB18C6 unmixed with Mo.

To expand the characterization of Mo chelation by AB18C6, the same experiment was performed using Mo concentrations (in  $\mu\text{M}$ ) of 6.25, 12.5, 25, 50, 100, and 200. UV-vis spectrophotometry and fluorescence spectroscopy used the same resolution and range, as shown in **Figure IV.5**. The extinction peak at  $\sim 295$  nm steadily decreased with increasing Mo concentration between 6.25  $\mu\text{M}$  and 50  $\mu\text{M}$ . This decrease reached a minimum at 50  $\mu\text{M}$  and did not continue to decrease for 100 or 200  $\mu\text{M}$ . The extinction peak at  $\sim 277$  nm increased in conjunction with the decrease of the 295-nm peak, steadily intensifying between 6.25  $\mu\text{M}$  and 50  $\mu\text{M}$  and remaining steady for 100 and 200  $\mu\text{M}$ . Gradual quenching of AB18C6's fluorescence peak at  $\sim 360$  nm was observed under increasing Mo concentrations, as shown in **Figure IV.5**. Full quenching of this fluorescence peak occurred at the 100  $\mu\text{M}$  concentration of Mo, indicating greater range of chelation quantification for fluorescence than for UV-vis. The absorption decrease at  $\sim 295$  nm or increase at  $\sim 277$  nm did not directly correlate with the increase in Mo concentration, suggesting that absorbance may be a complicated indicator of concentration for

this metal. However, these experiments indicate that a quantitative relationship between AB18C6's extinction profile and Mo concentration exists. Furthermore, fluorescence quenching is directly correlated with increasing Mo concentration, that demonstrates the quantitative potential for fluorescent detection of Mo through crown ether chelation.

## CONCLUSIONS

This study demonstrated that minor structural changes in 18C6 ethers modulate metal ion chelation with crown ethers. Furthermore, solution characteristics influence crown ether morphology and the strength of metal ion chelations. Crown ether structure and the solvent environment determine metal chelation characteristics. Optimal quantitation of metal ion concentrations will require additional studies of crown ether chelation under various conditions. The quantitative spectroscopic response of single metal ion species with crown ethers, as demonstrated here, can also be expanded to include multi-composition solutions characterized by suitable mathematical analysis. This study demonstrated the potential for UV-vis and fluorescence spectroscopy to quantify chelation of toxic metal ions by crown ethers. These results inform the design of future portable detection and quantification techniques for toxic metal ions in solution.

## CHAPTER V

### CONCLUSIONS

#### CHAPTER SUMMARIES & IMPACT

The overall goal of this research was to develop a portable, disposable sensor to detect toxic metal ions in urine via surface-enhanced Raman spectroscopy. This approach required the development of a simple fabrication strategy for integrating physically deposited SERS-active surfaces within fluidic channels prepared via soft lithography. Direct physical deposition of a SERS active surface within a PDMS channel was not publicly disclosed prior to the start of this project. Successful proof of concept also required the optimization of e-beam deposited Ag nanoparticles on ZnO to maximize surface enhancement in Raman spectra acquired with a 532-nm laser. This work was the first to systematically explore multiple fabrication parameters within this paradigm and directly examine the relationships among parameters and surface enhancements to Raman signals.

In Chapter II, Ag nanoparticle fabrication on ZnO via electron beam deposition was optimized for maximally surface enhanced Raman spectroscopy with a 532-nm laser. Four fabrication parameters were explored in this analysis; deposition rate, deposition thickness, anneal temperature, and anneal time. Ag nanoparticles were e-beam deposited onto ZnO at rates of 0.1 and 0.3 Å/s and thicknesses of 1 through 9 nm in 1-nm increments. These depositions were annealed at temperatures ranging from 50 to 400 °C for times ranging from 15 to 150 min. Nanoparticles deposited at 0.1 Å/s generally produced better surface enhancement than those deposited at 0.3 Å/s. Increasing nanoparticle film thickness produced larger and more densely populated nanoparticles, red-shifting and intensifying their plasmon absorption peak.

Nanoparticle film thicknesses between 5 and 9 nm produced good surface enhancement, with 7 nm providing the best enhancement. Annealing at temperatures less than or equal to 200 °C produced the best increase to surface enhancement of the nanoparticles through Ostwald ripening, with annealing at 200 °C for 60 min or 50 °C for 120 min providing the greatest increase in enhancement factor. This work is the first report to systematically explore the impact of fabrication conditions on the performance of a specific SERS sensor, and laid the foundation for the analysis of similar phenomena in other SERS sensing approaches.

Chapter III demonstrated the simple fabrication of SERS-active fluidic channels leveraging the dense nanoparticle formation of e-beam deposited silver. The channel mold was milled from aluminum, and designed to minimize the thickness of the channel top wall. This design was carried out based on preliminary measurements of &&& on PDMS that suggested minimizing PDMS in the optical path would be beneficial to sensing performance. The top wall thickness is, therefore, a compromise between sensing performance and the feasible fabrication of the SERS-active sensor in the channel. The channels were masked and a seed layer of ZnO was sputtered into the channel, on which ZnO nanowires were grown hydrothermally. Ag nanoparticles were then e-beam deposited and annealed according to the parameters identified in Chapter II. Nanowire growth from channel to channel was very inconsistent, due to the ZnO seed applied by sputtering rather than by e-beam deposition. E-beam deposition of ZnO seed is preferred over sputtering due to the growth of more uniform nanowires, but the unidirectionality of e-beam deposition means that only the bottom of the channel would be coated in ZnO, leaving the walls of the channel bare. Because of this, the hydrophobicity of PDMS inhibited intra-channel nanowire growth, necessitating sputtering of the ZnO seed. Sputter deposition is omnidirectional, coating all channel walls in ZnO. This is another example of the design and

fabrication constraints that must be overcome (or optimized) for useful SERS sensing from this uncommon substrate. Raman spectra of crystal violet in DI water were acquired through the PDMS wall on which the SERS substrate was fabricated. Crystal violet Raman peaks were clearly visible in spectra acquired of concentrations as low as 1  $\mu\text{M}$ , and spectra acquired of increasing concentrations of crystal violet exhibited a clear trend of increasing intensity, although saturation occurred at approximately 5  $\mu\text{M}$ , presumably due to molecular adsorption onto the sensing surface. Nanowire forests are inherently hydrophobic, so wettability of the sensing surface potentially compromises detection sensitivity and reliability. However, the reproducibility of spectral acquisition within the channel suggests that any negative consequences resulting from sensor hydrophobicity are inconsequential; perhaps the pressure created by injecting solutions into the channel is sufficient to overcome this hydrophobicity. Following SERS acquisition of crystal violet solutions in a channel, SERS-active substrates were fabricated on PDMS of the same thickness as the channel wall and were placed face-down in a reservoir, which was filled to the point of fluid contact with the sensing surface. Raman spectra were acquired through the PDMS substrate of micromolar melamine solutions. Multiple substrates exhibited clear melamine signal at concentrations as low as 1 to 2  $\mu\text{M}$ , which is well below the limit of 7.93  $\mu\text{M}$  melamine in infant formula, as set by the Codex Alimentarius Commission.<sup>186</sup> Spectral intensity was not clearly correlated with melamine concentration, and spectral intensity varied among and within substrates. The variability and lack of correlation with concentration, not observed for crystal violet sensing by SERS-active surfaces in the PDMS channel, may be associated with inconsistent nanowire growth and difficulty in wetting inherently hydrophobic beds of nanowires. The first problem is likely caused by the hydrophobicity of PDMS inhibiting precursor flow around the ZnO seed during hydrothermal

nanowire growth. The hydrophobicity of PDMS can be mitigated by fabricating channels out of a hydrophilic PDMS-PEO copolymer. This study was an important step in the development of a sensor for detecting toxic metals, demonstrating simple fabrication of channels with densely populated e-beam deposited Ag nanoparticles. Micromolar detection of crystal violet and melamine were successfully performed through PDMS of free molecules in solution. Functionalization of the sensing surface with chelating molecules will further increase detection sensitivity.

In Chapter IV, the chelation of toxic metals in solution by crown ethers was explored in multiple solutions. Equimolar solutions of AB18C6 and B18C6 and 13 different metals were mixed in 1:3 DMSO:DI water. These solutions were examined by UV-Vis spectrophotometry. Chelation of multiple toxic metals ions by AB18C6 was detected by a shift in light absorbance upon as compared to the spectrum of AB18C6 alone. A similar shift was not observed for B18C6 with any of the metals investigated. This result suggests that small changes in crown ether structure, such as the presence or absence of an amine in this case, can greatly affect which metals the crown ether will chelate. Further experimentation was pursued with AB18C6, expanding the library of toxic metals investigated to 22. Equimolar solutions of AB18C6 and these 22 metals were mixed in 1:1 DMSO:DI water and 1:3 DMSO:DI water, and were examined by UV-Vis spectrophotometry. Multiple metals were chelated by AB18C6 in both solutions, but there were a few metals chelated in one solution but not the other, and some metals were chelated more strongly in one solution but not the other. These results indicate that solvent can affect crown ether chelation of metal ions, illustrating the need to examine crown ether chelation in fluids indicated by the application, which would be urine in the case of SERS-based urinalysis. Importantly, this multiplicity of metal ion chelation by a single crown ether is



advantageous for multiplexed ion detection. Each ion will affect the crown ether's Raman spectrum differently, which can be elucidated with computational techniques such as principal component analysis (PCA). Multiple crown ethers that chelate different metal ions can be used in conjunction to determine the composition of metal ions in urine, including all 14 metals in the TEFSC biomonitoring panel. As and Mo were selected for further analysis based on strong chelation in 1:3 DMSO:DI water and fluorescence spectra of AB18C6 without and with equimolar solutions of each metal demonstrated fluorescent quenching of the crown ether's fluorescence peak. A 100  $\mu\text{M}$  solution of AB18C6 was mixed with solutions of Mo ranging from 1 nM to 100  $\mu\text{M}$ , and were examined with UV-Vis spectrophotometry and fluorescence spectroscopy. Concentration-correlated quenching of the crown ether's fluorescence peak and shifting of the crown ether's absorption peak was exhibited, with single-digit micromolar concentrations of Mo chelated by 100  $\mu\text{M}$  AB18C6 being distinguishable from the unmixed 100  $\mu\text{M}$  AB18C6 control. These experiments indicate the potential of fluorescence spectroscopy and UV-Vis spectrophotometry to corroborate SERS detection and quantification of toxic metals chelation, and to act as a dual sensing strategy for toxic metals in urine.

## SHORTCOMINGS

### **Significant Aim 1**

Only two deposition rates of Ag nanoparticles were explored, which provides an incomplete picture of how deposition rate affects nanoparticle formation, both before and after anneal. The scope of this optimization study was very large, and at the limit of what could realistically be accomplished in a reasonable time frame. Adding more even two more deposition

rates would have doubled the amount of work, resources, and time required to complete the study. In addition, nanoparticles were deposited on ZnO films rather than on nanowires. As the UV-vis spectrum in **Figure III.6** illustrates, the plasmon absorption peak for nanoparticles deposited on a bed of ZnO nanowires possesses a different profile than the spectra for nanoparticles deposited on a ZnO film, with two populations of nanoparticles exhibiting a plasmon peak at ~515 and shoulder at ~600 nm versus a single plasmon peak between 500 and 600 nm, as expected based on this study. As with increasing the number of deposition rates examined, performing this study on nanowires would have greatly increased the difficulty and time-consumption of the study, making it impossible to complete the study in a reasonable time frame. Thus, while the results from Chapter II are a good foundation for optimizing nanoparticle formation on ZnO nanowires, a more complete study would perform the exploration of nanoparticle fabrication parameters on nanowires rather than a film. Of course, doing so would add effective surface area as a variable that affects SERS enhancement. In addition, while a large population of substrates was available to analyze for deposition parameters, each data point in the annealing parameter space was represented by a single substrate. SERS sensitivity is notoriously difficult to control, being highly responsive to small changes in nanoparticle shape, structure, size, and density. It would have been preferable to have multiple substrates for each intersection of anneal time and temperature, to develop a statistically powerful understanding of how annealing parameters affect surface enhancement. To acquire even 3 substrates at each intersection would have tripled the amount of work and resources required to perform this study, making it infeasible for the scope of this study. While SEM images were acquired of representative substrates before annealing, it would have been advantageous to take SEM images of substrates after annealing to examine the effects of Ostwald ripening at each intersection of

anneal temperature and time. This was attempted, but high-quality images could not be acquired due to significant charging of the samples. Furthermore, atomic force microscopy would have been beneficial for acquiring information on how the height of the nanoparticles was affected by annealing and how height changes affect enhancement. Doing so would have required a significant amount of time and is better-suited for an investigation of a smaller parameter space.

### **Significant Aim 2**

While the work performed in Chapter III represents a significant proof of concept that the strategy of physically fabricating SERS-active substrates within a PDMS channel produced devices capable of sensitively detecting contaminants such as melamine, it is presented with multiple shortcomings that must be acknowledged. To truly minimize interference of PDMS, it would be best to consider not just the thickness of the PDMS wall, but also the strength of the PDMS wall. In Chapter III, the thickness of the PDMS wall was chosen to allow lenses with short-working distances to acquire SERS spectra through the wall, but a better way to choose that thickness would be to optimize wall thickness with the channels' ability to withstand expected fluidic pressure. Doing so would require a clearer understanding of expected fluidic pressure, and would be best accomplished when channel design is more clearly understood. Another significant issue with this work was the inconsistency of nanowire growth in both channels and on PDMS substrates. In both cases, this inconsistency appeared to be caused by the hydrophobicity of PDMS interfering with flow of precursors during hydrothermal nanowire growth. Sputtering of the ZnO seed was used instead of e-beam deposition in channels in an attempt to coat more of PDMS surface inside the channel, but nanowire growth remained inconsistent. A better solution might be to make channels out of a PDMS-PEO copolymer, which

has been shown to be more hydrophilic than PDMS by itself. SERS of both crystal violet and melamine should have been performed in multiple channels at each concentration to avoid the problem of adsorption saturation of the sensor, and to enable calculation of a limit of detection. Doing so would have required a large number of channels, and fabrication of SERS active substrates within channels was too inconsistent to develop the required number of channels.

### **Significant Aim 3**

While the work in Chapter IV developed a chelation profile for AB18C6 in multiple DMSO/DI water solutions, it is still unknown how binding the crown ether to the sensing surface would affect chelation equilibria. In order to complete the fabrication of toxic metals sensor, functionalization of the sensing surface within a channel with AB18C6 should have been accomplished and successful SERS of the crown ether with and without metals chelated should have been accomplished. While the results in Appendix C indicate that successful functionalization of SERS-active substrates with AB18C6 did occur, SERS spectra of the crown ether could not be acquired, meaning that surface coverage by the crown ether was likely insufficient to ensure a detectable crown ether SERS signal.

### **FUTURE WORK & POTENTIAL APPLICATIONS**

The detection of toxic metals in urine for military personnel is the application that drove this project, but the potential applications of this work extend well beyond that. There are many uses for a portable, disposable sensor to detect dilute analytes in fluids. Not only can untargeted sensing be performed, such as melamine in dairy products, but also targeted sensing, such as lead in drinking water. In order to achieve a rugged, multiplexed, portable detector for toxic metals in

urine, a great deal of work needs to be done. The first step will be to functionalize the SERS substrate with AB18C6 and perform Raman spectroscopy. Preliminary attempts to do so have been performed, the results of which are presented in APPENDIX C. The chelation profile of AB18C6 decorating the sensing substrate will then need to be assessed in real or synthetic using fluorescence spectroscopy, as the absorption peak for AB18C6 is coincident with ZnO's band edge, making UV-vis spectroscopy nonfunctional for this purpose. SERS spectra will then need to be acquired of the crown ether without and with each metal the crown ether chelates, to determine if multiplexing with the single crown ether is viable.

There are other aminated crown ethers that could be used to further multiplex toxic metal detection. Aminated crown ethers such as 2-aminomethyl-15-crown-5, 4'-aminodibenzo-18-crown-6, and 2-aminomethyl-18-crown-6 are commercially available, and others could be synthesized. Each crown ether will be individually bound to sensing surfaces and fluorescence-based assessment of chelation would be performed in urine. Crown will be chosen based on which metal ions they chelate, so that each of the 14 metals in the TEFSC biomonitoring panel (**Table I.1**) is chelated by at least one crown ether. The fluidic channel will be redesigned so that each crown ether functionalizes a separate bed of Ag-decorated ZnO nanowires. A classification algorithm will be developed to identify metals chelated by the device. One option is a hierarchical method based on which crown ethers are exhibiting chelation-induced spectral changes. Another option would be to perform principal component analysis on the spectra of crown ethers chelating different metals to identify principal components for use in the development of a classification algorithm.

## CONCLUSION

This dissertation describes the development of a portable, disposable sensor to detect analytes via surface enhanced Raman spectroscopy. The fabrication parameters of electron beam-deposited silver nanoparticles on ZnO films including deposition rate, film thickness, anneal temperature, and anneal time were evaluated for their effect on the nanoparticles' plasmon resonance and surface enhancement. It was determined that nanoparticles deposited at a rate of 0.1 Å/s provided better overall surface enhancement than those deposited at 0.3 Å/s, and that 7-nm films annealed at either 50 °C for 120 min or 200 °C for 60 min provided the best surface enhancement. These results were used to optimize silver nanoparticles deposited onto ZnO nanowire beds fabricated inside a PDMS channel designed so that these nanowire beds would be located on a thin PDMS wall, to minimize spectral interference from PDMS. To grow these nanowires, ZnO seed was sputtered into the channel and nanowires grown hydrothermally. Once the channel was completed, increasing concentrations of crystal violet in DI water from 1 – 10 µM were injected sequentially into the channel and SERS spectra were acquired. These spectra exhibited clear crystal violet peaks at the lowest concentrations evaluated, and peak intensities of crystal violet increased with increasing concentration, although saturation occurred due to crystal violet adsorption onto the sensing surface. The same sensing surface was deposited onto PDMS substrates and SERS spectra were acquired of melamine solutions ranging from 1 – 12 µM. Melamine Raman peaks were clearly visible in concentrations as low as 1 µM, well below the 7.93 µM maximum concentration allowed in infant formula. 4'-aminobenzo-18-crown-6 was shown to chelate multiple toxic metals, and both fluorescence spectroscopy and UV-vis spectrophotometry were demonstrated to be able to quantify toxic metals chelation by the crown ether. The work presented in this dissertation represents an important first step toward the development of a portable, multiplexed sensor to detect toxic metals in urine via

SERS, and demonstrates the viability of the proposed mechanic of targeting toxic metal ions with crown ethers and detecting them by SERS. This work will ultimately be instrumental in comprehensively monitoring military personnel with embedded fragments and developing a clearer understanding of the short- and long-term health effects of embedded fragments.

## APPENDIX A

### SUPPLEMENTARY INFORMATION FOR CHAPTER II

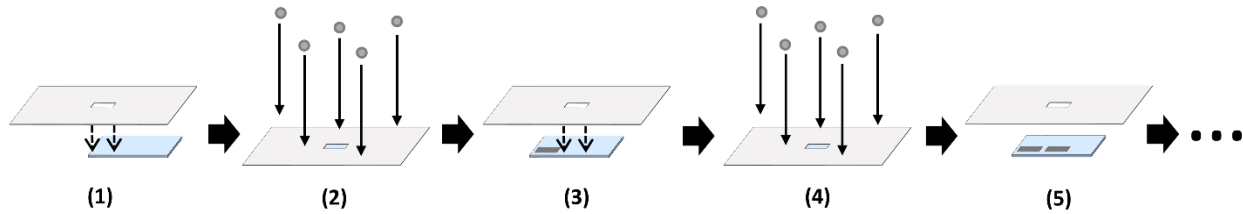


**Figure A.1:** Illustration of the Ag deposition process. Masks cut from aluminum foil were placed on top of each substrate in step (1) such that only a small portion of the substrates was exposed. Ag was then e-beam deposited in step (2), after which the masks were moved to expose a new portion of each substrate in step (3). Ag was again deposited in step (4), and the process was repeated from step (5) onward until 9 Ag films of different thicknesses were deposited on each substrate.

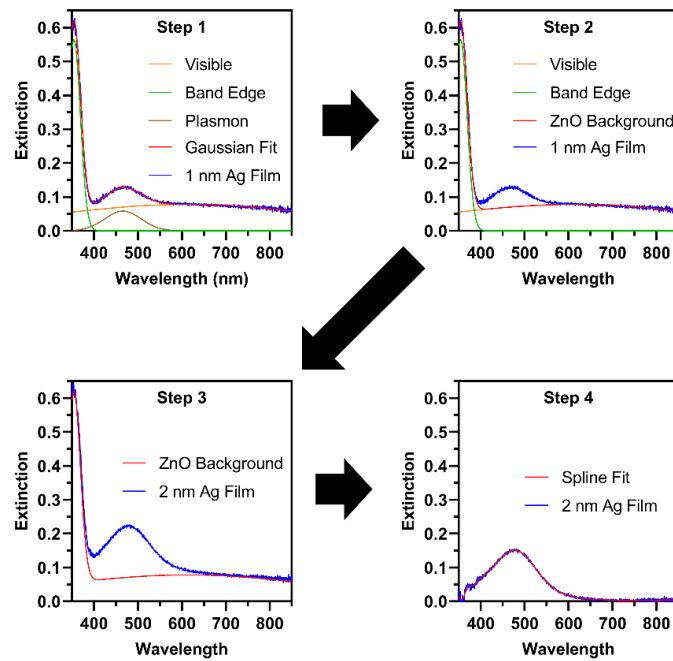


**Figure A.2:** Process for isolating Ag nanoparticle plasmon extinction, in which (Step 1) extinction spectra for 1-nm Ag films on each substrate were approximated with a tri-gaussian fit, (Step 2) the gaussian peaks associated with ZnO background were determined and summed, then (Step 3) subtracted from each film thickness on each substrate. The resultant plasmon peak was (Step 4) approximated with a spline fit to determine peak information.



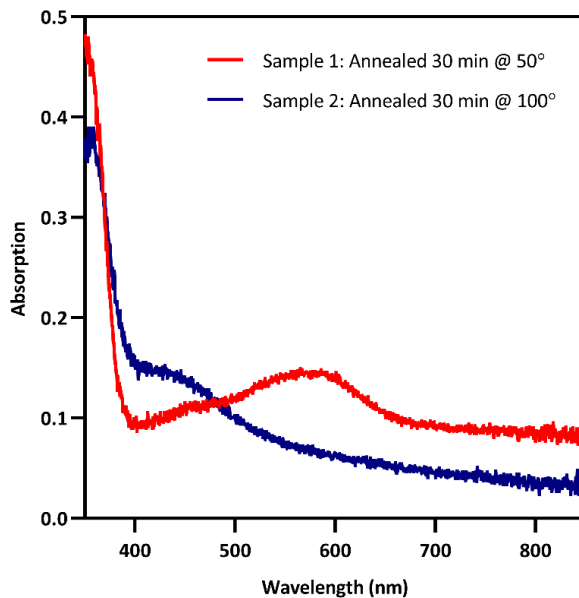


**Figure A.3:** UV-Vis of two Ag-decorated ZnO samples, illustrating the variability in ZnO absorptive background induced by the fabrication and anneal process

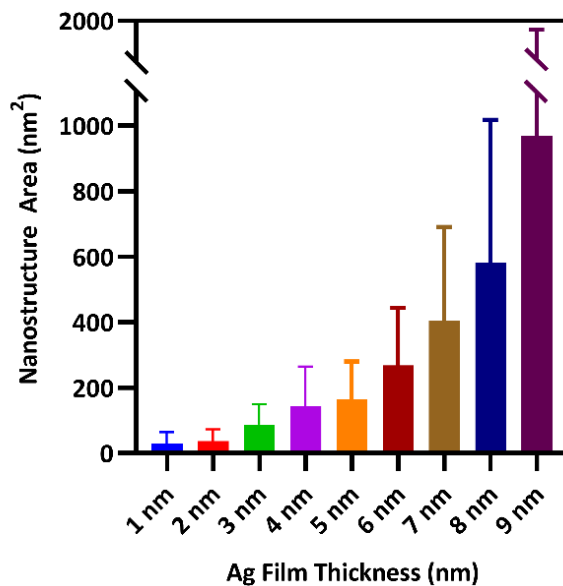


**Figure A.4:** Average area of nanostructures for each Ag film thickness, demonstrating increasing nanostructure size with increasing film thickness.

**Table A.1:** Benzene and non-benzene vibrational modes associated with crystal violet Raman peaks.  $\gamma$  = torsion,  $\delta$  = bending,  $\nu$  = stretching,  $\sigma$  = scissoring,  $\rho$  = rocking;  $s$  = symmetric,  $as$  = asymmetric

Raman Band (cm <sup>-1</sup> )	Non-Benzene Vibrational Modes	Benzene	Reference
208	$\gamma(\text{C-H})/\text{whole molecule breathing}$		187
225	$\nu_s(\text{C-C}_{\text{center-C}})$		188
345	$\gamma(\text{C-N-C})/\delta(\text{C-C}_{\text{center-C}})_l$		187–191
420	$\delta(\text{C-C}_{\text{center-C}})/\delta(\text{C-N-C})_l$	16a	187–190,192
441	$\delta(\text{C-C-C})_{\text{ring},l}/\delta(\text{C-N-C})/\delta_{as}(\text{C-C}_{\text{center-C}})_l$	16a	187,190–192
525	$\delta(\text{C-N-C})$	16b,6b	187,189,190
571	$\delta(\text{C-C-C})_l/\delta(\text{C-N-C})/\delta(\text{C-C}_{\text{center-C}})$	6a	187,189,190
605	$\delta(\text{C-C-C})/\delta(\text{C-N-C})/\nu_s(\text{C-C}_{\text{center-C}})$	6a	187,190
623		6b	187
730	$\nu_s(\text{C-N-C})$	4,17b	187,188,190
761	$\nu_s(\text{C-C}_{\text{center-C}})/\nu(\text{C-N-C})$	6a,17a	187,188,190
810		10a	187–190,192,193
825		10b,17b	187,189,190
915	$\delta(\text{C-C}_{\text{center-C}})$	12,17a	187,189,190,192
980		17a,18a	187,190
990	$\delta(\text{C-C-C})$	1	187,190
1130	$\delta(\text{C-C}_{\text{center-C}})/\nu(\text{C-N})$	15	187,188
1175	$\nu_{as}(\text{C-C}_{\text{center-C}})$	9a,9b	187–193
1300	$\nu(\text{C-C-C})/\delta(\text{C-C-C})_{\text{ring}}/\delta(\text{C-H})$		187,188,193
1345	$\delta(\text{C-N})/\delta(\text{C-C-C})_{\text{ring}}/\nu_{as}(\text{C-C}_{\text{center-C}})/\delta(\text{C-H})$		187
1374	$\nu(\text{C-N})/\nu_{as}(\text{C-C}_{\text{center-C}})/\delta(\text{C-H})$		187–193
1445	$\delta_{as}(\text{C-H}_3)$	19b	187–190
1490	$\delta_{as}(\text{C-H}_3)$	19a	187,189,190
1529	$\nu(\text{C}_{\text{ring-N}})/\delta_s(\text{C-H}_3)$	8b	187,188,191–193
1592		8a	187,188,190–193
1621		8a	187,188,190–193

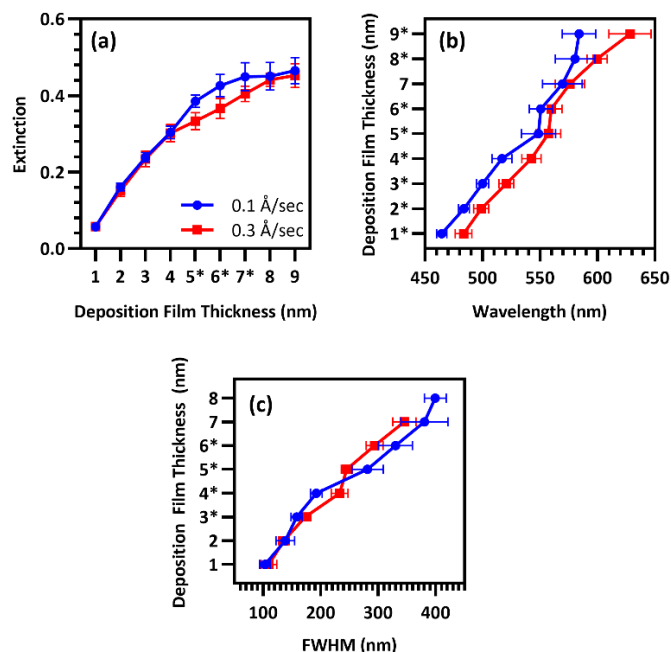


**Figure A.5:** Means of (a)peak intensity ( $n = 40$ ), (b)plasmon peak wavelength ( $n = 40$ ), and (c)plasmon peak FWHM for each film thickness of Group A (blue) and Group B (red). Statistical testing performed with two-way ANOVA,  $*p = 0.05$ .

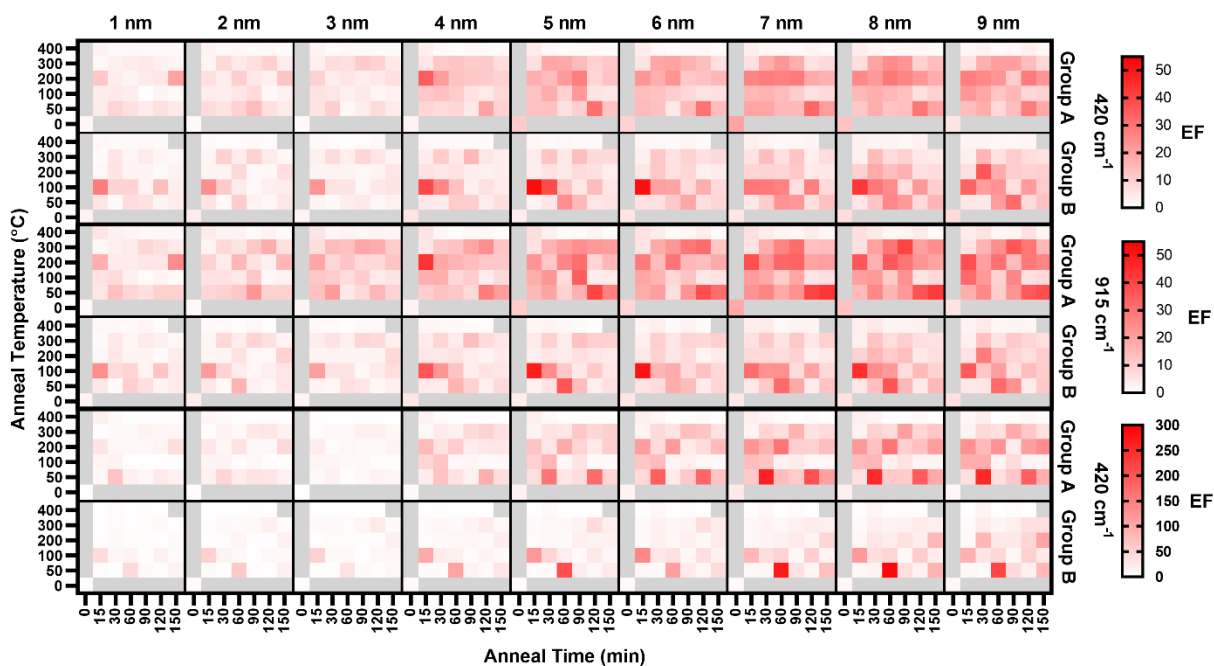


**Figure A.6:** Enhancement Factors for three analyzed peaks of the CV SERS spectra of each film thickness on each annealed substrate and the unannealed control for each rate group.

APPENDIX B

SUPPLEMENTARY INFORMATION FOR CHAPTER III

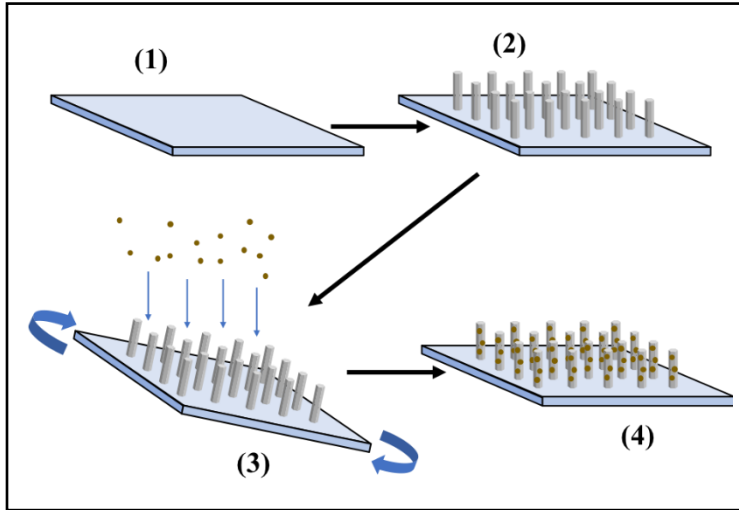


**Figure B.1:** Illustration of the Ag/ZnO nanoprobe fabrication process for PDMS substrates: (1) deposit 100-nm ZnO seed layer on PDMS, (2) hydrothermally grow ZnO nanowires, and (3) deposit Ag on the nanowires on an azimuthally rotated sample to get (4) a finished Ag/ZnO nanoprobe.

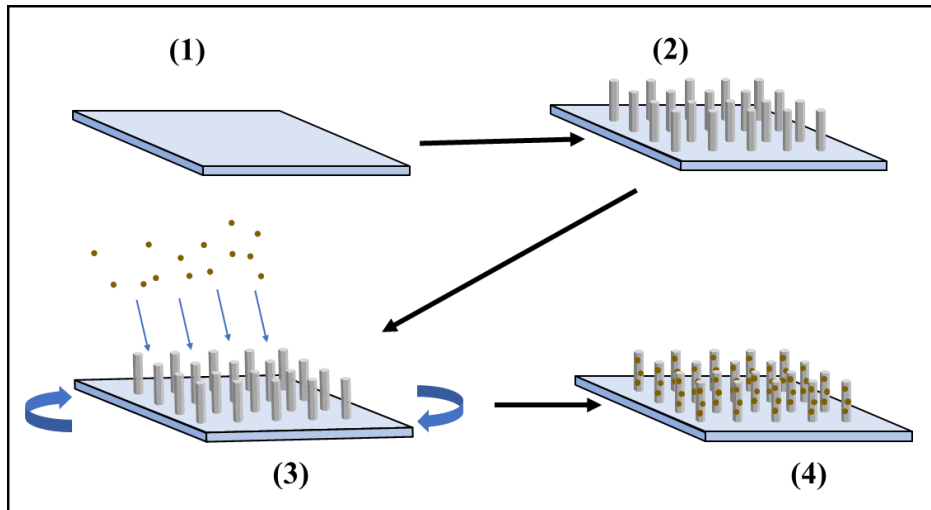


**Figure B.2:** Illustration of the Ag/ZnO nanoprobe fabrication process for PDMS channels: (1) deposit 100-nm ZnO seed layer on PDMS, (2) hydrothermally grow ZnO nanowires, and (3) deposit Ag from an angle on the nanowires inside a rotated channel to get (4) a finished Ag/ZnO nanoprobe.

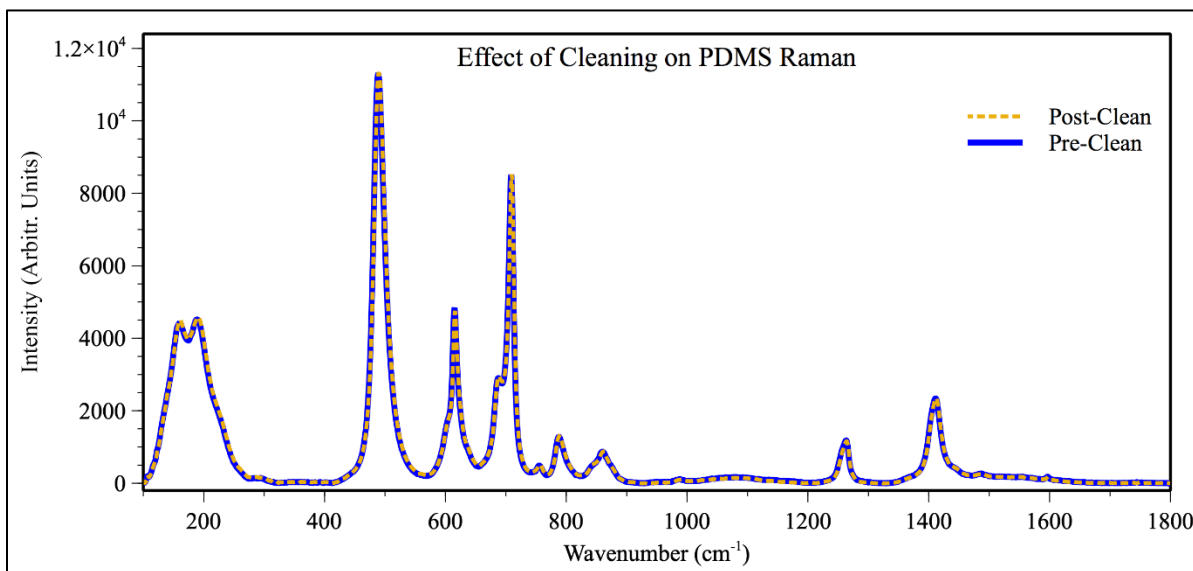


**Figure B.3:** Raman spectra of PDMS before and after the ALD-AMD cleaning process, demonstrating no spectral effects due to cleaning.

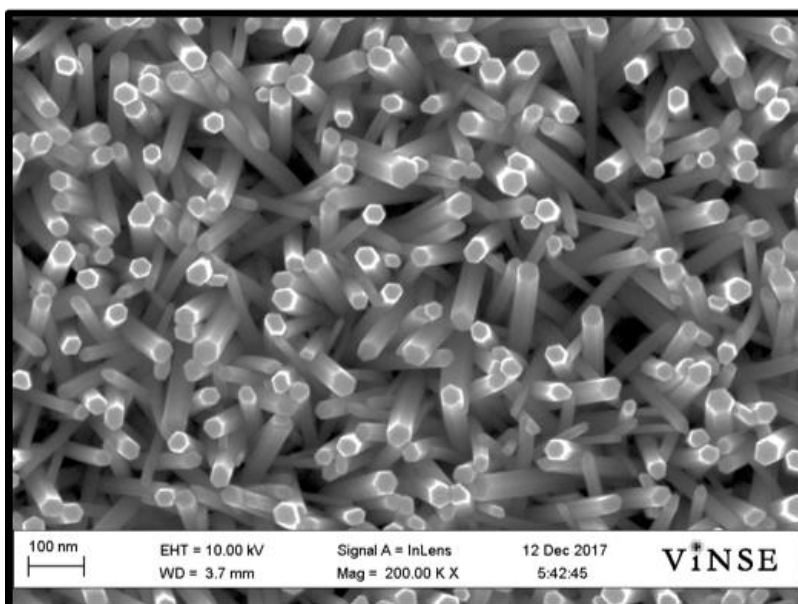


**Figure B.4:** SEM image of bare ZnO nanowires, exhibiting highly crystalline nanowires.

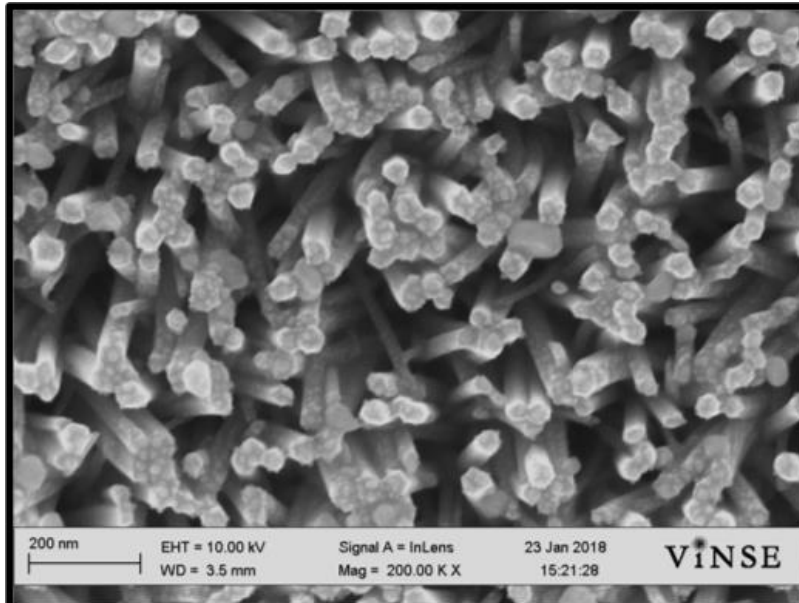


**Figure B.5:** SEM image of ZnO nanowires after Ag nanoparticle decoration, demonstrating dense nanoparticle formation on the sides of nanowires.

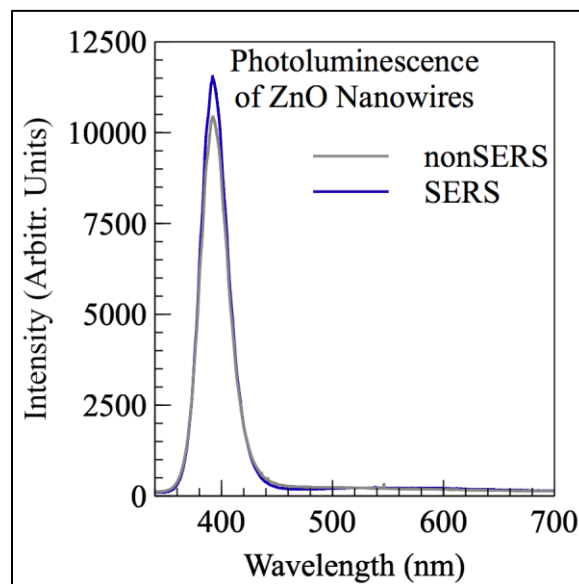


**Figure B.6:** PL of ZnO nanowires to be decorated with Ag nanoparticles and those to remain bare, demonstrating highly crystalline nature of the nanowires and the similarity between the two sets of nanowires.

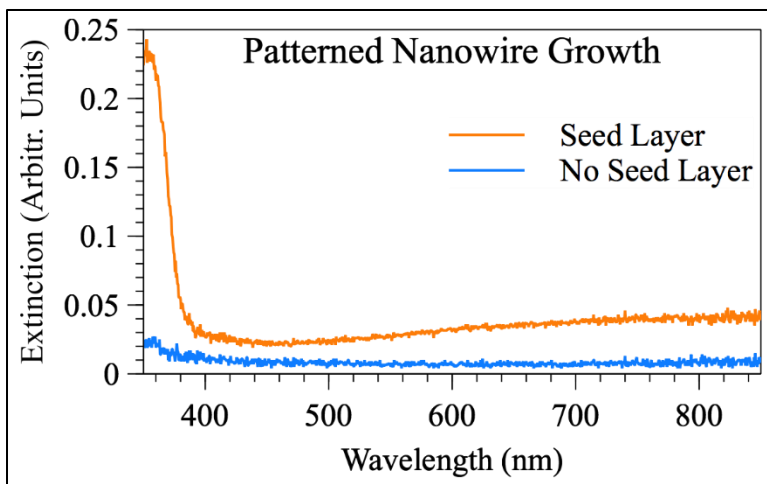


**Figure B.7:** UV-Vis extinction spectra after nanowire growth of the seeded and non-seeded portions of a patterned PDMS substrate, demonstrating the ability to pattern nanowire growth on PDMS by patterning the seed layer.

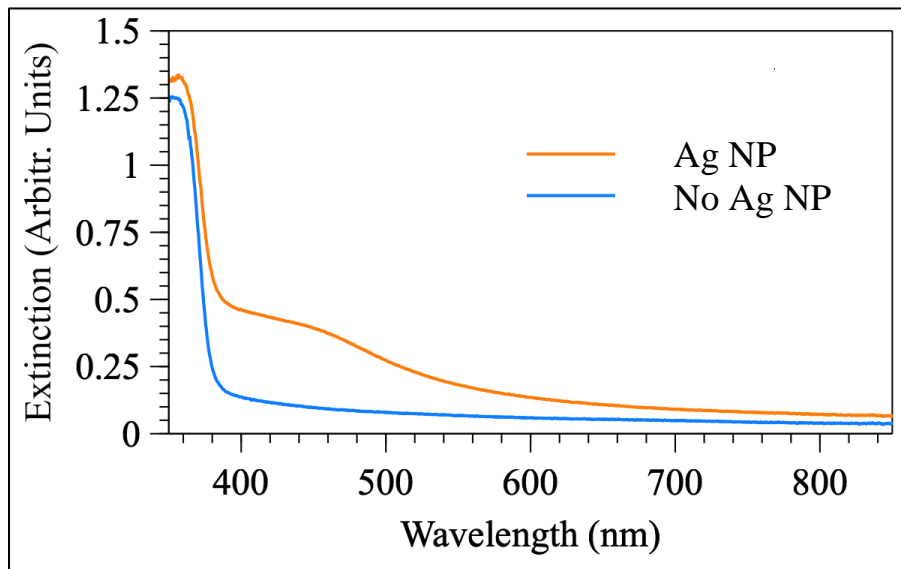


**Figure B.8:** UV-Vis extinction spectra of Ag/ZnO nanoprobe before and after Ag deposition, demonstrating the formation of plasmons, centered at ~450 nm.

**Table B.1:** Vibrational modes of PDMS in the fingerprint region:  $\gamma$  = torsion,  $\delta$  = bending,  $\nu$  = stretching,  $\sigma$  = scissoring,  $\rho$  = rocking; s = symmetric, as = asymmetric,  $\perp$  = out-of-plane,  $\parallel$  = in-plane

Raman Band ( $\text{cm}^{-1}$ )	Vibrational Modes	Reference
160	$\gamma_{\text{as}}(\text{C-Si-C})$	178,179
188	$\delta(\text{C-Si-C})/\delta(\text{C-Si-O})/\gamma_{\text{s}}(\text{C-Si-C})/\rho(\text{C-Si-C})/\sigma(\text{C-Si-C})$	175,178,179
488	$\nu_{\text{s}}(\text{Si-O-Si})$	175-179
615	$\nu(\text{Si-O-Si})/\nu(\text{Si-C})$	178
646	$\rho_{\text{as}}(\text{Si-C}_3)$	176
687	$\nu(\text{Si-C})/\rho(\text{C-H}_3)$	175,178,179
708	$\nu\text{-s}(\text{Si-C})/\delta(\text{C-H}_3)$	176-178
754	$\rho(\text{C-H}_3)/\rho_{\text{s}}(\text{Si-C}_3)/\nu(\text{Si-C})$	175,176,178
787	$\rho_{\text{as}}(\text{C-Si-C})/\nu_{\text{as}}(\text{C-Si-C})/\rho(\text{C-H}_3)$	176-179
845	$\rho_{\text{as}}(\text{C-Si-C})$	176
859	$\rho(\text{C-Si-C})/\rho(\text{C-H}_3)$	176-179
882	$\rho_{\text{as}}(\text{Si-C}_3)/\rho_{\text{as}}(\text{C-Si-C})$	176
1088	$\nu_{\text{as}}(\text{Si-O-Si})$	176
1262	$\delta_{\text{s}}(\text{C-H}_3)/\delta(\text{C-H}_2)$	176-179
1411	$\delta_{\text{as}}(\text{C-H}_3)/\delta(\text{C-H}_2)/\sigma(\text{C-H}_2)$	175-179

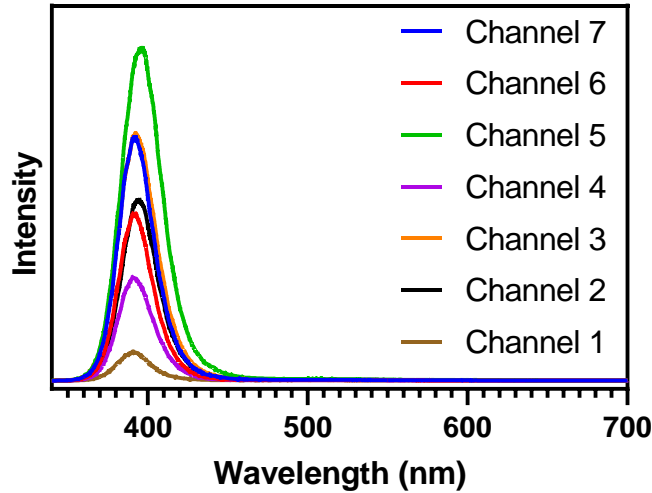


**Figure B.9:** Photoluminescence spectra of ZnO nanowires in 7 different PDMS channels, demonstrating variability in ZnO nanowire structure, though each still exhibits high crystallinity with few defects.



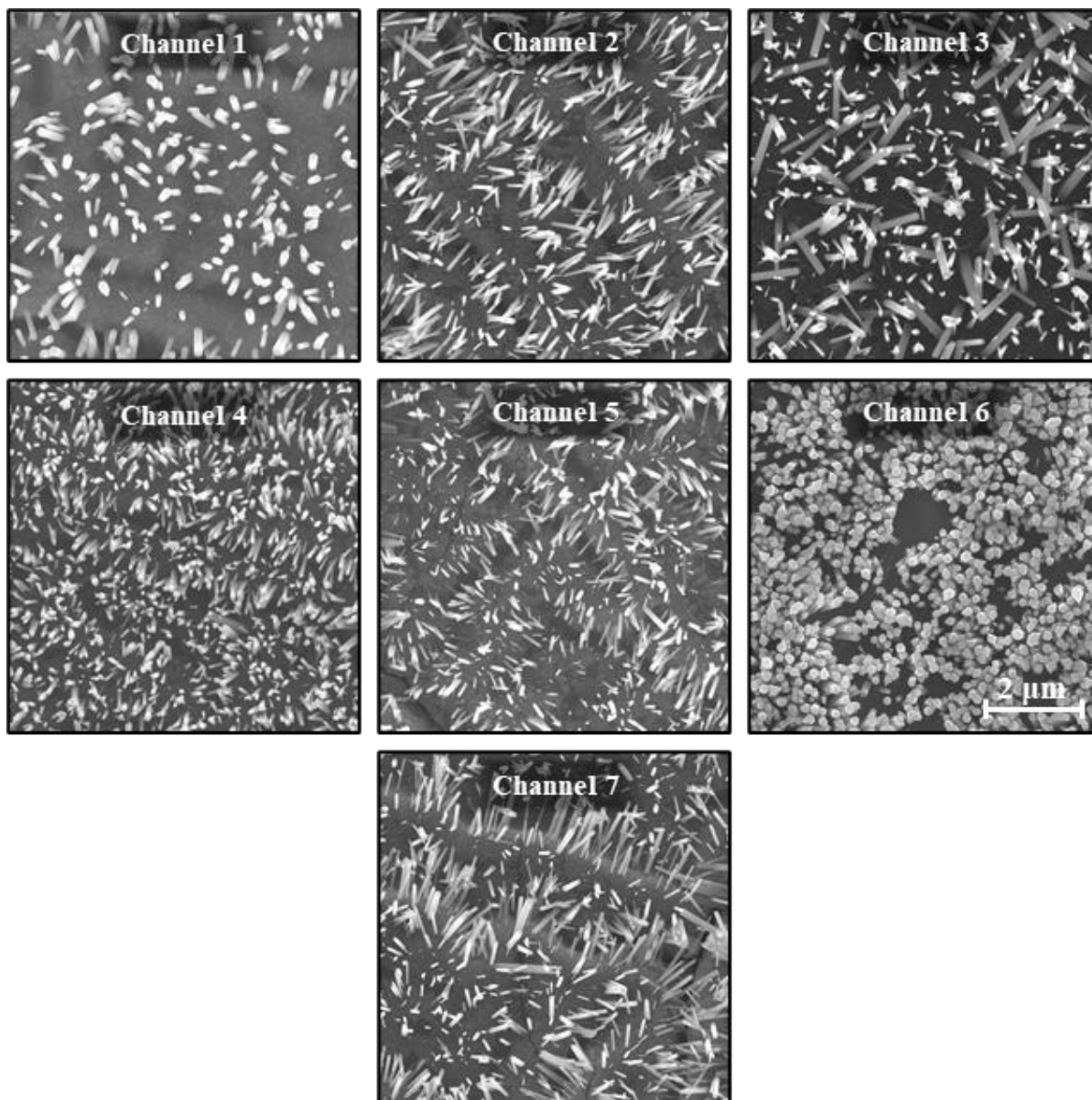


**Figure B.10:** SEM images of nanowires within PDMS channels on sputtered ZnO seed layers, illustrating the variability of nanowire growth on sputtered seed layers.

**Table B.2:** Vibrational modes of melamine in the fingerprint region:  $\gamma$  = torsion,  $\delta$  = bending,  $\nu$  = stretching,  $\sigma$  = scissoring; s = symmetric,  $\perp$  = out-of-plane

Raman Band ( $\text{cm}^{-1}$ )	Vibrational Modes	Reference
380	$\delta(\text{C-N})$	180,181
691	Ring Breathing	180,181
845	$\delta_{\perp}(\text{Ring})$	180,181
1235	$\delta(\text{N-H})$	181
1390	$\sigma(\text{NH}_2)/\nu(\text{C-N})/\delta_s(\text{Ring})$	181
1595	$\delta(\text{NH}_2)/\delta(\text{N-C-N})$	180

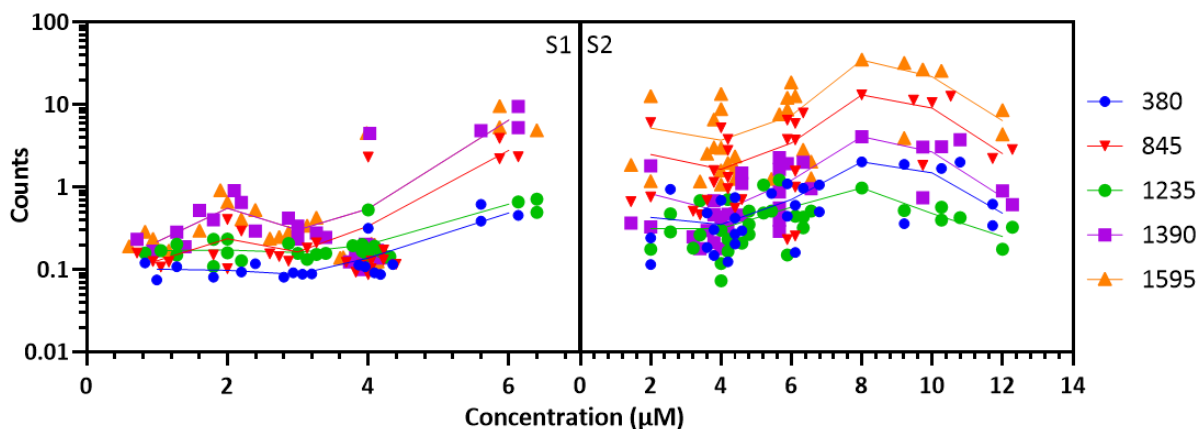


**Figure B.11:** Ratios of each melamine peak with the PDMS peak at 488  $\text{cm}^{-1}$  for each substrate, illustrating the consistency of melamine peak intensities relative to the overall signal intensity for each measurement.

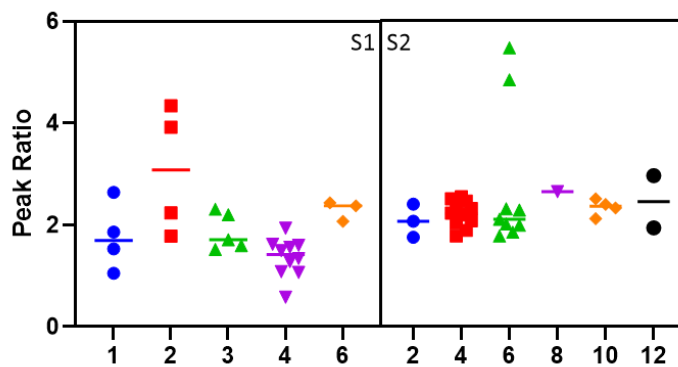


**Figure B.12:** Ratios of melamine peaks at 1595  $\text{cm}^{-1}$  to 845  $\text{cm}^{-1}$  for each melamine concentration measured for each substrate, illustrating internal signal consistency for all concentrations measured, and across substrates.

## APPENDIX C

### ADDITIONAL RESEARCH PERFORMED

#### Functionalizing Silver-Decorated Zinc Oxide Nanowires with 4'-Aminobenzo-18-Crown-6

Preliminary attempts were made to functionalize Ag-decorated ZnO nanowires with AB18C6. A 10- $\mu$ M solution of AB18C6 was prepared in 1:3 DMSO:DI water and a portion of that solution was set aside for future analysis as a positive control. An Ag-decorated ZnO nanowire substrate grown on fused silica was placed in this solution and the solution was stirred for 60 min before being incubated overnight at room temperature to facilitate functionalization. The substrate was then pulled out of the solution and the residual fluid was washed off with DI water. Crown ether solution was taken after incubation with the SERS substrate. UV-vis (**Figure C.1**: UV-vis spectra of the 100  $\mu$ M AB18C6 solution in 1:3 DMSO:DI water before and after incubation with an Ag-decorated ZnO nanowire substrate, with a spectrum of the solvent as a negative control

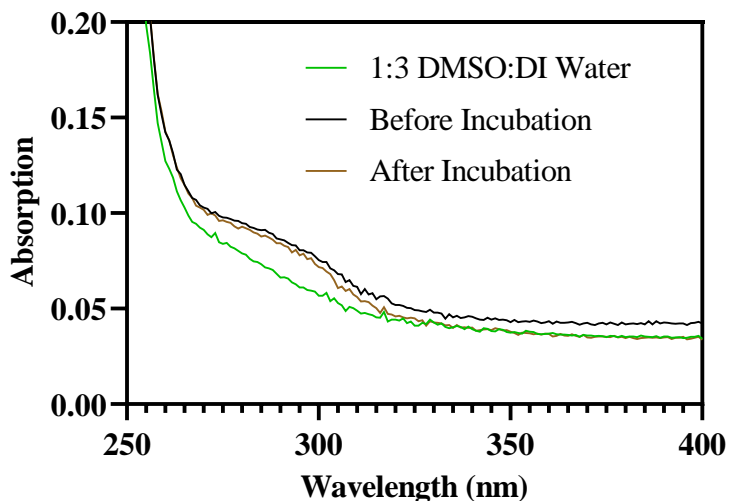


**Figure C.1:** UV-vis spectra of the 100  $\mu$ M AB18C6 solution in 1:3 DMSO:DI water before and after incubation with an Ag-decorated ZnO nanowire substrate, with a spectrum of the solvent as a negative control

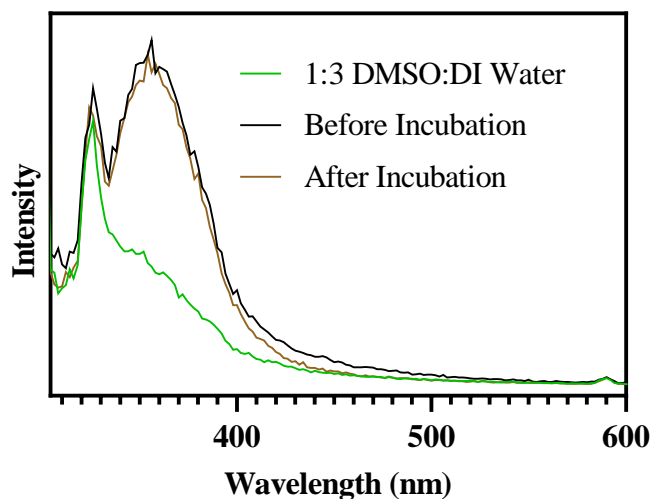


**Figure C.2:** UV-vis spectra of the 100  $\mu\text{M}$  AB18C6 solution in 1:3 DMSO:DI water before and after incubation with an Ag-decorated ZnO nanowire substrate, with a spectrum of the solvent as a negative control

negative control) and fluorescence spectra (**Figure C.2:** UV-vis spectra of the 100  $\mu\text{M}$  AB18C6 solution in 1:3 DMSO:DI water before and after incubation with an Ag-decorated ZnO nanowire substrate, with a spectrum of the solvent as a negative control) were acquired from solutions set aside before and after SERS surface functionalization, as well as 1:3 DMSO:DI water alone. The UV-vis spectrum for the post-incubation crown ether solution exhibits a decrease in intensity as compared to pre-incubation crown ether solution, which indicates that some of the crown ethers were attached to the sensing surface. The fluorescence spectrum for the post-incubation crown ether solution likewise exhibits a decrease in fluorescent intensity over the positive control, confirming that some crown ether was retained by the sensing surface.

## REFERENCES

- 1 J. Aurell, B. K. Gullett and D. Yamamoto, *Environmental Science & Technology*, 2012, **46**, 11004–11012.
- 2 J. M. Gaitens, J. A. Centeno, K. S. Squibb, M. Condon and M. A. McDiarmid, *Military Medicine*, 2016, **181**, e625–e629.
- 3 I. of Medicine, in *Gulf War and Health, Volume 9: Long-Term Effects of Blast Exposures*, National Academies Press, Washington, D.C., 2014, pp. 13–20.
- 4 I. of Medicine, in *Gulf War and Health, Volume 9: Long-Term Effects of Blast Exposures*, National Academies Press, Washington, D.C., 2014, pp. ix–xii.
- 5 M. A. Kane, C. E. Kasper and J. F. Kalinich, *Military Medicine*, 2009, **174**, 265–269.
- 6 D. P. Arfsten, K. R. Still, E. R. Wilfong, E. W. Johnson, S. M. McInturf, J. S. Eggers, D. J. Schaeffer and M. Y.-V. Bekkedal, *Journal of Toxicology and Environmental Health, Part A*, 2009, **Journal of**, 410–427.
- 7 J. Centeno, D. Rogers, G. van der Voet, E. Fornero, L. Zhang, F. Mullick, G. Chapman, A. Olabisi, D. Wagner, A. Stojadinovic and B. Potter, *International Journal of Environmental Research and Public Health*, 2014, **11**, 1261–1278.
- 8 S. Skaik, N. Abu-Shaban, N. Abu-Shaban, M. Barbieri, M. Barbieri, U. Giani and P. Manduca, *BMC International Health and Human Rights*, 2010, **10**, 17.
- 9 J. F. Kalinich and C. E. Kasper, *Public Health Reports*, 2016, **131**, 831–833.
- 10 C. A. Emond and J. F. Kalinich, *Health Physics*, 2012, **102**, 124–136.
- 11 J. F. Kalinich, V. B. Vergara and C. A. Emond, *Military Medicine*, 2008, **173**, 754–758.
- 12 C. B. Weese, *U.S. Army Medical Department Journal*, 2010, 22–29.
- 13 G. Taylor, V. Rush and A. Deck, *Screening Health Risk Assessment Burn Pit Exposures, Balad Air Base, Iraq and Addendum Report and Addendum Report*, 2008.
- 14 A. M. Szema, *Occupational medicine & health affairs*, , DOI:10.4172/2329-6879.1000117.
- 15 C. Rose, J. Abraham, D. Harkins, R. Miller, M. Morris, L. Zacher, R. Meehan, A. Szema, J. Tolle, M. King, D. Jackson, J. Lewis, A. Stahl, M. B. Lyles, M. Hodgson, R. Teichman, W. Salihi, G. Matwiyoff, G. Meeker, S. Mormon, K. Bird and C. Baird, *Journal of Occupational and Environmental Medicine*, 2012, **54**, 746–751.
- 16 J. Liu, N. Lezama, J. Gasper, J. Kawata, S. Morley, D. Helmer and P. Ciminera, *Journal of Occupational and Environmental Medicine*, 2016, **58**, e249–e255.
- 17 A. M. S. Conlin, C. DeSciociolo, C. J. Sevick, A. T. Bukowinski, C. J. Phillips and T. C. Smith, *Journal of Occupational and Environmental Medicine*, 2012, **54**, 689–697.
- 18 M. J. Falvo, O. Y. Osinubi, A. M. Sotolongo and D. A. Helmer, *Epidemiologic Reviews*, 2015, **37**, 116–130.
- 19 C. B. Weese and J. H. Abraham, *Inhalation Toxicology*, 2009, **21**, 291–296.
- 20 P. Kelleher, K. Pacheco and L. S. Newman, *Environmental Health Perspect*, 2000, **108**, 8685–8696.
- 21 B. Smith, C. A. Wong, E. J. Boyko, C. J. Phillips, G. D. Gackstetter, M. A. K. Ryan and T. C. Smith, *Journal of Occupational and Environmental Medicine*, 2012, **54**, 708–716.
- 22 T. M. Powell, T. C. Smith, I. G. Jacobson, E. J. Boyko, T. I. Hooper, G. D. Gackstetter, C. J. Phillips and B. Smith, *Journal of Occupational and Environmental Medicine*, 2012, **54**, 682–688.
- 23 P. Rohrbeck, Z. Hu and C. T. M. Mallon, *Journal of Occupational and Environmental Medicine*, 2016, **58**, S104–S110.
- 24 G. A. Loh, D. G. Bell and M. J. Morris, *Current Pulmonology Reports*, 2016, **5**, 86–93.

- 25M. J. Morris, L. L. Zacher and D. A. Jackson, *Military Medicine*, 2011, **176**, 1157–1161.
- 26J. M. Gaitens and M. A. McDiarmid, in *Airborne Hazards Related to Deployment*, eds. Borden Institute, C. P. Baird and D. K. Harkins, Government Printing Office, 2015, pp. 245–251.
- 27J. M. Gaitens, M. Condon, K. S. Squibb, J. A. Centeno and M. A. McDiarmid, *Journal of Occupational & Environmental Medicine*, 2017, **59**, 1056–1062.
- 28J. F. Kalinich, E. A. Vane, J. A. Centeno, J. M. Gaitens, K. S. Squibb, M. A. McDiarmid and C. E. Kasper, in *Annual Review of Nursing Research, Volume 32, 2014: Military and Veteran Innovations of Care*, ed. P. W. Kelley, Springer Publishing Co., New York, NY, 2014, pp. 63–78.
- 29J. M. Gaitens, C. D. Dorsey and M. A. McDiarmid, *European Journal of Oncology*, 2010, **15**, 77–90.
- 30H. T. Temiz, I. H. Boyaci, I. Grabchev and U. Tamer, *Spectrochimica Acta Part A: Molecular and Biomolecular Spectroscopy*, 2013, **116**, 339–347.
- 31O. O. Soldatkin, I. S. Kucherenko, V. M. Pyeshkova, A. L. Kukla, N. Jaffrezic-Renault, A. V. El'skaya, S. V. Dzyadevych and A. P. Soldatkin, *Bioelectrochemistry*, 2012, **83**, 25–30.
- 32C. P. Baird, *The Army Medical Department Journal*, 2013, 46–52.
- 33Evans Analytical Group, ICP-OES and ICP-MS Detection Limit Guidance, [http://www.nanoscience.co.jp/surface\\_analysis/pdf/icp-oes-ms-detection-limit-guidance-BR023.pdf](http://www.nanoscience.co.jp/surface_analysis/pdf/icp-oes-ms-detection-limit-guidance-BR023.pdf), (accessed March 28, 2018).
- 34S. J. Hill, T. A. Arowolo, O. T. Butler, S. R. N. Chenery, J. M. Cook, M. S. Cresser and D. L. Miles, *Journal of Analytical Atomic Spectrometry*, 2002, **17**, 284–317.
- 35K. L. Nuttall, W. H. Gordon, K. O. Ash and E. Ash, *Annals Of Clinical And Laboratory Science*, 1995, **25**, 264–271.
- 36E. M. Nolan and S. J. Lippard, *Chemical Reviews*, 2008, **108**, 3443–3480.
- 37J. Guo, Y. Chai, R. Yuan, Z. Song and Z. Zou, *Sensors and Actuators B: Chemical*, 2011, **155**, 639–645.
- 38M. H. Mashhadizadeh and H. Khani, *Anal. Methods*, 2010, **2**, 24–31.
- 39M. R. Ganjali, S. Aghabalazadeh, M. Khoobi, A. Ramazani, A. Foroumadi, A. Shafiee and P. Norouzi, *Int. J. Electrochem. Sci*, 2011, **6**, 52–62.
- 40V. Kumar Gupta, B. Sethi, N. Upadhyay, S. Kumar, R. Singh and L. P. Singh, *Int. J. Electrochem. Sci*, 2011, **6**, 650–663.
- 41M. H. Mashhadizadeh and R. P. Talemi, *Analytica Chimica Acta*, 2011, **692**, 109–115.
- 42B. Bansod, T. Kumar, R. Thakur, S. Rana and I. Singh, *Biosensors and Bioelectronics*, 2017, **94**, 443–455.
- 43P. Kumar, K.-H. Kim, V. Bansal, T. Lazarides and N. Kumar, *Journal of Industrial and Engineering Chemistry*, 2017, **54**, 30–43.
- 44A. Downes and A. Elfick, *Sensors (Basel, Switzerland)*, 2010, **10**, 1871–89.
- 45L. Fabris, *ChemNanoMat*, 2016, **2**, 249–258.
- 46C. V. Raman and K. S. Krishnan, *Nature*, 1928, **121**, 501–502.
- 47Raman Spectroscopy, [https://en.wikipedia.org/wiki/Raman\\_spectroscopy](https://en.wikipedia.org/wiki/Raman_spectroscopy), (accessed July 5, 2018).
- 48A. F. Chrimes, K. Khoshmanesh, P. R. Stoddart, A. Mitchell and K. Kalantar-zadeh, *Chemical Society reviews*, 2013, **42**, 5880–5906.
- 49M. Fleischmann, P. J. Hendra and A. J. McQuillan, *Chemical Physics Letters*, 1974, **26**, 163–166.

- 50I. J. Jahn, O. Žukovskaja, X.-S. Zheng, K. Weber, T. W. Bocklitz, D. Cialla-May and J. Popp, *The Analyst*, 2017, **142**, 1022–1047.
- 51A. Campion and P. Kambhampati, *Chemical Society Reviews*, 1998, **27**, 241.
- 52K. Kneipp, H. Kneipp and J. Kneipp, *Accounts of chemical research*, 2006, **39**, 443–50.
- 53J. R. Lombardi, R. L. Birke, T. Lu and J. Xu, *The Journal of Chemical Physics*, 1986, **84**, 4174.
- 54A. Esmailzadeh Kandjani, Y. M. Sabri, M. Mohammad-Taheri, V. Bansal and S. K. Bhargava, *Environmental Science & Technology*, 2015, **49**, 1578–1584.
- 55L. Chen, N. Qi, X. Wang, L. Chen, H. You and J. Li, *RSC Adv.*, 2014, **4**, 15055–15060.
- 56Y. Du, R. Liu, B. Liu, S. Wang, M.-Y. Han and Z. Zhang, *Analytical Chemistry*, 2013, **85**, 3160–3165.
- 57Y. Wang and J. Irudayaraj, *Chemical Communications*, 2011, **47**, 4394.
- 58Y. Shi, H. Wang, X. Jiang, B. Sun, B. Song, Y. Su and Y. He, *Analytical Chemistry*, 2016, **88**, 3723–3729.
- 59Y.-H. Sun, R.-M. Kong, D.-Q. Lu, X.-B. Zhang, H.-M. Meng, W. Tan, G.-L. Shen and R.-Q. Yu, *Chemical Communications*, 2011, **47**, 3840.
- 60M. Liu, Z. Wang, S. Zong, H. Chen, D. Zhu, L. Wu, G. Hu and Y. Cui, *ACS Applied Materials & Interfaces*, 2014, **6**, 7371–7379.
- 61L. Xu, H. Yin, W. Ma, H. Kuang, L. Wang and C. Xu, *Biosensors and Bioelectronics*, 2015, **67**, 472–476.
- 62C. E. McGhee, K. Y. Loh and Y. Lu, *Current Opinion in Biotechnology*, 2017, **45**, 191–201.
- 63D.-W. Li, W.-L. Zhai, Y.-T. Li and Y.-T. Long, *Microchimica Acta*, 2014, **181**, 23–43.
- 64M. Shaban, A. G. A. Hady and M. Serry, *IEEE Sensors Journal*, 2014, **14**, 436–441.
- 65M. S. Frost, Michael. J. Dempsey and D. E. Whitehead, *Sensors and Actuators B: Chemical*, 2015, **221**, 1003–1008.
- 66C. Ruan, W. Luo, W. Wang and B. Gu, *Analytica Chimica Acta*, 2007, **605**, 80–86.
- 67P. A. Mosier-Boss and M. D. Putnam, *Analytica Chimica Acta*, 2013, **801**, 70–77.
- 68Q. Zhou and T. Kim, *Sensors and Actuators B: Chemical*, 2016, **227**, 504–514.
- 69D. Lee, S. Lee, G. Hun Seong, J. Choo, E. Kyu Lee, D. Gweon and S. Lee, *Applied Spectroscopy*, 2006, **60**, 373–377.
- 70B. L. Darby and E. C. Le Ru, *Journal of the American Chemical Society*, 2014, **136**, 10965–10973.
- 71J.-A. Huang, Y.-L. Zhang, H. Ding and H.-B. Sun, *Advanced Optical Materials*, 2015, **3**, 618–633.
- 72H. Hwang, D. Han, Y.-J. Oh, Y.-K. Cho, K.-H. Jeong and J.-K. Park, *Lab on a Chip*, 2011, **11**, 2518.
- 73J. Zhou, K. Ren, Y. Zhao, W. Dai and H. Wu, *Analytical and Bioanalytical Chemistry*, 2012, **402**, 1601–1609.
- 74P. Yang, H. Yan, S. Mao, R. Russo, J. Johnson, R. Saykally, N. Morris, J. Pham, R. He and H.-J. Choi, *Advanced Functional Materials*, 2002, **12**, 323–331.
- 75D. C. Mayo, C. E. Marvinney, E. S. Bililign, J. R. McBride, R. R. Mu and R. F. Haglund, *Thin Solid Films*, 2014, **553**, 132–137.
- 76J. N. Anker, W. P. Hall, O. Lyandres, N. C. Shah, J. Zhao and R. P. Van Duyne, *Nature materials*, 2008, **7**, 442–53.
- 77J. W. Steed, *Coordination Chemistry Reviews*, 2001, **215**, 171–221.

- 78D. K. Sarfo, E. L. Izake, A. P. O'Mullane and G. A. Ayoko, *Sensors and Actuators B: Chemical*, 2018, **255**, 1945–1952.
- 79Y. Qian, Z. Zhang, W. Tian, L. Wen and L. Jiang, *Faraday Discuss.*, 2018, **210**, 101–111.
- 80D. K. Sarfo, A. Sivanesan, E. L. Izake and G. A. Ayoko, *RSC Adv.*, 2017, **7**, 21567–21575.
- 81M. Ansari Fard, G. H. Rounaghi, M. Chamsaz and K. Taheri, *J Incl Phenom Macrocycl Chem*, 2009, **64**, 49–56.
- 82H. J. Carmichael, *Journal of the Optical Society of America B*, 1987, **4**, 1588.
- 83M. R. Chedekel, S. K. Smith, P. W. Post, A. Pokora and D. L. Vessell, *Proceedings of the National Academy of Sciences of the United States*, 1978, **75**, 5395–5399.
- 84A. Savitzky and M. J. E. Golay, *Analytical Chemistry*, 1964, **36**, 1627–1639.
- 85L. Zhang and M. J. Henson, *Applied Spectroscopy*, 2007, **61**, 1015–1020.
- 86L. A. Austin, S. Osseiran and C. L. Evans, *The Analyst*, 2016, **141**, 476–503.
- 87C. A. Lieber and A. Mahadevan-Jansen, *Applied Spectroscopy, Vol. 57, Issue 11, pp. 1363-1367*, 2003, **57**, 1363–1367.
- 88M. N. Leger and A. G. Ryder, *Applied Spectroscopy*, 2006, **60**, 182–193.
- 89H. Fischer, *A Guide to U.S. Military Casualty Statistics: Operation Freedom's Sentinel, Operation Inherent Resolve, Operation New Dawn, Operation Iraqi Freedom, and Operation Enduring Freedom*, 2015.
- 90K. Cavanaugh, 2018.
- 91A. L. Cook, C. P. Haycook, A. K. Locke, R. R. Mu and T. D. Giorgio, *Nanoscale Adv.*, 2021, 407–417.
- 92S. Jayabal, A. Pandikumar, H. N. Lim, R. Ramaraj, T. Sun and N. M. Huang, *Analyst*, 2015, **140**, 2540–2555.
- 93M. S. Frost, Michael. J. Dempsey and D. E. Whitehead, *Sens. Actuators B Chem.*, 2015, **221**, 1003–1008.
- 94Y. Zeng, J. Ren, A. Shen and J. Hu, *ACS Appl. Mater. Inter.*, 2016, **8**, 27772–27778.
- 95C. Rosman, J. Prasad, A. Neiser, A. Henkel, J. Edgar and C. Sönnichsen, *Nano Letters*, 2013, **13**, 3243–3247.
- 96R. A. Halvorson and P. J. Vikesland, *Environmental Science & Technology*, 2010, **44**, 7749–7755.
- 97W. F. Pearman, S. M. Angel, J. L. Ferry and S. Hall, *Applied spectroscopy*, 2008, **62**, 727–32.
- 98N. E. Mircescu, M. Oltean, V. Chiş and N. Leopold, *Vibrational Spectroscopy*, 2012, **62**, 165–171.
- 99X. Wang, X. Qian, J. J. Beitler, Z. (Georgia) Chen, F. R. Khuri, M. M. Lewis, H. J.-C. Shin, S. Nie and D. M. Shin, *Cancer Res.*, 2011, **71**, 1526–1532.
- 100 R. M. Jarvis and R. Goodacre, *Analytical chemistry*, 2004, **76**, 40–47.
- 101 A. A. Yanik, M. Huang, O. Kamohara, A. Artar, T. W. Geisbert, J. H. Connor and H. Altug, *Nano Letters*, 2010, **10**, 4962–4969.
- 102 J. D. Driskell, K. M. Kwarta, R. J. Lipert, M. D. Porter, J. D. Neill and J. F. Ridpath, *Anal. Chem.*, 2005, **77**, 6147–6154.
- 103 H. Zhou, D. Yang, N. P. Ivleva, N. E. Mircescu, R. Niessner and C. Haisch, *Anal. Chem.*, 2014, **86**, 1525–1533.
- 104 T. T. X. Ong, E. W. Blanch and O. A. H. Jones, *Sci. Total Environ.*, 2020, **720**, 137601.
- 105 A. Sivanesan, E. Witkowska, W. Adamkiewicz, Ł. Dziewit, A. Kamińska and J. Waluk, *Analyst*, 2014, **139**, 1037–1043.



- 106 A. Kamińska, E. Witkowska, K. Winkler, I. Dziegielelewski, J. L. Weyher and J. Waluk, *Biosens. Bioelectron.*, 2015, **66**, 461–467.
- 107 A. M. Giovannozzi, F. Rolle, M. Segal, M. C. Abete, D. Marchis and A. M. Rossi, *Food Chem.*, 2014, **159**, 250–256.
- 108 D. S. Moore and R. J. Scharff, *Anal. Bioanal. Chem.*, 2009, **393**, 1571–1578.
- 109 A. Campion and P. Kambhampati, *Chem. Soc. Rev.*, 1998, **27**, 241–250.
- 110 K. Kneipp, H. Kneipp, I. Itzkan, R. R. Dasari and M. S. Feld, *J. Phys. Condens. Matter*, 2002, **14**, R597–R624.
- 111 T. Vo-Dinh, *Trends Anal. Chem.*, 1998, **17**, 557–582.
- 112 J. D. Caldwell, O. J. Glembocki, F. J. Bezares, M. I. Kariniemi, J. T. Niinistö, T. T. Hatanpää, R. W. Rendell, M. Ukaegbu, M. K. Ritala, S. M. Prokes, C. M. Hosten, M. A. Leskelä and R. Kasica, *Opt. Express*, 2011, **19**, 26056–26064.
- 113 K. Kneipp, H. Kneipp and J. Kneipp, *Acc. Chem. Res.*, 2006, **39**, 443–450.
- 114 D. Graham, K. Faulds and W. E. Smith, *Chem. Commun.*, 2006, 4363–4371.
- 115 R. Pilot, R. Signorini, C. Durante, L. Orian, M. Bhamidipati and L. Fabris, *Biosens.*, 2019, **9**, 57–156.
- 116 Y. Zhang, B. Walkenfort, J. H. Yoon, S. Schlücker and W. Xie, *Phys. Chem. Chem. Phys.*, 2015, **17**, 21120–21126.
- 117 P. A. Mosier-Boss, *Nanomaterials*, 2017, **7**, 142–172.
- 118 A. L. Cook, C. S. Carson, C. E. Marvinney, T. D. Giorgio and R. R. Mu, *J. Raman Spectrosc.*, 2017, **48**, 1116–1121.
- 119 B. H. Nguyen, V. H. Nguyen and H. N. Tran, *Adv. Nat. Sci: Nanosci. Nanotechnol.*, 2016, **7**, 033001–033012.
- 120 Y. Xie, S. Yang, Z. Mao, P. Li, C. Zhao, Z. Cohick, P.-H. Huang and T. J. Huang, *ACS Nano*, 2014, **8**, 12175–12184.
- 121 X. Wang, S. Xu, H. Li, J. Tao, B. Zhao and W. Xu, *J. Raman Spectrosc.*, 2012, **43**, 459–463.
- 122 A. Yu. Panarin, S. N. Terekhov, K. I. Kholostov and V. P. Bondarenko, *Appl. Surf. Sci.*, 2010, **256**, 6969–6976.
- 123 T. Szymborski, E. Witkowska, W. Adamkiewicz, J. Waluk and A. Kamińska, *Analyst*, 2014, **139**, 5061–5064.
- 124 Y. He, S. Su, T. Xu, Y. Zhong, J. A. Zapien, J. Li, C. Fan and S.-T. Lee, *Nano Today*, 2011, **6**, 122–130.
- 125 X. Liu, Q. Hu, Q. Wu, W. Zhang, Z. Fang and Q. Xie, *Colloids Surf. B*, 2009, **74**, 154–158.
- 126 A. Janotti and C. G. Van de Walle, *Rep. Prog. Phys.*, 2009, **72**, 126501–126530.
- 127 Z. Yi, X. Xu, X. Kang, Y. Zhao, S. Zhang, W. Yao, Y. Yi, J. Luo, C. Wang, Y. Yi and Y. Tang, *Surf. Coat. Tech.*, 2017, **324**, 257–263.
- 128 P.-H. Lei and C.-H. Cheng, *Mater. Sci. Semicond. Proc.*, 2017, **57**, 220–226.
- 129 Y. S. Park and J. R. Schneider, *Journal of Applied Physics*, 1968, **39**, 3049.
- 130 G. Barbillon, *Coatings*, 2019, **9**, 86.
- 131 D. C. Mayo, C. E. Marvinney, E. S. Bililign, J. R. McBride, R. R. Mu and R. F. Haglund, *Thin Solid Films*, 2014, **553**, 132–137.
- 132 E. Thouti, N. Chander, V. Dutta and V. K. Komarala, *J. Opt.*, 2013, **15**, 035005–035012.
- 133 S. Rezaee, *Results Phys.*, 2018, **9**, 1521–1524.

- 134 B. Amin-Ahmadi, H. Idrissi, M. Galceran, M. S. Colla, J. P. Raskin, T. Pardoen, S. Godet and D. Schryvers, *Thin Solid Films*, 2013, **539**, 145–150.
- 135 M. Bechelany, X. Maeder, J. Riesterer, J. Hankache, D. Lerose, S. Christiansen, J. Michler and L. Philippe, *Cryst. Growth Des.*, 2010, **10**, 587–596.
- 136 J. Schindelin, I. Arganda-Carreras, E. Frise, V. Kaynig, M. Longair, T. Pietzsch, S. Preibisch, C. Rueden, S. Saalfeld, B. Schmid, J.-Y. Tinevez, D. J. White, V. Hartenstein, K. Eliceiri, P. Tomancak and A. Cardona, *Nat. Methods*, 2012, **9**, 676–682.
- 137 C. A. Schneider, W. S. Rasband and K. W. Eliceiri, *Nat. Methods*, 2012, **9**, 671–675.
- 138 *MATLAB R2019a*, The Mathworks, Inc., Natick, Massachusetts, United States.
- 139 Y. Nishijima, Y. Hashimoto, L. Rosa, J. B. Khurgin and S. Juodkazis, *Adv. Opt. Mater.*, 2014, **2**, 382–388.
- 140 J. Dunkers and H. Ishida, *Spectrochim. Acta A*, 1995, **51**, 855–867.
- 141 A. Krylov, A. Vtyurin, P. Petkov, I. Senkovska, M. Maliuta, V. Bon, T. Heine, S. Kaskel and E. Slyusareva, *Phys. Chem. Chem. Phys.*, 2017, **19**, 32099–32104.
- 142 C. A. Patil, I. J. Pence, C. A. Lieber and A. Mahadevan-Jansen, *Opt. Lett.*, *OL*, 2014, **39**, 303–306.
- 143 H. Sato, H. Chiba, H. Tashiro and Y. Ozaki, *J. Biomed. Opt.*, 2001, **6**, 366.
- 144 S. J. Cho, Y.-H. Ahn, K. K. Maiti, U. S. S. Dinish, C. Y. Fu, P. Thoniyot, M. Olivo and Y.-T. Chang, *Chemical Communications*, 2010, **46**, 722–724.
- 145 D. He, B. Hu, Q.-F. Yao, K. Wang and S.-H. Yu, *ACS Nano*, 2009, **3**, 3993–4002.
- 146 C.-L. Zhang, K.-P. Lv, H.-P. Cong and S.-H. Yu, *Small*, 2012, **8**, 648–653.
- 147 A. J. Chung, Y. Suk Huh and D. Erickson, *Nanoscale*, 2011, **3**, 2903–2908.
- 148 T. K. Sinha, S. K. Ghosh, R. Maiti, S. Jana, B. Adhikari, D. Mandal and S. K. Ray, *ACS Appl. Mater. Interfaces*, 2016, **8**, 14986–14993.
- 149 J. Guo, F. Zeng, J. Guo and X. Ma, *Journal of Materials Science & Technology*, 2020, **37**, 96–103.
- 150 K. B. Kim, J.-H. Han, H. Choi, H. C. Kim and T. D. Chung, *Small*, 2012, **8**, 378–383.
- 151 Y.-J. Oh and K.-H. Jeong, *Lab on a Chip*, 2014, **14**, 865.
- 152 H.-Y. Wu and B. T. Cunningham, *Nanoscale*, 2014, **6**, 5162–5171.
- 153 C. Novara, A. Lamberti, A. Chiadò, A. Virga, P. Rivolo, F. Geobaldo and F. Giorgis, *RSC Advances*, 2016, **6**, 21865–21870.
- 154 H. Pu, W. Xiao and D.-W. Sun, *Trends in Food Science & Technology*, 2017, **70**, 114–126.
- 155 Z. Kang, Y. Gu, X. Yan, Z. Bai, Y. Liu, S. Liu, X. Zhang, Z. Zhang, X. Zhang and Y. Zhang, *Biosensors & bioelectronics*, 2015, **64**, 499–504.
- 156 Y. Xie, S. Yang, Z. Mao, P. Li, C. Zhao, Z. Cohick, P.-H. Huang and T. J. Huang, *ACS nano*, 2014, **8**, 12175–12184.
- 157 S. H. Lee, H. J. Lee, D. Oh, S. W. Lee, H. Goto, R. Buckmaster, T. Yasukawa, T. Matsue, S.-K. Hong, H. Ko, M.-W. Cho and T. Yao, *The journal of physical chemistry. B*, 2006, **110**, 3856–9.
- 158 M. Ladanov, P. Algarin-Amaris, G. Matthews, M. Ram, S. Thomas, A. Kumar and J. Wang, *Nanotechnology*, 2013, **24**, 375301.
- 159 Y. Zhang, B. Walkenfort, J. H. Yoon, S. Schlücker and W. Xie, *Physical Chemistry Chemical Physics*, 2015, **17**, 21120–21126.
- 160 A. L. Cook, C. S. Carson, C. E. Marvinney, T. D. Giorgio and R. R. Mu, *Journal of Raman Spectroscopy*, 2017, **48**, 1116–1121.

- 161 A. Janotti and C. G. Van de Walle, *Reports on Progress in Physics*, 2009, **72**, 126501.
- 162 D. C. Mayo, J. R. Nolen, A. Cook, R. R. Mu and R. F. Haglund, eds. A. V. Kabashin, D. B. Geohegan and J. J. Dubowski, San Francisco, California, United States, 2016, p. 97370I.
- 163 Y. Suzuki and A. Tachibana, *Applied optics*, 1975, **14**, 2809–10.
- 164 C. A. Bennett, *Principles of Physical Optics*, John Wiley & Sons, Hoboken, NJ, 1st edn., 2008.
- 165 A. Sengupta, N. Brar and E. J. Davis, *Journal of Colloid and Interface Science*, 2007, **309**, 36–43.
- 166 S. S. Masango, R. A. Hackler, N. Large, A.-I. Henry, M. O. McAnally, G. C. Schatz, P. C. Stair and R. P. Van Duyne, *Nano Letters*, 2016, **16**, 4251–4259.
- 167 J. Wang, X. Gao, H. Sun, B. Su and C. Gao, *Materials Letters*, 2016, **162**, 142–145.
- 168 M. V. Cañamares, C. Chenal, R. L. Birke and J. R. Lombardi, *Journal of Physical Chemistry C*, 2008, **112**, 20295–20300.
- 169 W. Meng, F. Hu, L.-Y. Zhang, X.-H. Jiang, L.-D. Lu and X. Wang, *Journal of Molecular Structure*, 2013, **1035**, 326–331.
- 170 T. Watanabe and B. Pettinger, *Chemical Physics Letters*, 1982, **89**, 501–507.
- 171 L. Angeloni, G. Smulevich and M. P. Marzocchi, *Journal of Raman Spectroscopy*, 1979, **8**, 305–310.
- 172 E. J. Liang, X. L. Ye and W. Kiefer, *Journal of Physical Chemistry A*, 1997, **101**, 7330–7335.
- 173 F. A. Harraz, A. A. Ismail, B. Houcine, S. A. Al-Sayari, A. Al-Hajry and M. S. Al-Assiri, *Applied Surface Science*, 2015, **331**, 241–247.
- 174 M. A. Palafox, *International Journal of Quantum Chemistry*, 2000, **77**, 661–684.
- 175 L. A. Leites, S. Bukalov, T. S. Yadritzeva, M. K. Mokhov, B. A. Antipova, T. M. Frunze and V. V Dement, *Macromolecules*, 1992, **25**, 2991–2993.
- 176 M. J. Shenton, H. Herman and G. C. Stevens, *Polymer International*, 2000, **49**, 1007–1013.
- 177 R. P. S. De Campos, I. V. P. Yoshida, M. C. Breitreitz, R. J. Poppi and J. A. F. Da Silva, *Spectrochimica Acta Part A: Molecular and Biomolecular Spectroscopy*, 2013, **100**, 67–71.
- 178 L. Bistričić, V. Borjanović, L. Mikac and V. Dananić, *Vibrational Spectroscopy*, 2013, **68**, 1–10.
- 179 L. Jayes, A. P. Hard, C. Séné, S. F. Parker and U. A. Jayasooriya, *Analytical Chemistry*, 2003, **75**, 742–746.
- 180 N. E. Mircescu, M. Oltean, V. Chiş and N. Leopold, *Vib. Spectrosc.*, 2012, **62**, 165–171.
- 181 X. Chen, Y. Hu, J. Gao, Y. Zhang and S. Li, *Appl Spectrosc*, 2013, **67**, 491–497.
- 182 K. S. Dogbevi, B. K. D. Ngo, C. W. Blake, M. A. Grunlan and G. L. Coté, *ACS Appl. Polym. Mater.*, 2020, **2**, 1731–1738.
- 183 A. L. Cook, F. Xue and T. D. Giorgio, in *Proceedings of The 6th World Congress on Recent Advances in Nanotechnology*, Avestia, 2021.
- 184 J. W. Steed, *Coordination Chemistry Reviews*, 2001, **215**, 171–221.
- 185 Y. K. Agrawal, P. Shrivastav and S. K. Menon, *Separation and Purification Technology*, 2000, **20**, 177–183.
- 186 R. Li, G. Yang, J. Yang, J. Han, J. Liu and M. Huang, *Food Control*, 2016, **68**, 14–19.
- 187 M. V. Cañamares, C. Chenal, R. L. Birke and J. R. Lombardi, *J. Phys. Chem. C*, 2008, **112**, 20295–20300.
- 188 E. J. Liang, X. L. Ye and W. Kiefer, *J. Phys. Chem. A*, 1997, **101**, 7330–7335.

- 189 T. Watanabe and B. Pettinger, *Chemical Physics Letters*, 1982, **89**, 501–507.
- 190 L. Angeloni, G. Smulevich and M. P. Marzocchi, *J. Raman Spectrosc.*, 1979, **8**, 305–310.
- 191 F. A. Harraz, A. A. Ismail, H. Bouzid, S. A. Al-Sayari, A. Al-Hajry and M. S. Al-Assiri, *Applied Surface Science*, 2015, **331**, 241–247.
- 192 W. Meng, F. Hu, L.-Y. Zhang, X.-H. Jiang, L.-D. Lu and X. Wang, *Journal of Molecular Structure*, 2013, **1035**, 326–331.
- 193 J. Wang, X. Gao, H. Sun, B. Su and C. Gao, *Materials Letters*, 2016, **162**, 142–145.